

THE DESIGN AND CONSTRUCTION OF AN ELECTROCALORIC EFFECT (ECE)  
REFRIGERATION FACILITY

by

Nathan Haggerty

A thesis submitted in partial fulfillment of

the requirements for the degree of

Master of Science

(Mechanical Engineering)

at the

UNIVERSITY OF WISCONSIN – MADISON

2013

This page intentionally left blank

APPROVED BY

---

PROFESSOR GREGORY F. NELLIS

---

PROFESSOR SANFORD A. KLEIN

DATE: \_\_\_\_\_

This page intentionally left blank

**ABSTRACT**

The electrocaloric effect (ECE) could be utilized to create an efficient, low cooling power refrigeration cycle. The electrocaloric effect results from entropy changes caused by an external electric field. This entropy variation induces a temperature change within the electrocaloric material and the temperature variations are used to cool a load.

A numerical MATLAB model of a parallel plate electrocaloric refrigeration cycle was previously created. This thesis uses the existing model to design an electrocaloric refrigeration cycle while maximizing the cooling power of the cycle. Next, possible methods of constructing the optimized electrocaloric refrigeration cycle are examined.

In January 2013 it was determined that no electrocaloric material would be available for this project. Therefore, a regenerative heat exchanger of the same geometry as the optimized electrocaloric refrigeration system was built with passive regenerator films instead of electrocaloric films. This was done so that a comparison between the experimental device and the modeled results could be accomplished. The experimental device showed that, once the support structure of the heat exchanger was taken into account, the effectiveness between the experimental and modeled results as a constant offset of roughly 0.18 .

## **ACKNOWLEDGEMENTS**

First I want to thank my parents for pushing me to succeed academically. Thank you for helping me for long hours when I was struggling early in my academic career. Your love and support mean everything to me.

Next I want to thank my advisors Greg Nellis and Sanford Klein. Without your support, knowledge, and expertise I would have never have accomplished my project. Whenever I was stuck you always pointed me in the correct direction.

Without my high school mentor and coach, Jeff Lindlief, I doubt that I would have been successful in college. You taught how to work hard and persevere through difficult situations. You not only turned my life around physically, but academically as well.

I want to give a big shout out to Mark, Tom and everyone else at the student shop. You taught me how to manufacture systems starting from square one. Before working with you I don't think I knew which side of a hammer is used to hit things.

Thank you Kyle Rule, John Edlebeck Brad Moore, Erik Alar, Bryan Leyde, Amir Jahromi, Avi Friedman, Joe Shinnars, Kelsey McCusker and everyone else at the Solar Energy Lab. I doubt that I could have completed my classes without all of your help and when I was stuck on my research you were always happy to lend me a helping hand. I am glad that we had the opportunity to participate in all of our office shenanigans. I don't think I will be buying shelled peanuts any time soon and I feel like I am going to keep finding Congrats Brad ribbons in random places for years to come.

## TABLE OF CONTENTS

<b>ABSTRACT.....</b>	<b>I</b>
<b>ACKNOWLEDGEMENTS.....</b>	<b>II</b>
<b>TABLE OF CONTENTS.....</b>	<b>III</b>
<b>TABLE OF FIGURES.....</b>	<b>VI</b>
<b>TABLE OF TABLES.....</b>	<b>XI</b>
<b>NOMENCLATURE.....</b>	<b>XII</b>
<b>CHAPTER 1: LITERATURE REVIEW.....</b>	<b>1</b>
1.1 Motivation.....	1
1.2 The Carnot Cycle .....	1
1.3 Vapor Compression Cycles.....	2
1.4 Peltier Thermoelectric Effect .....	2
1.5 Magnetocaloric Effect (MCE) .....	3
1.6 Electrocaloric Effect (ECE) .....	4
1.7 Current ECE Refrigeration Systems .....	5
1.8 Advantages and Disadvantages of EC Refrigeration .....	7
1.9 Intent of Project .....	7
1.10 References.....	7
<b>CHAPTER 2: CREATION OF A MATLAB MODEL.....</b>	<b>9</b>
2.1 Steady State Modeling Assumptions .....	10
2.2 Thermodynamics of Electrocaloric materials.....	10
2.3 Electrocaloric Material (Regenerator) Thermal Energy Balance .....	14
2.4 Fluid Thermal Energy Balance .....	19
2.5 Correlations .....	21
2.6 Discretizing Energy Balances .....	23
2.7 Achieving a Steady State Solution.....	29
2.8 Post Processing.....	31
2.9 Quasi Transient Modeling Analysis .....	31
2.9.1 Transient Model Assumptions .....	32

2.9.2	Quasi Transient Model Operation .....	33
2.9.3	Transient Model results .....	35
2.10	References.....	36
<b>CHAPTER 3:    ELECTROCALORIC REFRIGERATOR PARAMETER OPTIMIZATION.....</b>		<b>37</b>
3.1	Qualitative View of a Transient Fluid Particle .....	38
3.2	Steady State Two Film ECE Bed Optimization .....	39
3.2.1	Minimum Blow Time.....	40
3.2.2	Channel Thickness.....	41
3.2.3	Mass Flow Rate Optimization .....	43
3.2.4	Steady State Optimization Results.....	45
3.3	References.....	45
<b>CHAPTER 4:    PROTOTYPE DESIGN .....</b>		<b>46</b>
4.1	Initial EC Bed Design.....	46
4.2	Second ECE Bed Design Iteration .....	48
4.2.1	Calculated Pressure Drop.....	51
4.2.2	Cold Space Sizing.....	53
4.2.3	Thermal Resistance Analysis .....	54
4.3	Electrical System Design.....	58
4.3.1	ECE Film Electrical Capacitance .....	58
4.3.2	Electrical Circuit Design.....	60
4.4	Warm Heat Exchanger .....	64
4.5	Cold Heat Exchanger .....	65
4.6	Pump .....	65
4.7	References.....	67
<b>CHAPTER 5:    PROTOTYPE CONSTRUCTION .....</b>		<b>68</b>
5.1	Initial ECE Bed Prototype Construction.....	68
5.2	Prototype Construction Problems.....	72
5.3	Flow Visualization Prototype .....	73
5.4	System Operating as a Regenerative Heat Exchanger .....	77

5.4.1	A study of Non-uniform Fluid Channel Thicknesses .....	81
5.4.2	Tensioning the Regenerator Films .....	86
5.4.3	Manufacturing the Heat Transfer Prototype .....	90
5.5	Sealing the Heat Transfer Device .....	100
5.6	Building the Second Heat Transfer Device .....	101
5.7	Manifold Test .....	104
5.8	Vacuum Chamber .....	112
5.9	Measurement System .....	114
5.9.1	Uncertainty Analysis .....	117
5.10	References.....	120
<b>CHAPTER 6:</b>	<b>EXPERIMENTAL RESULTS .....</b>	<b>121</b>
6.1	Measured Pressure Drop .....	121
6.2	Thermal Results.....	126
6.2.1	Calculating effectiveness: .....	132
6.2.2	Axial Conduction and NTU Dominated Regions .....	137
6.2.3	Support Structure Capacitance .....	140
6.3	A Comparison Between Experimental Results and Modeled Predictions .....	142
6.3.1	Compensating for the Support Structure in the Model.....	143
6.3.2	Fitting the Model to Experimental Data .....	146
6.4	Model Sensitivity Analysis .....	147
6.5	Conclusions.....	150
6.6	Next Steps and Future Work .....	153
6.7	References.....	154

**TABLE OF FIGURES**

Figure 1-1: The Electrocaloric Refrigeration Cycle (Scott, 2011).....	4
Figure 2-1: One bed diagram of the proposed electrocaloric refrigeration system (Knier, 2012). .....	9
Figure 2-2: Regenerator material energy balance (Knier, 2012) .....	15
Figure 2-3: Fluid energy balance (Knier, 2012).....	19
Figure 2-4: Discretized computational grid for the MATLAB model (Knier, 2012).....	24
Figure 2-5: The model's heat exchanger geometry.....	33
Figure 3-1: A system view of the proposed ECE refrigeration cycle.....	37
Figure 3-2: Tracking a fluid particle through one complete steady state cycle of the proposed electrocaloric refrigeration system .....	39
Figure 3-3: The initial cooling power as a function of the mass flow rate for various channel thicknesses.....	41
Figure 3-4: The maximum cooling power as a function of load temperature for various channel thicknesses. ....	42
Figure 3-5: The cooling power to a load temperature of 283 K as a function of the mass flow rate for various channel thicknesses .....	43
Figure 3-6: The maximum possible cooling power from a two film ECE refrigeration bed with a channel thickness of 0.076 mm and the mass flow rate required to achieve that cooling power. ....	44
Figure 4-1: The Initial design of the demonstration device.....	47
Figure 4-2: Exploded view of the second design iteration .....	48
Figure 4-3: Thermal resistor network.....	54
Figure 4-4: An 11 layer multilayer ECE film arrangement. ....	59
Figure 4-5: The circuit diagram for a one bed ECE refrigeration system.....	60
Figure 4-6: The four important electrical states of the proposed ECE refrigeration cycle. ...	61
Figure 4-7: The complete ECE refrigeration system's circuit diagram. ....	63
Figure 4-8: The effectiveness of the cold heat exchanger as a function of the length over the diameter of the heat exchanger. ....	64
Figure 4-9: An NE-1000 New Era Pump Systems, Inc. Syringe pump (NE-1000 Programmable Single Syringe Pump, 2013) .....	66
Figure 4-10: New Era Pump Systems, Inc. Ana-Box – closed loop analog sensor interface... ..	66
Figure 5-1: The initial design of the film tensioning rig. ....	68
Figure 5-2: Epoxying the water tubing to the external manifolds.....	69
Figure 5-3: Tensioning layer with spacing adhesive .....	69
Figure 5-4: Reinforcing plate.....	70
Figure 5-5: Tensioning layer assembly adhered to the reinforcing plate.....	70

Figure 5-6: Closed EC bed .....	71
Figure 5-7: Completed initial prototype. ....	72
Figure 5-8: The improved tensioning rig.....	73
Figure 5-9: A clear prototype of the proposed ECE refrigeration system .....	74
Figure 5-10: A one second time-lapse of the injection of die into a clear ECE refrigeration bed prototype. ....	75
Figure 5-11: Fluid flow can be seen going around the fluid channel. ....	76
Figure 5-12: Trapped air within the ECE bed when using the surfactant based air reduction method.....	77
Figure 5-13: Correlation between the center temperature and the heat transfer across one stack of regenerator films when the cold space is 298 [k]. ....	78
Figure 5-14: Qualitative view tracking a fluid particle through the proposed regenerative heat exchanger design. ....	80
Figure 5-15: The ratio of the pressure drop through a bed consisting of one non uniform channel over the pressure drop of a bed consisting of entirely nominal channels as a function of the relative thickness of the non-uniform channel compared to the nominal channels .....	83
Figure 5-16: The ratio of mass flow rate through a non-uniform channel over the mass flow rate through a nominal channel within the same 11 channel device as a function the thickness of a non-uniform channel over the thickness of a nominal channel.....	84
Figure 5-17: Pressure drop as a function of internal manifold thickness. The blue dot denotes the nominal channel thickness. ....	85
Figure 5-18: The force balance for an angled beam under tension (Young, 2002).....	86
Figure 5-19: The deflection at the center of the regenerator film as a function of the applied tensile force .....	89
Figure 5-20: The planned layout of the regenerative heat exchanger that simulates the electrocaloric refrigeration cycle .....	90
Figure 5-21: Transfer tape stencils beside the corresponding transfer tape cutouts. ....	91
Figure 5-22: The layout of one repeated layer of the regenerative heat exchanger .....	92
Figure 5-23: (a) A top down view of the completed stack of 10 regenerator films, (b) a close up view of the future location of the internal manifolds, (c) the corner of the regenerative films and (d) the edge of the spacing layer.....	93
Figure 5-24: (a) The tensioning layer was placed on the tensioning jig and slits (b) were cut in the tensioning layer. ....	94
Figure 5-25: Tensioning the stacks of regenerative films using the tensioning jig. ....	95

Figure 5-26: The internal manifolds (a) adhered to the tensioning layer, (b) the second set of internal manifolds placed directly on top of the first set with their adhesive facing upward and (c) the internal manifolds installed on the port plate. ....	96
Figure 5-27: (a) A close up view of the separation that occurred from cutting of the stainless steel spacers with arrows designating the locations of the deformations and (b) an exaggerated illustration of the deformation. ....	97
Figure 5-28: (a) Top view of the heat exchanger after the center heater was installed and (b) the heater mounted in the device. ....	98
Figure 5-29: A view of the port plate after it was adhered to the regenerative heat exchanger. ....	99
Figure 5-30: (a) The bottom of the external manifold. (b) The top of the external manifold. ....	99
Figure 5-31: (a) The regenerative heat exchanger with the two external manifolds installed and (b) the edge of the heat exchanger after it was sealed with epoxy. ....	100
Figure 5-32: The transient pressure of the bed when the epoxy gave way. ....	101
Figure 5-33: Regenerator assembly being cut with a slitting saw on a mill. ....	102
Figure 5-34: The bottom of one of the external manifolds after the fluid channel had been plugged with Stycast 1266. ....	103
Figure 5-35: Clamping the external manifolds while the epoxy is applied to ensure that the fluid channel stay open. ....	104
Figure 5-36: Exploded view of the manifold test device. ....	105
Figure 5-37: (a) One external manifold with adhesive to temporarily hold it in place, (b) the port plate side of the device with internal and external manifolds attached, (c) the reinforcing plate with internal manifolds attached and (d) the assembled manifold test device before sealing with epoxy. ....	106
Figure 5-38: The second iteration of the manifold test. ....	107
Figure 5-39: The internal manifold test installed in the system (a) with C clamps installed and (b) without C clamps. ....	108
Figure 5-40: The pressure drop through the manifold test device for various volumetric flow rates and the model predicted pressure drop assuming an internal manifold channel thickness of 56 $\mu$ m. ....	109
Figure 5-41: A qualitative view of the deformation and forces within the manifold test device when in pumping mode (a) and qualitative view of the deformation and forces within the manifold test device when in withdrawing mode (b). Red arrows denote forces. ....	110
Figure 5-42: The insulating vacuum chamber with electrical and fluid feedthroughs. ....	113
Figure 5-43: (a) The fluid feedthrough into the vacuum chamber and (b) the wire feedthrough. ....	114

Figure 5-44: (a) bottom view of the regenerator mounted in the vacuum and (b) a top view of the mounted regenerator.....	114
Figure 5-45: The series temperature measurement circuit.....	115
Figure 5-46: The parallel temperature measurement circuit.....	116
Figure 5-47: Heater power and thermistor resistance uncertainties.....	118
Figure 5-48: The measurement error and total error as a function of thermistor temperature .....	119
Figure 6-1: A comparison of the measured and calculated pressure drop for the first heat transfer device that was constructed. ....	122
Figure 6-2: Boundary layers accounted for in the EES duct flow pressure drop model.....	123
Figure 6-3: The measured pressure drop and calculated pressure drop through the second heat transfer device. ....	124
Figure 6-4: The measured pressure drop and the calculated pressure drop assuming that the internal manifold gaps are 0.025 mm larger than their nominal value. ....	125
Figure 6-5: Temperature sensor locations.....	126
Figure 6-6: Transient temperatures with T1 placed directly below the internal manifolds, T2 at the center of the bed and T3 on the external manifold closest to T1.....	127
Figure 6-7: A zoomed in view of the attenuation that occurs through the external manifolds. ....	128
Figure 6-8: Temperature as a function of Heater power when the pump was controlling the flow direction and when the computer was controlling the flow direction. ....	129
Figure 6-9: Verification that the temperature at the two ends of the device is out of phase. ....	131
Figure 6-10: Experimental heat exchanger effectiveness as a function of Reynolds number .....	136
Figure 6-11: Axial conduction parameter as a function of Reynolds number.....	138
Figure 6-12: Calculated number of transfer units (NTU) as a function of Reynolds number .....	139
Figure 6-13: Modeled effectiveness and experimentally determined effectiveness as a function of Reynolds number without compensating for the support structure. ....	142
Figure 6-14: Modeled effectiveness and experimentally determined effectiveness as a function of Reynolds number after compensating for the support structure. ....	145
Figure 6-15: Optimized modeled effectiveness and the experimental effectiveness as a function of Reynolds number. ....	147
Figure 6-16: An examination of the regenerator effectiveness for several regenerator capacitance values while the thermal conductivity is set to a constant $62.27 \text{ W/m}^2\text{-K}$ .....	148

Figure 6-17: An examination of the regenerator effectiveness for several axial conduction resistances while the specific capacity of the regenerator material is set to a constant 15000 J/kg-K..... 149

## TABLE OF TABLES

Table 2-1: Input parameters for the transient model operation .....	35
Table 3-1: Fixed independent bed parameters .....	40
Table 3-2: Summary table of ECE bed dimension and operating conditions .....	45
Table 4-1: Layers of the two film electrocaloric refrigeration device .....	50
Table 4-2: Pressure drop across various portions of the fluid channel within the EC refrigeration system (Munson, Young, Okiishi, & Huebsch, 2009). .....	53
Table 5-1: A comparison of select heat transfer related properties between PVDF and Strategic Polymer Sciences' electrocaloric polymer. (Iguchi, dos Santos, & Gregorio Jr., 2007), (Knier, 2012) .....	80
Table 5-2: Manufacturer provided voltage uncertainties for the data acquisition card used .....	117
Table 5-3: Multimeter resistance uncertainty .....	118
Table 5-4: Manufacturer provided pressure transducer calibration data.....	120
Table 6-1: A summary of the axial conduction resistances .....	132
Table 6-2: Temperature data various mass flow rates with a heater power of 1 watt and a blow time of 10 seconds .....	135
Table 6-3: The measured temperatures and calculated effectiveness for several trials while operating at a flow rate of 22.4 mL/min, a 10 second blow time and 1 watt of power .....	137
Table 6-4: The thermal capacitance for the major parts of the prototype .....	141

## Nomenclature

$A$	Area ( $m^2$ )
$A_s$	Surface area
$A_c$	Cross sectional area of a stack of films ( $m^2$ )
$AR$	Area ratio (-)
$a_s$	The ratio of total surface area to the volume of the bed (1/m)
$\alpha$	Thermal diffusivity ( $m^2/s$ )
$\alpha_i$	Thermal diffusivity of polyethylene ( $m^2/s$ )
$c$	Specific heat capacity (J/kg-K)
	The number of species present (-)
$c_c$	Specific heat capacity of the cold side heat exchanger (J/kg-K)
$c_E$	Specific heat capacity at constant electric field (J/kg-K)
$c_{max}$	Maximum specific heat capacity (J/kg-K)
$c_{min}$	Minimum specific heat capacity (J/kg-K)
$c_f$	Specific heat capacity of the working fluid (J/kg-K)
$c_r$	Specific heat capacity of the regenerator material (J/kg-K)
$C$	Total electrical capacitance of one electrocaloric film (F)
$C_c$	Total thermal capacitance of the cold side heat exchanger (J/K)
$C_s$	Effective thermal capacitance of the support structure (J/K)
$C_L$	Electrical capacitance of one layer of the electrocaloric film (F)
$\dot{C}_{min}$	Minimum heat capacity rate (W/K)
$C$	Total capacitance of the regenerator material (J/K)
$C_f$	Specific heat capacity of a fluid (J/kg-K)
$d_{in}$	Inside diameter (m)
$d_{out}$	Outside diameter (m)
$D_h$	Hydraulic diameter (m)
$D$	Diameter (m)
$De$	Change in energy (J)
$Dt$	change in time (s)
$\Delta P$	Pressure difference (Pa)
$\Delta t$	Length of one time step (s)
$\Delta T$	Temperature difference (K)
$\Delta V$	Voltage difference (V)
$\Delta x$	Length of one spatial step (m)
$\varepsilon$	Porosity (-)
	Effectiveness (-)
$\varepsilon_0$	Permeability of free space (8.854e-12 F/m)

$\varepsilon_{hx}$	Heat exchanger effectiveness (-)
$E$	Electric field (V/m)
$E_{max}$	Maximum allowable electric field applied to the electrocaloric film (V/m)
$f$	Frequency (Hz)
	Darcy friction factor (-)
	Number of intensive properties required to fix a thermodynamic state (-)
$f_{fan}$	Fanning Friction factor (-)
$g$	Acceleration of gravity (9.81 m/s <sup>2</sup> )
$h$	Specific enthalpy (J/kg)
$h_f$	specific enthalpy of the working fluid (J/kg-s)
$\bar{h}$	Average heat transfer coefficient (W/m <sup>2</sup> -K)
$\bar{h}_c$	Average heat transfer coefficient between the working fluid and the wall of the cold space (W/m <sup>2</sup> -K)
$h_{L,minor}$	Minor head loss (Pa)
$h_{L,major}$	Major head loss (Pa)
$H_B$	Height of one bed (m)
$I$	Current (A)
$I_{max}$	Maximum current draw (A)
$I_{ss}$	Steady state current (A)
$k$	Thermal conductivity (W/m-K)
	Loading factor (-)
$k_{eff}$	Effective bed thermal conductivity (W/m-K)
$k_e$	Thermal conductivity of the electrocaloric material (W/m-K)
$k_f$	Thermal conductivity of a fluid (W/m-K)
$k_{SS}$	Thermal conductivity of stainless steel (W/m-K)
$K_L$	Loss coefficient (-)
$K_{rel}$	Relative permeability (-)
$l$	Length (m)
$l_c$	Length of the cold space (m)
$l_{chan}$	Length of one fluid channel (m)
$L_d$	Thermal wave diffusion depth (m)
$L_e$	Length of one electrocaloric film (m)
$L_{end}$	Length of the end cap (m)
$L_{hx}$	Heat exchanger length (m)
$LC$	hysteresis loss coefficient (%)
$\lambda$	Axial conduction parameter (-)
$M$	Number of nodes in space (-)

$M_A$	Moment at point A (N-m)
$m$	Mass (kg)
$\dot{m}$	Mass flow rate (kg/s)
$\mu_f$	Fluid viscosity (Pa-s)
$N$	Number of nodes in time (-)
$N_e$	Number of electrocaloric films (-)
$NTU$	Number of transfer units (-)
$Nu$	Nusselt number (-)
$OBJ$	Objective function (-)
$p$	Number of phases (-) Pressure (Pa)
$P$	Polarization (Coulomb/m <sup>2</sup> ) Tensile force (N)
$q$	Energy transferred by heat (J)
$\dot{q}$	Thermal energy transfer rate (W)
$q_{loss}$	Thermal energy generation due to hysteresis (W)
$Q$	Thermal energy transferred (J)
$Q_{max}$	Maximum possible thermal energy transferred (J)
$\dot{Q}_c$	Cooling power provided to the cold side of the bed (W)
$\dot{Q}_{c,s}$	Heat transfer from the fluid inside the cold space to the outside surface of the cold space (W)
$\dot{Q}_h$	Heating power provided to the warm side of the bed (W)
$\dot{Q}_{h,s}$	Heat transfer from the warm space to the outside surface of the cold space through the support structure only (W)
$\dot{Q}_{leak}$	Heat leak through the support structure
$\dot{Q}_{r,s}$	Heat transfer from the outside surface of the cold space to the environment due to radiation (W)
$\rho$	Density (kg/m <sup>3</sup> )
$\rho_c$	Density of cold side heat exchanger (kg/m <sup>3</sup> )
$\rho_f$	Density of the working fluid (kg/m <sup>3</sup> )
$\rho_r$	Density of regenerator material (kg/m <sup>3</sup> )
$r$	Radius (m)
$R$	Thermal resistance (K/W)
$R_A$	Reaction force at point A (N)
$R_{ac}$	Axial conduction resistance (K/W)
$R_{cond,c}$	Conduction resistance between the inner wall of the cold space to the outer wall of the cold space (J/kg-K-s)

$R_{conv,c}$	Convection resistance between the working fluid and the wall of the cold space through the support structure only (J/kg-K-s)
$R_e$	Electrical resistance ( $\Omega$ )
$R_{flow}$	Flow resistance (1/m-s)
$R_{flow,tot}$	Total Flow resistance (1/m-s)
$R_{tot}$	Total thermal resistance (K/W)
$R_r$	Reference resistance ( $\Omega$ )
$R_{rad}$	Radiation resistance between the surface of the bed and the surroundings (K/W)
$Re$	Reynolds number (-)
$s$	Specific entropy (J/kg-K)
$s_{ref}$	Reference specific entropy (J/kg-K)
$S_{gen}$	Entropy generation (W/K)
$\dot{S}_{gen}$	Specific entropy generation rate (J/kg-K-s)
$\theta_A$	Angle between beam and the x axis at point A (rad)
$t$	Time (s)
$t_b$	Time for one blow (s)
$t_c$	Time to charge the electrocaloric film (s)
$th_{chan}$	Thickness of one fluid channel (m)
$t_{CTHB}$	Time of the cold to hot blow (s)
$t_d$	Time to discharge the electrocaloric film (s)
$t_{HTCB}$	Time of the hot to cold blow (s)
$th_{chan}$	Thickness of the fluid channel (m)
$th_e$	Electrocaloric film thickness (m)
$th_{end}$	Thickness of one of the end caps (m)
$th_L$	Thickness of one layer of the electrocaloric film (m)
$t_p$	Polarization time (s)
$T$	Temperature (K)
$T_{amb}$	Ambient temperature (K)
$T_C$	Temperature of the cold side of the bed (K)
$T_f$	Temperature of the working fluid (K)
$T_H$	Temperature of the warm side of the bed (K)
$T_{ini}$	Initial temperature (K)
$T_r$	Temperature of the regenerator material (K)
$T_{ref}$	Reference Temperature (K)
$T_s$	Temperature at the surface of the device just outside of the cold space (K)
$TC_i$	Current temperature of the cold side heat exchanger (K)
$TC_{i+1}$	Temperature of the cold side heat exchanger at the next time step (K)

$TF_i$	Current temperature of the fluid exiting the cold side of the ECE bed (K)
$u$	Specific internal energy (J/kg)
$u_f$	Specific internal energy of the working fluid (J/kg)
$u_r$	Specific internal energy of the regenerator material (J/kg)
$\dot{u}$	Total energy transfer rate into a control volume (W)
$UA$	Conductance (W/K)
$v$	Velocity (m/s)
$V$	Volume (m <sup>3</sup> ) Voltage (V)
$V_b$	Volume of water moved during each blow process (m <sup>3</sup> )
$V_c$	Volume of the cold space, the fluid volume between the two electrocaloric films (m <sup>3</sup> )
$V_{chan}$	Volume of one fluid channel (m <sup>3</sup> )
$V_{in}$	Voltage applied by the power supply (V)
$V_{max}$	Maximum allowable voltage applied to the leads of the electrocaloric films (V)
$w$	Energy transferred in the form of work (J)
$w_c$	Width of the cold space (m)
$w_{chan}$	Width of the fluid channel (m)
$w_e$	Width of one electrocaloric film (m)
$w_{end}$	Width of one of the end caps (m)
$\dot{w}$	Rate of work transferred (W)
$\omega$	Angular frequency (rad/s)
$x$	Position along the x axis in a Cartesian coordinate system (m)
$y$	Position along the y axis in a Cartesian coordinate system (m)

This page intentionally left blank



## **CHAPTER 1: LITERATURE REVIEW**

### *1.1 Motivation*

Due to the Second Law of Thermodynamics, exergy is required any time that thermal energy is transferred from a low temperature reservoir to a high temperature reservoir. Cycles that are designed to accomplish this are called refrigeration cycles. Refrigeration systems are widely used in applications such as human comfort, food preservation, electronics cooling, gas liquefaction and deep space detectors. The most extensively used refrigeration cycle is the vapor compression refrigeration cycle. However, other refrigeration methods, that do not require moving parts, are being developed for environments where the vapor compression cycle is not ideal.

### *1.2 The Carnot Cycle*

The Carnot Cycle is a theoretical cycle that provides the upper efficiency limit for all refrigeration cycles operating between two thermal reservoirs. This cycle consists of a reversible, isothermal increase in entropy at the cold reservoir temperature followed by a reversible, adiabatic and isentropic temperature change from the cold reservoir temperature to the warm reservoir temperature. Entropy is then reversibly and isothermally rejected at the warm reservoir temperature and, finally, there is a reversible, adiabatic and isentropic temperature change back to the cold reservoir temperature (Klein & Nellis, 2012).

The Carnot cycle consists entirely of reversible processes. However, The Second Law suggests that the cooling power of a reversible cycle would be zero. This implies that some irreversibilities are necessary for all practical refrigeration cycles.

### *1.3 Vapor Compression Cycles*

Vapor compression refrigeration cycles are the most common refrigeration cycles and are commonly used for human comfort and food preservation. These refrigeration systems are a well-developed technology, however, they are limited in the physical size due to the compressor that they require and often use environmentally harmful refrigerants. Vapor compression cycles usually use a positive displacement compressor, an evaporator and a condenser. The compressor of these systems can induce vibrations into the system which, for some applications, is not desirable.

### *1.4 Peltier Thermoelectric Effect*

The Peltier Effect is caused by joining dissimilar metals and applying a current to induce a heat flow through the device. Current refrigeration systems utilizing the Peltier Effect have coefficient of performances (COP's) much lower than current vapor compression cycles. However these devices can be built extremely small and are economically viable for refrigeration systems less than 50W (Diekmann, Cooperman, & Brodrick, 2011). In addition, these devices require large DC currents to operate effectively and therefore generate significant Ohmic heating. As a result, typical coefficients of performance for these devices range from 0.4 to 0.7 (Lu, Rozic, & Zhang, 2010).

In general, since solid state cooling methods do not have any moving parts, they can be small, often have high reliabilities, low noise and do not vibrate. Because of these advantages, the Peltier Thermoelectric Effect is often used in sensitive applications such as cooling electronics.

### *1.5 Magnetocaloric Effect (MCE)*

A subset of materials undergo a change in temperature when exposed to a changing magnetic field. This temperature change is caused by entropy changes within the material. In these cycles, a strong magnetic field is applied to a magnetocaloric material causing the magnetic dipoles to align, therefore decreasing the entropy of the material. This decrease in entropy is balanced by an increase temperature. Ideally, the result is an isentropic temperature increase. After some of the heat is rejected, the magnetic field is removed and the magnetic dipoles unalign. This causes an increase in entropy which is balanced by a decrease in temperature. Ideally, the result is an isentropic temperature decrease. This decrease in temperature is used for refrigeration (Quintero, Ghivelder, Gomes, Sacanell, & Parisi, 2012).

Producing the magnetic field, on the order of 1 tesla, required for magnetocaloric refrigeration is difficult because it requires an electromagnet with a large number of wrappings and a strong current. Frequently, to facilitate the required current, superconducting wire is required which, in turn, requires a significant cryogenic cooling system to be in place.

### 1.6 Electrocaloric Effect (ECE)

The electrocaloric effect is commonly thought to be the electrical equivalent to the MCE. In the ECE, an applied electric field causes the dipoles of a dielectric material to align, therefore, decreasing the entropy of the material. Like in the magnetocaloric effect, the decrease of entropy due to the alignment of the ions is balanced by an increase of entropy in the form of an increase in temperature. Thermal energy is rejected and then the electric field is then removed to provide temperatures below ambient. Typically, the temperature change induced by the ECE is smaller than the temperature change induced by the MCE. An electrocaloric refrigeration cycle is shown in Figure 1-1.

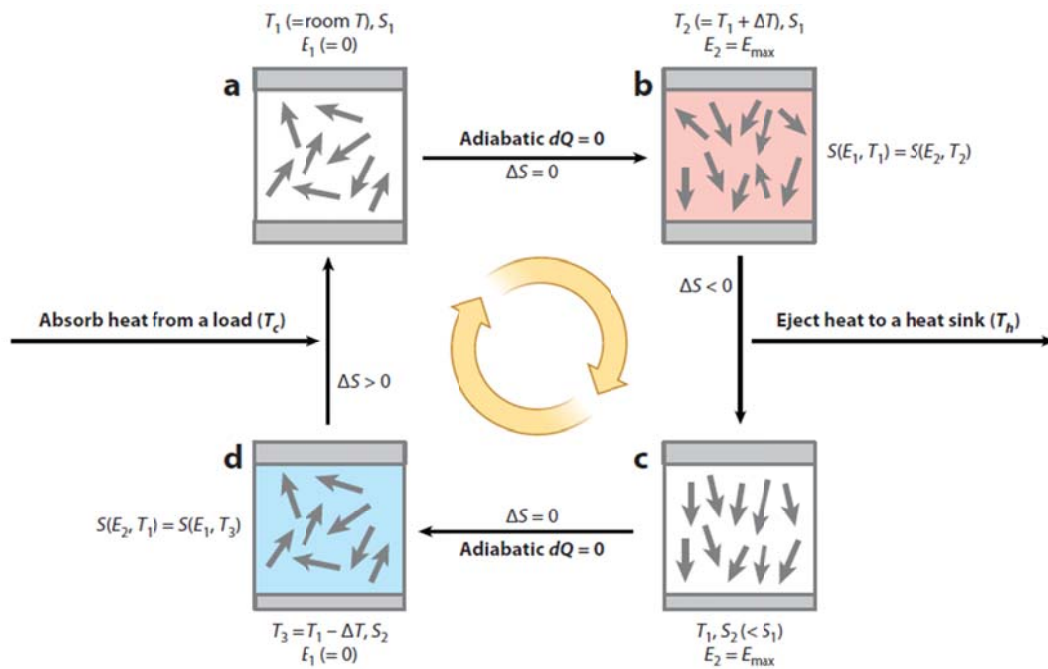


Figure 1-1: The Electrocaloric Refrigeration Cycle (Scott, 2011)

Initially, state a, the electrocaloric material is at ambient conditions. When an electric field is applied in state b, the ions rotate to align with one another and the electrocaloric

material compensates this decrease in entropy by increasing in temperature. If it is assumed that there are no irreversibilities, the entropy change due to the alignment of the ions is equal to the change in entropy due to the increase in temperature. Heat is then rejected from state b to state c while the material is experiencing the constant electric field.

The electric field then is removed in state d. When the electric field is removed the ions regain their random orientations with one another. This increases the entropy of the material. The material, again, compensates by decreasing in temperature. The material then absorbs thermal energy from the load to revert back to state a. This process is then repeated. However, because electrocaloric materials are not perfect, a hysteresis loss occurs when the ions align and unalign from one another (Knier, 2012).

### *1.7 Current ECE Refrigeration Systems*

Refrigeration cycles utilizing the ECE have been built. One of these cycles relies on the physical movement of the ECE film to come in contact with the heat sink and the thermal load (Jia & Ju, 2011). The maximum temperature difference of this device is limited by the temperature difference of the electrocaloric material. Also, by requiring a motor to physically move the EC material, this method of utilizing the ECE eliminates some of the advantages of solid state cooling.

Another method of utilizing the ECE involves moving a regenerator axially while the regenerator is continually in contact with the electrocaloric films (Gu, Qian, Li, Craven, & Zhu, 2013). Both of these methods are unable to provide continuous cooling to the thermal

load and require linear actuators near the device being cooled. Linear movement has the potential to induce vibrations into the system which is undesirable for sensitive systems.

A method that does not require motors to operate was developed by Neil Mathur and Alexandr Mischenko. Their method utilizes heat switches to direct the thermal energy to the load and heat sink. Although this technique does not require any moving parts, it is still limited by the temperature difference of the electrocaloric material that is used (Mathur & Mischenko, 2006).

An alternative electrocaloric refrigeration system that does not have these disadvantages is the fluid based system developed by Sinyavsky and Brodyansky (Sinyavsky & Brodyansky, 1992). In this device, fluid flows past two blocks of electrocaloric material that are operated out of phase of one another to allow for continuous cooling of a central heat exchanger. In Sinyavsky and Brodyansky's design, a pump is required but it can be placed far from sensitive components.

The electrocaloric material used during Sinyavsky and Brodyansky's experiments was capable of a temperature difference of 1.5K while the maximum achieved temperature difference of the device was nearly 5K (Sinyavsky & Brodyansky, 1992). This shows how a relatively small electrocaloric temperature difference can be magnified to achieve a much larger temperature difference. Recent advances in material science will allow for significant improvements to Sinyavsky and Brodyansky's design.

### *1.8 Advantages and Disadvantages of EC Refrigeration*

Electrocaloric materials are difficult to manufacture and require high electric fields to display significant temperature changes (Lu, Rozic, & Zhang, 2010). Due to the small volume of the electrocaloric material that can be currently manufactured, it is expected that any system that is built will provide a low cooling power. However, these refrigeration cycles can be built with very low volume. This is because, unlike magnetic refrigeration cycles, electrocaloric refrigeration cycles do not require large coils of wire or permanent magnets to generate the required electric field. The coefficient of performance, for a continuous cooling electrocaloric refrigeration system has been estimated to be up to 16 (Ju, 2010).

### *1.9 Intent of Project*

A two film, solid state, continuous, fluid based electrocaloric refrigeration cycle will be built inside a vacuum in order to demonstrate its feasibility and to improve on previous designs. The auxiliary facility will be designed and fabricated to facilitate testing of future electrocaloric refrigeration cycles. Finally, modeling results will be compared to experimental data in an attempt to validate the theoretical results.

### *1.10 References*

- Diekmann, J., Cooperman, A., & Brodrick, J. (2011). Solid-State Cooling, Part 1. ASHRAE Journal, 82-84.
- Gu, H., Qian, X., Li, X., Craven, B., & Zhu, W. (2013). A chip scale electrocaloric effect based cooling device. Applied Physics, 1077-3118.
- Jia, Y., & Ju, S. (2011). A solid-state refrigerator based on the electrocaloric effect. Applied Physics Letters.
- Ju, S. Y. (2010). Solid-State Refrigeration Based on the Electrocaloric Effect for Electronics Cooling. Journal of Electronic Packaging, 1-6.

Klein, S., & Nellis, G. (2012). *Thermodynamics*. New York: Cambridge University Press.

Knier, B. J. (2012). *A Thermodynamic Analysis of an Electrocaloric Effect (ECE) Refrigeration Cycle*. University of Wisconsin - Madison.

Lu, S. G., Rozic, B., & Zhang, Q. M. (2010). *Electrocaloric Effect (ECE) in Ferroelectric Polymer*. *Ferroelectrics*.

Mathur, N., & Mischenko, A. (2006). Patent No. 056809. United States of America.

Quintero, M., Ghivelder, L., Gomes, A. M., Sacanell, J., & Parisi, F. (2012). *Enthalpy change in the magnetocaloric effect*. *Journal of Applied Physics*.

Scott, J. F. (2011). *Electrocaloric Materials*. *Annual Review of Materials Research*, 229-240.

Sinyavsky, Y. V., & Brodyansky, V. M. (1992). *Experimental Testing of Electrocaloric Cooling with Transparent Ferroelectric Ceramic as a Working Body*. *Ferroelectrics*, 321-325.



the bed, flowing from right to left, at a constant cold temperature,  $T_c$ , that is equal to the cold space temperature. Thermal energy is deposited to the fluid as it flows through the bed and is removed as it passes through the rejection heat exchanger. This process then repeats.

### *2.1 Steady State Modeling Assumptions*

The steady state model assumes that the refrigeration system has achieved a periodic steady state. It also assumes that each heat exchanger has perfect effectiveness and, therefore, all of the fluid entering the device is exactly at the reservoir temperature. In addition, the heat exchanger geometry is neglected and the flow is evenly distributed between the fluid channels. The flow is assumed to be laminar, hydrodynamically and thermally fully developed.

The refrigerator bed is assumed to be externally adiabatic and the support structure of the bed is neglected. Each channel and each film is identical such that the bed has a constant cross section. It is assumed that each node is differential in the X direction of Figure 2-1 but spans the entire device in the Y and Z directions. Therefore, it is assumed that there is a single mean value of temperature for each node.

### *2.2 Thermodynamics of Electrocaloric materials*

It is useful to understand the temperature-electric field-entropy relationship because this relationship drives the heat transfer to and from the working fluid. The phase rule of thermodynamics states:

$$f = c - p + 2 \quad (2.1)$$

where  $f$  is the number of intensive properties required to fix the state,  $c$  is the number of species present and  $p$  is the number of phases present. In the case of an electrocaloric material, there is one species and one phase present. Therefore two intensive properties are required to fix the state of the electrocaloric material. The Applied electric field,  $E$ , is assumed to be one of these properties. Therefore, entropy,  $s$ , can be represented as a function of the temperature,  $T$ , and applied electric field,  $E$ :

$$s = s(T, E) \quad (2.2)$$

Taking the total derivative, equation (2.2) becomes:

$$ds = \left. \frac{\partial s}{\partial E} \right|_T dE + \left. \frac{\partial s}{\partial T} \right|_E dT \quad (2.3)$$

Integrating from a reference entropy to the entropy of interest:

$$\Delta s = s - s_{ref} = \int_{E_{ref}}^E \left. \frac{\partial s}{\partial E} \right|_T dE + \int_{T_{ref}}^T \left. \frac{\partial s}{\partial T} \right|_E dT \quad (2.4)$$

Equation (2.4) describes the change in entropy of an electrocaloric material. The manufacturer of the electrocaloric material has provided a correlation for the partial derivative of entropy with respect to the electric field at a constant temperature. This correlation can be found in section 2.5. The partial derivative of entropy with respect to temperature at a constant electric field can be simplified into known quantities. Neglecting potential and kinetic energy effects, the first law of thermodynamics for a closed system states:

$$du = \delta q + \delta w \quad (2.5)$$

where  $du$  is a differential amount of internal energy of the closed system and  $\delta q$  is a differential amount of heat entering the closed system. Differential work,  $\delta w$ , for electrocaloric materials is defined as:

$$\delta w \equiv E dP \quad (2.6)$$

where  $P$  is the polarization of the electrocaloric material. Therefore the first law of thermodynamics in terms of specific units can be written as:

$$du = \delta q + E dP \quad (2.7)$$

Similarly, the second law of thermodynamics for a closed system is:

$$\frac{\delta q}{T} + \delta S_{gen} = ds \quad (2.8)$$

Assuming a reversible process the second law can be written as:

$$\delta q = T ds \quad (2.9)$$

Substituting (2.9) into (2.7) yields:

$$du = T ds + E dP \quad (2.10)$$

Enthalpy,  $h$ , can also be defined as:

$$h \equiv u - EP \quad (2.11)$$

The total derivative of enthalpy is:

$$dh = du - E dP - P dE \quad (2.12)$$

Substituting (2.7), a fundamental property relation can be written as:

$$dh = TdS - PdE \quad (2.13)$$

Additionally, from the phase rule, it can be said that:

$$s = f(h, E) \quad (2.14)$$

And using the chain rule, the temperature dependence of entropy can be found to be:

$$\left. \frac{\partial s}{\partial T} \right|_E = \left. \frac{\partial s}{\partial h} \right|_E \left. \frac{\partial h}{\partial T} \right|_E + \left. \frac{\partial s}{\partial E} \right|_h \left. \frac{\partial E}{\partial T} \right|_E \quad (2.15)$$

Since:

$$\left. \frac{\partial E}{\partial T} \right|_E = 0 \quad (2.16)$$

Equation (2.15) becomes:

$$\left. \frac{\partial s}{\partial T} \right|_E = \left. \frac{\partial s}{\partial h} \right|_E \left. \frac{\partial h}{\partial T} \right|_E \quad (2.17)$$

From equation (2.13) it can be stated that:

$$\left. \frac{\partial s}{\partial h} \right|_E = \frac{1}{T} \quad (2.18)$$

Substituting the definition of  $c_E$ , the specific heat at constant field:

$$\left. \frac{\partial h}{\partial T} \right|_E = c_E \quad (2.19)$$

into equation (2.17) yields:

$$\left. \frac{\partial s}{\partial T} \right|_E = \frac{c_E}{T} \quad (2.20)$$

Equation (2.20) is exactly the integrand of the second integral on the right hand side of equation (2.4). This allows entropy to be evaluated at any state as long as a reference state is defined.

### 2.3 Electrocaloric Material (Regenerator) Thermal Energy Balance

In order to simplify the regenerator and fluid energy balances several parameters were defined out of the bed geometry and properties. First, the porosity,  $\varepsilon$ , is defined as ratio of fluid volume to the total bed volume:

$$\varepsilon = \frac{th_{chan}}{th_e + th_{chan}} \quad (2.21)$$

where  $th_{chan}$  is the fluid channel thickness and  $th_e$  is the thickness of one electrocaloric film. Because each fluid channel is bounded by a regenerative electrocaloric film on both sides, the cross sectional area of the bed,  $A_c$  is:

$$A_c = w_{chan}(N_e(th_e + th_{chan}) - th_{chan}) \quad (2.22)$$

where  $N_e$  is the number of electrocaloric films that make up the bed and  $w_{chan}$  is the channel width defined in Figure 2-1. As it was previously discussed, a weighted average effective thermal conductivity,  $k_{eff}$ , was used to simplify the energy balances:

$$k_{eff} = \frac{k_e th_e + k_f th_{chan}}{th_e + th_{chan}} \quad (2.23)$$

Where  $k_e$  is the thermal conductivity of the electrocaloric films and  $k_f$  is the thermal conductivity of the working fluid. By using the effective conductivity model it allows the thermal conductivity term to be neglected from the fluid thermal energy balance and included only in the regenerator material's energy balance. The thermal energy balance on

the regenerator material, shown in Figure 2-2, includes conduction, convection to the fluid, the electrical work associated with polarizing the material, and a hysteresis loss.

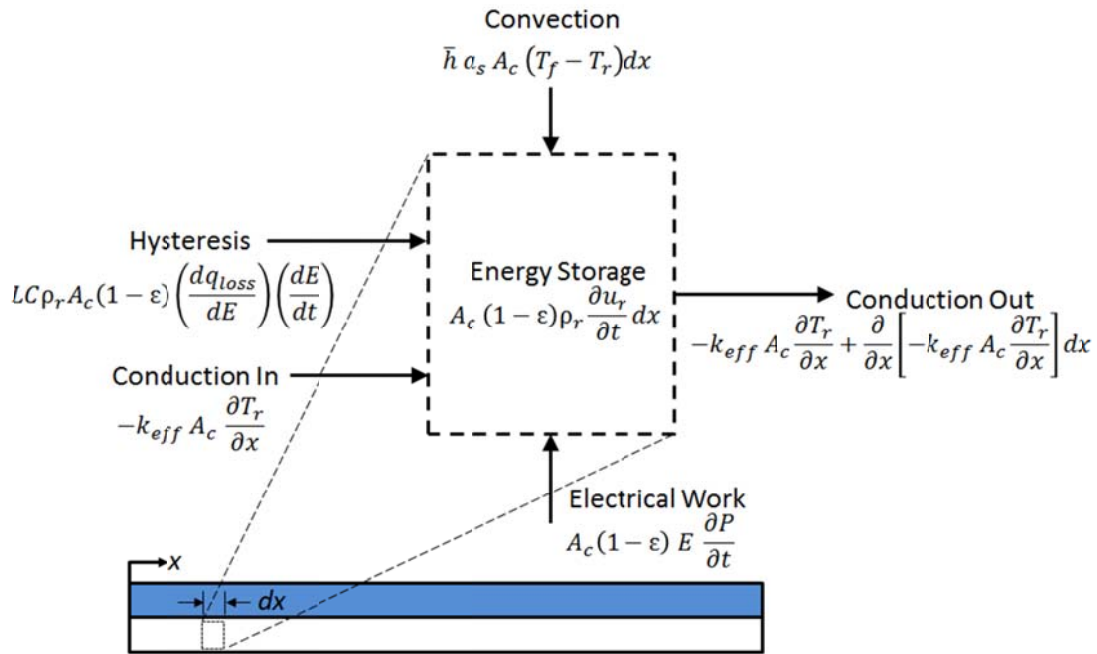


Figure 2-2: Regenerator material energy balance (Knier, 2012)

Remembering that, since energy is conserved, the general energy balance is:

$$Energy_{in} = Energy_{out} + Energy_{stored} \quad (2.24)$$

Therefore the regenerative energy balance can be written as:

$$\begin{aligned}
 & LC \rho_r A_c (1 - \epsilon) \left( \frac{dq_{loss}}{dE} \right) \left( \frac{dE}{dt} \right) dx + \bar{h} a_s A_c (T_f - T_r) dx + A_c (1 - \epsilon) E \frac{\partial P}{\partial t} dx \\
 & - k_{eff} A_c \frac{\partial T_r}{\partial x} \\
 & = -k_{eff} A_c \frac{\partial T_r}{\partial x} + \frac{\partial}{\partial x} \left[ -k_{eff} A_c \frac{\partial T_r}{\partial x} \right] dx + \rho_r A_c (1 - \epsilon) \frac{\partial u_r}{\partial t} dx
 \end{aligned} \quad (2.25)$$

where the loss coefficient,  $LC$ , is a constant used to define percent hysteresis loss,  $\rho_r$  is the density of the regenerative material,  $A_c$  is the cross sectional area of the bed perpendicular to fluid flow,  $\varepsilon$  is the porosity of the bed,  $q_{loss}$  is the heat generated by hysteresis,  $E$  is the applied electric field,  $t$  is time,  $\bar{h}$  is the average convective heat transfer coefficient between the fluid and the regenerator material,  $a_s$  is the ratio of total surface area to the volume of the bed,  $T_f$  is the fluid temperature,  $T_r$  is the regenerator material,  $P$  is the polarization of the electrocaloric regenerative material,  $K_{eff}$  is the effective conductivity of the bed:

The conduction terms can be subtracted from equation (2.25) to produce:

$$\begin{aligned}
 LC \rho_r A_c (1 - \varepsilon) \left( \frac{dq_{loss}}{dE} \right) \left( \frac{dE}{dt} \right) + \bar{h} a_s A_c (T_f - T_r) + A_c (1 - \varepsilon) E \frac{\partial P}{\partial t} \\
 + k_{eff} A_c \frac{\partial^2 T_r}{\partial x^2} = \rho_r A_c (1 - \varepsilon) \frac{\partial u_r}{\partial t}
 \end{aligned} \tag{2.26}$$

Moving the electrical work term to the right hand side of the equation and combining like terms, the energy balance becomes:

$$\begin{aligned}
 LC \rho_r A_c (1 - \varepsilon) \left( \frac{dq_{loss}}{dE} \right) \left( \frac{dE}{dt} \right) + \bar{h} a_s A_c (T_f - T_r) + k_{eff} A_c \frac{\partial^2 T_r}{\partial x^2} \\
 = \rho_r A_c (1 - \varepsilon) \left[ \frac{\partial u_r}{\partial t} - \frac{E}{\rho_r} \frac{\partial P}{\partial t} \right]
 \end{aligned} \tag{2.27}$$

As it was previously mentioned, the differential work due to polarization is defined as:

$$dw \equiv E dP \tag{2.28}$$

As a result time derivative of work is:

$$d\dot{w} = E \frac{\partial P}{\partial t} \quad (2.29)$$

Additionally, the time derivative of the specific internal energy for an incompressible material can be written as:

$$d\dot{u} = \rho_r \frac{\partial u_r}{\partial t} \quad (2.30)$$

Also, from the first law of thermodynamics:

$$d\dot{u} = d\dot{q} + d\dot{w} \quad (2.31)$$

Therefore substituting equation (2.29) and (2.30) into the first law of thermodynamics, equation (2.31), and solving for the differential heat rate becomes:

$$d\dot{q} = \frac{\partial u_r}{\partial t} - \frac{E}{\rho_r} \frac{\partial P}{\partial t} \quad (2.32)$$

Second law of thermodynamics for a differential control volume without mass flow on a specific rate basis is:

$$\frac{d\dot{q}}{T_r} + d\dot{s}_{gen} = \frac{\partial s}{\partial t} \quad (2.33)$$

Assuming that this process is reversible, the entropy generation term is zero (a separate term was created to account for the irreversible hysteresis effects). Therefore substituting the differential heat term from equation (2.32), the entropy equation becomes:

$$\frac{\partial u_r}{\partial t} - \frac{E}{\rho_r} \frac{\partial P}{\partial t} = T_r \frac{\partial s}{\partial t} \quad (2.34)$$

Using the chain rule the time derivative of entropy can be written as:

$$\frac{\partial s}{\partial t} = \left. \frac{\partial s}{\partial T} \right|_E \frac{\partial T_r}{\partial t} + \left. \frac{\partial s}{\partial E} \right|_T \frac{\partial E}{\partial t} \quad (2.35)$$

It was previously shown in equation (2.20) that:

$$\left. \frac{\partial s}{\partial T} \right|_E = \frac{c_E}{T} \quad (2.36)$$

If equations (2.35) and (2.36) are both substituted into equation (2.34) the following equation is produced.

$$\frac{\partial u_r}{\partial t} - \frac{E}{\rho_r} \frac{\partial P}{\partial t} = T_r \left[ \frac{c_E}{T_r} \frac{\partial T_r}{\partial t} + \left. \frac{\partial s}{\partial E} \right|_T \frac{\partial E}{\partial t} \right] \quad (2.37)$$

Noticing that the left hand side of equation (2.37) is exactly what is in the brackets on the right hand side of equation (2.27). The regenerator energy balance becomes:

$$\begin{aligned} LC \rho_r A_c (1 - \varepsilon) \left( \frac{dq_{loss}}{dE} \right) \left( \frac{dE}{dt} \right) + \bar{h} a_s A_c (T_f - T_r) + k_{eff} A_c \frac{\partial^2 T_r}{\partial x^2} \\ = \rho_r A_c (1 - \varepsilon) c_E \frac{\partial T_r}{\partial t} + \rho_r A_c (1 - \varepsilon) T_r \left. \frac{\partial s}{\partial E} \right|_T \frac{\partial E}{\partial t} \end{aligned} \quad (2.38)$$

The Nusselt number is:

$$Nu = \frac{h d_h}{k_f} \quad (2.39)$$

where  $d_h$  is the hydraulic diameter of one fluid channel. Substituting equation (2.39) for the heat transfer coefficient in equation (2.38), the working thermal energy balance becomes:

$$\begin{aligned} & \frac{Nu k_f}{d_h} a_s A_c (T_f - T_r) - k_{eff} A_c \frac{\partial^2 T_r}{\partial x^2} - \rho_r A_c (1 - \varepsilon) c_E \frac{\partial T_r}{\partial t} \\ & = \rho_r A_c (1 - \varepsilon) T_r \left. \frac{\partial s_r}{\partial E} \right|_T \frac{\partial E}{\partial t} - LC \rho_r A_c (1 - \varepsilon) \left( \frac{dq_{loss}}{dE} \right) \left( \frac{dE}{dt} \right) \end{aligned} \quad (2.40)$$

The equation above is the regenerative energy balance that will be discretized and solved in the numerical model.

#### 2.4 Fluid Thermal Energy Balance

Creating a differential control element on the fluid within the fluid of the bed, a thermal energy balance can be conducted:

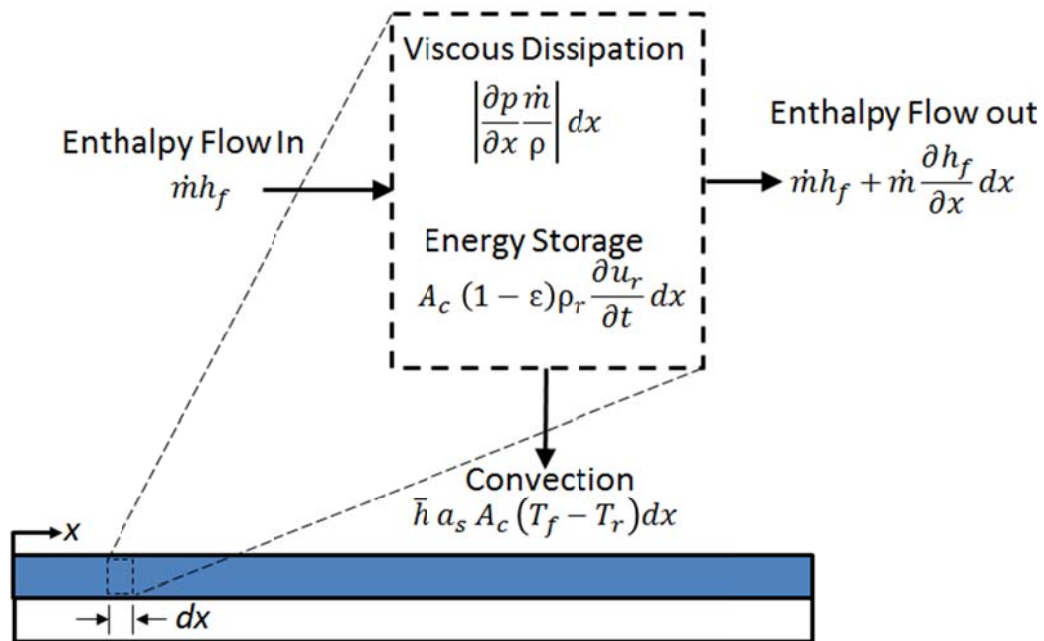


Figure 2-3: Fluid energy balance (Knier, 2012)

The heat transfer due to conduction was omitted and instead was included in the regenerator energy balance. Also, since the viscous generation term can be thought of as a

thermal energy generation term, the energy balance suggested by Figure 2-3 and equation (2.24) is:

$$\dot{m} h_f + \left| \frac{\partial p}{\partial x} \frac{\dot{m}}{\rho_f} \right| dx = \dot{m} h_f + \dot{m} \frac{\partial h_f}{\partial x} dx + \bar{h} a_s A_c (T_f - T_r) dx + \rho_f A_c \varepsilon \frac{\partial u_f}{\partial t} dx \quad (2.41)$$

where  $\dot{m}$  is the mass flow rate of fluid through the device  $h_f$  is the enthalpy of the fluid,  $a_s$  is the surface area between the fluid and electrocaloric material,  $p$  is the pressure and  $\rho_f$  is the density of the fluid. By substituting in that the internal energy of the fluid is the specific heat capacity of the fluid multiplied by the fluid temperature:

$$u_f = T_f c_f \quad (2.42)$$

Substituting this into equation (2.41) and taking the pressure-volume term of the enthalpy to be insignificant since the fluid is incompressible; the fluid energy balance reduces to:

$$\dot{m} c_f \frac{\partial T_f}{\partial x} + \bar{h} a_s A_c (T_f - T_r) + \rho_f A_c \varepsilon c_f \frac{\partial T_f}{\partial t} = \left| \frac{\partial p}{\partial x} \frac{\dot{m}}{\rho_f} \right| \quad (2.43)$$

The pressure loss is can be modeled by the Darcy-Weisbach equation:

$$\frac{\partial p}{\partial x} = f \frac{1}{d_h} \rho_f \frac{V^2}{2} \quad (2.44)$$

where the fluid velocity,  $V$ , is the average fluid velocity within each of these channels is:

$$V = \frac{\dot{m}}{A_c \varepsilon} \quad (2.45)$$

Substituting the fluid velocity and Darcy-Weisbach equations into the fluid energy balance, the fluid energy balance can be written as:

$$\dot{m}c_f \frac{\partial T_f}{\partial x} + \bar{h} a_s A_c (T_f - T_r) + \rho_f A_c \varepsilon c_f \frac{\partial T_f}{\partial t} = \left| \frac{f \dot{m}^3}{2\rho_f^2 A_c^2 \varepsilon^2 d_h} \right| \quad (2.46)$$

Finally, using the Nusselt number equation, (2.39), the heat transfer coefficient can be eliminated from the fluid energy balance:

$$\dot{m}c_f \frac{\partial T_f}{\partial x} + \frac{Nu k_f}{d_h} a_s A_c (T_f - T_r) + \rho_f A_c \varepsilon c_f \frac{\partial T_f}{\partial t} = \left| \frac{f \dot{m}^3}{2\rho_f^2 A_c^2 \varepsilon^2 d_h} \right| \quad (2.47)$$

Equation (2.47) is the working fluid energy balance that will be discretized for the numerical model. For laminar flow in a duct with a small area ratio, the friction factor,  $f$ , is:

$$f = \frac{96}{Re_{d_h}} \quad (2.48)$$

The Reynolds number based on hydraulic diameter is defined as:

$$Re = \frac{\rho_f V d_h}{\mu_f} \quad (2.49)$$

The velocity from equation (2.45) can be substituted into the Reynolds number to become:

$$Re = \frac{\rho_f \dot{m} d_h}{A_c \varepsilon \mu_f} \quad (2.50)$$

## 2.5 Correlations

Several correlations were used to determine the unknown parameters in the energy balances. First, the Nusselt can be modeled for two limits, for a constant heat flux or a constant temperature. To obtain a conservative heat transfer coefficient, the duct walls were assumed to have a constant temperature. The Nusselt number correlation for duct flow with constant wall temperature is (Nellis & Klein, 2009):

$$Nu = 7.541(1 - 2.610AR + 4.970AR^2 - 5.119AR^2 + 2.702AR^4 - 0.548AR^5) \quad (2.51)$$

Where AR is the aspect ratio:

$$AR = \frac{th_{chan}}{w_{chan}} \quad (2.52)$$

Where  $th_{chan}$  is the thickness of the fluid channel and  $w_{chan}$  is the width of the fluid channel.

The fluid channels have a very small thickness compared to their width, therefore the Nusselt number can be assumed to be a constant 7.541 (Shah, London, Irvine, & Hartnett, 1978).

The manufacturer of the electrocaloric material has provided data for the heat generated due to hysteresis,  $q_{loss}$  (J/kg)/cycle), to be:

$$q_{loss} = a E^2 + b E^3$$

$$a = 1.41368e - 14 \frac{J m^2}{V^2} \quad (2.53)$$

$$b = 5.6326e - 24 \frac{J m^2}{V^2}$$

Where E is the electric field experienced by the electrocaloric material. The manufacturer has also provided data on the rate of entropy change with respect to the electric field:

$$\left. \frac{\partial s}{\partial E} \right|_T = -C_1 - 2C_2 E(t) \quad (2.54)$$

$$C_1 = 7.95835e - 8 \frac{J m}{kg K V^2}$$

$$C_2 = 3.14744e - 15 \frac{J m^2}{kg K V^2}$$

The time derivative of the electric field found in the hysteresis term of the regenerator energy balance is assumed to be a linear relationship between zero and the user defined blow time and applied electric field. The specific heat capacity,  $c_E$ , is assumed to be a constant 1500 kg/kg-K, the density of the regenerator,  $\rho_f$ , was a constant 1800 kg/m<sup>3</sup> and the thermal conductivity of the regenerator material,  $k_r$ , to be 0.2 W/m-K.

The thermal conductivity of the heat transfer fluid, water, was assumed to be temperature dependent

$$k_f = -0.788067979 + 0.0076057397 T - 9.95274466e - 6 T^2 \quad (2.55)$$

The kinematic viscosity was assumed to be temperature dependent:

$$\begin{aligned} \mu_f = & 0.858711949 - 0.0105634322 T_f + 4.89832293T_f^2 \pm 1.01322089e \\ & - 7 T_f^3 + 7.88119624e - 11T_f^4 \end{aligned} \quad (2.56)$$

## 2.6 Discretizing Energy Balances

The two energy balances equations, (2.40) and (2.47), are coupled, second order with respect to space, first order with respect to time, partial differential equations. These equations include temperature dependent properties and, therefore, an analytical solution is infeasible. Instead a numerical method solution was developed using the computational grid in Figure 2-4.

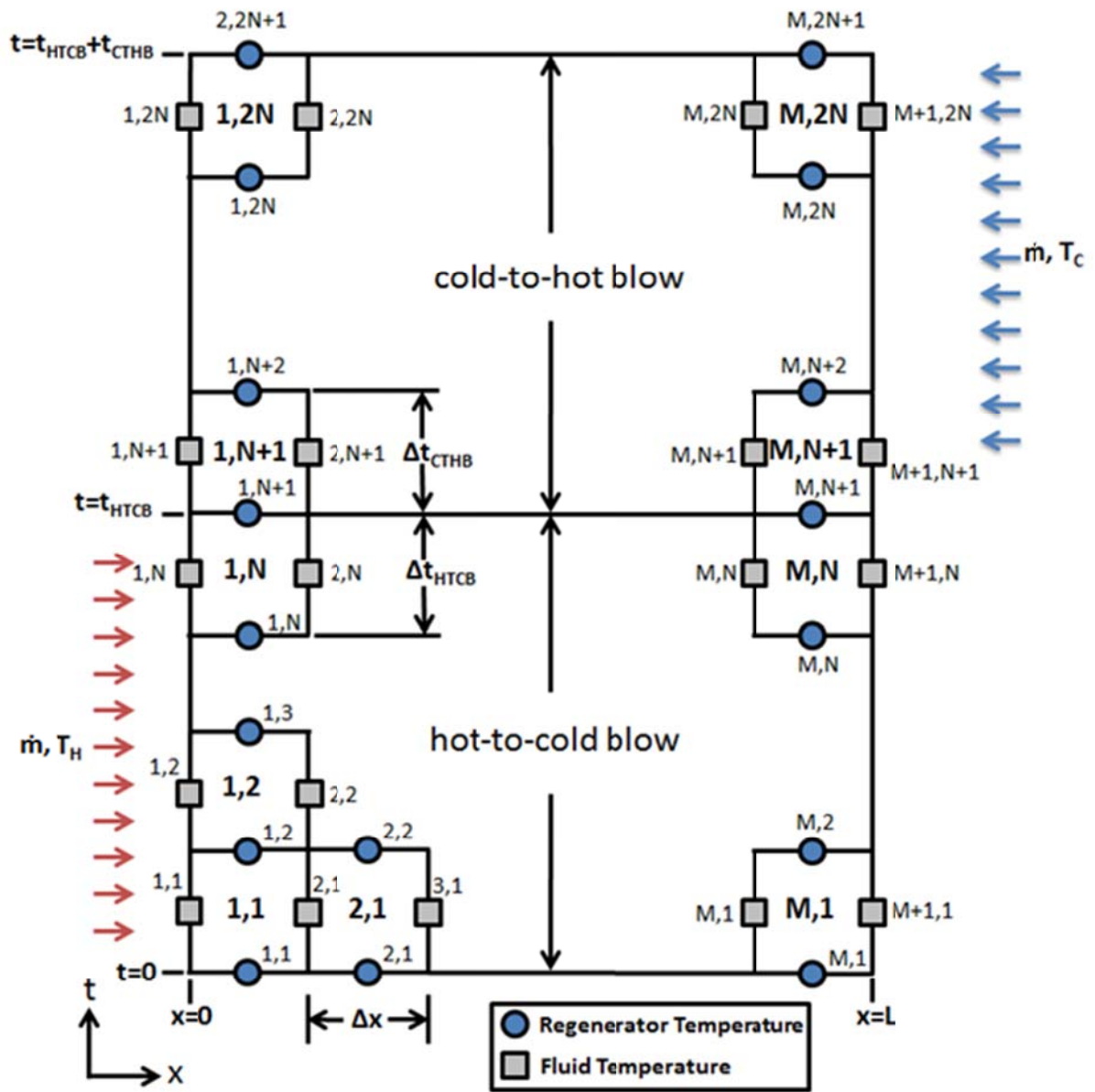


Figure 2-4: Discretized computational grid for the MATLAB model (Knier, 2012)

In order to solve a numerical model, space, and time must be discretized. Time is discretized such that:

$$\Delta t = \frac{t_{HTCB}}{N} = \frac{t_{CTHB}}{N} \quad (2.57)$$

where  $\Delta t$  is the length of one time step in seconds,  $t_{HTCB}$  and  $t_{CTHB}$  are the length of the hot to cold blow and the cold to hot blow respectively.  $N$  is the number of time steps for each blow process. The equations must also be discretized in space such that:

$$\Delta x = \frac{L_{film}}{M} \quad (2.58)$$

where  $\Delta x$  is the length of one spatial step in meters and  $M$  is the total number of spatial steps. To simplify the time derivatives of the energy balances, the fluid temperature is evaluated at the average of two positions such that the discretized fluid temperature is:

$$T_f = \frac{T_{f\ i,j} + T_{f\ i,j+1}}{2} \quad (2.59)$$

Similarly the discretized regenerator temperature is averaged over two time values:

$$T_r = \frac{T_{r\ i,j} + T_{r\ i+1,j}}{2} \quad (2.60)$$

Also the partial derivative of temperature of the regenerator is the difference of the regenerator temperatures over the length of one time step:

$$\frac{\partial T_r}{\partial t} = \frac{T_{r\ i,j} - T_{r\ i,j+1}}{\Delta t} \quad (2.61)$$

In addition, the second partial spatial derivative of the regenerator temperature can be discretized by:

$$\frac{\partial^2 T_r}{\partial x^2} = \frac{T_{r\ i+1,j} + T_{r\ i-1,j} - 2T_{r\ i,j}}{\Delta x} + \frac{T_{r\ i+1,j+1} + T_{r\ i-1,j+1} - 2T_{r\ i,j+1}}{\Delta x} \quad (2.62)$$

For simplicity, the transient term from the fluid energy balance is placed in the regenerator energy balance. Therefore the working regenerator thermal energy balance is

$$\begin{aligned}
& \rho_r A_c (1 - \varepsilon) c_E \frac{\partial T_r}{\partial t} + \rho_f A_c \varepsilon c_f \frac{\partial T_f}{\partial t} + \rho_r A_c (1 - \varepsilon) T_r \left. \frac{\partial s_r}{\partial E} \right|_T \frac{\partial E}{\partial t} \\
& - LC \rho_r A_c (1 - \varepsilon) \left( \frac{dq_{loss}}{dE} \right) \left( \frac{dE}{dt} \right) \\
& = \frac{Nu k_f}{d_h} a_s A_c (T_f - T_r) - k_{eff} A_c \frac{\partial^2 T_r}{\partial x^2}
\end{aligned} \tag{2.63}$$

Discretizing the regenerator by substituting equations (2.59), (2.60), (2.61) and (2.62) into energy balance found in equation (2.63) and collecting like terms yields:

$$\begin{aligned}
& T_{r\ i,j} \left[ -\frac{Nu^* k_f^*}{2 d_h} a_s A_c \Delta x \Delta t - \frac{k_{eff} A_c \Delta t}{2 \Delta x} - \frac{k_{eff} A_c \Delta t}{2 \Delta x} + \rho_r A_c (1 - \varepsilon) C_E^* \Delta x \right. \\
& \quad \left. + \rho_f A_c \varepsilon c_f^* \Delta x \right] \\
& + T_{r\ i,j+1} \left[ -\frac{Nu^* k_f^*}{2 d_h} a_s A_c \Delta x \Delta t - \frac{k_{eff} A_c \Delta t}{2 \Delta x} - \frac{k_{eff} A_c \Delta t}{2 \Delta x} \right. \\
& \quad \left. - \rho_r A_c (1 - \varepsilon) C_E^* \Delta x - \rho_f A_c \varepsilon c_f^* \Delta x \right] + T_{f\ i,j} \left[ \frac{Nu^* k_f^*}{2 d_h} a_s A_c \Delta x \Delta t \right] \\
& + T_{f\ i+1,j} \left[ \frac{Nu^* k_f^*}{2 d_h} a_s A_c \Delta x \Delta t \right] + T_{r\ i-1,j} \left[ \frac{k_{eff} A_c \Delta t}{2 \Delta x} \right] \\
& + T_{r\ i-1,j+1} \left[ \frac{k_{eff} A_c \Delta t}{2 \Delta x} \right] + T_{r\ i+1,j} \left[ \frac{k_{eff} A_c \Delta t}{2 \Delta x} \right] \\
& + T_{r\ i+1,j+1} \left[ \frac{k_{eff} A_c \Delta t}{2 \Delta x} \right] \\
& = \rho_r A_c (1 - \varepsilon) \left( \frac{T_{r\ i,j} + T_{r\ i+1,j}}{2} \right) \left. \frac{\partial s_r}{\partial E} \right|_T \frac{\partial E}{\partial t} \\
& - LC \rho_r A_c (1 - \varepsilon) \left( \frac{dq_{loss}}{dE} \right) \left( \frac{dE}{dt} \right)
\end{aligned} \tag{2.64}$$

for  $i=1..M$  for  $j=1..2N$

An iterative solution is used to solve equation (2.64). The superscript \* denotes that the guess values were used to determine the quantity. The guess values that are used are from the previous iteration. It has already been determined that the fluid energy balance is:

$$\dot{m}c_f \frac{\partial T_f}{\partial x} + \frac{Nu k_f}{d_h} a_s A_c (T_f - T_r) + \rho_f A_c \varepsilon c_f \frac{\partial T_f}{\partial t} = \left| \frac{f \dot{m}^3}{2\rho_f^2 A_c^2 \varepsilon^2 d_h} \right| \quad (2.65)$$

During the hot to cold blow, the flow is flowing in the positive-x so therefore the discretized time derivative of the fluid temperature is:

$$\frac{\partial T_f}{\partial x} = \frac{T_{f\ i+1,j} - T_{f\ i,j}}{\Delta x} \quad (2.66)$$

Substituting equations (2.59), (2.60) and (2.66) into equation (2.65), the discretized fluid energy balance for the hot to cold blow becomes:

$$\begin{aligned} \dot{m}c_f^* \frac{T_{f\ i+1,j} - T_{f\ i,j}}{\Delta x} + \frac{Nu^* k_f^*}{d_h} a_s A_c \left( \frac{T_{f\ i,j} + T_{f\ i,j+1}}{2} - \frac{T_{r\ i,j} + T_{r\ i+1,j}}{2} \right) \\ + \rho_f A_c \varepsilon c_f^* \left[ \frac{T_{f\ i+1,j} - T_{f\ i,j}}{\Delta x} \right] = \left| \frac{f^* \dot{m}^3}{2\rho_f^2 A_c^2 \varepsilon^2 d_h} \right| \end{aligned} \quad (2.67)$$

For I =1..m For j=1..N

Rearranging into a form more easily solved by matrix inversion the discretized fluid energy balance for the hot to cold blow becomes:

$$\begin{aligned}
& T_{f\ i,j} \left[ \dot{m}c_f^* - \frac{Nu^* k_f^*}{d_h} a_s A_c \Delta x \right] + T_{f\ i+1,j} \left[ -\dot{m}c_f^* - \frac{Nu^* k_f^*}{d_h} a_s A_c \Delta x \right] \\
& + T_{r\ i,j} \left[ \frac{Nu^* k_f^*}{d_h} a_s A_c \Delta x \right] + T_{r\ i,j+1} \left[ \frac{Nu^* k_f^*}{d_h} a_s A_c \Delta x \right] \\
& = - \left| \frac{f^* \dot{m}^3 \Delta x}{2\rho_f^2 A_c^2 \varepsilon^2 d_h} \right|
\end{aligned} \tag{2.68}$$

For  $l=1..M$  For  $j=1..N$

The cold to hot blow the flow is in the negative-x direction and therefore the discretized time derivative of the fluid temperature becomes:

$$\frac{\partial T_f}{\partial x} = \frac{T_{f\ i,j} - T_{f\ i+1,j}}{\Delta x} \tag{2.69}$$

Similarly, substituting equations, (2.59), (2.60), and (2.69) into equation (2.65) and rearranging yields the following discretized energy balance for the cold to hot blow:

$$\begin{aligned}
& T_{f\ i,j} \left[ -\dot{m}c_f^* - \frac{Nu^* k_f^*}{d_h} a_s A_c \Delta x \right] + T_{f\ i+1,j} \left[ \dot{m}c_f^* - \frac{Nu^* k_f^*}{d_h} a_s A_c \Delta x \right] \\
& + T_{r\ i,j} \left[ \frac{Nu^* k_f^*}{d_h} a_s A_c \Delta x \right] + T_{r\ i,j+1} \left[ \frac{Nu^* k_f^*}{d_h} a_s A_c \Delta x \right] \\
& = - \left| \frac{f^* \dot{m}^3 \Delta x}{2\rho_f^2 A_c^2 \varepsilon^2 d_h} \right|
\end{aligned} \tag{2.70}$$

For  $i=1..M$  For  $j=1..N$

The superscript \* denotes that the guess values were used to determine the quantity.

### 2.7 Achieving a Steady State Solution

Since a steady state model is desired, it implies that the temperature at the end of each cycle should be constrained to be the same as the temperature at the beginning of each cycle:

$$T_{r\ i,1} = T_{r\ i,N+1} \text{ for } i = 1..M \quad (2.71)$$

As it was previously mentioned, all of the fluid entering the bed during the Hot to Cold Blow is at the warm space temperature:

$$T_{f\ 1,j} = T_H \text{ for } j = 1..N \quad (2.72)$$

In addition, the fluid temperature entering the bed during the Cold to Hot temperature is the cold reservoir temperature,  $T_C$ :

$$T_{f\ M+1,j} = T_C \quad (2.73)$$

To simultaneously solve the two energy balances they must be put into matrix format:

$$\underline{\underline{A}} \underline{\underline{X}} = \underline{\underline{b}} \quad (2.74)$$

The Matrices can be set up in any order as long as the order is known. Where the  $\underline{\underline{A}}$  matrix is:

$$\underline{\underline{A}} = \left[ \begin{array}{l} \text{Row 1: Regenerator energy ballance for 1,1} \\ \text{Row 2: Regenerator energy ballance for 2,1} \\ \dots \\ \text{Row M: Regenerator energy ballance for M, 1} \\ \text{Row M + 1: Regenerator energy ballance for 1,2} \\ \dots \\ \text{Row (2 N + 1)M: Regenerator energy ballance for M, 2N + 1} \\ \text{Row (2 N + 1)M + 1: Fluid energy ballance for 1,1} \\ \dots \\ \text{Row (2 N + 1)M + M + 1: Fluid energy ballance for M + 1,1} \\ \text{Row (2 N + 1)M + M + 2 :: Fluid energy ballance for 2,1} \\ \dots \\ \text{Row (2 N + 1)M + 2N(M + 1): Fluid energy ballance for M + 1,2N} \end{array} \right] \quad (2.75)$$

The solution to equation (2.58),  $\underline{\underline{X}}$ , then becomes:

$$\underline{\underline{X}} = \left[ \begin{array}{l} X_1 = T_{r,1,1} \\ X_2 = T_{r,2,1} \\ \dots \\ X_M = T_{r,1,2} \\ X_{M+1} = T_{r,1,2} \\ \dots \\ X_{(2N+1)M} = T_{r,2N+1,M} \\ X_{(2N+1)M+1} = T_{f,1,1} \\ \dots \\ X_{(2N+1)M+M+1} = T_{f,M+1,1} \\ X_{(2N+1)M+M+2} = T_{f,1,2} \\ \dots \\ X_{(2N+1)M+2N(M+1)} = T_{f,M+1,2N} \end{array} \right] \quad (2.76)$$

Since an iterative solution is required, guess values for both the fluid and electrocaloric material need to be supplied. For a reasonable set of guess values, both the regenerator and fluid within the bed were assumed to initially have a linear distribution between the warm space temperature and the cold space temperature at each time step. The solution for the previous iteration is used for the guess values for each subsequent iteration until the solution converges.

### 2.8 Post Processing

One of the important parameters for the electrocaloric refrigeration cycle is the amount of cooling and heating power out of the two ends of the bed. An average of the total heat provided over the time of one complete cycle yields the cooling and heating provided in watts to each end of the bed. Therefore the cooling power provided is:

$$\dot{Q}_c = \frac{\int_0^{t_B} \dot{m} c_f (T_c - T_f|_{x=L,t})}{2t_B} \quad (2.77)$$

The heating power provided to the warm side of the bed is consequently:

$$\dot{Q}_H = \frac{\int_{t_B}^{2t_B} \dot{m} c_f (T_c - T_f|_{x=L,t})}{2t_B} \quad (2.78)$$

For the initial design, the cooling power, determined by equation (2.77), will be maximized.

### 2.9 Quasi Transient Modeling Analysis

A quasi transient model of the refrigeration system was created to obtain a rough idea of the minimum theoretical temperature and roughly how much time it might take to achieve these temperatures. The transient model works by looping the steady state model upon itself and then it changes the boundary temperatures after each complete cycle.

The steady state model is initially run through one complete steady state cycle assuming that the boundary conditions are equal to the ambient temperature. The model then produces the temperature of the water exiting the bed at each time step. These temperatures are used to calculate the temperature of the cold side heat exchanger as a function of time for the duration of one cycle.

At the end of each cycle the temperature of the cold heat exchanger is used for the initial condition of the next steady state run of the ECE bed. This process repeats until the desired time has been reached.

### *2.9.1 Transient Model Assumptions*

The transient model assumes constant ECE material properties and that the fluid flowing through the bed is incompressible with constant specific heat, temperature dependent thermal conductivity and kinematic viscosity.

Fluid flow is assumed to be laminar and the water entering the bed is at ambient temperature. Like the steady state model, the transient model uses an effective conductivity model included in the regenerator energy balance and assumes uniform bed geometry with constant channel thicknesses. The ECE bed and cold heat exchanger are assumed to be externally adiabatic. The cold heat exchanger has infinite thermal conductivity and radiation is neglected. For each cycle the cold side of the bed is constant and is equal to the temperature of the cold heat exchanger (Knier, 2012).

“The electrocaloric effect was assumed to be a polynomial function of only electric field, with no dependence on temperature.” These assumptions might be valid for small temperature ranges. “However, a property curve fit or equation of the state could be implemented to more accurately represent the material, if this data were available.” (Knier, 2012)

This model likely overestimates the speed at which the cooling takes place and the minimum possible temperature because it neglects the thermal conduction through the

walls of the support structure of the refrigeration system. In reality, it is also likely that the water entering the bed will be above ambient temperature because the heat rejection heat exchanger will not have an effectiveness of one.

### 2.9.2 Quasi Transient Model Operation

The Nusselt number,  $Nu$ , for a uniform wall temperature and fully developed flow is 3.66 (Nellis & Klein, 2009). Using the definition of the Nusselt number the average heat transfer coefficient on the inside of a simple tube heat exchanger,  $\bar{h}$ , in is:

$$\bar{h} = \frac{Nu k_f}{2 r} \quad (2.79)$$

where  $k_f$  is the thermal conductivity of the working fluid, assumed to be water, and  $r$  is the inside radius of the heat exchanger, shown in Figure 2-5.

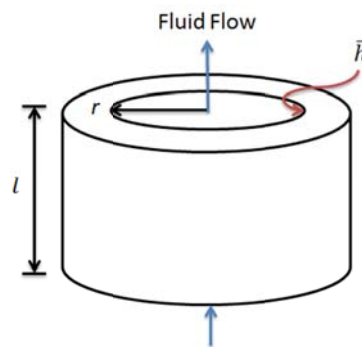


Figure 2-5: The model's heat exchanger geometry

Since the heat exchanger used is assumed to have a single working fluid, the total thermal resistance,  $R_{tot}$ , consists only of the resistance due to convection:

$$R_{tot} = \frac{1}{\bar{h} 2 r \pi l} \quad (2.80)$$

where  $l$  is the length of the heat exchanger. The conductance of the heat exchanger,  $UA$ , is the inverse of the total thermal resistance.

$$UA = \frac{1}{R_{tot}} \quad (2.81)$$

Since there is only one fluid involved with the cold side heat exchanger the minimum heat capacity rate,  $\dot{C}_{min}$  is:

$$\dot{C}_{min} = c_f \dot{m} \quad (2.82)$$

where  $\dot{m}$  is the user specified mass flow rate and  $c_f$  is the specific heat of the working fluid.

The number of transfer units for this heat exchanger,  $NTU$ , can be calculated:

$$NTU = \frac{UA}{\dot{C}_{min}} \quad (2.83)$$

Finally for a one fluid the heat exchanger the effectiveness,  $\varepsilon$ , is:

$$\varepsilon_{hx} = 1 - e^{-NTU} \quad (2.84)$$

Since time is discretized, the difference in energy of the heat exchanger between the current time step and the next time step,  $De$ , is:

$$De = \varepsilon_{hx} \dot{m} c_f (T_{c,j} - T_{f,M+1,j}) Dt \quad (2.85)$$

Where  $T_{c,j}$  is the current temperature of the cold side heat exchanger,  $T_{f,M+1,j}$  is the temperature of the fluid flowing out of the bed at the current time step determined from the steady state model and  $Dt$  is the length of one time step in seconds. Assuming the cold heat exchanger can be treated as a lumped capacitance, the temperature of the cold heat exchanger at the next time step  $TC_{i+1}$  is:

$$T_{c j+1} = T_{c j} - \frac{De}{C_c} \quad (2.86)$$

Where  $C_c$  is the heat capacity of the cold side heat exchanger. The cold heat exchanger's temperature is only incremented during the hot to cold blow. During the cold to hot blow, the temperature of the cold heat exchanger is assumed to be constant since it is externally adiabatic.

### 2.9.3 Transient Model results

A one hour model was completed, using the parameters shown in Table 2-1.

**Table 2-1: Input parameters for the transient model operation**

<b>Model Input</b>	<b>Value</b>
Film Length, $L_e$	2.8 cm
Film Width, $w_e$	2.0 cm
Bed Height, $H_B$	0.272 mm
Aspect Ratio, AR	1.4
Cross Sectional Area, $A_c$	5.44 mm <sup>2</sup>
Films, $N_e$	2
Film Thickness, $th_e$	196 μm
Mass Flow Rate, $\dot{m}$	0.11 kg/s
Half Cycle Time, $t_b$	1.63 sec
Polarization Time, $t_p$	0.02 sec
Fluid Channel Thickness, $th_{chan}$	0.076 mm
Bed Porosity, $\epsilon$	0.28
Specific Heat of the Cold Heat Exchanger, $c_c$	384.4 J/kg-K (copper)
Density of Cold Heat Exchanger $\rho_c$	8934 kg/m <sup>3</sup> (copper)
Outside Diameter, $d_{out}$	3.175 mm
Inside Diameter, $d_{in}$	1.5494 mm
Length of the Cold Heat Exchanger, $L_{hx}$	9.33 cm
Initial Temperature, $T_{ini}$	298 k
Ambient Temperature, $T_{amb}$	298K
Hysteresis, LC	3 %

A one hour transient model was completed and the model predicted that the cold mass will reach a temperature of 257[k] in about 1000 seconds. According to this model, if external heating was not added, the water within the bed would likely freeze. However, the minimum temperature will likely be much greater than the temperature predicted by the transient model due to conduction through the support structure of the bed. In addition, it was assumed that the electrocaloric effect was not a function of temperature. It is very likely that electrocaloric effect is temperature dependent. As it was previously mentioned, data about this relationship is unavailable.

### *2.10 References*

- Knier, B. J. (2012). A Thermodynamic Analysis of an Electrocaloric Effect (ECE) Refrigeration Cycle. University of Wisconsin - Madison.
- Nellis, G., & Klein, S. (2009). Heat Transfer. New York: Cambridge University Press.
- Shah, R. K., London, A. L., Irvine, T. F., & Hartnett, J. P. (1978). Laminar Flow Forced Convection in Ducts. New York: Academic Press.

### CHAPTER 3: *ELECTROCALORIC REFRIGERATOR PARAMETER OPTIMIZATION*

A two film, fluid-based electrocaloric refrigeration cycle is under design. The objective is to demonstrate the feasibility of fluid based electrocaloric refrigeration. The proposed ECE refrigeration system, presented in Figure 3-1, consists of two ECE beds.

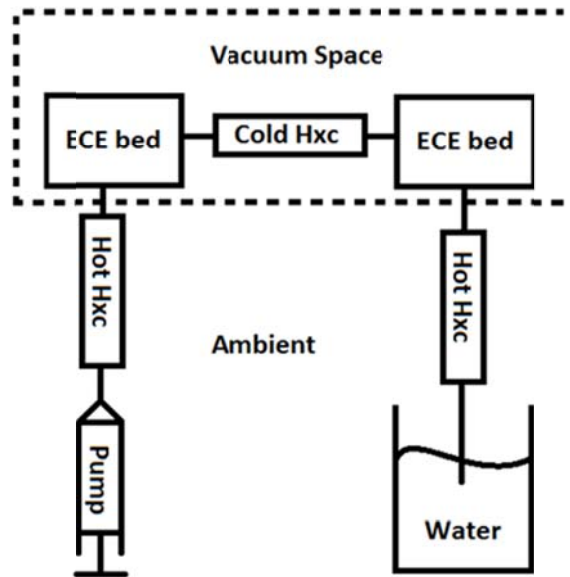


Figure 3-1: A system view of the proposed ECE refrigeration cycle.

The device will work by oscillating fluid, in this case water, across two, one-film EC beds operating out of phase from one another to allow continuous cooling to a cold heat exchanger. The oscillating fluid flow will be induced by a syringe pump connected to one of the hot heat exchangers. The hot heat exchangers will reject the exhaust energy from one of the EC beds.

Due to the very low expected cooling power out of each of the beds, both EC beds and the cold heat exchanger will be placed in a vacuum. A vacuum is used provide good thermal isolation in an attempt to maximize the temperature difference between the cold heat

exchanger and the ambient surroundings. What follows is the optimization of a two film ECE bed, hot heat exchanger, cold heat exchanger and the pump.

### *3.1 Qualitative View of a Transient Fluid Particle*

A qualitative view of the steady state electrocaloric refrigeration system operation can be obtained by tracking the temperature of a fluid particle through one complete cycle.

Initially, in Figure 3-2, the fluid particle is at ambient temperature and film 1 is at its cooled state while film 2 is at its warm state. As the particle flows from position 1 to position 2, thermal energy from the particle is deposited into the cold EC film. As the fluid particle travels through the cold space from position 2 to position 3 it retains a constant temperature that is below the ambient temperature. Next, from position 3 to position 4 the fluid particle absorbs thermal energy from the electrocaloric film and rises to a temperature above the ambient temperature. The fluid particle rises to above ambient temperature because of the hysteresis and other irreversibilities associated with polarizing and depolarizing the electrocaloric films. Heat is then rejected from the particle to the ambient conditions until the particle is back at ambient temperature.

The fluid flow direction is then reversed so that the state of the films can be switched such that film 1 is at its warm state while film 2 is at its cold state. The fluid particle then undergoes the same thermal changes as it did in the first flow direction until the particle is back at its original state.

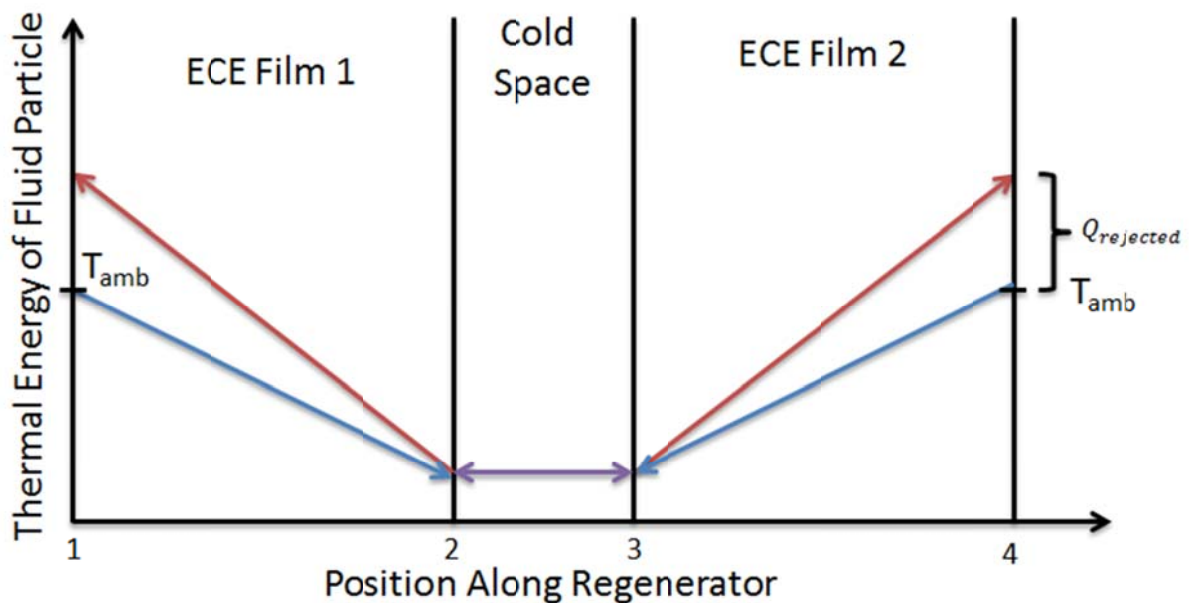


Figure 3-2: Tracking a fluid particle through one complete steady state cycle of the proposed electrocaloric refrigeration system

The cooling power of the bed could be increased by decreasing the time per cycle. This would be possible if the fluid particle, starting at position 1 traveled only to position 3 before the flow direction and film states were reversed.

### 3.2 Steady State Two Film ECE Bed Optimization

The non-fixed independent parameters of the bed design are the blow time, channel thickness and the heat transfer fluid's mass flow rate. What follows is an analysis in order to optimize these parameters. Due to the material, model and manufacturing capabilities, the independent parameters found in Table 3-1 have been fixed.

Table 3-1: Fixed independent bed parameters

Independent Bed Parameter	Value
Heat Rejection Temperature, $T_h$	298 K
Film Length, $L_e$	2.8 cm
Film Width, $W_e$	2.0 cm
Aspect Ratio, AR	1.4
Beds	1
Films, $N_e$	2
Film thickness, $th_e$	196 $\mu\text{m}$
Hysteresis loss, LC	3%
Maximum Electric Field, $E_{\text{max}}$	80 MV/m

### 3.2.1 Minimum Blow Time

Due to the thermal diffusion through the thickness of the electrocaloric film, there is a minimum time for heat to exit the EC film. This puts a lower bound on the time of one blow.

The thermal diffusion length,  $L_d$  is approximately (Knier, 2012):

$$th_e = L_d = \sqrt{\frac{2\alpha}{\omega}} \text{ where: } \alpha = \frac{K}{\rho c} \text{ and } \omega = 2\pi f \quad (3.1)$$

Where  $L_d$  is the thermal diffusion wave depth and  $\alpha$  denotes thermal diffusivity of the electrocaloric material. The ECE films have properties: thermal conductivity,  $k_e = 0.2\text{W/m-K}$ , density,  $\rho_r = 1800\text{kg/m}^3$  and specific heat,  $c_r = 1500\text{J/kg-K}$  (Knier, 2012). When  $f$  is the frequency in Hz, the minimum blow time is:

$$t_b = \frac{1}{f} \quad (3.2)$$

This results in a minimum blow time of 1.63 seconds. Since a shorter cycle time should result in a higher cooling power, a blow time of 1.63 seconds was chosen. A shorter blow time could be used but would result in a significant drop in efficiency because the system would not take advantage of all of the electrocaloric material that is available.

### 3.2.2 Channel Thickness

The maximum cooling power will occur when the load temperature is equal to the heat rejection temperature (i.e. there is no temperature difference across the bed). Figure 3-3 shows the model predicted cooling power in this limit is a function of both the fluid channel thickness and mass flow rate. The input parameters in Table 3-1 were used to generate this plot.

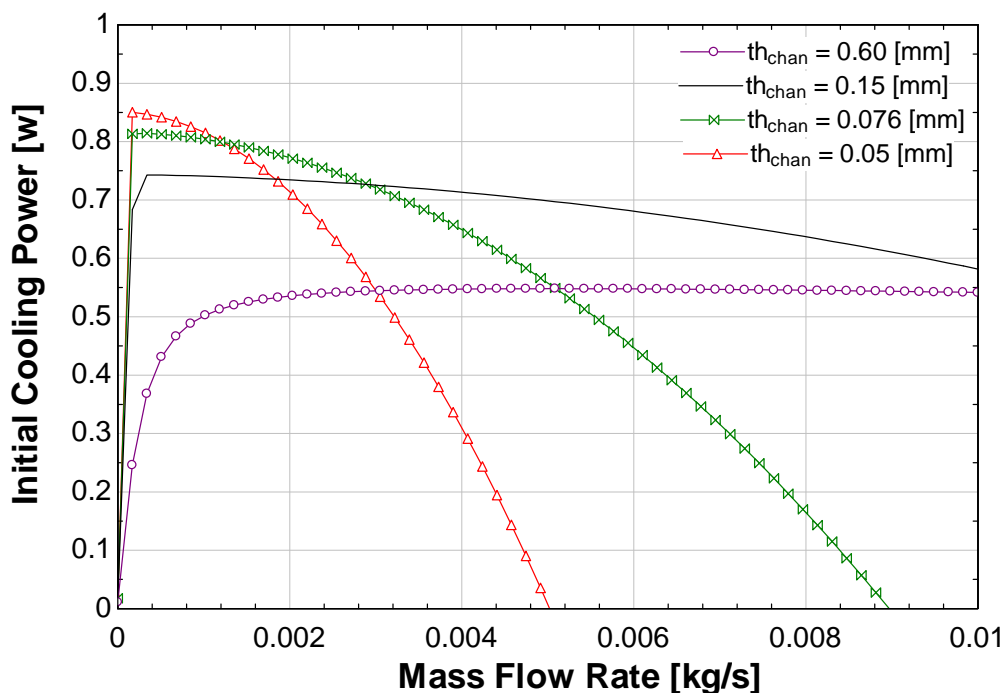


Figure 3-3: The initial cooling power as a function of the mass flow rate for various channel thicknesses

Figure 3-4 shows the maximum cooling power as a function of mass flow rate when the load temperature is 283 K and the heat rejection temperature is 298K. It can be seen, in Figure 3-4, that the model predicts that the maximum available cooling power decreases as the load temperature decreases.

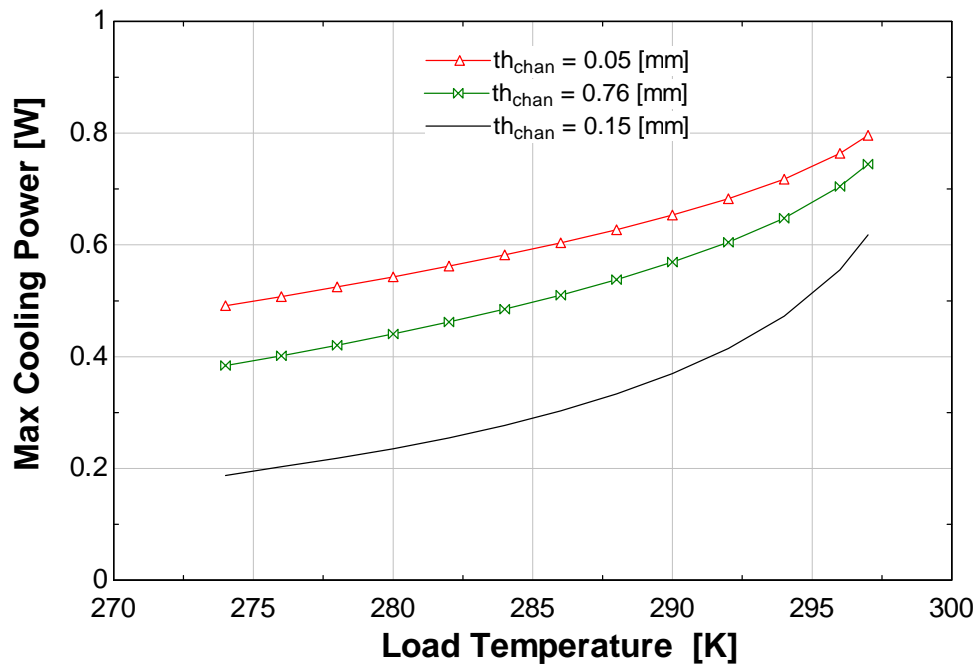


Figure 3-4: The maximum cooling power as a function of load temperature for various channel thicknesses.

By extrapolating this affect and plotting the maximum cooling power as a function of load temperature for several channel thicknesses it can be seen, in Figure 3-5, that, under optimized conditions, the model predicts that the available cooling power decreases as the channel thickness increases.

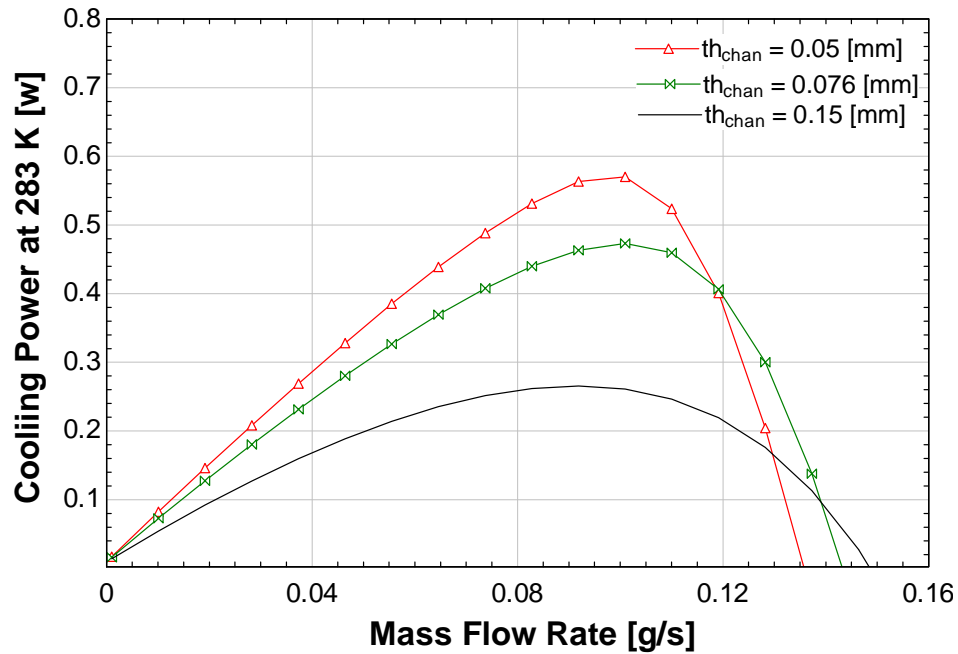


Figure 3-5: The cooling power to a load temperature of 283 K as a function of the mass flow rate for various channel thicknesses

Due to manufacturing limitations, it is difficult to produce small channel thicknesses. A channel thickness of 0.076 mm is a reasonable channel thickness that can be produced using modern CNC machining or other methods. Alternatively, it is also possible to use very thin channel spacers to control the channel thickness. Due to ease of manufacturing the use of channel spacers is recommended. If more a more accurate and precise method of manufacturing is available it is recommended to go with the smallest channel thickness that is reliably manufacturable. For the remainder of this analysis it will be assumed that the ECE bed has a channel thickness of 0.076 mm.

### 3.2.3 Mass Flow Rate Optimization

As the load temperature decreases, the mass flow rate that produces the maximum cooling power also decreases. Since the available cooling powers are very small, it is necessary to

maximize the cooling power in order to achieve measurable results in the demonstration device. Therefore, the mass flow rate of the system should change as a function of the load temperature. Figure 3-6 shows the model predicted relationship between the mass flow rate required to achieve the maximum cooling power and the load temperature.

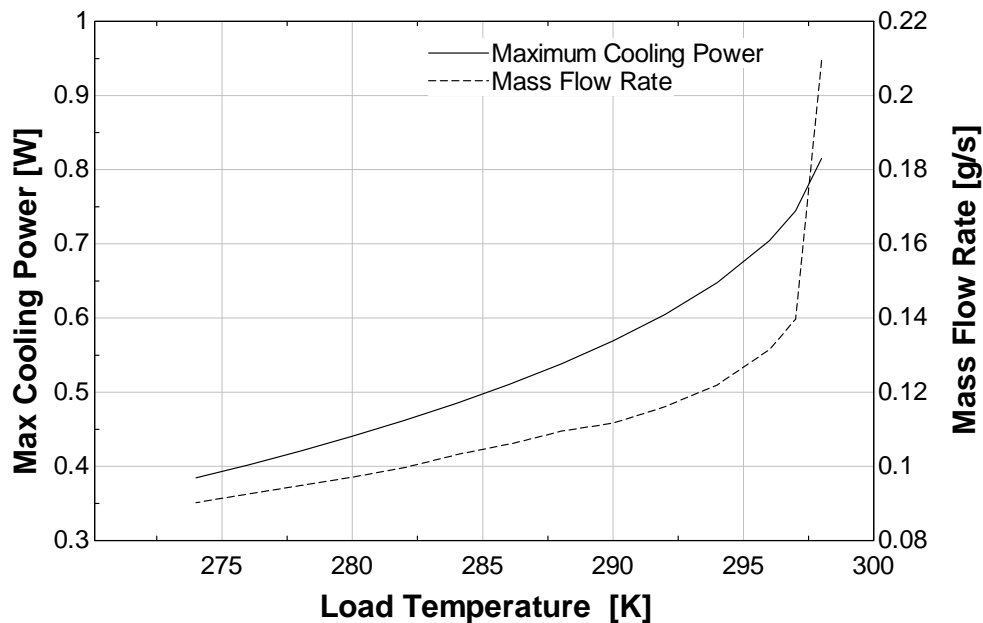


Figure 3-6: The maximum possible cooling power from a two film ECE refrigeration bed with a channel thickness of 0.076 mm and the mass flow rate required to achieve that cooling power.

Load temperatures below 274 K were not investigated because the water within the bed would be at risk of freezing and therefore render the device inoperable. However 274 K should not be approached because local temperatures may cause ice crystals to form even when the bulk temperature of the fluid is above the freezing point. If the mass flow rate cannot vary with temperature, a mass flow rate of 0.11 g/s is recommended in order to maximize the cooling power for most load temperatures.

### 3.2.4 Steady State Optimization Results

The bed dimensions and operating conditions for the optimized two film ECE bed are presented in Table 3-2.

**Table 3-2: Summary table of ECE bed dimension and operating conditions**

<b>Independent Bed Parameter</b>	<b>Value</b>
Heat Rejection Temperature, $T_H$	298 K
Film Length, $L_e$	2.8 cm
Film Width $w_e$	2.0 cm
Bed Height, $H_B$	0.272 mm
Aspect Ratio, $AR$	1.4
Cross sectional area, $A_c$	5.44 mm <sup>2</sup>
Films, $N_e$	2
Film thickness, $th_e$	196 $\mu$ m
Half Cycle Time, $t_b$	1.63 sec
Polarization time, $T_p$	0.02 sec
Fluid channel thickness, $th_{chan}$	0.076 mm
Bed porosity, $\epsilon$	0.28
Applied Hysteresis loss, $LC$	3%
Maximum Electric Field, $E_{max}$	80 MV/m

In order to maximize the cooling power of a two film ECE refrigeration bed, with the film specified in Table 3-2, a blow time of 1.63 seconds and the smallest channel thickness that can be reasonably manufactured (taken to be 0.076 mm here) should be used. If possible, the mass flow rate should be varied with load temperature according to Figure 3-6.

However, if a constant mass flow rate is necessary, a reasonable flow rate is 0.11 g/s.

### 3.3 References

Knier, B. J. (2012). A Thermodynamic Analysis of an Electrocaloric Effect (ECE) Refrigeration Cycle. University of Wisconsin - Madison.

## **CHAPTER 4: PROTOTYPE DESIGN**

### *4.1 Initial EC Bed Design*

The initial design of the ECE refrigeration system included two, one-film ECE beds operating out of phase from one another to allow for continuous cooling of a heat exchanger located between the beds. Due to the very small required channel thicknesses determined from the modeling analysis, tight tolerances are required to obtain uniform channel thicknesses. Two common methods to archive tight tolerances are using CNC machining and using spacers that have uniform thicknesses.

In this design, channel spacers were used to control the channel thickness instead of directly machining the surrounding material. This method was chosen because there was greater confidence in being able to produce reproducible channel thicknesses.

The first iteration of the ECE bed, shown in Figure 4-1, consisted of two large metal end caps and a gasket to provide a seal from the external vacuum. Next two plastic insulating plates were to be inlaid into the metal end caps. These two insulating plates would clamp the ECE film and spacer to one another to create the cooling space of the ECE bed. Two fluid ports would be drilled through one of the end caps and one of the insulating plates so that a tube for fluid flow could be inserted and epoxied into place.

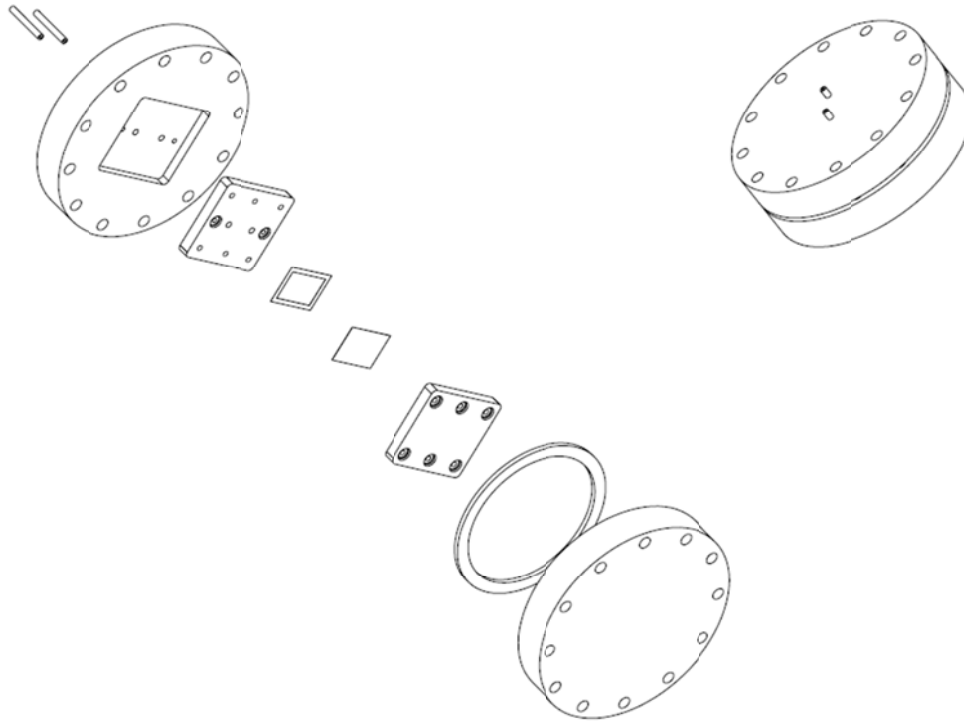


**Figure 4-1: The Initial design of the demonstration device.**

Since the ECE films are difficult to obtain, the first design iteration consisted of a bed that could be opened so that the films could be removed undamaged. This option also added the additional functionality of using the channel thickness as an independent parameter.

Channel thickness could be changed by opening the bed and replacing the internal spacer.

There were several problems with the initial design that resulted in future design iterations.

First, during each blow process a small volume of water, 0.18mL, will travel through a given cross section of the device. Therefore, it was expected that the water would get stuck in the relatively large amount of required piping between the ECE beds and the heat exchanger.

In addition, the thickness of the device would eliminate the advantage gained by placing the device inside a vacuum. This is because there is not enough time for the inside of the device to thermally communicate with the outside of the device during duration of one blow. This can be seen by the thermal wave diffusion depth,  $L_d$ :

$$L_d = 2 * \sqrt{\alpha * t_b} = 0.8 \text{ mm} \quad (4.1)$$

where the thermal diffusivity of polyethylene,  $\alpha$ , is  $9.5 * 10^{-8} \text{ m}^2/\text{s}$  and the time of one blow,  $t_b$ , is 1.6 s. Finally, due to the large size of the ECE beds, the capacitance of the bed would likely overwhelm the cooling effect of the ECE films.

#### 4.2 Second ECE Bed Design Iteration

In the second design iteration of the electrocaloric refrigeration system, the capability to remove the ECE films was sacrificed in order to reduce the thermal capacitance of the bed. This design, shown in Figure 4-2, includes a fluid channel on both sides of each ECE film.

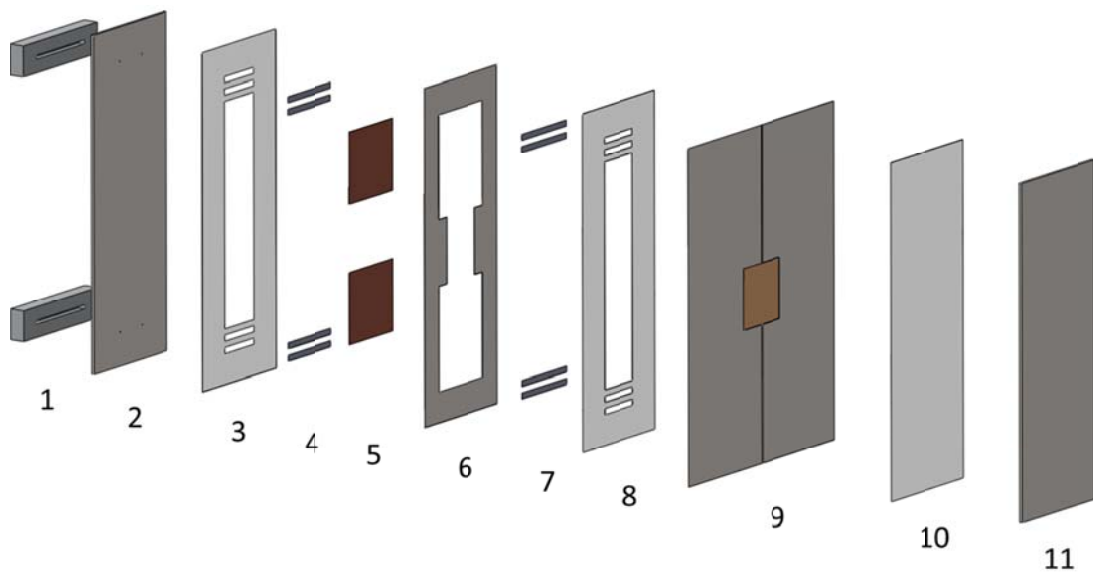


Figure 4-2: Exploded view of the second design iteration

To achieve uniform channel thicknesses, the design consists of stacked layers of steel shim stock and an adhesive transfer tape. In Figure 4-2, layer 1 of the bed consists of two external manifolds that act to help to distribute the fluid flow across the channel width. Due to the axial symmetry of the bed design, an even amount of water should flow through each hole drilled in the port plate of layer 2.

Layer 3 of the ECE bed consists of a layer of transfer tape that is used for both an adhesive and as a channel spacer. Next, 4 internal manifolds are stuck to the transfer tape in layer 4. The role of these internal manifolds is to temporarily reduce the cross section of the fluid channel to induce a higher pressure drop than the surrounding channel. The higher pressure drop should more evenly distribute the water flow along both the width and height of the channel.

The next layer, 5, consists of the two ECE films. The leads of each of the ECE films will be threaded through two small holes drilled into layer 2. Layer 6 consists of a spacer that is 0.196mm thick, the same thickness as the ECE film, placed around the ECE films and the internal manifolds. In reality it is likely that the spacer will be 0.2mm thick since .0196mm sheet steel is not readily available. The additional space should be absorbed by the transfer tape. Layers 7 and 8 consist of identical internal manifolds and a layer of transfer tape as layers 4 and 3 respectively. Layer 9 is a piece of sheet stock that is cut in half to allow for adding tension into the EC films. Adding tension into the films it should help ensure that the fluid channels on either side of the films are uniform. In addition, a film heater is set into this layer such that the thickness of the sheet stock is equal to the thickness of the film

heater. Finally layers 10 and 11 are a final layer of transfer tape and the final reinforcing plate respectively. Table 4-1 below summarizes the parts for the two film electrocaloric refrigeration cycle.

**Table 4-1: Layers of the two film electrocaloric refrigeration device**

<b>Layer</b>	<b>Name</b>	<b>Function</b>
1	External Manifolds	Initially splits the flow in two along the width of the channel.
2	Port Plate	Adds reinforcement to the device, allows fluid and heater wires to travel through the reinforcing structure.
3	Transfer Tape	Spaces and adheres the electrocaloric films and internal manifolds to the port plate.
4	Internal Manifold	Induces a large pressure drop to distribute the fluid flow evenly across the width of the fluid channel.
5	Electrocaloric films	Provides the cooling power to the device
6	Spacer	Spaces the other layers of the device in an equal distance as the electrocaloric film.
7	Internal manifolds	Induces a large pressure drop to distribute the fluid flow evenly across the width of the fluid channel.
8	Transfer Tape	Spaces and adheres the electrocaloric films and internal manifolds to the tensioning layer.
9	Tensioning Layer and Film Heater	Adds tension to the electrocaloric films to achieve uniform channel thicknesses and heats the center of the device when necessary.
10	Transfer Tape	Adheres the tensioning layer to the reinforcing plate
11	Reinforcing plate	Acts as a reinforcing structure for the device

The chosen adhesive was 3M's 467 MP adhesive. The thickness of this adhesive was experimentally determined to be 0.0022". This adhesive has high bond strength, good moisture resistance and it adheres well to metal (3M, 2012).

#### 4.2.1 Calculated Pressure Drop

The expected pressure drop across a non-uniform fluid channel can be calculated by summing the minor and major head losses (Munson, Young, Okiishi, & Huebsch, 2009). The major head loss can be calculated by:

$$h_{L,major} = \frac{f l v^2}{2 D_h g} \quad (4.2)$$

where  $f$  is the Darcy friction factor,  $l$  is the length of the fluid channel,  $v$  is the average velocity of fluid flow,  $D_h$  is the hydraulic diameter and  $g$  is the acceleration of gravity. The minor losses in the proposed refrigeration system are mainly due to the contracting expanding and directional changes of the fluid channel. The Darcy Friction Factor for a fully developed laminar flow in a round tube can be approximated by (Nellis & Klein, 2009):

$$f = \frac{64}{Re_{d_h}} \quad (4.3)$$

However for a rectangular duct with a small aspect ratio the friction factor becomes (Nellis & Klein, 2009):

$$f = \frac{96}{Re_{d_h}} \quad (4.4)$$

The minor head loss can be determined by:

$$h_{L,minor} = \frac{K_L v^2}{2 g} \quad (4.5)$$

Where  $K_L$  is the minor loss coefficient and is a function of the type of minor loss. The minor loss coefficients are presented in Table 4-2. Alternatively, the EES duct flow command van

be used to calculate the major head losses. For the case of laminar forced convection, EES calculates the Fanning Friction Factor through the correlation (Kakac, Shah, & Aung, 1987):

$$f_{fan} Re = 24(1 - 1.3553\alpha^* + 1.9467\alpha^{*2} - 1.7012\alpha^{*3} + 0.9564\alpha^{*4} - 0.2537\alpha^{*5}) \quad (4.6)$$

Where  $\alpha^*$  is:

$$\alpha^* = \frac{th_{chan}}{w_{chan}} \quad (4.7)$$

EES then accounts for the entry length by using a corrected form of equation (4.6) using data provided by Shah and London. The Fanning Friction factor relates to the Darcy Friction Factor by:

$$f_{fan} = \frac{1}{4} f \quad (4.8)$$

Table 4-2 below gives the minor and major head losses for a half symmetry model including both the correlation found in of the refrigeration bed.

Table 4-2: Pressure drop across various portions of the fluid channel within the EC refrigeration system (Munson, Young, Okiishi, & Huebsch, 2009).

Description	$K_L$	Pressure Drop, Darcy (Pa)	Pressure Drop, EES (Pa)
Constriction into the External Manifold	0.5	25.7	25.7
Flow Through the External Manifold Port	-	267.4	327.7
Expansion into External Manifold Dividing Channel	1	51.4	51.4
External Manifold Branched Blow	2	102.8	102.8
Flow Through the External Manifold Dividing Channel	-	155.0	203.3
Contraction into the Port Plate Hole	0.5	6.4	6.4
Flow Through the Port Plate	-	12.8	25.7
Expansion out of the Port Plate Hole	1	12.9	12.9
Contraction into the First Internal Manifold	0.5	5.2	5.2
Flow Through the First Internal Manifold	-	1813	2725
Expansion out of the First Internal Manifold	1	10.1	10.1
Flow through the Manifold Gap	-	3.5	5.4
Contraction, Flow and Expansion Through Second Internal Manifold	-	1832	2751
Flow Through the Film Channels	-	3399	5080
Flow Through Half the Cold Space	-	12.6	19.0

Since a half symmetry model is used, the total pressure drop is two times the sum of the minor and major losses in Table 4-2 above. Therefore, the EES calculated pressure drop is 22.7 Kpa and the Darcy pressure drop is 15.4 Kpa.

#### 4.2.2 Cold Space Sizing

In order to ensure continuous cooling, the combined volume of two fluid channels and the cold space should be less than the volume of one blow process. From the model optimization in section 3.2, the volume of one blow is approximately 0.18 mL. Assuming that the fluid channel thickness is the transfer tape thickness, the volume of one of the fluid channels,  $V_{chan}$  is:

$$V_{chan} = th_{chan} * w_{chan} * l_{chan} \quad (4.9)$$

where  $W_{chan}$  is the active width of the ECE films and the length of the channel,  $l_{chan}$  is the active length of the ECE film, 3 cm. The volume of the cold space,  $V_c$  is:

$$V_c = l_c * (2 * th_{chan} + th_e) * w_c \quad (4.10)$$

To achieve continuous cooling, the volume of two fluid channels and the cold space should be equal to or less than the volume one blow, 0.18 mL, so that a water particle is able to travel from the warm space to the far end of the cold space in one blow:

$$(2 * V_{chan} + V_c) \leq V_b \quad (4.11)$$

This results in a maximum cold space length of approximately 1.8 cm.

#### 4.2.3 Thermal Resistance Analysis

A thermal resistor network, shown in Figure 4-3, was then used to analyze the heat transfer characteristics of the second design iteration of the ECE bed.

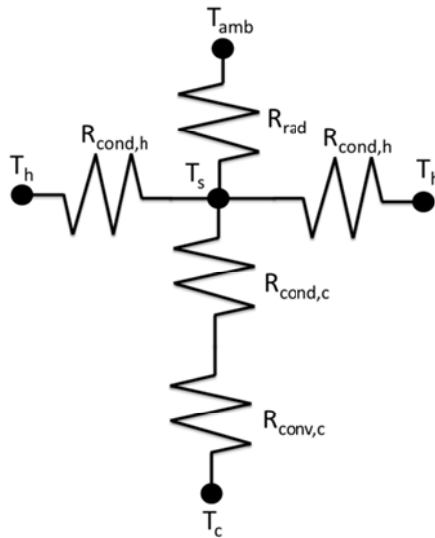


Figure 4-3: Thermal resistor network

A half symmetry thermal resistor network was used to determine both the surface temperature of the ECE bed above the cold space and the heat flux from the warm side of the bed to the cold space of the ECE bed. The system will reach steady state when the heat flux equals the cooling power provided by the films.

The resistance to convection on the inside of the cold space,  $R_{conv,c}$  is:

$$R_{conv,c} = \frac{1}{\bar{h}_c * L_{chan} * W_{chan}} = 0.23 \frac{K}{W} \quad (4.12)$$

where,  $h_c = 7151 \text{ W/m}^2\text{-K}$  and is the convection coefficient between the water and of the walls of the cold space.  $h_c$  can be determined by assuming a constant wall temperature where the Nusselt number for the fully developed laminar flow is 3.66 (Nellis & Klein, 2009). In this case, the duct flow command in the Engineering Equation Solver (EES) software was used to determine  $h_c$ .  $L_{chan} = 3 \text{ cm}$  is the length of the channel between the two electrocaloric films and the width of the channel,  $W_{chan} = 2 \text{ cm}$ . The resistance to conduction between the fluid channel and the outside of the bed,  $R_{cond,c}$  is:

$$R_{cond,c} = \frac{th_{end}}{k_{ss} * L_{chan} * W_{chan}} = 0.14 \frac{K}{W} \quad (4.13)$$

The thermal conductivity of the stainless steel that is used for the reinforcing plates is  $k_{ss}$  and the thickness of reinforcing plates,  $th_{end}$ , is 1.22mm. A coupled set of equations must be solved in order to solve for the temperatures at each node and the heat transfer rates between each set of nodes.

Radiation was assumed to occur over half of the area of the bed at the cold temperature of the ECE bed. The thermal resistance due to radiation,  $R_{rad}$  is:

$$R_{rad} = \frac{1}{W_{end} * L_{end} * \frac{1}{2} * \varepsilon * (T_c + T_{amb}^2) * (T_c + T_{amb})} = 59.21 \frac{K}{W} \quad (4.14)$$

where the width of the end cap,  $W_{end} = 5.08$  cm and the length of the end cap,  $L_{end} = 13$  cm.

The conduction resistance between the warm side of the bed and the center of the device,  $R_{cond,h}$  is therefore:

$$R_{cond,h} = \frac{\frac{l_{end}}{2}}{k_{ss} * th_{end} * w_{end}} = 75.69 \frac{K}{W} \quad (4.15)$$

where the length of the end cap,  $l_{end}$ , is 0.14 m. The heat transfer rate between the water in the cold space and the outside surface of the bed,  $\dot{Q}_{c,s}$  is:

$$\dot{Q}_{c,s} = \frac{T_s - T_c}{R_{conv,c} + R_{cond,c}} \quad (4.16)$$

The heat transfer rate between the warm side of the ECE bed and the surface of the cold space,  $\dot{Q}_{h,s}$  is:

$$\dot{Q}_{h,s} = \frac{T_h - T_s}{R_{cond,h}} \quad (4.17)$$

The heat transfer rate between the outside environment and the surface of the bed,  $\dot{Q}_{r,s}$  is determined by:

$$\dot{Q}_{r,s} = \frac{T_{amb} - T_s}{R_{rad}} \quad (4.18)$$

An energy balance is then conducted around the surface node of the resistance network:

$$2 * \dot{Q}_{h,s} + \dot{Q}_{r,s} = \dot{Q}_{c,s} \quad (4.19)$$

Since the resistor network was a half symmetry model, the total heat transfer rate from both warm sides of the bed to the water located in the cold space,  $\dot{Q}_{leak}$  can be found by:

$$\dot{Q}_{leak} = 2 * \dot{Q}_{c,s} \quad (4.20)$$

By assuming that the heat transfer rate from the warm sides of the bed to the cold space is equal to the rate at which the films can cool the cold space, the calculated temperatures will be under steady state conditions.

$$\frac{\int_{cycle} \dot{Q}_{leak} dt}{t_{cycle}} = \frac{\int_{cycle} \dot{Q}_c dt}{t_{cycle}} \quad (4.21)$$

Where the right hand side of equation (4.21) is a realistic cooling power provided from the ECE bed and is determined from the modeling analysis, taken to be 0.5w. Finally, by making the assumption that the warm ends of the bed are held at a constant ambient temperature and that low carbon steel is used for the support structure, the steady state cold space temperature is 297.9K and the steady state surface temperature is 298.0K. The warm ends of the bed could be held at a constant temperature by providing a thermal link to the walls of the vacuum vessel.

Since, through this simple calculation, the outside of the bed was found to be approximately equal to the temperature of water in the cold space. The temperature sensors and a film heater can be placed on the outside of the bed instead of being directly submerged in the water located in the cold space. This modification allows for thermistors to be used instead of thermocouples and makes manufacturing easier.

If the reinforcing plates are made of a lower thermal conductivity material, stainless steel, instead of low carbon steel,  $T_c$  drops to 294.1 K while the surface temperature remains very close to the cold space water temperature. As a result, stainless steel should be used for the support structure instead of low carbon steel. For this analysis the thermal resistance of the adhesive has been neglected.

### *4.3 Electrical System Design*

Due to the strong electric fields required to produce measurable temperature differences using the electrocaloric effect, a high voltage must be applied to the leads of the electrocaloric film. A simple circuit must be designed that allows for charging and discharging the films at regular intervals.

#### *4.3.1 ECE Film Electrical Capacitance*

Figure 4-4 shows the multi-layer arrangement of a single ECE film. Due to the geometry of the films, they can modeled as capacitor.

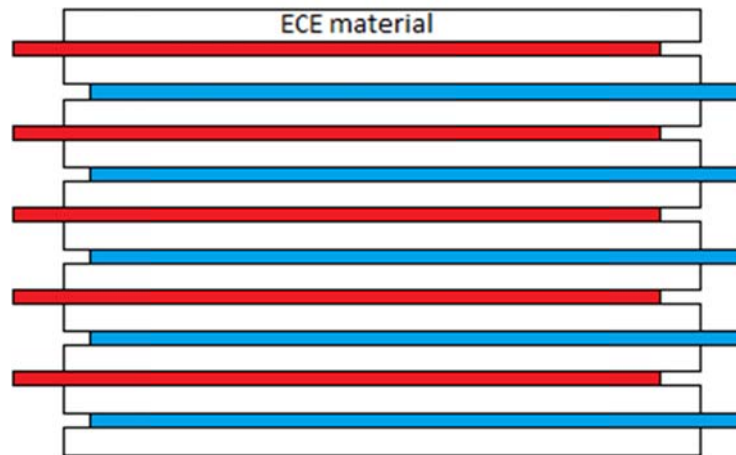


Figure 4-4: An 11 layer multilayer ECE film arrangement.

In order to achieve the high electric fields that are required in the ECE films for effective operation thin conducting electrodes, represented by the thin shaded layers, are placed between layers of ECE material. The thickness of each of the electrodes is on the order of a nanometer. The films that will be used to construct the demonstration device are 24 layers thick with a total thickness of  $196 \mu\text{m}$ . Therefore the individual layer film thickness can be approximated by:

$$th_L = \frac{th_e}{N_{ece}} = 8.17 \mu\text{m} \quad (4.22)$$

Since the maximum applied electric field,  $E_{max}$ , is  $80 \times 10^6 \text{ V/m}$ , in order to prevent film degradation the voltage difference between the electrodes should not exceed:

$$V_{max} = E_{max} * th_L = 652.8 \text{ V} \quad (4.23)$$

Operating at this voltage would likely destroy the film and, therefore,  $V_{max}$  should only be

used to specify a power supply. The permittivity of the electrocaloric polymers is a function of both the rate that the capacitor is charged and discharged, the temperature of the material and the applied electric field (Lu, Rozic, & Zhang, 2010). The film's manufacturer provided an estimated capacitance of 400 nf.

#### 4.3.2 Electrical Circuit Design

The circuit diagram for a one film refrigeration system is presented in Figure 4-5.

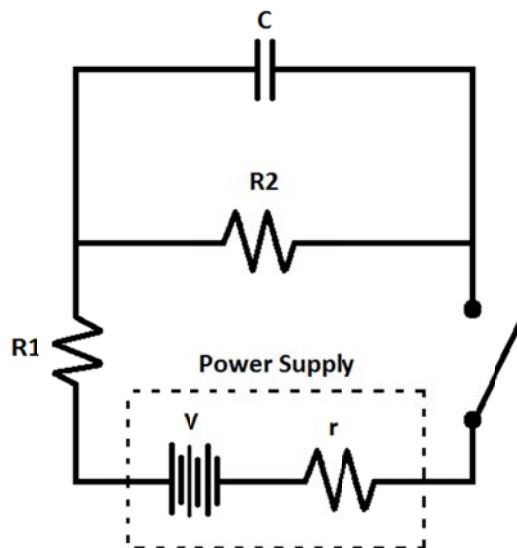


Figure 4-5: The circuit diagram for a one bed ECE refrigeration system.

The EC bed is modeled as a capacitor and the resistors are used to limit the current out of the power supply. The four states of the circuit shown in Figure 4-5 are shown in Figure 4-6.

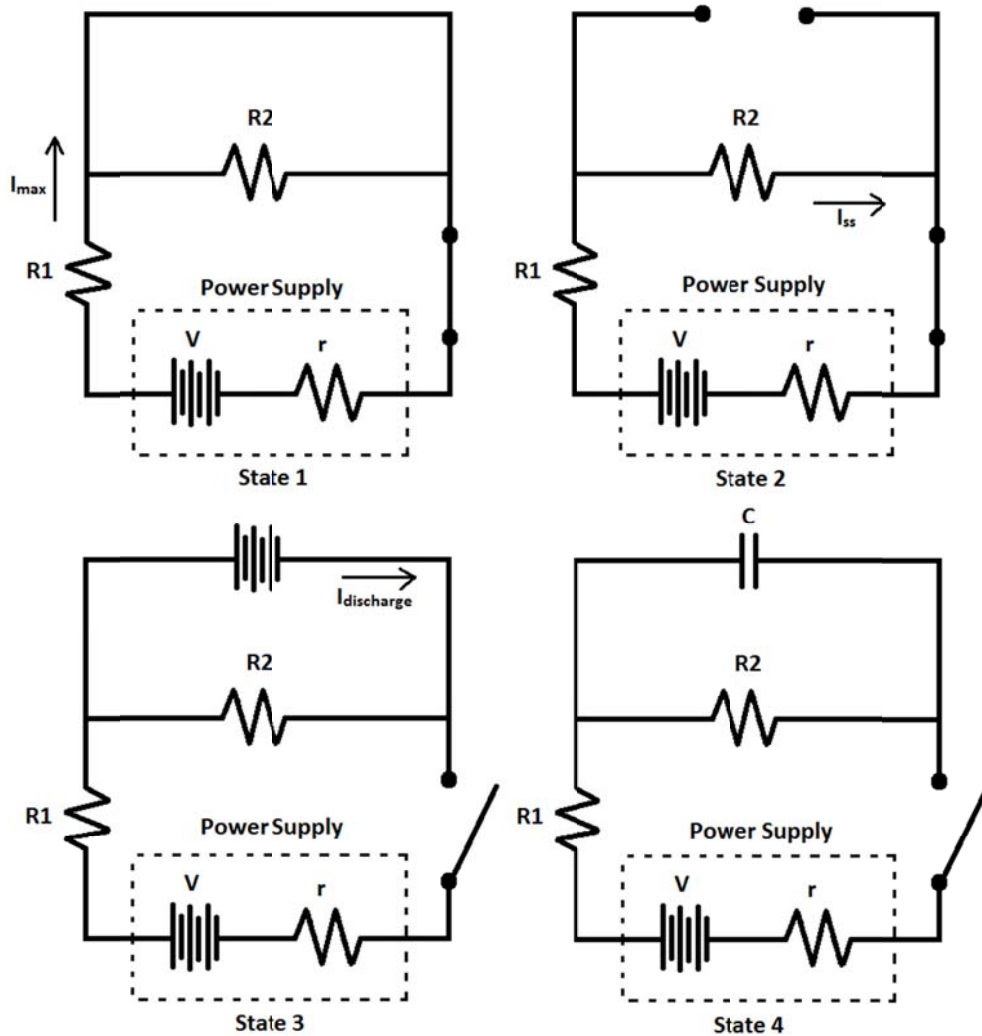


Figure 4-6: The four important electrical states of the proposed ECE refrigeration cycle.

In state 1, a voltage is instantaneously applied, and initially, while the electrodes are charging, the bed can be modeled as short circuit. The maximum current draw,  $I_{max}$  will occur during this state. State 2 occurs once the film has been charged and, in this state, the EC bed rejects energy during the cold to hot blow. Once the EC film has been fully charged, the film can be modeled as an open circuit, and therefore, the current from the power supply drops to a steady state value,  $I_{ss}$ . Although the voltage supply could be removed

during this state, it is continuously applied to prevent capacitor leakage and to ensure that there is constant electric field within the EC film. In state 3 the voltage is removed and the EC film is allowed to discharge. During the initial discharge period, the capacitor can be modeled as a voltage source. Finally, during state 4 no current is flowing through the system and the EC bed absorbs energy during the hot to cold blow.

The circuit components must be specified so that the current, film charge time and film discharge time are reasonable. Assuming that the maximum current,  $I_{max}$  can be no greater than the rated power supply current of 60 mA and the applied voltage,  $V_{in}$ , can be no greater than 750 V the resistance  $R_1$  is:

$$R_{e,1} = \frac{V_{in}}{I_{max}} = 12.5 \text{ k}\Omega \quad (4.24)$$

When the voltage across the capacitor,  $V_{max}$ , is 652.8 V, the resistance,  $R_{e,2}$ , can be found by the voltage divider rule:

$$\frac{R_{e,2}}{R_{e,1} + R_{e,2}} = \frac{V_{max}}{V_{in}} \quad (4.25)$$

$R_{e,2}$  is found to be 84 k $\Omega$ . The time to charge the capacitor,  $t_c$  is then found by using the RC time constant assuming that the capacitor is fully charged within 5 time constants (Hayt, Kimmerly, & Durbin, 2007):

$$t_c = \frac{R_{e,1} R_{e,2} C}{5 (R_{e,1} + R_{e,2})} = 0.022 \text{ s} \quad (4.26)$$

where the real capacitance of one film,  $C$ , was provided by the film manufacturer, Strategic

Polymer Sciences, to be approximately 400 nF. The time to discharge the capacitor  $t_d$  is additionally found through an RC time constant relationship:

$$t_d = \frac{R_{e,2} C}{5} = 0.17s \quad (4.27)$$

The steady state current,  $I_{ss}$ , is then found through Ohms law:

$$I_{ss} = \frac{V_{in}}{(R_{e,1} + R_{e,2})} = 7.8 \text{ mA} \quad (4.28)$$

The complete circuit diagram for the two bed EC refrigeration system is shown in Figure 4-7.

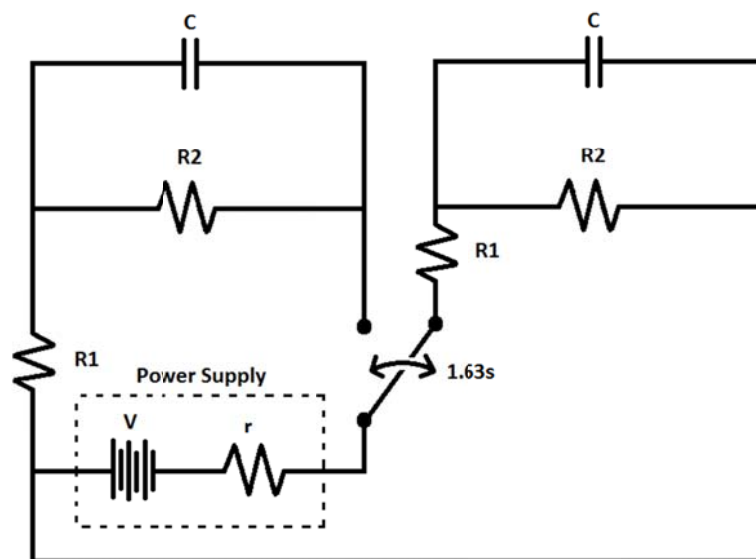


Figure 4-7: The complete ECE refrigeration system's circuit diagram.

The switch will change positions every 1.63 seconds and, as a result, even though there are two ECE films in operation, the current will never be greater than 60mA. This circuit also guarantees that the two ECE beds are always exactly out of phase from one another.

#### 4.4 Warm Heat Exchanger

In order to reduce the cooling time, the effectiveness of the heat exchanger. The external manifold will act at the heat rejection heat exchanger. The external manifold will be made from copper because it is commonly available, has a low specific heat and high thermal conductivity compared to most metals. This will allow thermal energy to be conducted out of the vacuum chamber more effectively.

By assuming that the volume of the water in the heat exchanger tube is equal to the volume of water that is expelled by the EC bed in one blow, the volume of the water within the heat exchanger is fixed. Therefore, the diameter of the tubing has a significant effect on the effectiveness of the heat exchanger. Plotting the heat exchanger effectiveness, found in Equation (2.84), as a function of length over diameter, Figure 4-8 is produced.

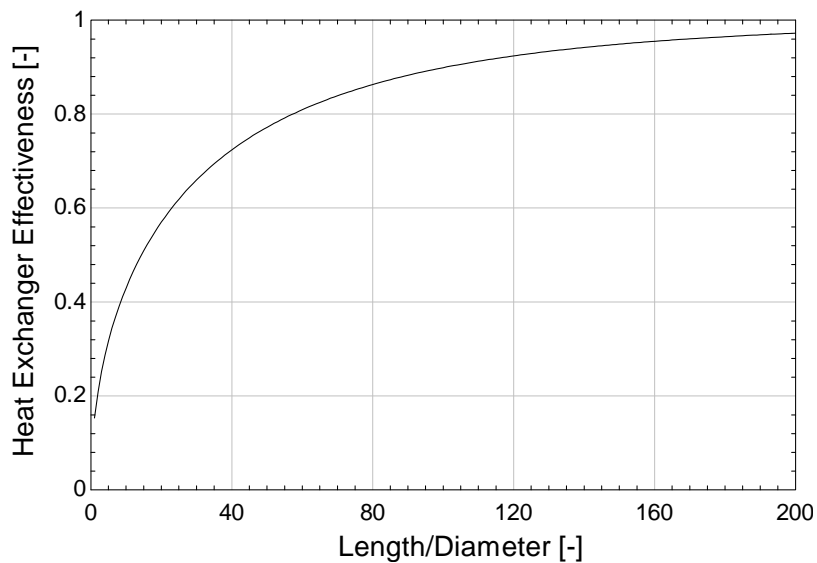


Figure 4-8: The effectiveness of the cold heat exchanger as a function of the length over the diameter of the heat exchanger.

It can be seen that the smaller diameter and longer the heat exchanger, the higher the heat exchanger effectiveness. Therefore, to minimize the temperature difference between the external manifold and the working fluid, the heat exchanger should use the smallest diameter copper tubing and that is readily available as long as the pump is still able to push the water through the system at the desired mass flow rate. Copper tubing that has an inside diameter of 1.4mm is available.

#### *4.5 Cold Heat Exchanger*

The cold space between the two EC films will act as the cold heat exchanger for the demonstration device. It is not desirable to maximize heat transfer between the working fluid and the walls of the demonstration device since the temperature of the fluid within the cold space is to be minimized.

#### *4.6 Pump*

Traditional unidirectional pumps were initially examined, but to achieve the required oscillating flow through the EC bed a complex plumbing system would be necessary. Therefore, to facilitate the required oscillating flow a syringe pump is recommended.

The demonstration device will use a model NE-1000 syringe pump from New Era Pump Systems Inc. These syringe pumps, shown in Figure 4-9, are computer programmable, capable of infusion and drawing, and can produce an estimated 900 kpa of pressure when dispensing 0.11g/s of water while using a 3cc HSW Norm-ject syringe (NE-1000 Programmable Single Syringe Pump, 2013).



Figure 4-9: An NE-1000 New Era Pump Systems, Inc. Syringe pump (NE-1000 Programmable Single Syringe Pump, 2013)

The direction of the flow will be controlled by an analog sensor interface. This device is capable to change the pump program based on a voltage. This makes it possible to indirectly control the pump from Labview and will allow the pumping direction to be synchronized with the electrocaloric films.

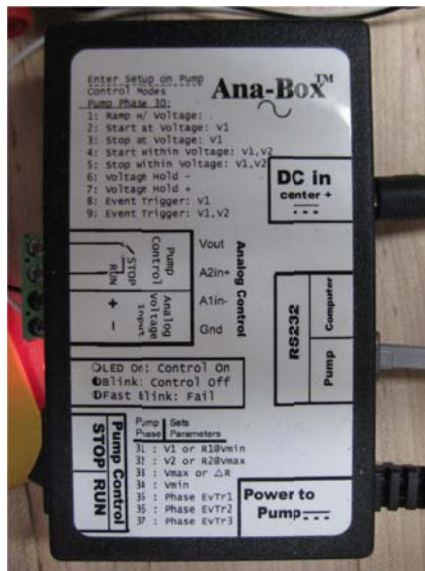


Figure 4-10: New Era Pump Systems, Inc. Ana-Box – closed loop analog sensor interface.

#### 4.7 References

- NE-1000 Programmable Single Syringe Pump. (2013). Retrieved January 8, 2013, from New Era Pump Systems Inc.: <http://www.syringepump.com/NE-1000.php>
- 3M. (2012). High Performance Adhesive Transfer Tapes with Adhesive 200MP. St. Paul: 3M Converter Markets.
- Hayt, W., Kimmerly, J., & Durbin, S. (2007). Engineering Circuit Analysis. New York: McGraw-Hill.
- Knier, B. J. (2012). A Thermodynamic Analysis of an Electrocaloric Effect (ECE) Refrigeration Cycle. University of Wisconsin - Madison.
- Lu, S. G., Rozic, B., & Zhang, Q. M. (2010). Electrocaloric Effect (ECE) in Ferroelectric Polymer. *Ferroelectrics*.
- Munson, Young, Okiishi, & Huebsch. (2009). Fundamentals of Fluid Mechanics. Jefferson City: R. R. Donnelley.
- Nellis, G., & Klein, S. (2009). Heat Transfer. New York: Cambridge University Press.

## CHAPTER 5: PROTOTYPE CONSTRUCTION

### 5.1 Initial ECE Bed Prototype Construction

The purpose of the initial prototype was to explore manufacturing techniques and to verify that the design is feasible. The first step in the prototype construction was to build the tensioning jig that would add a known amount tension into the EC films. This was done to ensure that the fluid channels on either side of the ECE films have a consistent channel thickness. Figure 5-1 shows the initial design of the tensioning rig.



Figure 5-1: The initial design of the film tensioning rig.

After the EC films have been adhered to the tensioning layer, the tensioning rig will pull on the tensioning layer of the ECE bed therefore adding the desired tension. Once the external

manifolds had been machined from aluminum, PVC fluid tubes were directly epoxied to the external manifolds using Devcon 5 minute epoxy. This step can be seen in Figure 5-2.



**Figure 5-2: Epoxying the water tubing to the external manifolds.**

Separately, the tensioning layer, shown in Figure 5-3, was cut from a sheet of .051mm low carbon steel and one of the spacing layers of adhesive was applied.



**Figure 5-3: Tensioning layer with spacing adhesive**

Next, adhesive was placed on the reinforcing plate and the plate was placed on the tensioning rig, shown in Figure 5-4.

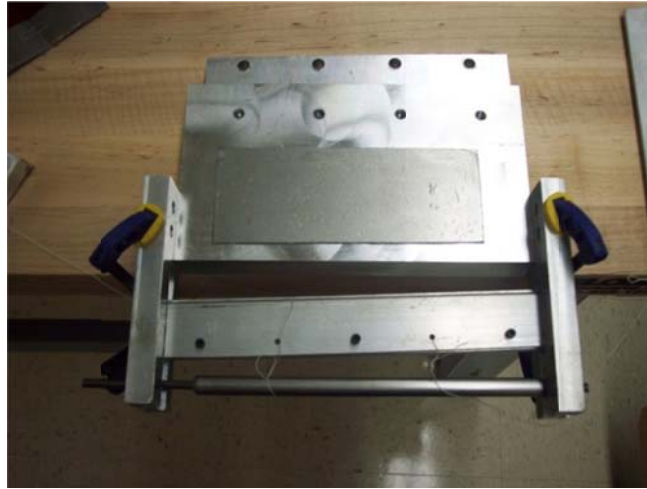


**Figure 5-4: Reinforcing plate**

The mock ECE films, made out of 0.127 mm Kapton film, were placed on the tensioning layer and were put under about 5 N of tension. While the films were under tension, the entire film assembly was adhered to the reinforcing plate. Next, Figure 5-5 shows the assembly after the internal manifolds were installed.

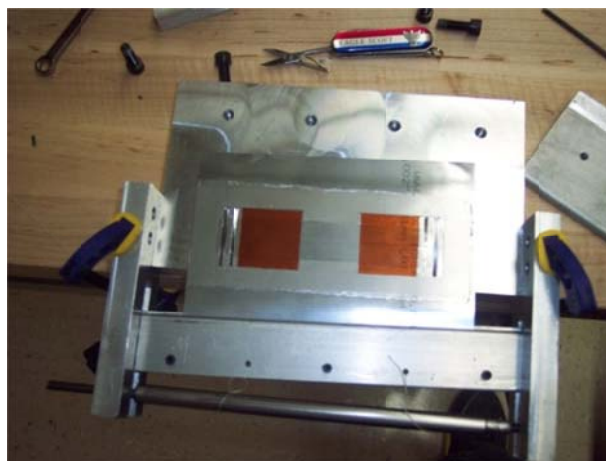


**Figure 5-5: Tensioning layer assembly adhered to the reinforcing plate**

Another spacing layer of adhesive was applied to the port plate and a second set of internal manifolds were installed. Pins placed through the holes in the port plate were used to align the inside layers with one another when connecting the two halves of the EC bed. The two external manifolds were then adhered to the closed bed. Figure 5-6 shows the closed EC bed.

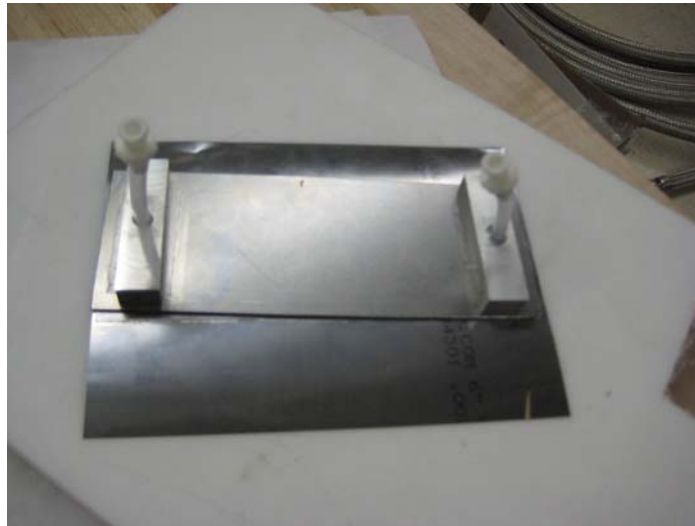


**Figure 5-6: Closed EC bed**

The excess tensioning layer was trimmed and Devcon 5 minute epoxy was used to seal the edges. Figure 5-7 shows the completed prototype.

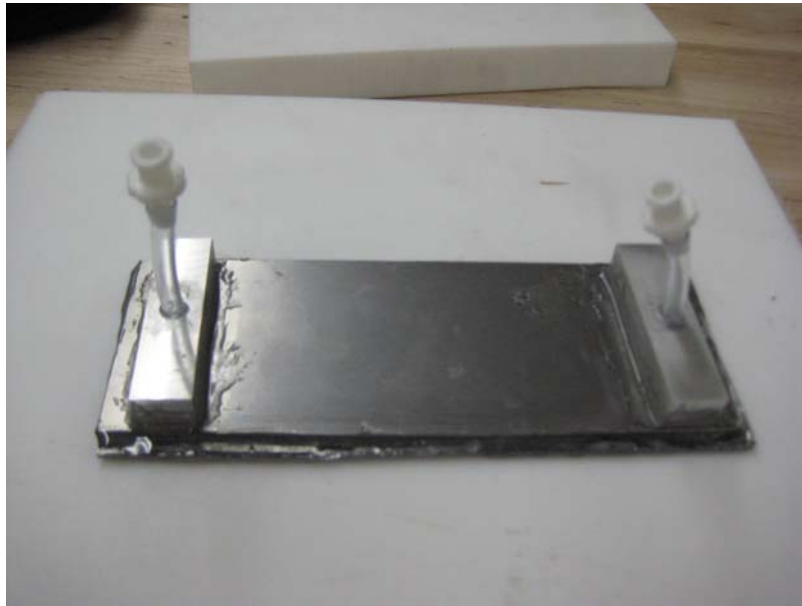


**Figure 5-7: Completed initial prototype.**

### *5.2 Prototype Construction Problems*

The construction of the EC bed should be improved in order to achieve greater manufacturing consistency before the final bed is constructed. First, while tensioning the EC films, it was difficult to place the reinforcing plate under the tensioning layer. To attempt to solve this problem, a pocket was machined out of the tensioning rig and a movable insert was placed in the pocket so that the reinforcing plate could be raised from the bottom while the films are under tension.

The second problem with the construction of the initial prototype was that it was difficult to align each layer on top of one another accurately by hand. Therefore, two aligning pins will be placed into the insert of the tensioning rig. Additionally, corresponding holes will be drilled into each layer of the demonstration device. This will produce two holes in the final

bed; these holes will be epoxied closed similar to how the edges of the initial prototype were sealed. Figure 5-8 below shows the improved tensioning rig.

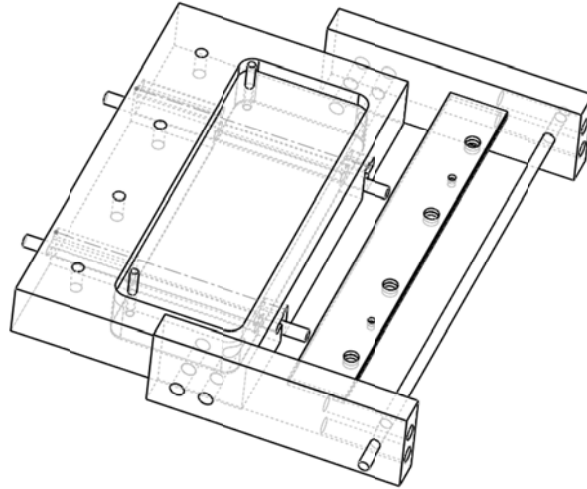


**Figure 5-8: The improved tensioning rig**

The measured pressure drop when the syringe pump was withdrawing was  $9.88 \pm 0.53$  Kpa and during infusing the pressure drop was  $8.87 \pm 0.53$  Kpa. These values are significantly different than the predicted pressure drop of 22Kpa. The section on flow visualization, 5.3, provides further insight on why the pressure drop is smaller than expected.

### *5.3 Flow Visualization Prototype*

To get achieve a better understanding of the flow pattern within the ECE bed, a clear device was constructed out of acrylic. This bed was constructed with the same manufacturing methods as the original prototype and is shown in Figure 5-9 below.



**Figure 5-9: A clear prototype of the proposed ECE refrigeration system**

Water was then pumped through the clear bed at 1.1mL/second and a dye was injected to visualize the flow. Figure 5-10 shows the flow in one second increments.



**Figure 5-10: A one second time-lapse of the injection of die into a clear ECE refrigeration bed prototype.**

It can be seen that the flow is distributed well along the width of the fluid channel. This test provided no information on the flow distribution of the water along the thickness of the fluid channel.

Figure 5-10 also shows that air pockets were trapped within the bed when the bed was initially charged with water. These pockets disturb the natural flow patterns and will likely prevent heat transfer from the water within the cold space. In addition, a small amount of water can be seen to be traveling through the adhesive layer of the bed and around edge the ECE films in Figure 5-11.

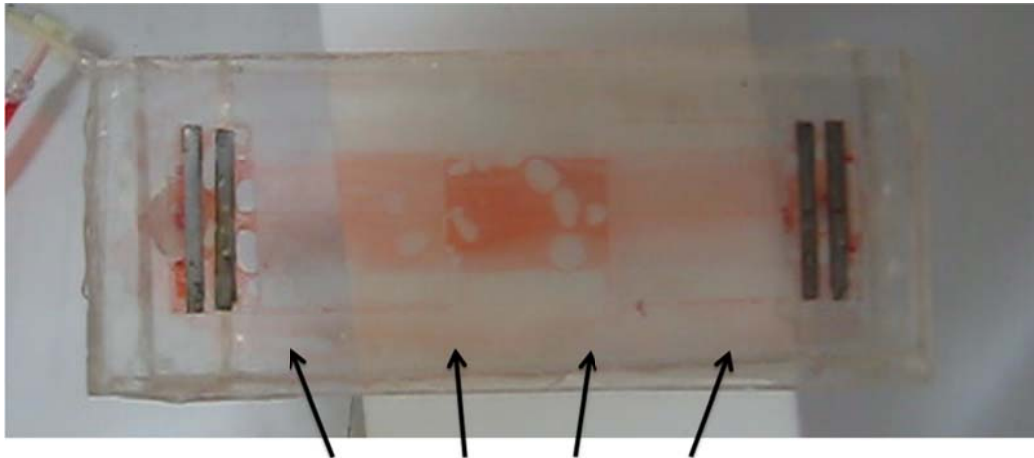


**Figure 5-11: Fluid flow can be seen going around the fluid channel.**

This is likely one of the contributing factors that resulted in the measured pressure drop differing from the predicted. According to the adhesive's manufacturer, the adhesive used as the channel spacer has poor adhesion to polymers but excellent adhesion to metals. Therefore, it is anticipated that when metal is used for future designs, fluid will not flow between the layers of the device.

Adding a surfactant to the water, in this case organic dish soap, and filling the bed slowly while the bed was orientated vertically dramatically decreased the trapped air within the ECE bed. Figure 5-12 below shows the air trapped in the bed.

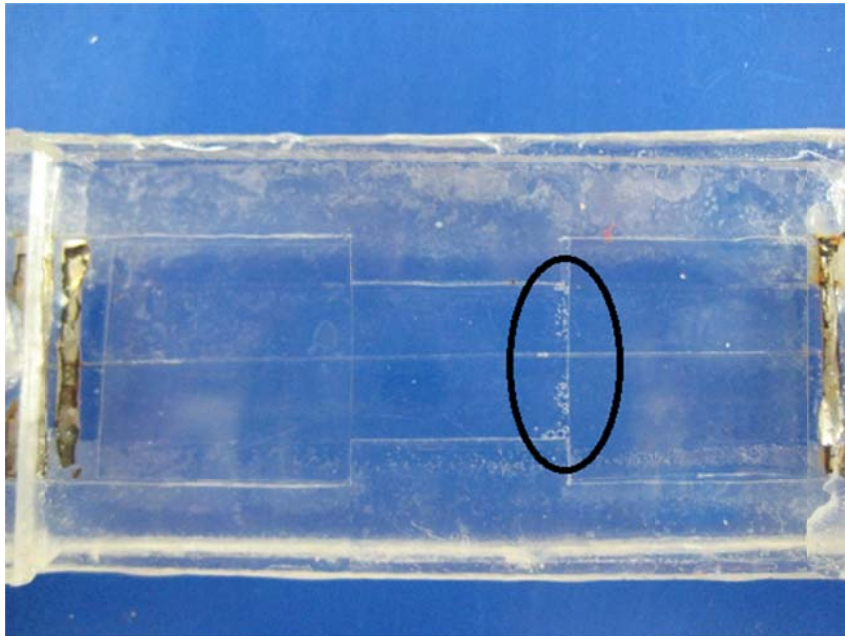


Figure 5-12: Trapped air within the ECE bed when using the surfactant based air reduction method.

This method did not completely eliminate the air trapped in the device but should provide a sufficient starting point for charging future experiments with water. Ideally, the space within the bed would be completely evacuated and then water added to the evacuated space. This would likely further reduce the amount of air trapped in the bed.

Finally, after completing several tests, the original low carbon steel internal manifolds of the demonstration device started to show significant rust, as seen in Figure 5-12. Therefore, low carbon steel should be excluded from future designs.

#### 5.4 System Operating as a Regenerative Heat Exchanger

In January 2013 word was received that electrocaloric films would not be available for this project. However, some model validation can be accomplished by comparing the model to a regenerative heat exchanger of similar geometry. This can be done by turning the

electrocaloric effect off (by setting the applied electric field to zero in the model) and by setting the cold space to a temperature that is above the warm space temperature. These modifications effectively model the ECE refrigeration device as a regenerative heat exchanger with heat being generated at the center of the device.

Using the input parameters presented in Table 2-1 for various numbers of films, a plot, shown in Figure 5-13, was generated that correlates the temperature at the warm space of the regenerative heat exchanger to the heat transfer across one stack of regenerator films

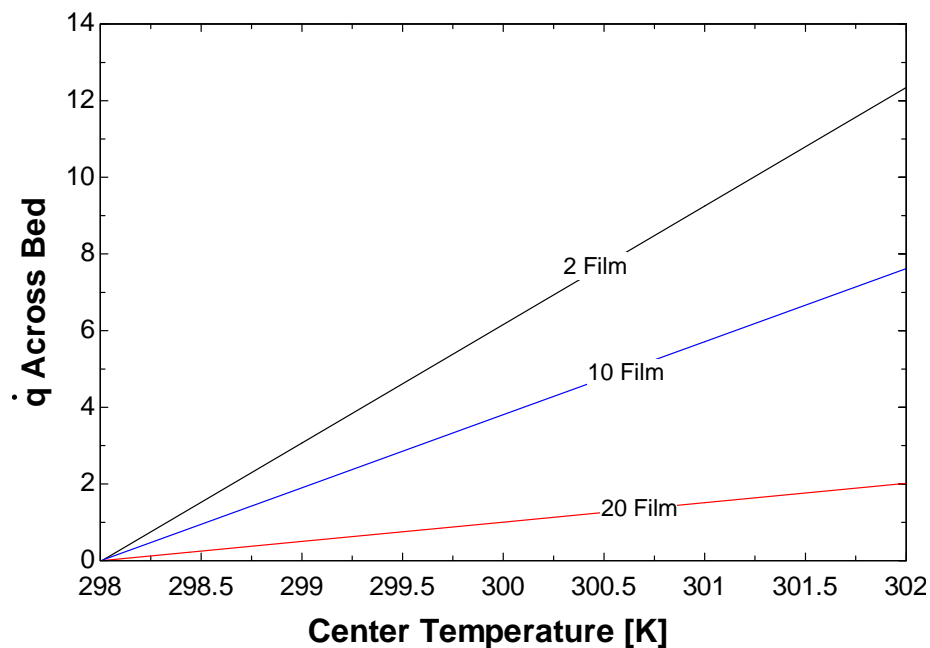


Figure 5-13: Correlation between the center temperature and the heat transfer across one stack of regenerator films when the cold space is 298 [k].

By controlling the amount of thermal energy that flows across the bed and by measuring the temperature difference on each side of the bed, a physical device can be compared to the model through a plot similar to Figure 5-13. Alternatively, the modeled heat exchanger

effectiveness could be plotted as a function of a non-dimensional flow parameter such as the Reynolds number.

A film heater will be placed in the center of the bed where the cold space will be in the final electrocaloric refrigeration device. This heater will allow a comparison between the model and physical experiment. Assuming an ideal regenerator, a qualitative view of the cycle can be obtained by tracking a fluid particle through one complete cycle of steady state operation, shown in Figure 5-14.

Starting at position, 1 the fluid particle is at equilibrium with its surroundings. As the fluid particle is pumped through the regenerative films between position 1 and 2, the warm regenerative films convect thermal energy to the fluid, simultaneously cooling the regenerative films. Then, as the fluid particle passes by the film heater, traveling from position 2 to 3, it absorbs additional thermal energy. At this point the fluid particle enters a second set of regenerative films which are at a lower temperature than the fluid particle. As the fluid particle travels from position 3 to position 4 it transfers thermal energy to the regenerative films.

When the fluid particle arrives at state 4 it will be at a higher temperature than the surroundings. Therefore, at position 4 the fluid particle is able to reject heat to the surroundings. The flow direction is then reversed and the process is repeated.

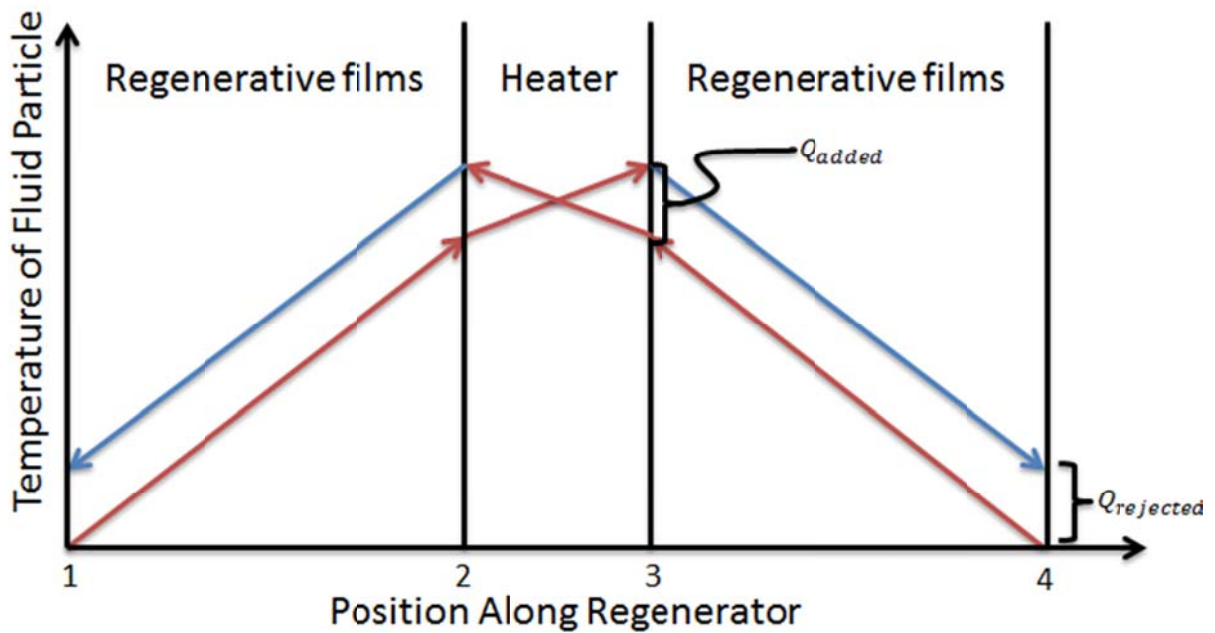


Figure 5-14: Qualitative view tracking a fluid particle through the proposed regenerative heat exchanger design.

In order to maximize the similarity between the regenerative heat exchanger and a real electrocaloric refrigeration cycle, the material of the regenerative films will be made from polyvinylidene fluoride (PVDF). The electrocaloric films manufactured by Strategic Polymer Sciences are derived from PVDF (Zhang, Bharti, & Zhao, 1998). A table comparing the heat transfer properties of these two polymers is presented in Table 5-1 below.

Table 5-1: A comparison of select heat transfer related properties between PVDF and Strategic Polymer Sciences' electrocaloric polymer. (Iguchi, dos Santos, & Gregorio Jr., 2007), (Knier, 2012)

Property	PVDF	Electrocaloric Polymer	Percent difference
Thermal Conductivity, $k$ , (W/m-K)	0.26	0.20	23.1%
Specific heat capacity, $c$ , (J/kg-K)	1325	1500	-11.6%
Density, $\rho$ , (kg/m <sup>3</sup> )	1775	1800	-1.3%
Volumetric heat capacity, $c_v$ , (J/m <sup>3</sup> -K)	$2.35 \cdot 10^6$	$2.70 \cdot 10^6$	-13.0%

#### 5.4.1 A study of Non-uniform Fluid Channel Thicknesses

To study the effect of non-uniform channel thicknesses in the regenerator stack, a flow resistance concept was used that is similar to the use of thermal resistances in a heat transfer problem or electrical resistances in problems involving electricity:

$$I = \frac{\Delta V}{R_{ele}} \quad \dot{q} = \frac{\Delta T}{R} \quad (5.1)$$

The flow resistances should therefore have the form:

$$\dot{m} = \frac{\Delta P}{R_{flow}} \quad (5.2)$$

The Darcy-Weisbach equation states that (Munson, Young, Okiishi, & Huebsch, 2009):

$$\Delta P = f \frac{L}{D_h} \rho \frac{v^2}{2} \quad (5.3)$$

where  $f$  is the friction factor,  $L$ , is the length of the fluid channel  $D_h$  is the hydraulic diameter,  $\rho$  is the fluid density and  $v$  is the velocity of the flow. Since the flow is fully developed and laminar, the friction factor is:

$$f = \frac{64}{Re} \quad (5.4)$$

where,  $Re$  is the Reynolds number. Equation (5.3) can then be written as:

$$\Delta P = \frac{64}{Re} \frac{L}{D_h} \rho \frac{v^2}{2} \quad (5.5)$$

The Reynolds number for internal flow is:

$$Re = \frac{\rho V D_h}{\mu_f} \quad (5.6)$$

Therefore, after rearranging, the pressure drop can be written as:

$$\Delta P = \frac{32 \mu_f L v A_{xc} \rho}{D_h^2 A_{xc} \rho} \quad (5.7)$$

Since mass flow rate is:

$$\dot{m} = v A_{xc} \rho \quad (5.8)$$

Equation (5.7) can be written as:

$$\dot{m} = \Delta P \frac{32 \mu L}{D_h^2 A_{xc} \rho} \quad (5.9)$$

Therefore flow resistance for a laminar fully developed channel is:

$$R_{flow} = \frac{D_h^2 A_{xc} \rho}{32 \mu L} \quad (5.10)$$

For laminar flow, the flow resistance is only a function of geometry and fluid properties.

Since all of the channels are in parallel the total flow resistance,  $R_{flow,tot}$  is:

$$R_{flow,tot} = \frac{1}{\sum_{i=1}^N \frac{1}{R_{flow,i}}}$$

where N is the total number of channels. The ratio of the pressure drop through a bed consisting of one non uniform channel over the pressure drop of a bed consisting of entirely nominal channels is plotted as a function of the thickness of the non-uniform channel over the nominal channel thickness in Figure 5-15.

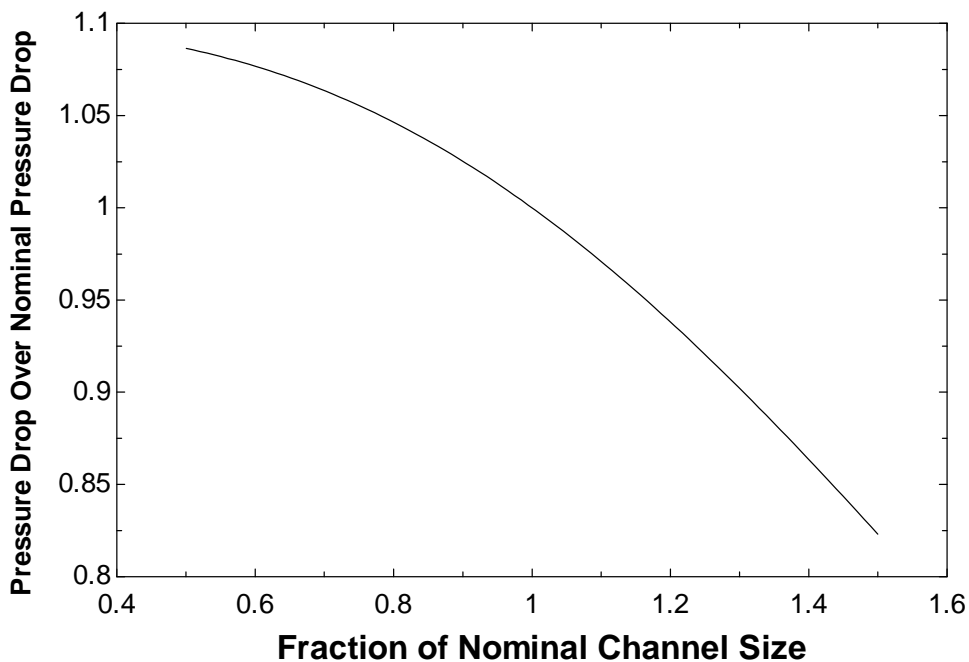


**Figure 5-15: The ratio of the pressure drop through a bed consisting of one non uniform channel over the pressure drop of a bed consisting of entirely nominal channels as a function of the relative thickness of the non-uniform channel compared to the nominal channels**

Figure 5-15 assumes the nominal channel thickness of 56  $\mu\text{m}$  and shows that varying the thickness of just one channel has a significant effect on the pressure drop of the entire bed. In the case that one channel does not have the same thickness as the others, the distribution of the mass flow rate will change such that more fluid flows through the larger channels. This will effectively reduce the capacitance of the regenerator films because heat will not transfer between the films and the fluid in the channel as well. This effect can be seen in Figure 5-16.

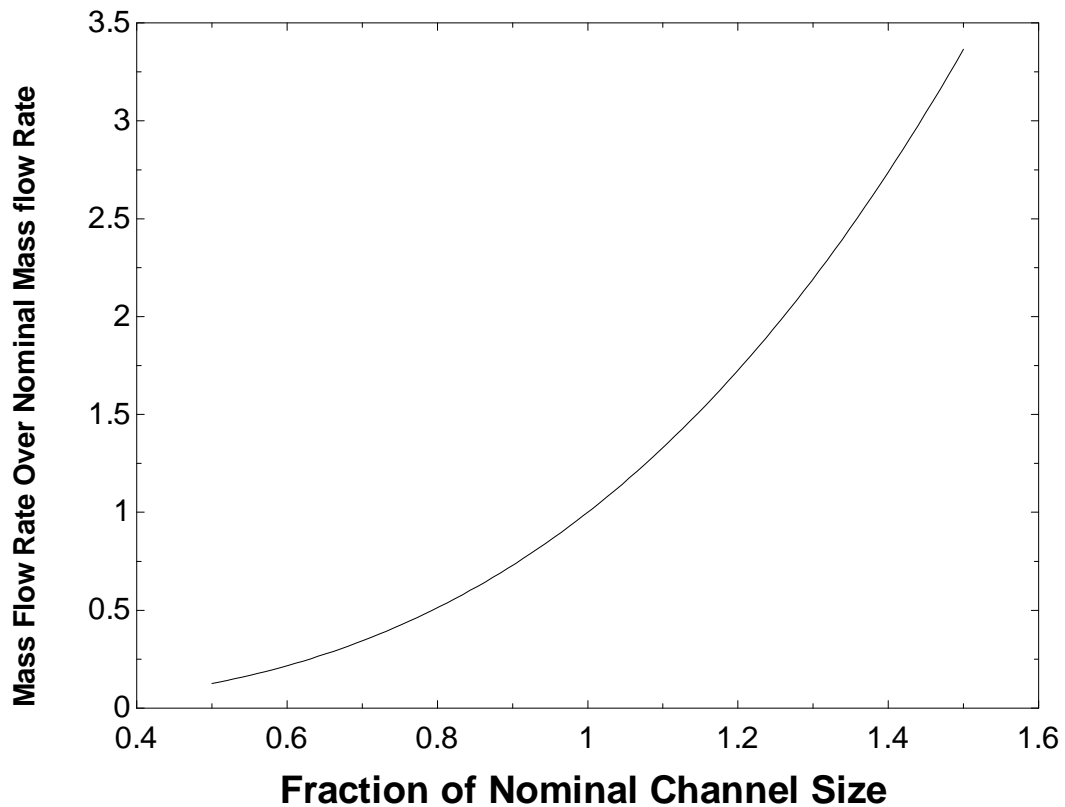


Figure 5-16: The ratio of mass flow rate through a non-uniform channel over the mass flow rate through a nominal channel within the same 11 channel device as a function the thickness of a non-uniform channel over the thickness of a nominal channel.

The mass flow rate through a non-uniform channel has a strong dependence on the fluid channel thickness. A 5% variation in channel thickness yields approximately a 15% change mass flow rate. Therefore, it is important to make sure that the fluid channels are uniform in order to maximize the heat transfer between the water and the regenerator films. A 5% non-uniformity a reasonable goal for the fluid channels within this device.

The flow within the device is distributed along the width of the fluid channel by the internal manifolds. These manifolds consist of restrictions in channel thickness to induce a pressure

drop. The internal manifolds should induce a pressure drop that is large compared to the pressure drop through the regenerator bed. Therefore the flow should distribute itself along the width of the fluid channel evenly. As Figure 5-17 shows, the pressure drop is strongly dependent on the height of the channel through each internal manifold. The pressures in Figure 5-17 were calculated using the duct flow function in EES.

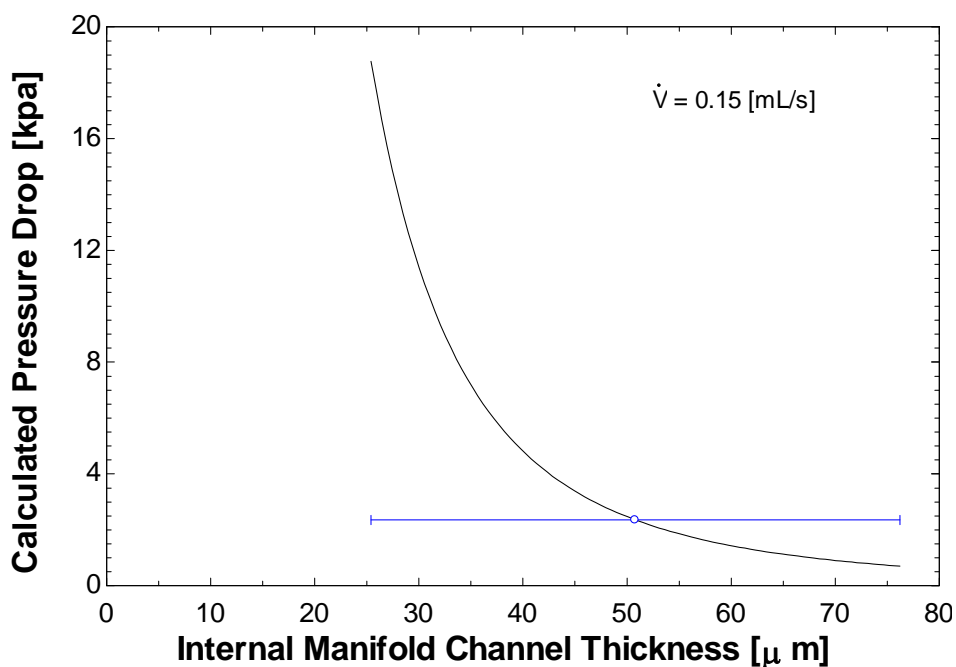


Figure 5-17: Pressure drop as a function of internal manifold thickness. The blue dot denotes the nominal channel thickness.

The dot in Figure 5-17 denotes the nominal channel height. An error of 25 microns (0.001 inches) in the thickness of the internal manifolds is reasonable because the pieces of metal that are used to create the internal manifolds were sanded by hand. This creates a large uncertainty in the measured pressure drop of the internal manifolds.

#### 5.4.2 Tensioning the Regenerator Films

One method of ensuring that the fluid channels within the regenerator bed are within 5% of their nominal value is to add tension to the films to reduce their deflection. Figure 5-18 shows a force balance on one film.

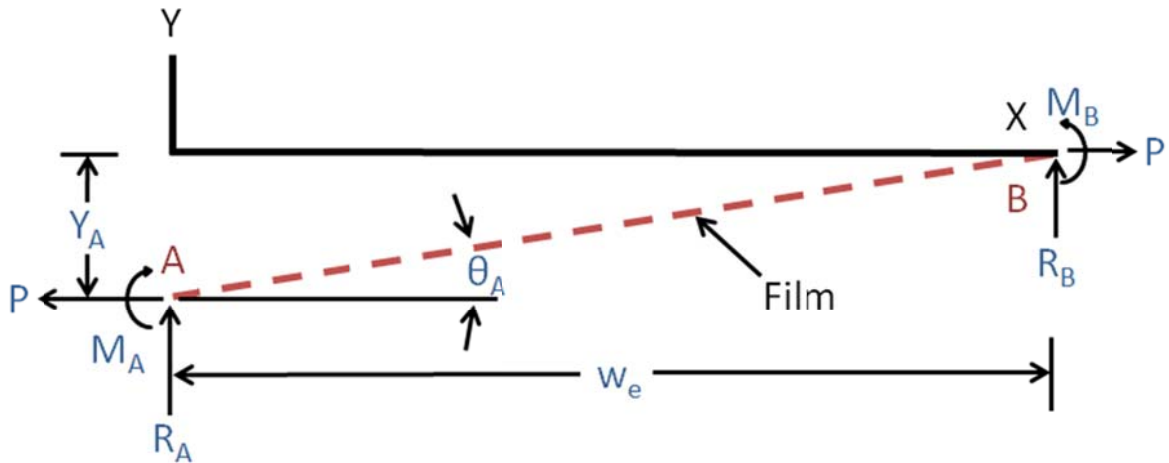


Figure 5-18: The force balance for an angled beam under tension (Young, 2002).

The equation for the Y coordinate of an angled beam under axial tension is (Young, 2002):

$$y(x) = y_A + \frac{\theta_A}{k} F_2 + \frac{M_A}{P} F_3 + \frac{R_A}{P k} F_4 + w_e T_y \quad (5.11)$$

where  $y_A$  is the Y coordinate of point A,  $\theta_A$  is the angle between the film and the x axis,  $k$  is the loading factor,  $M_a$  is the moment at point A,  $P$  is the magnitude of the tensile force placed on the beam,  $R_A$  is the reaction force at point A and  $w_e$  is the length of the electrocaloric film as designated in Figure 2-1.  $F_2$ ,  $F_3$  and  $F_4$  and  $T_y$  are functions of X and are defined in equations (5.18), (5.19) and (5.20). When the beam is horizontal ( $\theta_A = 0$ ), the

$\frac{\theta_A}{k} F_2$  term drops out of the equation and therefore the deflection equation, (5.11), reduces

to:

$$y = \frac{M_A}{P} F_3 + \frac{R_A}{P k} F_4 + w_e T_y \quad (5.12)$$

The loading factor,  $k$ , is defined as:

$$k = \sqrt{\frac{P}{E I}} \quad (5.13)$$

Where  $E$  is the modulus of elasticity and the second moment of area,  $I$ , is:

$$I = \frac{L_e h^3}{12} \quad (5.14)$$

The reaction force at point A,  $R_a$ , is:

$$R_a = \frac{w_a}{K} \frac{C_3 C a_4 - C_2 C a_5}{C_3^2 - C_2 C_4}$$

$$C_2 = \sinh(K w_e)$$

$$C_3 = \cosh(K w_e) - 1$$

$$C_4 = \sinh(K w_e) - K w_e \quad (5.15)$$

$$C a_3 = \cosh(K * (w_e - a)) - 1$$

$$C a_4 = \sinh(K * (w_e - a)) - K(w_e - a)$$

$$C a_5 = C a_3 - \frac{K^2}{2} (w_e - a)^2$$

The variable  $a$  is the  $x$  coordinate of the starting position of the distributed load relative to the origin. Since, in this case, the distributed load spans the entire beam,  $a$  is taken to be 0.

$w_a$  is the distributed load placed on the beam:

$$w_a = \frac{f_g}{w_e} \quad (5.16)$$

In equation (5.16)  $f_g$  is the total weight of the beam. The moment at point  $a$ , can be found

by:

$$M_a = -\frac{w_a}{K} \frac{C_3 C a_4 - C_3 C a_5}{C_3^2 - C_2 C_4}$$

$$C_3 = \cosh(K w_e) - 1$$

$$C_4 = \sinh(K w_e) - K w_e \quad (5.17)$$

$$C a_3 = \cosh(K * (w_e - a)) - 1$$

$$C a_4 = \sinh(K * (w_e - a)) - K(w_e - a)$$

$$C a_5 = C a_3 - \frac{K^2}{2} (w_e - a)^2$$

In equation (5.12)  $F_3$  and  $F_4$  are functions of  $x$ :

$$F_3 = \cosh(K x) - 1 \quad (5.18)$$

$$F_4 = \sinh(K x) - K x \quad (5.19)$$

The cofactor,  $LT_y$ , is defined as

$$LT_y = -\frac{W}{P K^2} F a_5 \quad (5.20)$$

Where  $F a_5$  is a function of  $x$ :

$$F a_5 = F a_3 - \frac{K^2}{2} (x - a)^2 \quad (5.21)$$

$$F a_3 = \cosh(K(x - a)) - 1 \quad (5.22)$$

Using equation (5.12), the deflection at the center of the film was plotted as a function of the applied tensile stress. This plot is shown in Figure 5-19.

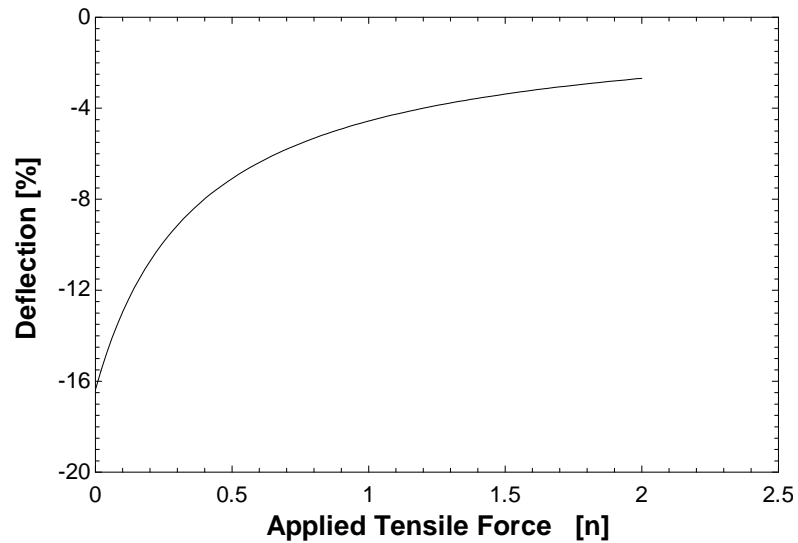


Figure 5-19: The deflection at the center of the regenerator film as a function of the applied tensile force

As it was previously mentioned in section 5.4.1, it is desirable to have the film deflect less than 5% of the fluid channel thickness. Therefore more than 0.86 N of tensile force should be placed in each film such that the deflection is less than 2.8  $\mu\text{m}$ . Since 1 kg weights are readily available, each bed of films will be placed under 9.81 N of tension. Assuming a perfect distribution of tension through the stack of films each film will experience 0.981 N of tension, yielding a predicted deflection of 4.6% or approximately 2.6  $\mu\text{m}$ .

### 5.4.3 Manufacturing the Heat Transfer Prototype

The regenerative heat exchanger has a similar design to the previous prototypes. The device, shown in Figure 5-20, has two holes for alignment pins in all of the layers of the assembly help align the layers relative to one another during construction. A heater is also placed in the center of the device so that the temperature difference across each bed can be correlated to the model predicted temperature difference for various values of heater power.

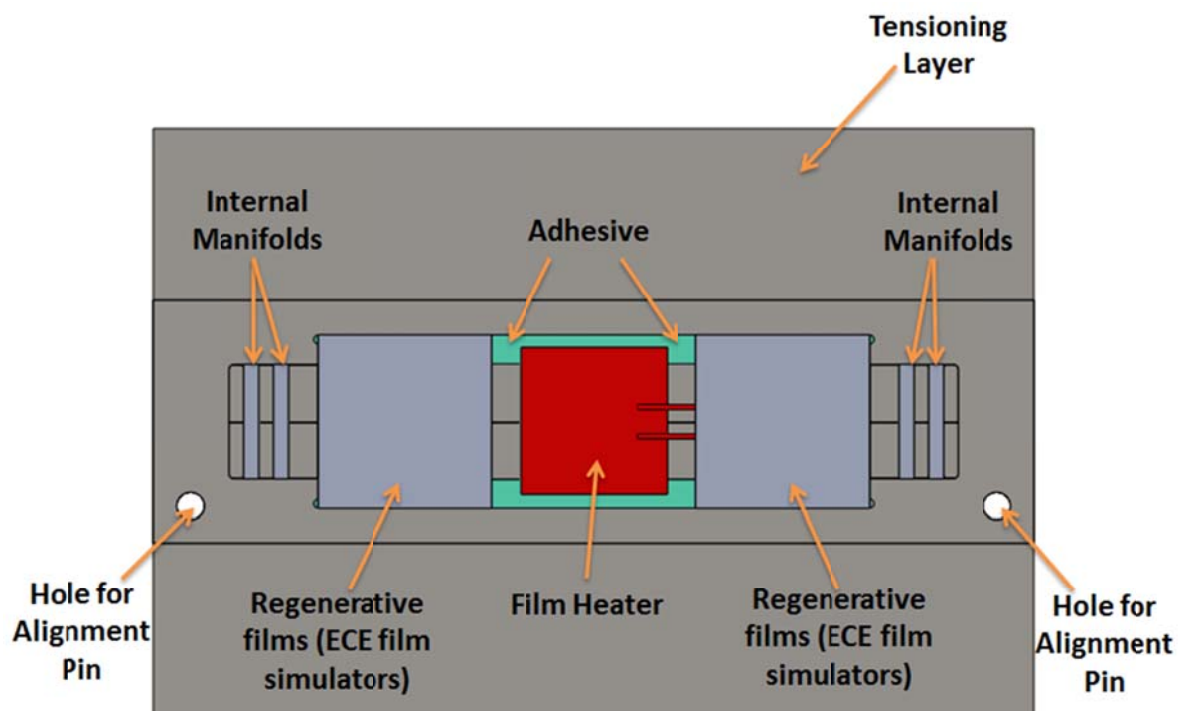


Figure 5-20: The planned layout of the regenerative heat exchanger that simulates the electrocaloric refrigeration cycle

A 2 axis CNC mill was used to machine stencils for the layers made out of transfer tape. A knife was then used to cut the transfer tape into the correct shape. Figure 5-21 shows the stencils and transfer tape cutouts.

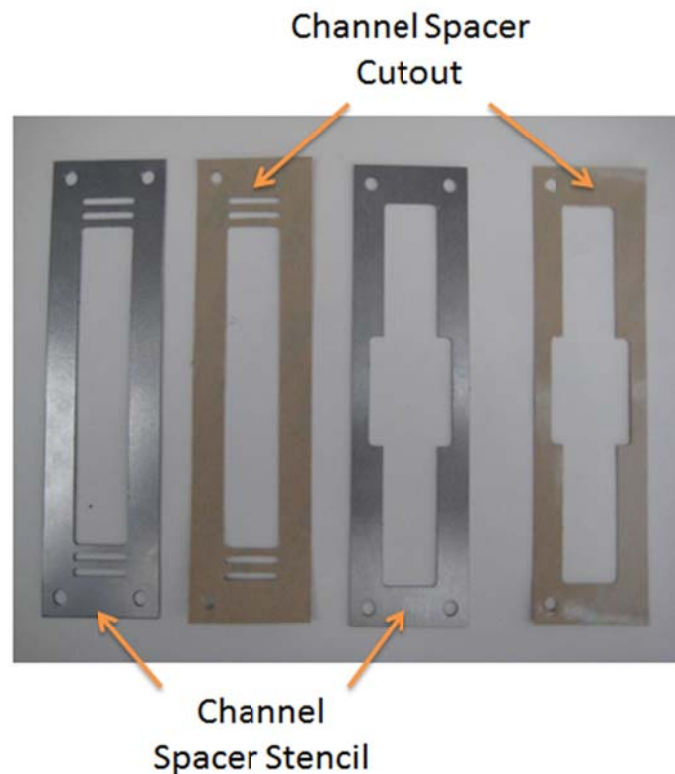


Figure 5-21: Transfer tape stencils beside the corresponding transfer tape cutouts.

The spacer layers were cut with a wire EDM machine by Wireworks Engineering in Madison WI while the PVDF regenerator films were cut using a stencil and then sanded to 3cm by 3cm squares. The stack of regenerator films was created by repeating a layer of transfer tape, a film spacer then the regenerator films. This process was repeated until a stack of 10 layers had been completed. Figure 5-22 shows one layer that was used to create the beds of regenerator films.

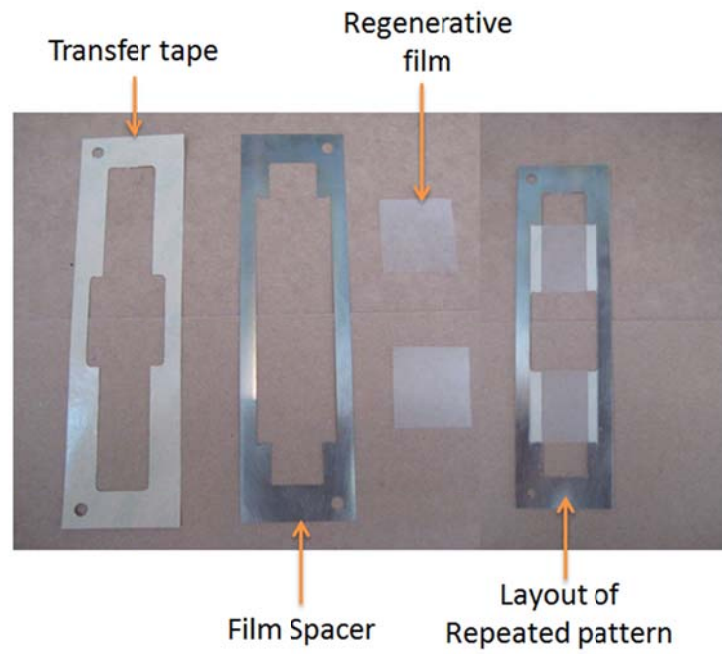
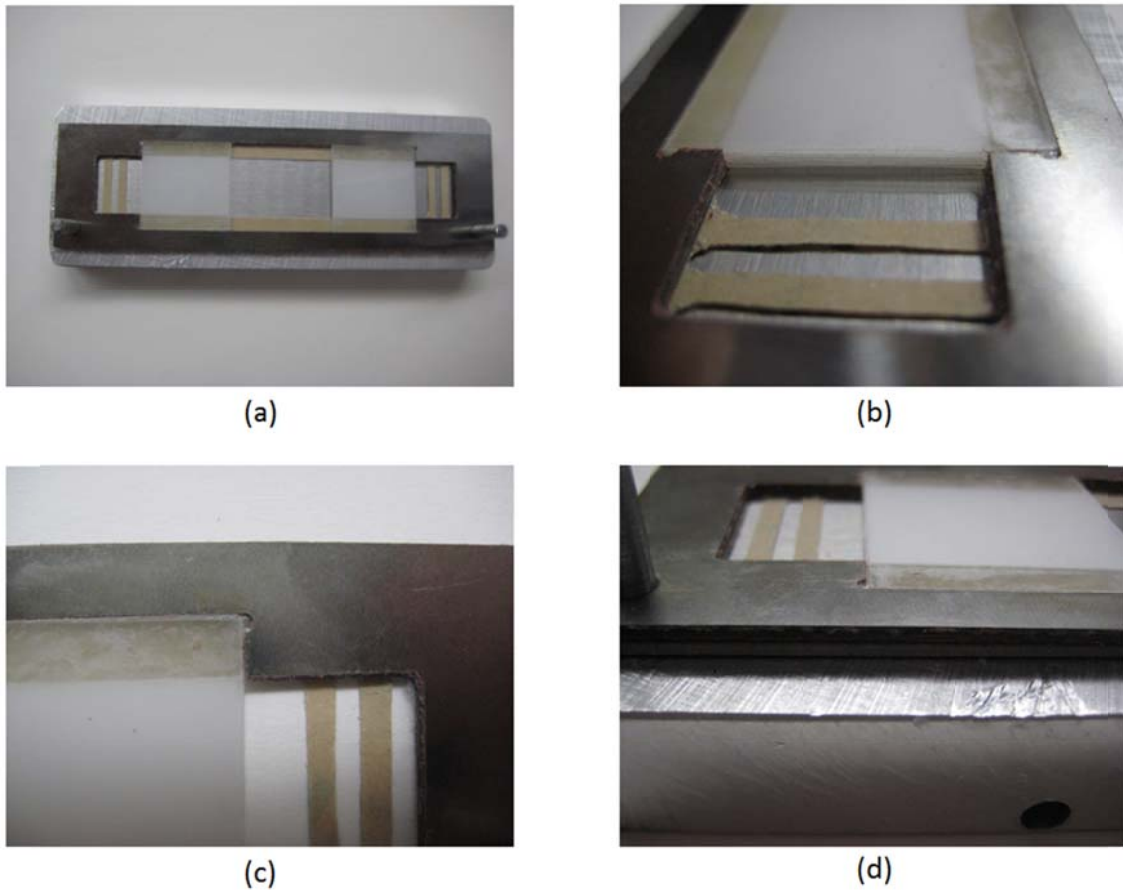


Figure 5-22: The layout of one repeated layer of the regenerative heat exchanger

The completed bed of regenerator films is shown in Figure 5-23.



**Figure 5-23: (a) A top down view of the completed stack of 10 regenerator films, (b) a close up view of the future location of the internal manifolds, (c) the corner of the regenerative films and (d) the edge of the spacing layer**

The overall thickness of the assembly was measured with a micrometer and was found to be  $1.803 \text{ mm} \pm 0.006 \text{ mm}$ . Previous geometric modeling predicted the thickness of this assembly to be  $1.829 \text{ mm}$ . Therefore the fluid channels are roughly  $0.0026 \text{ mm}$  or 4.6% undersized. This gives some indication that the fluid channels through the stack of regenerator films are near the predicted values.

In order to ensure that the thickness of the fluid channels between the regenerative films were uniform and the thickness was equal to the desired value of  $5.59 \times 10^{-5} \text{ m}$ , tension

was placed in each stack of films. This was accomplished by cutting slits in the stainless steel spacers lengthwise down the assembly with a Dremel tool as shown in Figure 5-24.

Two slits were then cut down the center of the tensioning layer such that the middle portion remained uncut. This helped to ensure that the slit in the regenerative film assembly aligned with the slit in the tensioning layer when the regenerative film assembly was placed on the alignment pins. Once the regenerative film assembly was attached to the tensioning layer with transfer tape, the slits in the tensioning layer were extended so that the tensioning layer was cut into two pieces.

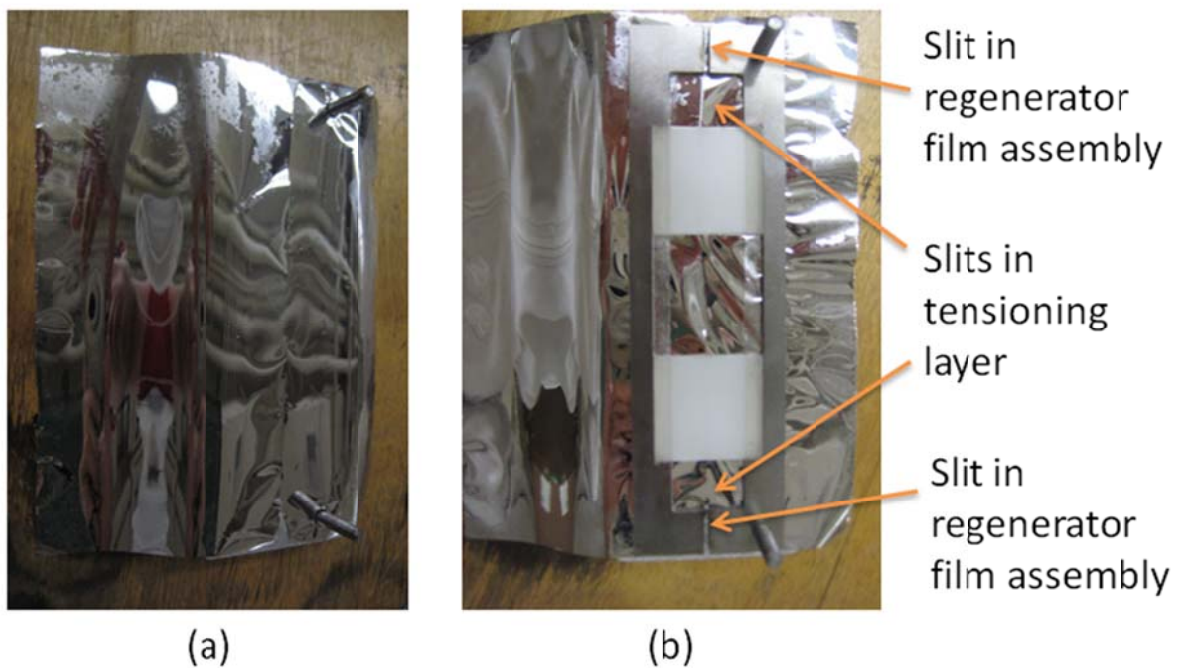


Figure 5-24: (a) The tensioning layer was placed on the tensioning jig and slits (b) were cut in the tensioning layer.

Next, the entire assembly was placed into the tensioning jig shown in Figure 5-25. A 1 kg weight and two 500 g weights were used to add the 9.81 N of tension in each bed as

specified by Section 5.4.2. The tension was added by hanging the weights over a pulley. This then pulled on the tensioning layer and, since the tensioning layer was cut into two pieces, the two halves were held together only by the stacks of regenerator films. This ensured that the correct tensile force was placed in each stack of films. Then, while the films were under tension, the reinforcing plate was raised from underneath using the lifting rods and adhered to the tensioning layer. As a result, the tension in the films was permanent.

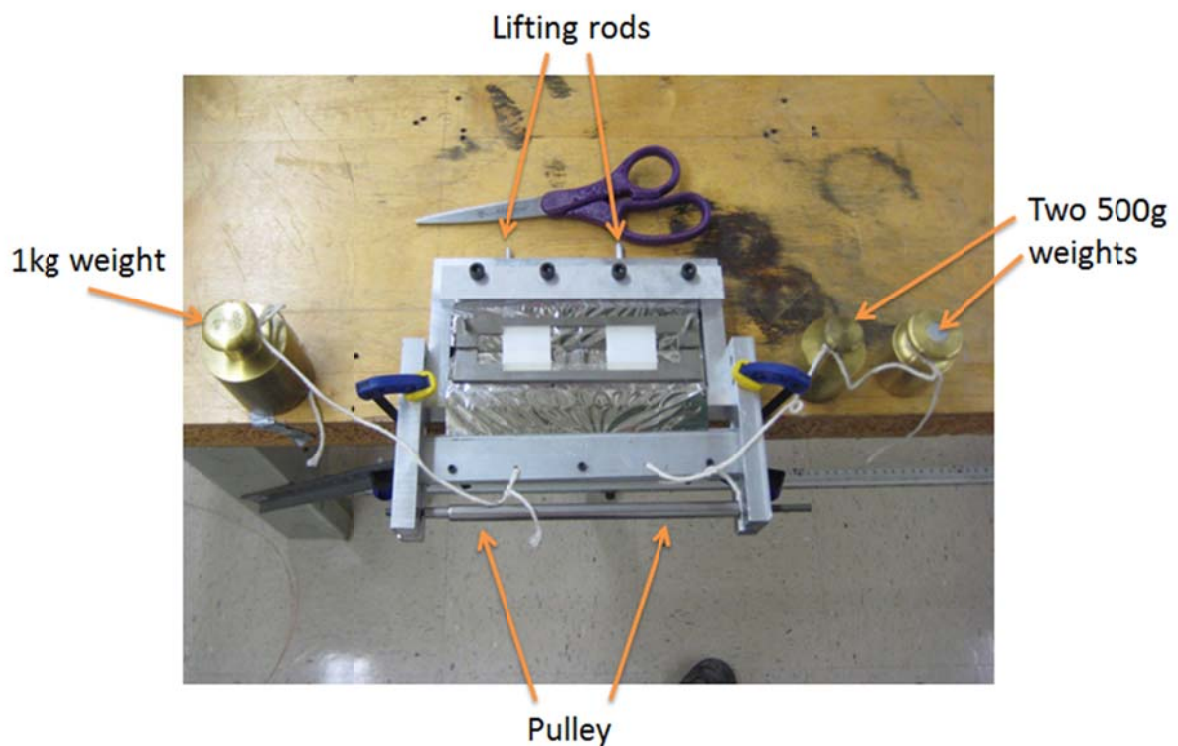
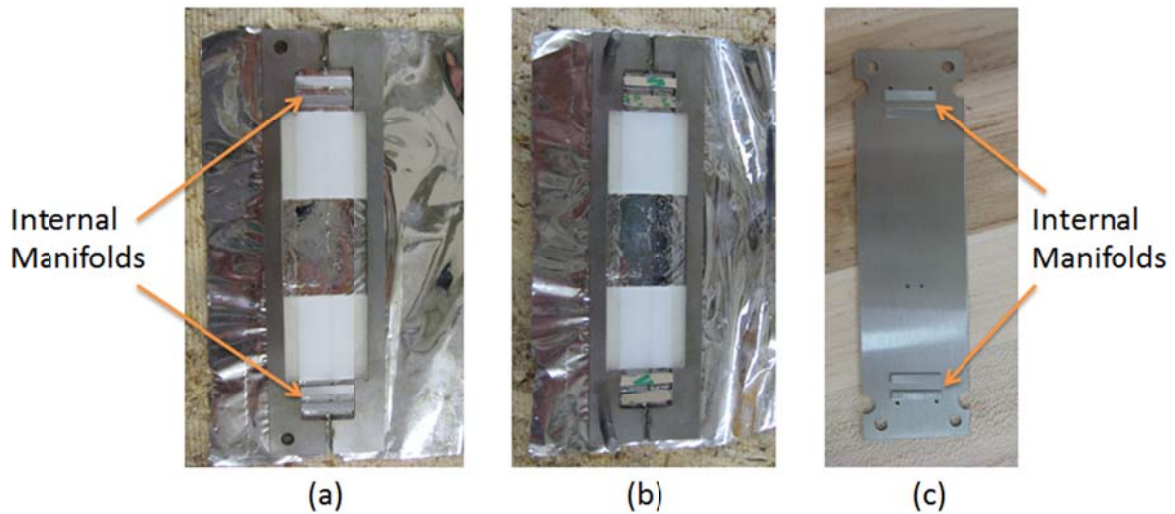


Figure 5-25: Tensioning the stacks of regenerative films using the tensioning jig.

The internal manifolds were then adhered to the tensioning layer using transfer tape. To position the manifolds in the correct location, a spacer was used and then removed once they had been installed. Once the first set of internal manifolds was adhered to the

tensioning layer, a small amount of epoxy was placed at the corners in an attempt to prevent fluid from going around the internal manifolds.

To position the internal manifolds on the port plate side, the second set of internal manifolds were placed on top of the installed manifolds with the transfer tape oriented up and then the port plate was lowered onto the existing assembly using the alignment pins. The port plate could then be lifted off the assembly with the external manifolds attached. No epoxy was added to the edges of the port plate internal manifolds in order to eliminate the possibility that the epoxy obstructed one of the manifolds or prevented the two halves from fitting tightly on top one another.



**Figure 5-26: The internal manifolds (a) adhered to the tensioning layer, (b) the second set of internal manifolds placed directly on top of the first set with their adhesive facing upward and (c) the internal manifolds installed on the port plate.**

While placing the internal manifolds onto the port plate, it was discovered that where the Dremel was used to cut through the stainless steel, the layers had begun to peel off of one another. This only occurred immediately adjacent to the region that was cut. The thickness of the assembly near the regenerator films retained the same difference from the predicted model as the original measurement. Figure 5-27 (b) shows an exaggerated image of this deformation.

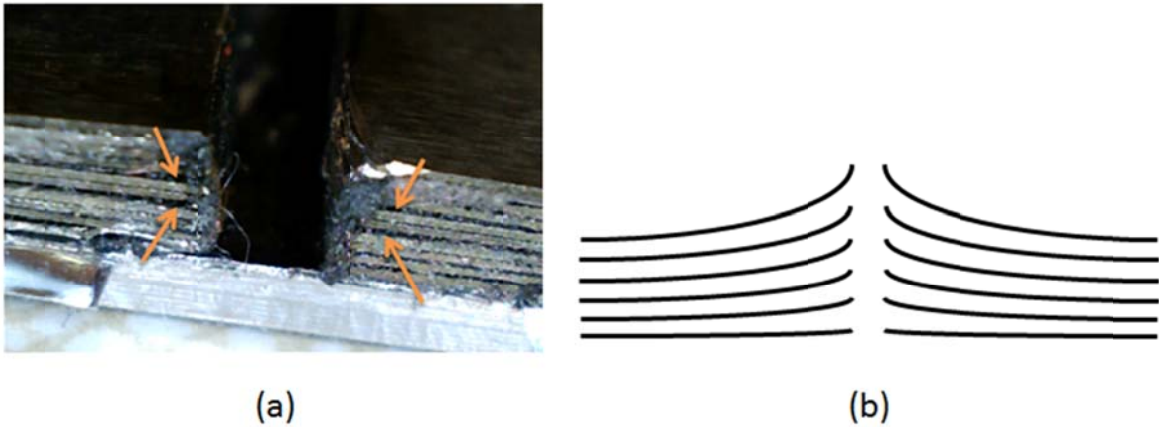


**Figure 5-27: (a) A close up view of the separation that occurred from cutting of the stainless steel spacers with arrows designating the locations of the deformations and (b) an exaggerated illustration of the deformation.**

To ensure that the top reinforcing plate could be installed flush with the regenerator assembly, the stainless steel spacers were sanded, shown in Figure 5-28, using 100 grit sand paper and a marble block. The 5 watt heater was then mounted between the two stacks of regenerator films.

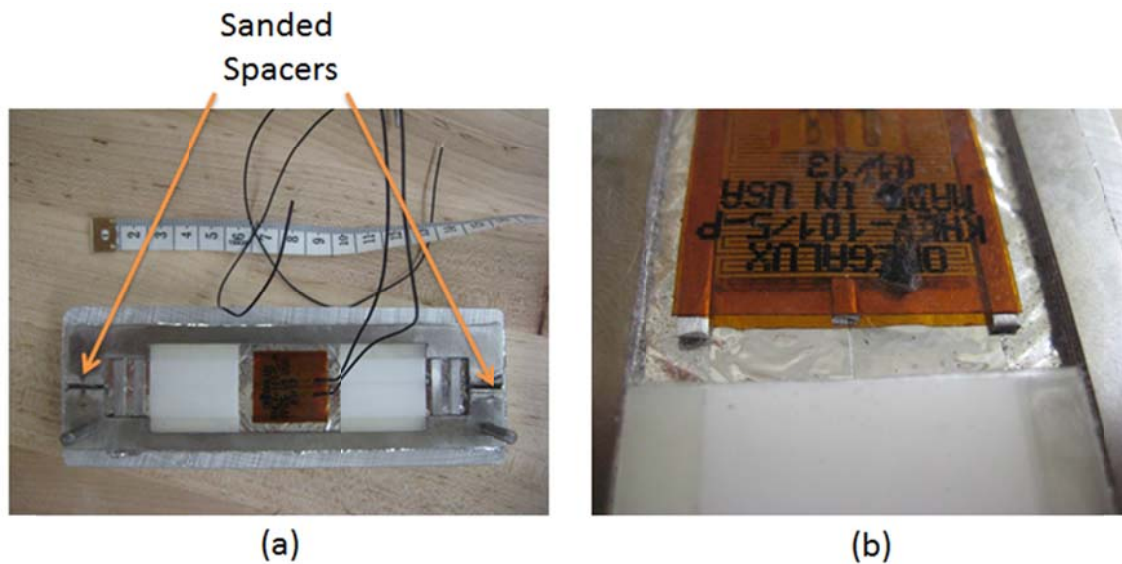


**Figure 5-28: (a) Top view of the heat exchanger after the center heater was installed and (b) the heater mounted in the device.**

As shown in section 5.4.1, a small variation in channel thickness will significantly change the mass flow rate through the fluid channel. Therefore, as an extra precaution, the channel immediately adjacent to the port plate was closed using a small amount of epoxy when the port plate was placed over the assembly. This reduced the number of fluid channels on both regenerator film stacks from 11 to 10. Epoxy was then used to seal around the heater wires. Figure 5-29 below shows the regenerator after the port plate was installed. Two cutouts on each side of the port plate aided in aligning the external manifolds during their insulation.

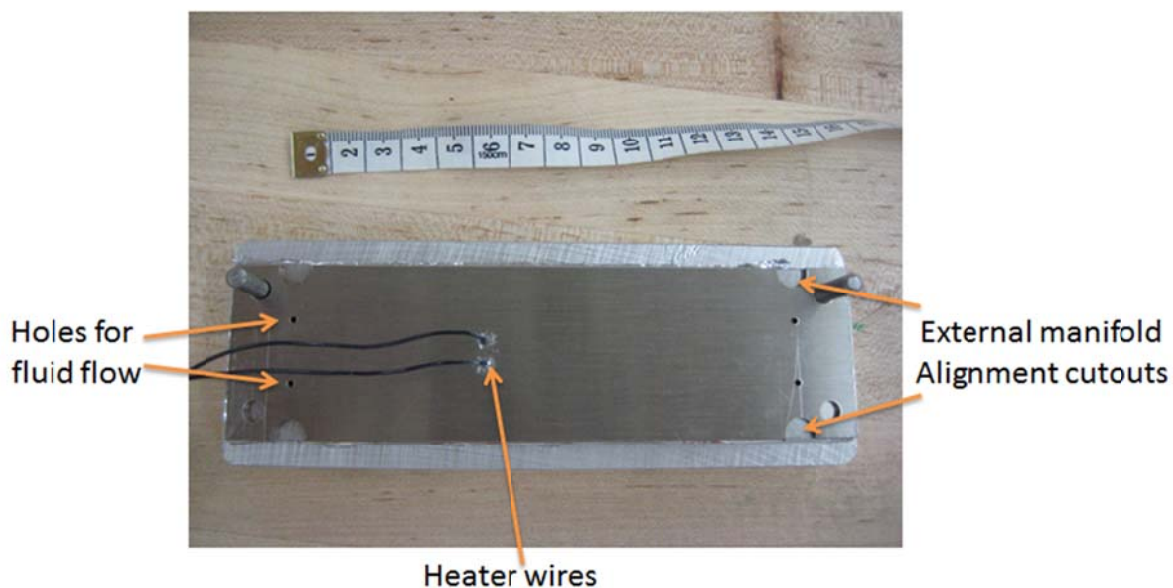


Figure 5-29: A view of the port plate after it was adhered to the regenerative heat exchanger

The external manifold, shown in Figure 5-30, splits the flow into two using symmetry and is made from copper to aid in the removal of heat from the device.

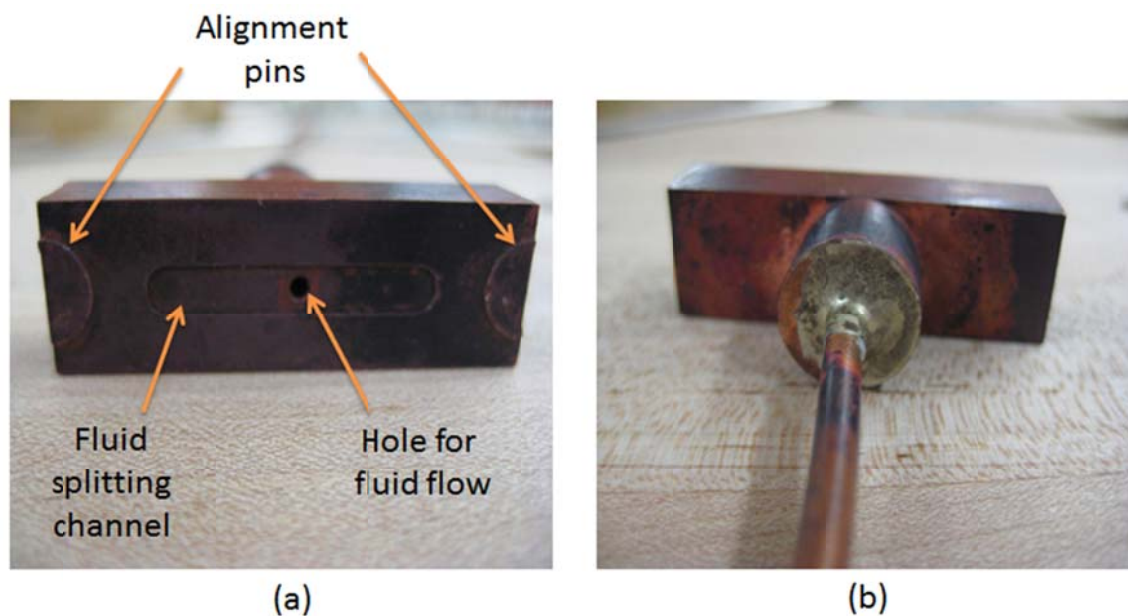
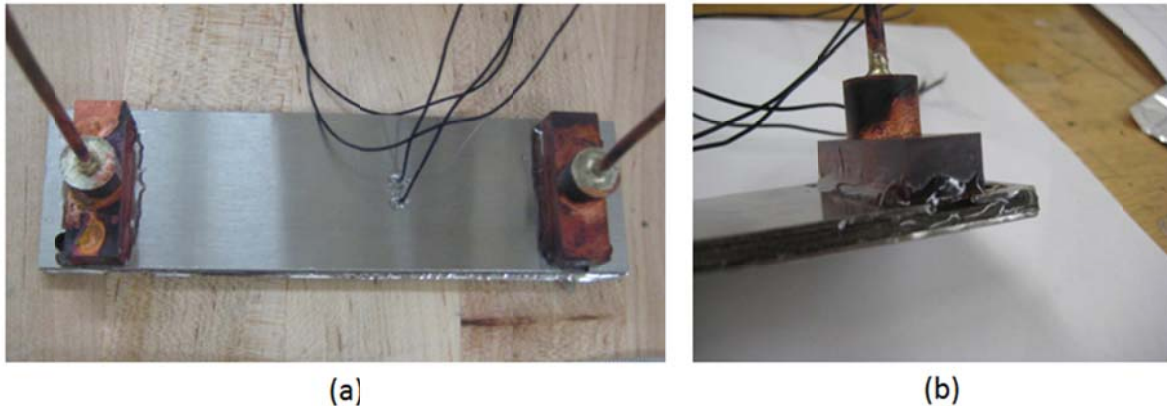


Figure 5-30: (a) The bottom of the external manifold. (b) The top of the external manifold.

Finally, in Figure 5-31, the tensioning layer was trimmed and the edges were sealed with epoxy.



**Figure 5-31: (a) The regenerative heat exchanger with the two external manifolds installed and (b) the edge of the heat exchanger after it was sealed with epoxy.**

### *5.5 Sealing the Heat Transfer Device*

Sealing the edges of the bed with the 5 minute Devcon epoxy was difficult. First, since the epoxy has a 5 minute working there was not enough time to properly degas the epoxy before applying it. The short curing time allowed several layers to be applied in rapid succession but the epoxy's high viscosity did not allow it flow into the gaps well. Finally, while the bed eventually sealed, the epoxy would often spontaneously leak.

Figure 5-32 shows the transient pressure within the heat transfer device when the system was pressurized and the inlet and outlet were both sealed. The sharp decline in pressure demonstrates how the epoxy would start spontaneously leaking.

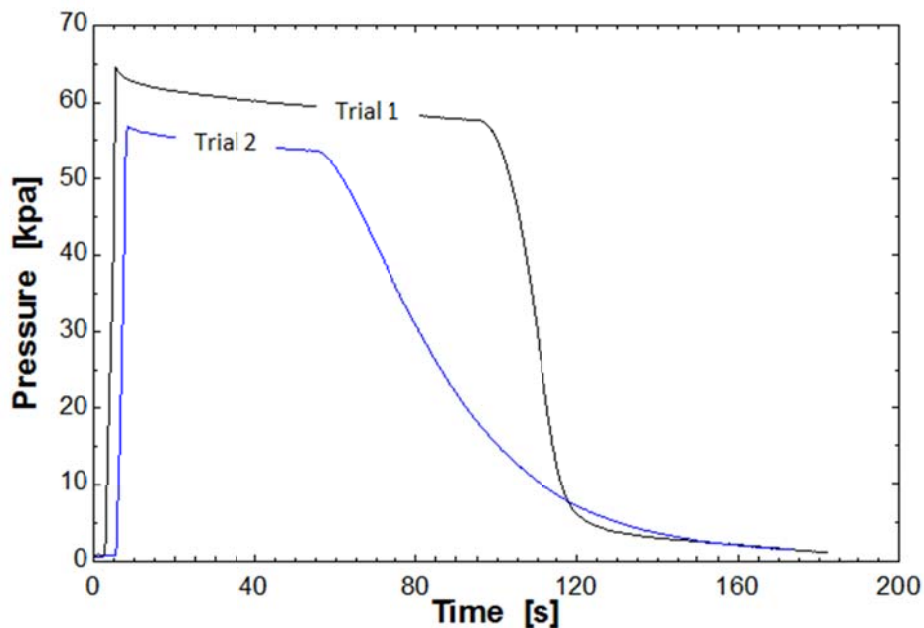
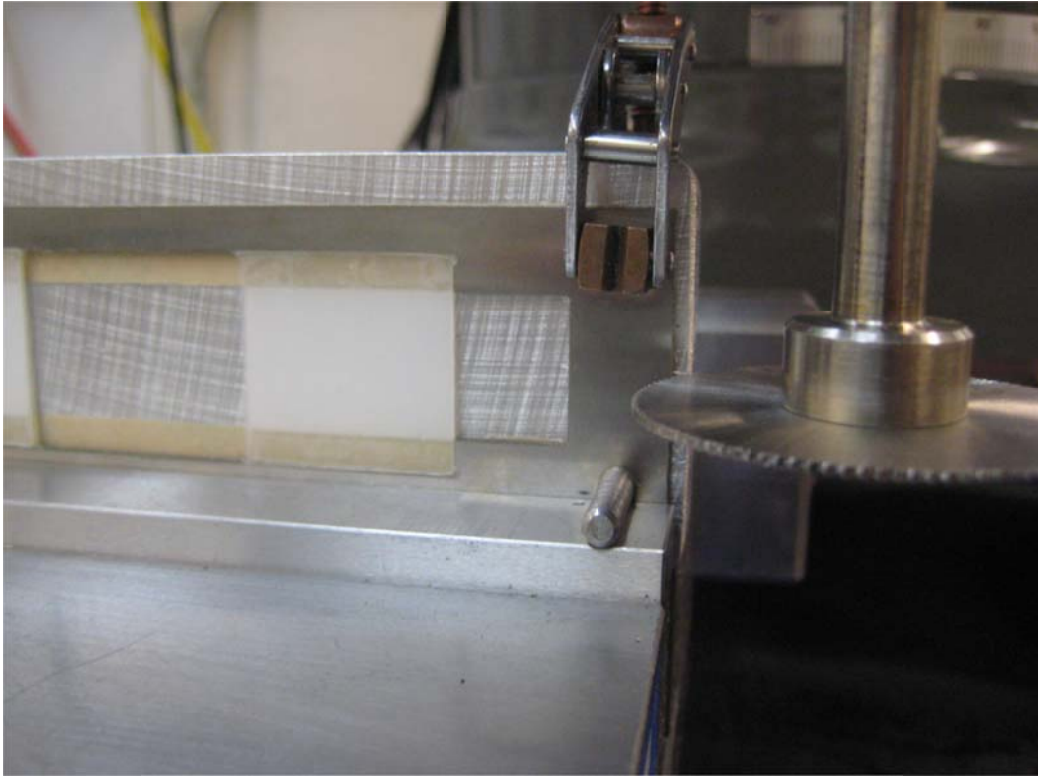


Figure 5-32: The transient pressure of the bed when the epoxy gave way.

Eventually, a slight vacuum was pulled on the inside of the device and a small amount of super glue was added to the external surface. The super glue seeped into the gaps well but also sealed the channel completely near one of the external manifolds. This rendered the device unusable and therefore a second device needed to be built. This second heat transfer device will be sealed exclusively with degassed Stycast 1266 epoxy.

### 5.6 Building the Second Heat Transfer Device

A second heat transfer device was built that was similar to the first except for a few manufacturing and material differences. First, a slitting saw was used because it was predicted that it would minimize the delamination that occurred in Figure 5-27. The slitting saw is shown in Figure 5-33.



**Figure 5-33: Regenerator assembly being cut with a slitting saw on a mill.**

The slitting saw applied pressure normal to the surface being cut and therefore compressed the layers together during the cutting process. As a result, delamination of the film spacers was minimized; however, some did still occur. The resulting delamination was most likely due to a small burr that formed on each of the 10 film spacers.

If another heat transfer prototype is required, the film spacers should be cut with a wire EDM prior to installation. In addition, a second pair of alignment pins should be used to ensure proper placement of the two halves of each film spacer. These alignment pins could be removed before the films are tensioned.

Next, Instead of using a 0.013mm plastic sheet for the tensioning layer a 0.025mm brass sheet was used. This was because the plastic sheet was difficult to cut and put into the correct position.

Degassed Stycast 1266 was used almost exclusively to seal the device with the exception of filling the large gaps near the slit in the regenerator assembly and around the heater wires. Stycast 1266 was much better at sealing the bed than the five minute epoxy. However, due low viscosity of Stycast 1266 it seeped beneath the two external manifolds and completely blocked the fluid passage. Fortunately, the external manifolds were able to be removed without damaging the rest of the device. Figure 5-34 shows the bottom of one of the external manifolds after the fluid channel had been filled with epoxy.



**Figure 5-34: The bottom of one of the external manifolds after the fluid channel had been plugged with Stycast 1266.**

Once the two external manifolds were removed, they were cleaned to remove the remaining epoxy and to clear the fluid channels. After cleaning, the external manifolds were

clamped into position to ensure that the epoxy could not flow under them and close the fluid channel. The clamped external manifolds are shown in Figure 5-35.

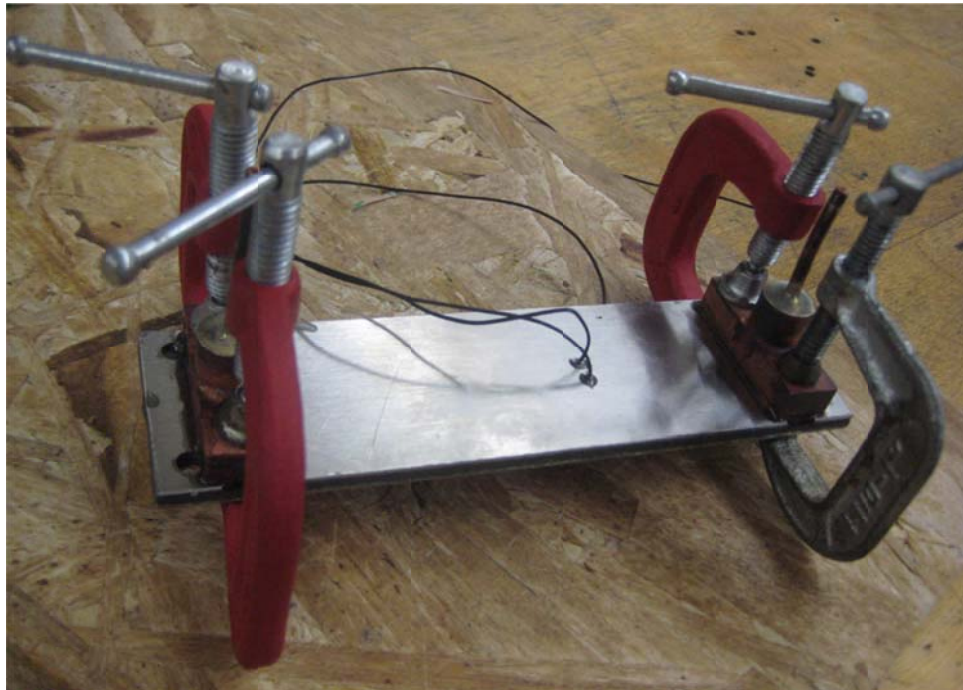


**Figure 5-35: Clamping the external manifolds while the epoxy is applied to ensure that the fluid channel stay open.**

A second layer of 1266 epoxy was applied and the entire assembly was installed into the vacuum assembly.

### *5.7 Manifold Test*

The manifolds of the device were isolated in a separate device so that ways of charging the system could be examined. As it was previously discussed, the pressure drop through the internal manifolds is very dependent on the internal manifold channel thickness. Also, in the design for the internal manifold test, the thickness of the internal manifolds is set by the transfer tape thickness. Therefore, if the pressure drop across the internal manifolds agrees reasonably with the modeled values, the thickness of the transfer tape can be verified. As a

result, this helps to confirm that the fluid channels in the regenerator device are near their expected values. Figure 5-36 shows an exploded view of the manifold test device.

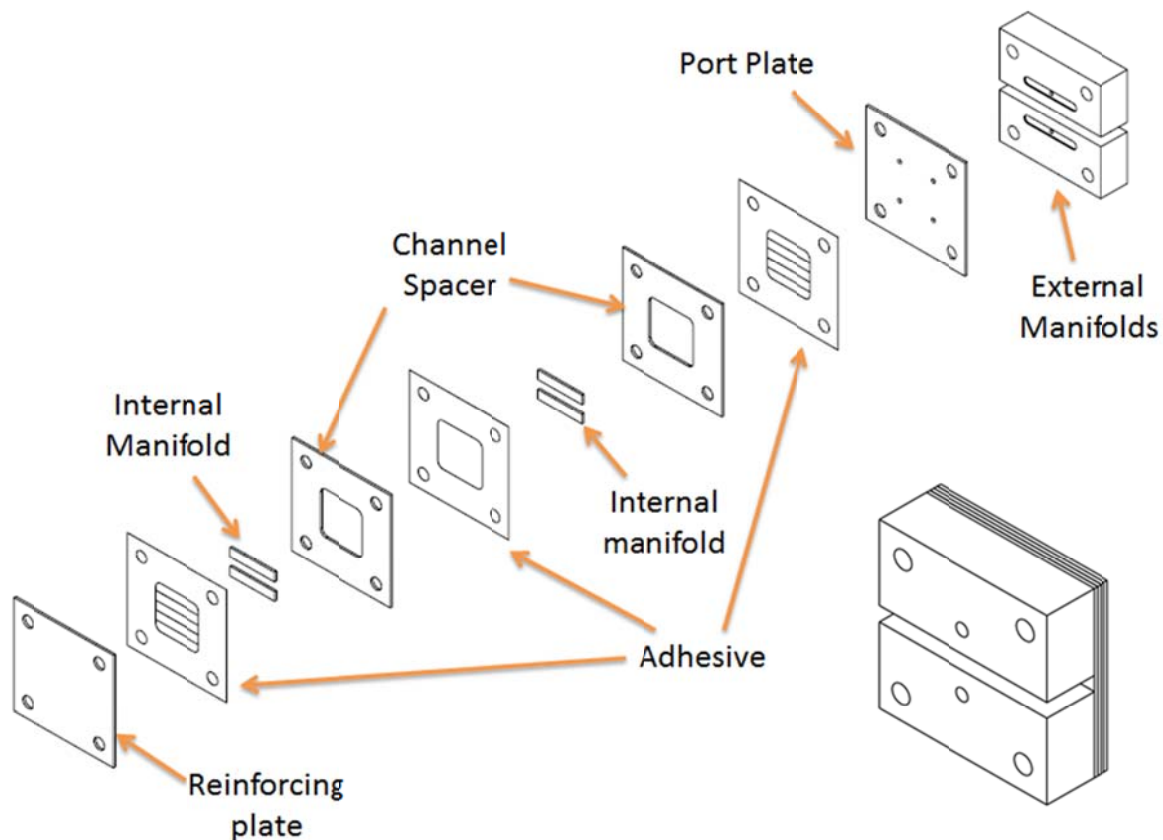
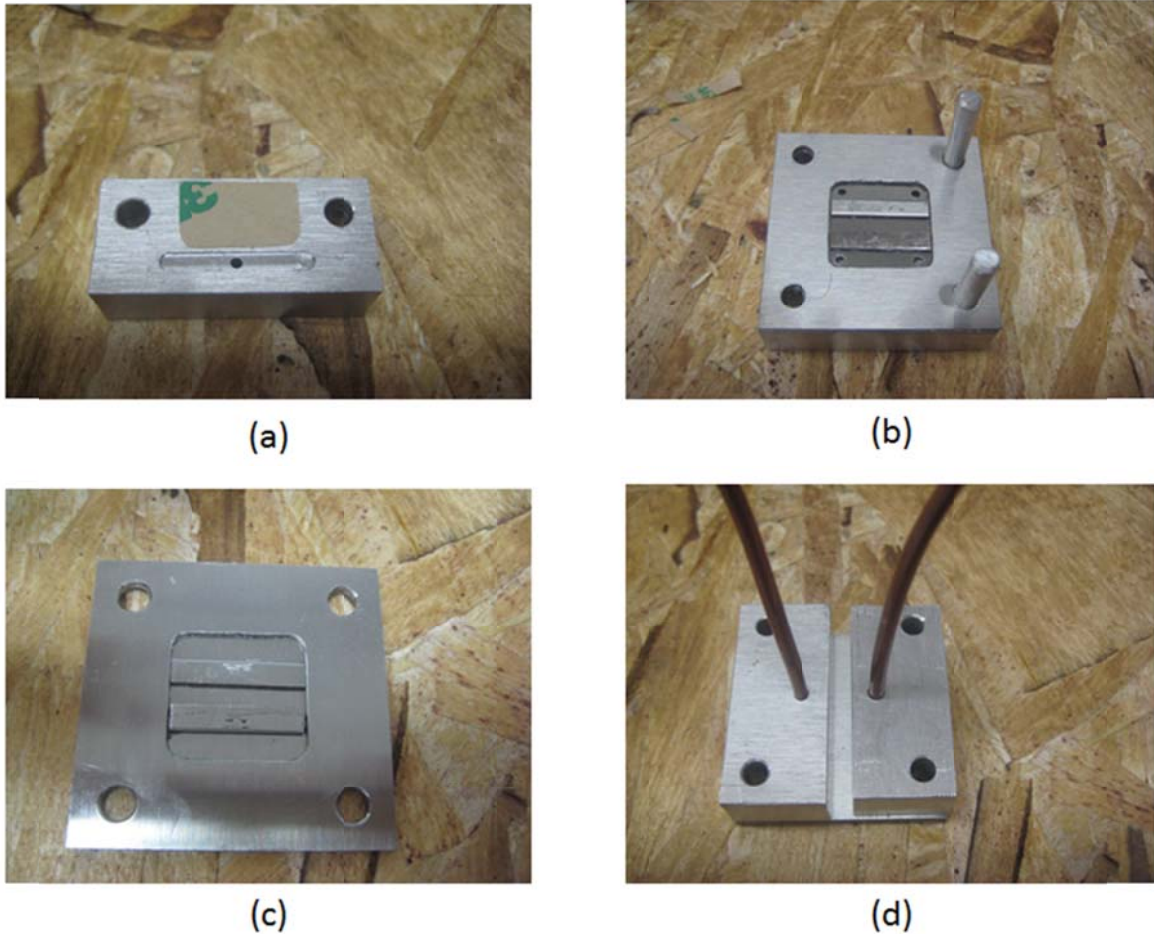


Figure 5-36: Exploded view of the manifold test device.

The dimensions of the internal manifolds in this test are identical to the dimensions of the manifolds in the heat transfer device. Figure 5-37 shows the assembly processes of the experimental manifold device.



**Figure 5-37: (a) One external manifold with adhesive to temporarily hold it in place, (b) the port plate side of the device with internal and external manifolds attached, (c) the reinforcing plate with internal manifolds attached and (d) the assembled manifold test device before sealing with epoxy.**

Initially, the external manifold in (a) of Figure 5-37 was attached to the port plate. Then, one of the channel spacers and two halves of the internal manifolds were adhered to the port plate in order to produce the assembly shown in (b). Separately, in (c), a second channel spacer and the second two halves of the internal manifolds were adhered to the reinforcing plate and the two assemblies in (b) and (c) were adhered together to produce the assembly in (d). Next, the edges of the device and were sealed with epoxy and the tubing installed.

Due to the low viscosity of the Stycast 1266 epoxy, it seeped too far into the gap between the copper tubing and the two external manifolds and completely sealed the fluid channel. This is not an issue at the locations where the transfer tape acts as a buffer between the epoxy and the fluid channel.

A second set of manifolds will be built where Devcon 5 minute epoxy will be used to seal the gaps around the tubing and Stycast 1266 will be used to seal the rest of the device. In addition each set of internal manifolds will be machined out of the channel spacers instead of being completely separate parts. Finally, the corners were rounded to make the corners easier to seal with epoxy. Figure 1-1 below shows an assembly view of the second iteration manifold test.

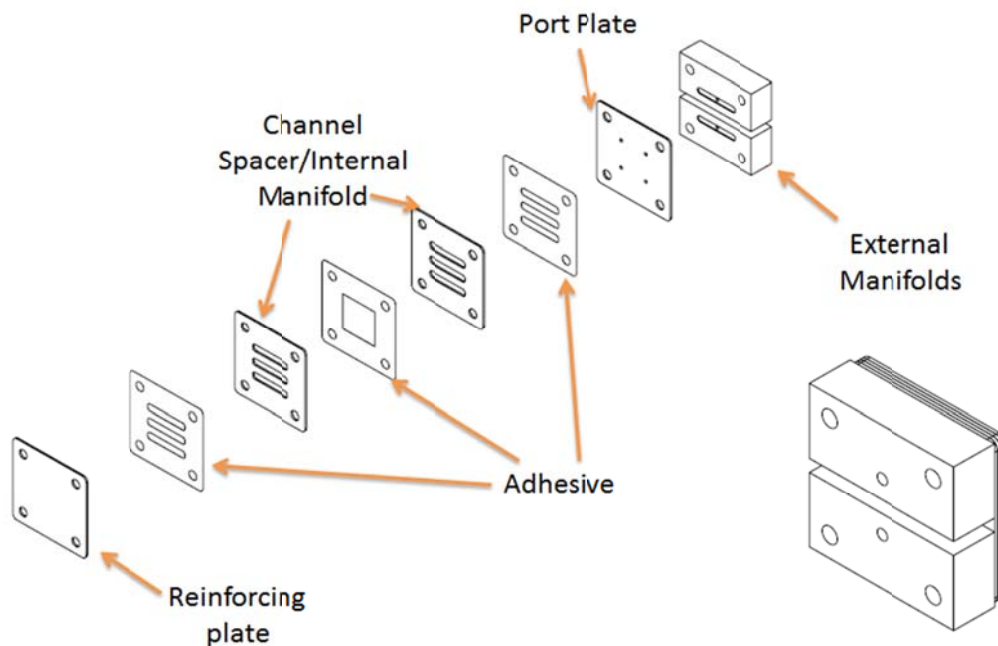
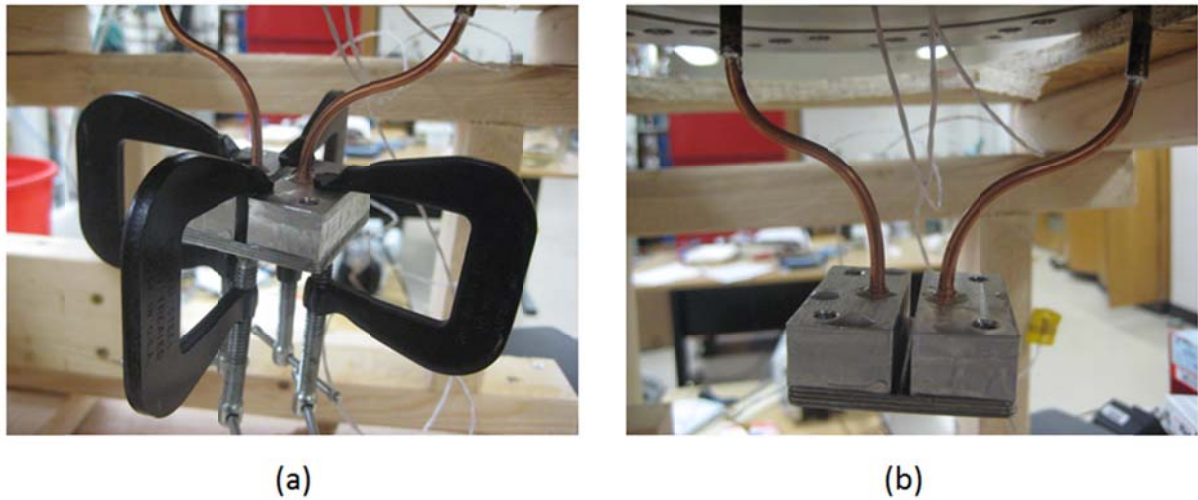


Figure 5-38: The second iteration of the manifold test

This second internal manifold test device was built and installed into the system. Initially, in Figure 5-39, to ensure that the epoxy remained under compression, C clamps were placed around the perimeter of the device.



**Figure 5-39: The internal manifold test installed in the system (a) with C clamps installed and (b) without C clamps.**

The pressure drop through the device was measured with the C clamps in place and again when the clamps removed for various volumetric flow rates. The pressure drop data was then compared to model predicted values. This plot can be found in Figure 5-40.

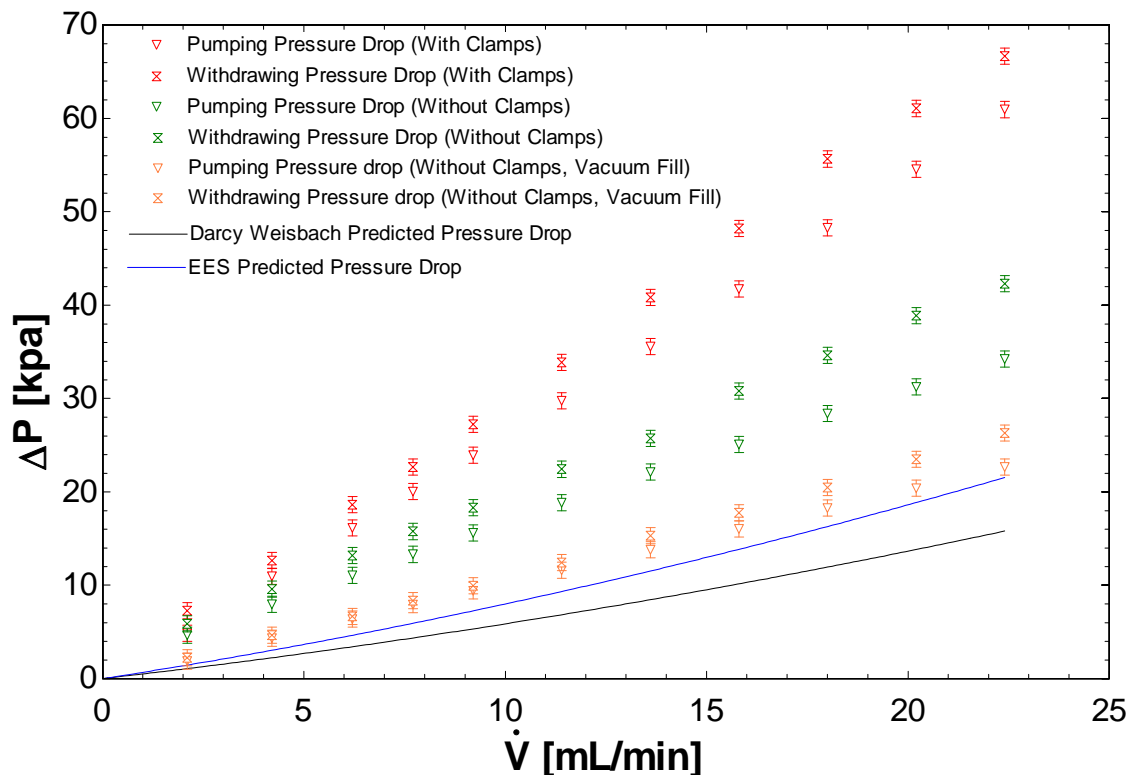


Figure 5-40: The pressure drop through the manifold test device for various volumetric flow rates and the model predicted pressure drop assuming an internal manifold channel thickness of 56 $\mu$ m.

In Figure 5-40, the pressure drop is greater when the clamps are in place. This is likely due to the clamps compressing the space between the internal manifolds. Once the clamps were removed the pressure drop decreased. As noted in section 5.4.1, a small variation in the channel thickness can have a significant effect on the pressure drop.

Also, the pressure drop while the syringe is being compressed (pumping mode) is less than the pressure drop when the syringe is being withdrawn. This is likely due pressures induced by the pump deforming the walls of the device. This effect is illustrated in Figure 5-41 below.

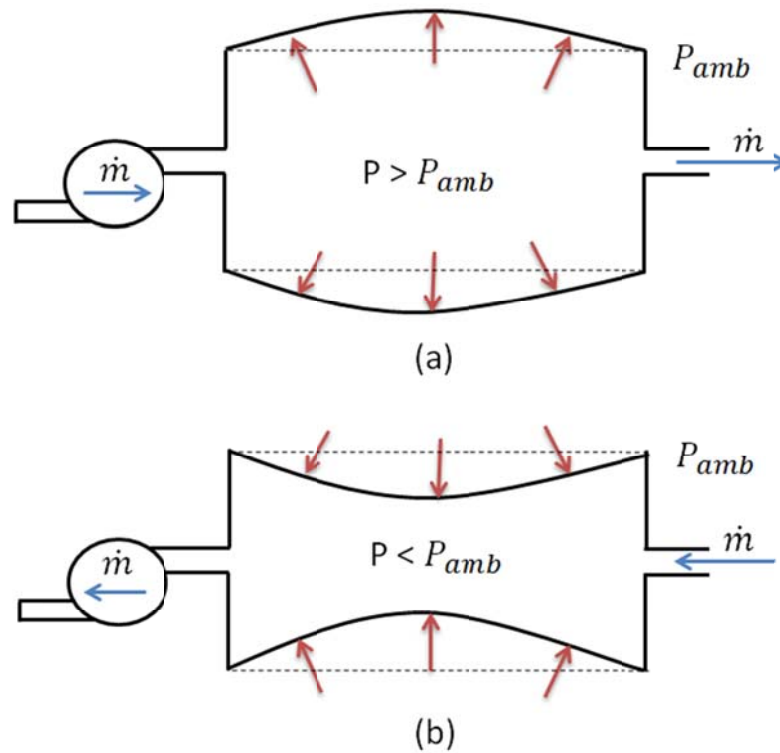


Figure 5-41: A qualitative view of the deformation and forces within the manifold test device when in pumping mode (a) and qualitative view of the deformation and forces within the manifold test device when in withdrawing mode (b). Red arrows denote forces.

When in pumping mode, the pressure on the inside of the device is greater than the ambient pressure and therefore the device will slightly deform outward. This deformation increases the channel size and therefore the pressure drop will decrease. When the pump is in withdrawing mode, the pressure on the outside of the device is larger than the inside, and therefore, the device will slightly deform inwards. The inward deformation decreases the channel thickness and the pressure increases as a result.

At higher volumetric flow rates, there is a larger difference in pressure drop between the pumping mode and the withdrawing mode. At larger volumetric flow rates the pressure

difference between the inside and outside of the device is greater and therefore causes larger deformations.

However, even after taking into account for the deformations due to the pressure differences and the clamps the pressure drop still significantly differs from the model predicted values. In addition to the possibility of the channel being smaller than expected, the increase pressure drop could be a result of some air being trapped in the channel. Air in the channel would restrict the channel size and thereby increasing the pressure drop. To explore this possibility the fluid channel was evacuated and then water was introduced into the evacuated line to minimize the amount of air trapped within the system.

Once the air had been removed, the pressure drop through the fluid channel decreased significantly and the experimental data reasonably agrees with the calculated predictions. Figure 5-40 presents the experimental data for the case when the manifold test device was evacuated and then filled. The difference in the pressure drop could be due to flow being trapped into the corners of the fluid channel.

This test helped to finalize some of the manufacturing techniques and the experimental procedure that will be used for the final heat transfer prototype. First, the Stycast 1266 epoxy was much better at sealing the edges of the bed than the Devcon 5 minute epoxy and it would not spontaneously leak. Next, the clamps were useful when sealing the edges of the device but should not be in place during testing. In addition, the fluid channel should be evacuated and then filled with water to reduce the air trapped in the system. Finally, it is

likely that the transfer tape creates channels near the expected thickness of 0.0588mm because the pressure drop was near the modeled values.

### 5.8 *Vacuum Chamber*

The regenerative heat exchanger will be placed in a vacuum to provide insulation. The insulating vacuum chamber that was constructed is shown in Figure 5-42. The system requires a pump to energize the required oscillating flow within the heat exchanger; therefore, two fluid feedthroughs were constructed to allow an external pump to provide fluid to the bed while maintaining a vacuum seal. Finally, an electrical vacuum feed through was created to allow operation of the film heater and to provide electrical connections for temperature sensors through the vacuum wall.

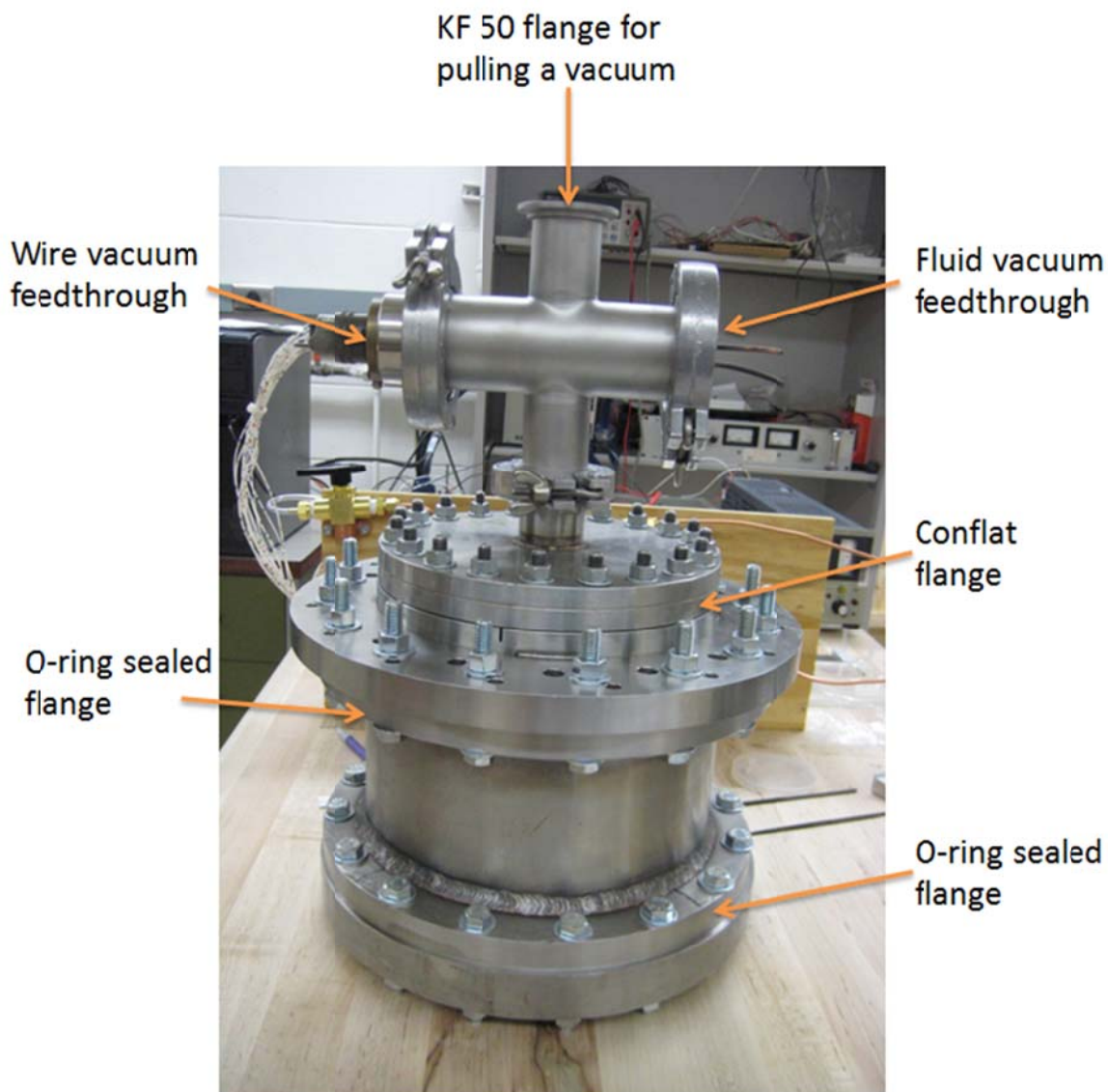


Figure 5-42: The insulating vacuum chamber with electrical and fluid feedthroughs

The fluid feedthrough was simply made by brazing pieces of copper tubing through a stainless steel KF 50 flange. The wire feedthrough was created by mounting a dedicated wire feedthrough on a KF 50 nipple flange. These feedthroughs are shown in Figure 5-43.

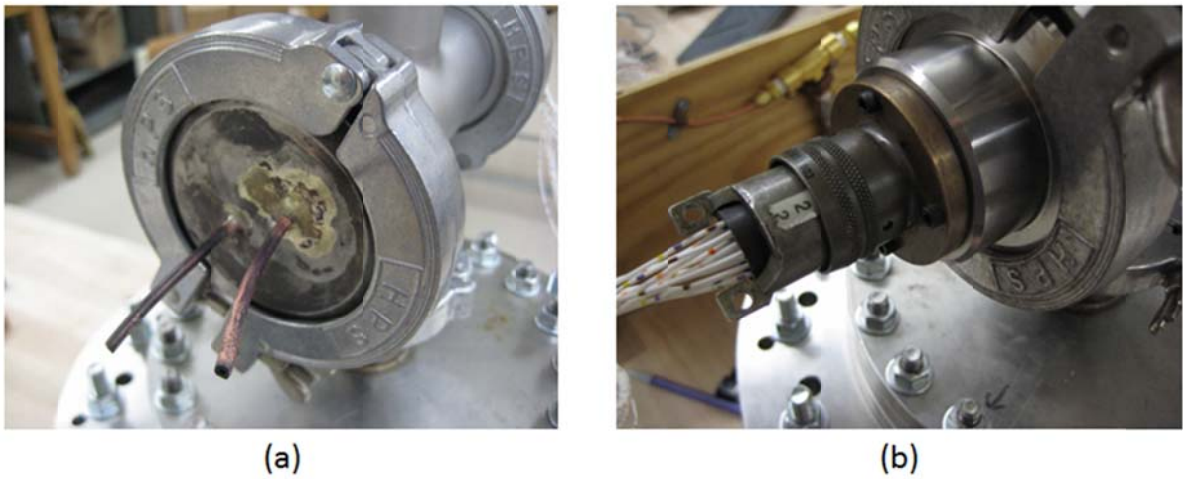


Figure 5-43: (a) The fluid feedthrough into the vacuum chamber and (b) the wire feedthrough

The regenerator, shown in Figure 5-44, was then mounted in the vacuum chamber and the thermistors attached to the surface.

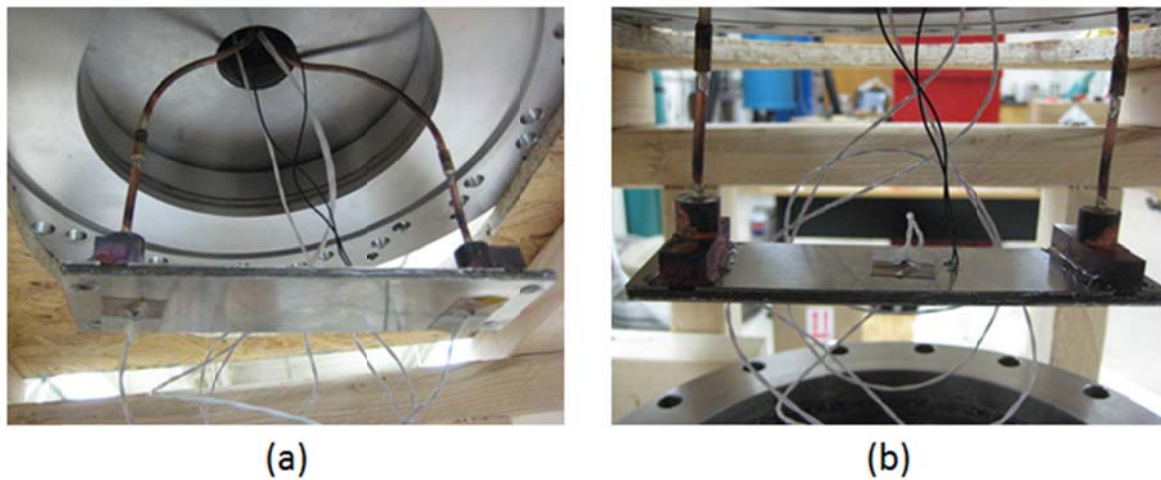


Figure 5-44: (a) bottom view of the regenerator mounted in the vacuum and (b) a top view of the mounted regenerator.

### 5.9 Measurement System

Three thermistors are used to determine the temperature at various locations along the regenerator bed.

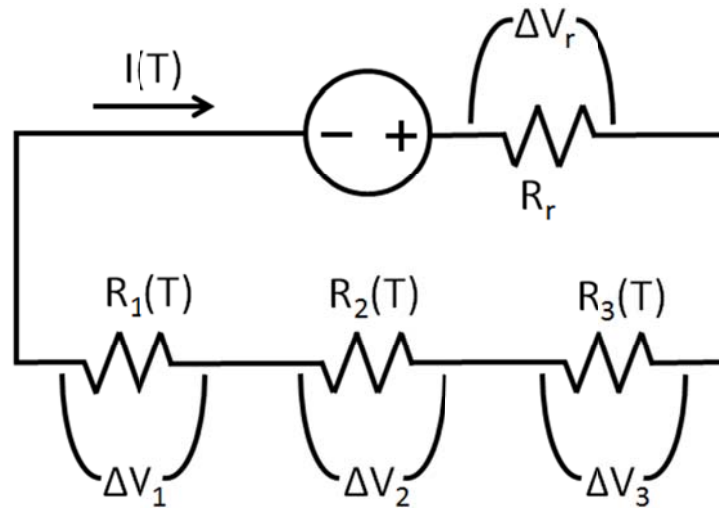


Figure 5-45: The series temperature measurement circuit.

A constant voltage is applied through a series circuit that includes a reference resistor,  $R_r$ , of a known resistance and three thermistors denoted on the circuit diagram as resistors,  $R_1$ ,  $R_2$  and  $R_3$ . Labview reads the voltage drop across each of the four resistances. The current through the series circuit is determined by using Ohms law over the reference resistor:

$$I(T) = \frac{\Delta V_r}{R_r} \quad (5.23)$$

Since the resistance of each of the thermistors is a function of temperature, the current through the circuit is also a function of temperature. This method of determining the current allows Labview to determine the current through the circuit at all times. The voltage drop across each of the thermistors is also read by Labview to determine the resistance through Ohms law:

$$R_{e,i}(T) = \frac{\Delta V_i}{I(T)} \quad (5.24)$$

Finally, the resistance of each of the thermistors is used to linearly interpolate between data points of the thermistor resistance-temperature correlation data that are provided by the thermistor's manufacturer.

Wiring all three thermistors and the reference resistor in series resulted in the voltage drop across each of the thermistors to be dependent on the voltage drop of the other thermistors. For example, if one of the three thermistors was heated the system would display a slight increase in temperature on the remaining two thermistors. It was expected that the current would change to prevent this dependence. To resolve this issue, the thermistors were wired in parallel and two additional reference resistors were added to produce the circuit shown in Figure 5-46 below.

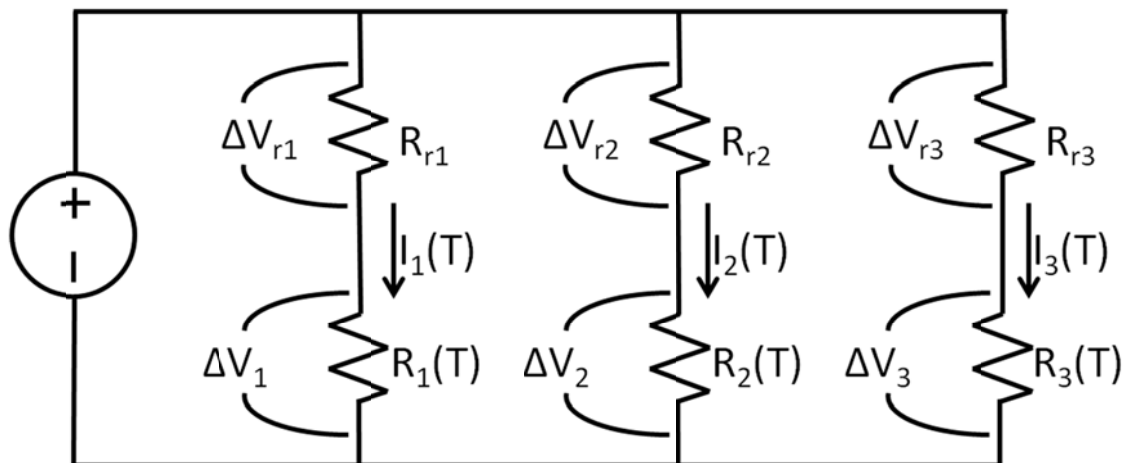


Figure 5-46: The parallel temperature measurement circuit.

Like before, the voltage drop across the reference resistor is used to determine the current flowing through each leg of the circuit. The current along with the voltage drop across each thermistor is then used to determine the resistance of each thermistor. This resistance is

compared to the manufacturer provided resistance-temperature relationship to determine the temperature at each thermistor. The new circuit design, shown in Figure 5-46, resolved the dependence issues of the resistors.

A similar measurement method is used to determine the power delivered to the heater. The voltage drop is measured across a known resistance and the current is determined through ohms law. Next, the total thermal generation of the film heater is calculated from the current and resistance of the heater.

#### 5.9.1 Uncertainty Analysis

The data acquisition (DAQ) card used for this experiment was a National Instruments 6220 DAQ card with 16 bit voltage input. The DAQ card reads voltages from -10 to 10 volts. The manufacturer provided uncertainties are presented in Table 5-2 below

**Table 5-2: Manufacturer provided voltage uncertainties for the data acquisition card used**

<b>Positive Scale (V)</b>	<b>Negative Scale (V)</b>	<b>Absolute Accuracy (<math>\mu</math>V)</b>
10	-10	3100
5	-5	1620
1	-1	360
0.2	-0.2	112

A digital multimeter was used to determine the resistance of the reference resistors in both the temperature measurement circuit and heater circuits. It was also used to measure the resistance of the film heater. The digital multimeter that was used was a Hewlett Packard 34410A multimeter. The manufacturer published uncertainty is presented in Table 5-3: below.

Table 5-3: Multimeter resistance uncertainty

Range	Uncertainty
100Ω	0.01%+.004 Ω
1000Ω	0.01%+.01 Ω

The temperature measurements were conducted using omega SA1-TH-44007-40-T thermistors with a published accuracy of  $\pm 0.2$  C. EES was used to propagate the uncertainty for the power and resistance measurements. The results of the uncertainty propagation for typical voltage and current values are shown in Figure 5-47.

$P_{\text{heater}} = 1.213 \pm 0.0009888$ [W]		
$R_{\text{heater}} = 149.6 \pm 0.01896$ [Ω]	$\partial P_{\text{heater}} / \partial R_{\text{heater}} = 0.00811$	2.42 %
$R_{\text{heater,ref}} = 49.97 \pm 0.008997$ [Ω]	$\partial P_{\text{heater}} / \partial R_{\text{heater,ref}} = -0.04856$	19.52 %
$R_{\text{therm,ref}} = 411.5 \pm 0.0511$ [Ω]	$\partial P_{\text{heater}} / \partial R_{\text{therm,ref}} = 0$	0.00 %
$V_{\text{heater,ref}} = 4.5 \pm 0.00162$ [V]	$\partial P_{\text{heater}} / \partial V_{\text{heater,ref}} = 0.5393$	78.06 %
$V_{\text{therm,ref}} = 0.196 \pm 0.00036$ [V]	$\partial P_{\text{heater}} / \partial V_{\text{therm,ref}} = 0$	0.00 %
$V_{\text{thermistor}} = 2.5 \pm 0.00162$ [V]	$\partial P_{\text{heater}} / \partial V_{\text{thermistor}} = 0$	0.00 %
<hr/>		
$R_{\text{therm}} = 5249 \pm 10.24$ [Ω]		
$R_{\text{heater}} = 149.6 \pm 0.01896$ [Ω]	$\partial R_{\text{therm}} / \partial R_{\text{heater}} = 0$	0.00 %
$R_{\text{heater,ref}} = 49.97 \pm 0.008997$ [Ω]	$\partial R_{\text{therm}} / \partial R_{\text{heater,ref}} = 0$	0.00 %
$R_{\text{therm,ref}} = 411.5 \pm 0.0511$ [Ω]	$\partial R_{\text{therm}} / \partial R_{\text{therm,ref}} = 12.76$	0.40 %
$V_{\text{heater,ref}} = 4.5 \pm 0.00162$ [V]	$\partial R_{\text{therm}} / \partial V_{\text{heater,ref}} = 0$	0.00 %
$V_{\text{therm,ref}} = 0.196 \pm 0.00036$ [V]	$\partial R_{\text{therm}} / \partial V_{\text{therm,ref}} = -26779$	88.57 %
$V_{\text{thermistor}} = 2.5 \pm 0.00162$ [V]	$\partial R_{\text{therm}} / \partial V_{\text{thermistor}} = 2099$	11.02 %

Figure 5-47: Heater power and thermistor resistance uncertainties

The resistance of each thermistor was then correlated to a manufacturer provided resistance-temperature relationship and a linear correlation was used between data points. The measurement uncertainty of the thermistor resistance is dependent on the temperature of the thermistor. The measurement and absolute uncertainties as a function of thermistor temperature are presented in Figure 5-48 below.

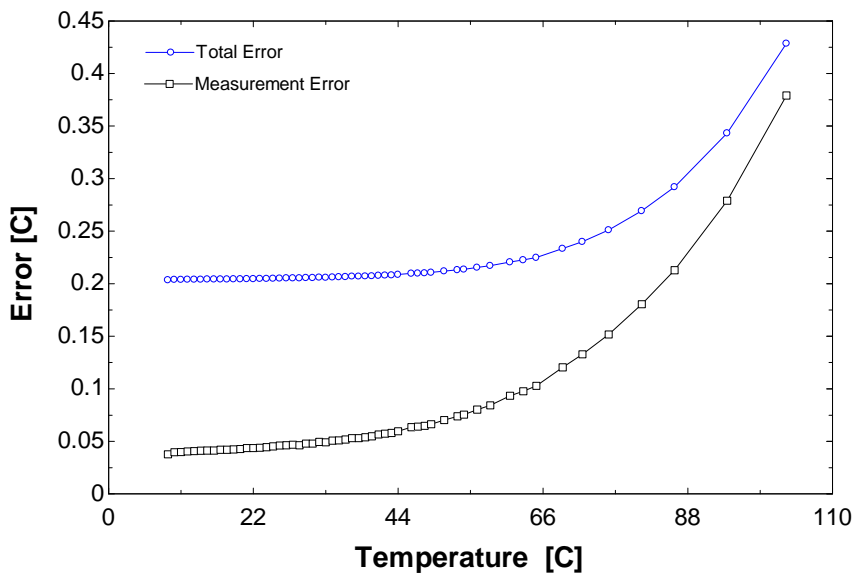


Figure 5-48: The measurement error and total error as a function of thermistor temperature

The total error in Figure 5-48 is the combination of the measurement uncertainty and the 0.2 C error associated with the manufacturer provided temperature-resistance relationship. The measurement uncertainty is reasonable below approximately 85 C and it is anticipated that the temperatures will not exceed this value during testing.

The pressure measurements were conducted using an Omega engineering PX219-30V15GI pressure transducer with a manufacturer published accuracy of  $\pm 0.50$  Kpa. The pressure transducer is rated from vacuum to 103.4 kpa gauge and the manufacturer provided calibration data can be found in Table 5-4.

Table 5-4: Manufacturer provided pressure transducer calibration data

Scale	Measured Voltage (V)	Theoretical voltage (V)
Zero	-0.0028	0.0008
½ Scale	2.5044	2.5017
Full Scale	4.9989	5.0025
½ Scale	2.5053	2.5017
Zero	-0.0019	0.0008

A linear curve fit was conducted on the calibration data to provide the working calibration curve:

$$p = 40.519 V - 101.27 \quad (5.25)$$

where  $p$  is the measured pressure in kilopascals and  $V$  is the pressure transducer output voltage in volts.

### 5.10 References

- Iguchi, C. Y., dos Santos, W. N., & Gregorio Jr., R. (2007). Determination of thermal properties of pyroelectric polymers, copolymers and blends by the laser flash technique. *Polymer Testing*, 788-792.
- Knier, B. J. (2012). *A Thermodynamic Analysis of an Electrocaloric Effect (ECE) Refrigeration Cycle*. University of Wisconsin - Madison.
- Munson, Young, Okiishi, & Huebsch. (2009). *Fundamentals of Fluid Mechanics*. Jefferson City: R. R. Donnelley.
- Young, W. C. (2002). *Roark's Formulas for Stress and Strain*. New York: McGraw-Hill Companies Inc.

## **CHAPTER 6: EXPERIMENTAL RESULTS**

The experimental device described in section 5.6 will be used to examine the differences between the experimental and modeled results. It will not be possible to provide a complete validation of the model described in chapter 2 because no electrocaloric films could be obtained. Instead the experimental device simply operates as a passive regenerative heat exchanger.

### *6.1 Measured Pressure Drop*

To gain greater confidence that the geometry is near its expected values, the pressure drop was measured and the pressure drop through the external tubing was subtracted. This pressure difference provides an experimental estimate of the pressure drop across the entire device, including both sets of manifolds and both stacks of films. The measured pressure drop through the device was then compared with the calculated values from section 4.2.1. Figure 6-1 shows a comparison between the measured and the calculated pressure drops for the first thermal prototype.

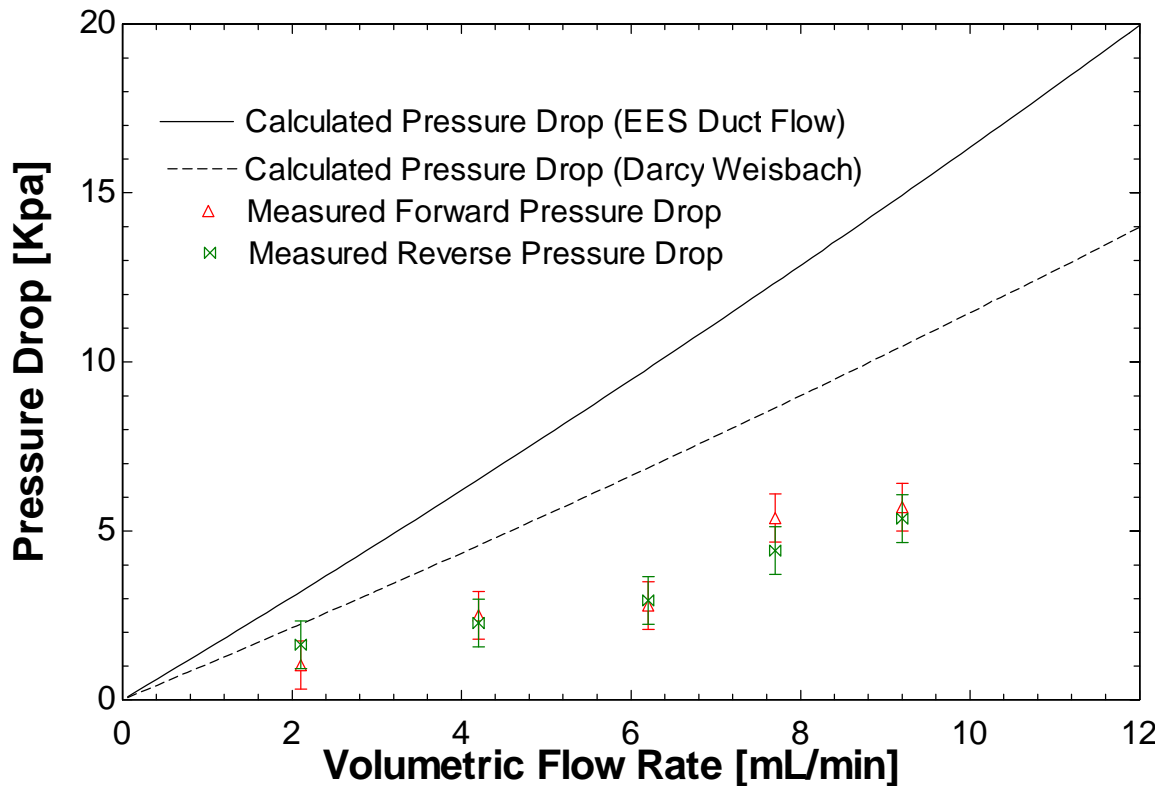


Figure 6-1: A comparison of the measured and calculated pressure drop for the first heat transfer device that was constructed.

The measured forward pressure drop was collected while the syringe was infusing and the reverse pressure drop data was collected during the syringe's draw stroke. In Figure 6-1 the solid line uses the EES duct flow pressure drop model to calculate the major head losses and the dotted line uses the Darcy Weisbach pressure drop model to calculate the friction (major) losses. The EES duct flow command assumes that there is a new developing region for each major head loss that is calculated. For example, the EES duct flow command assumes that there is a new developing region for the flow as it passes through the internal manifolds and another developing region as the flow passes through gap between the internal manifolds. Figure 6-2 shows how the EES duct flow pressure drop model would

account the boundary layers of a series of restrictions. This geometry is very similar to the flow geometry through the internal manifolds.

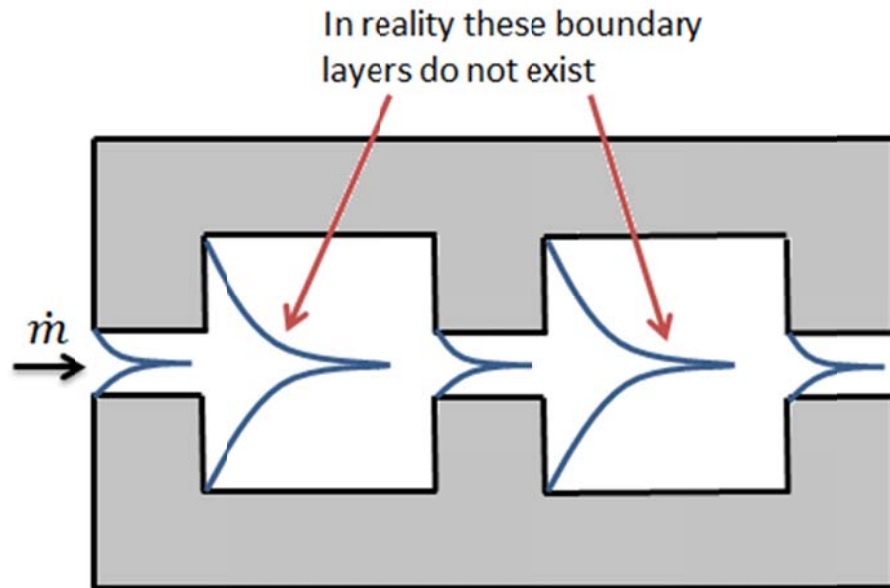


Figure 6-2: Boundary layers accounted for in the EES duct flow pressure drop model

By summing the EES duct flow pressure drop the model assumes that there is a new boundary layer for each of the larger channels, however, in reality, these boundary layers do not exist. The pressure drop through a developing region is larger than the developed region and, as a result, using the EES command to calculate the major head losses likely over-estimates the total pressure drop.

The Darcy Weisbach method neglects the developing region entirely. For the geometry that was used, the developing region should not be accounted for each time the channel geometry changes. Therefore, the pressure drop data should be between the Darcy Weisbach pressure and the EES calculated pressure drop. The difference between how the

developing region is accounted for is one of the main reasons that the two calculated lines in Figure 6-1 to not match.

Next, the pressure drop through the second heat transfer prototype was tested. The experimental data are plotted with the modeled pressure drop in Figure 6-4.

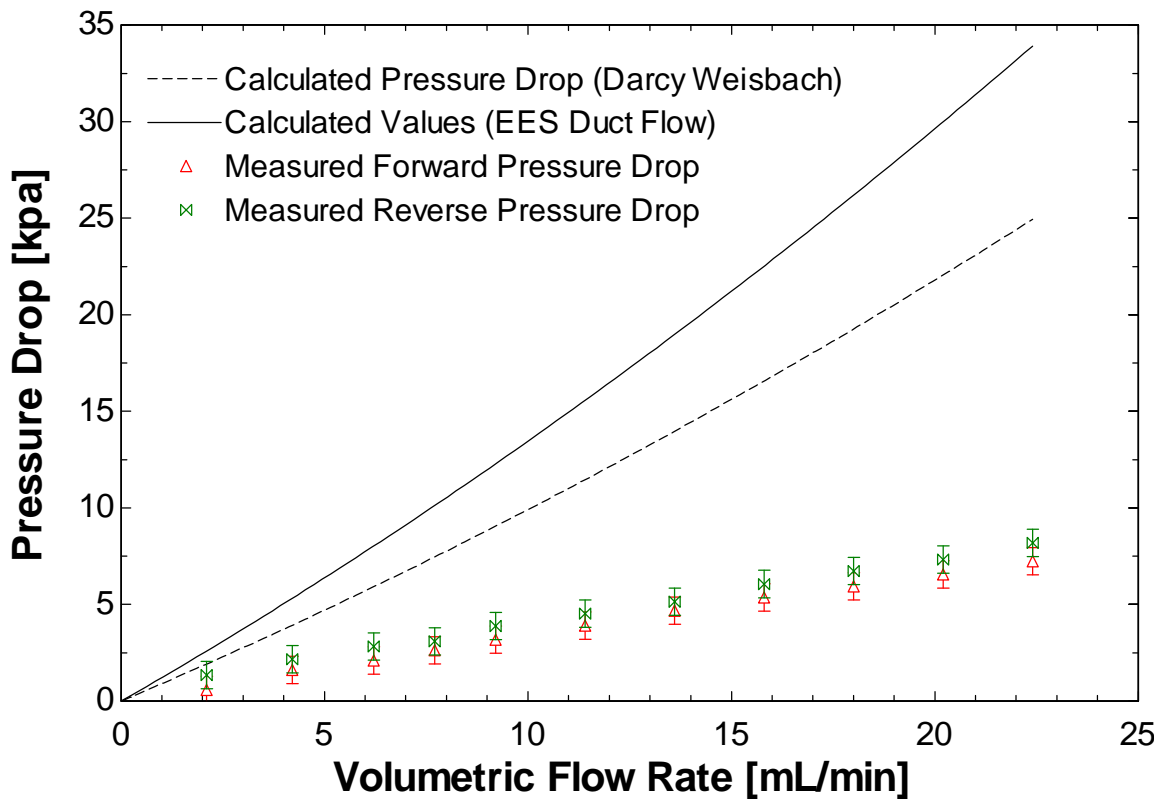


Figure 6-3: The measured pressure drop and calculated pressure drop through the second heat transfer device.

By looking at Figure 6-3 and Figure 6-1 it can be seen that the pressure drop through the device does not closely match with the calculated values. However, as discussed in section 5.4.1, the pressure drop through the internal manifolds is highly dependent on the channel thickness through the manifolds. Due to the manufacturing processes, a tolerance of  $\pm 0.025\text{mm}$  on the channel thickness is reasonable because the internal manifolds were

sanded to size by hand. In Figure 6-4, the pressure drop through the device and the calculated pressure drop, assuming that all four internal manifold channels are 0.025mm larger than their nominal value, are plotted as a function of the volumetric flow rate.

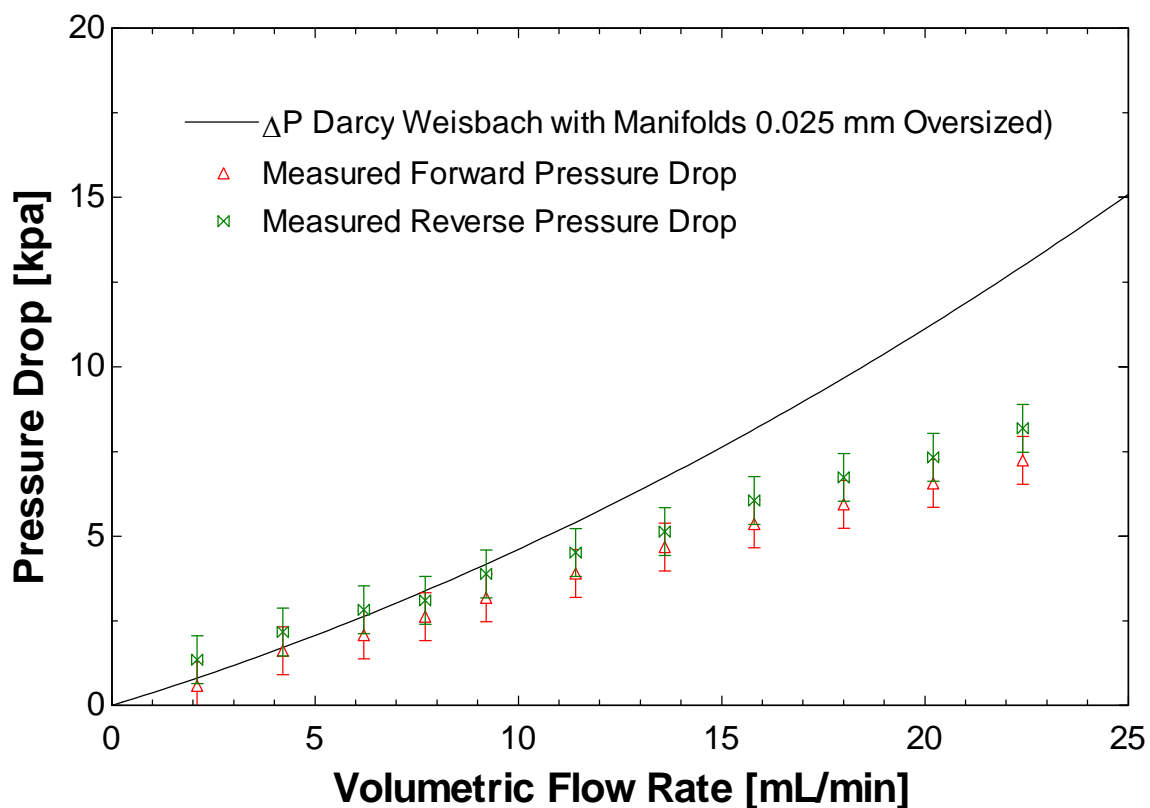


Figure 6-4: The measured pressure drop and the calculated pressure drop assuming that the internal manifold gaps are 0.025 mm larger than their nominal value.

When assuming that the internal manifolds are 0.025mm larger than their nominal values, the measured pressure drop is near the calculated pressure drop. At larger flow rates the flow could be passing through the small gaps on either end of the internal manifolds created because the manifolds cut to length by hand. Using only the pressure drop through the entire device, it is not possible to gain an accurate insight into the pressure drop of the

isolated stacks of films. The pressure drop is reasonable but the thermal measurements should give an additional insight into the processes occurring within the device.

## 6.2 Thermal Results

The experimental device could not be sealed reliably and therefore data could not be taken in the vacuum chamber. Instead, all data were collected at uninsulated, atmospheric conditions. Initially, temperature sensor T1 was placed on the stainless steel reinforcing plate directly outside of the internal manifolds while temperature sensor T3 was placed on the external manifold on the same side of the device. Figure 6-5 shows the locations of the temperature sensors.

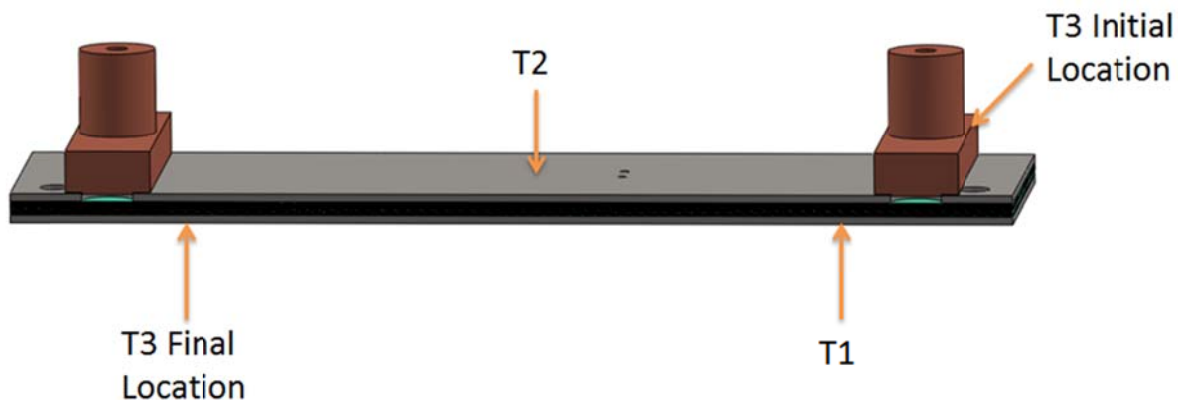


Figure 6-5: Temperature sensor locations

The temperature was recorded while 1 watt of power was dissipated by the heater and the pump pumped operated at 33.4 mL/min with a 5.6 second blow time. Temperature data plotted against time in Figure 6-6.

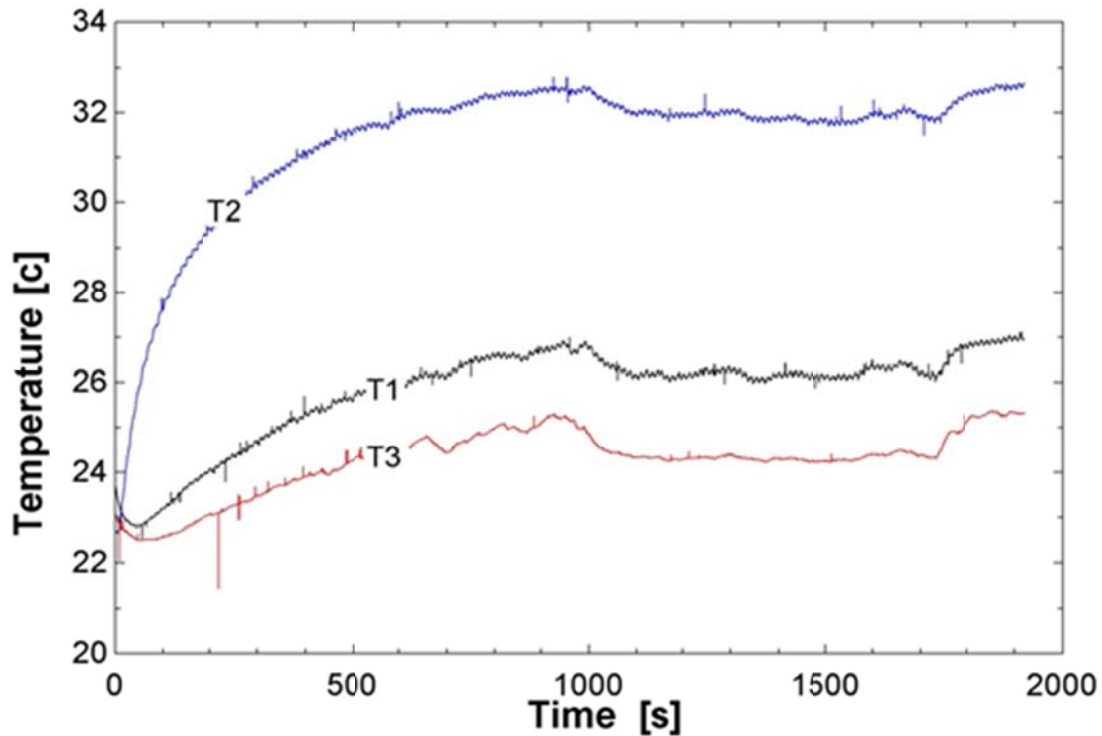


Figure 6-6: Transient temperatures with T1 placed directly below the internal manifolds, T2 at the center of the bed and T3 on the external manifold closest to T1.

First, there is a thermal difference between temperature sensors T1 and T3. Since the temperature of the fluid is assumed to be the same at T1 and T3, and because the temperature through the stainless steel is higher than the measurement on the external manifold, T1 must be measuring a temperature closer to the fluid temperature than T3. In addition, the observed thermal wave attenuation is much smaller in T1 than T3.

In 5.6 seconds a thermal wave will penetrate about 50mm into copper. Even though external manifolds are only 12.7 mm thick, the thermal wave experiences significant attenuation as it moves through the material. A zoomed in view of Figure 6-6 is shown in Figure 6-7.

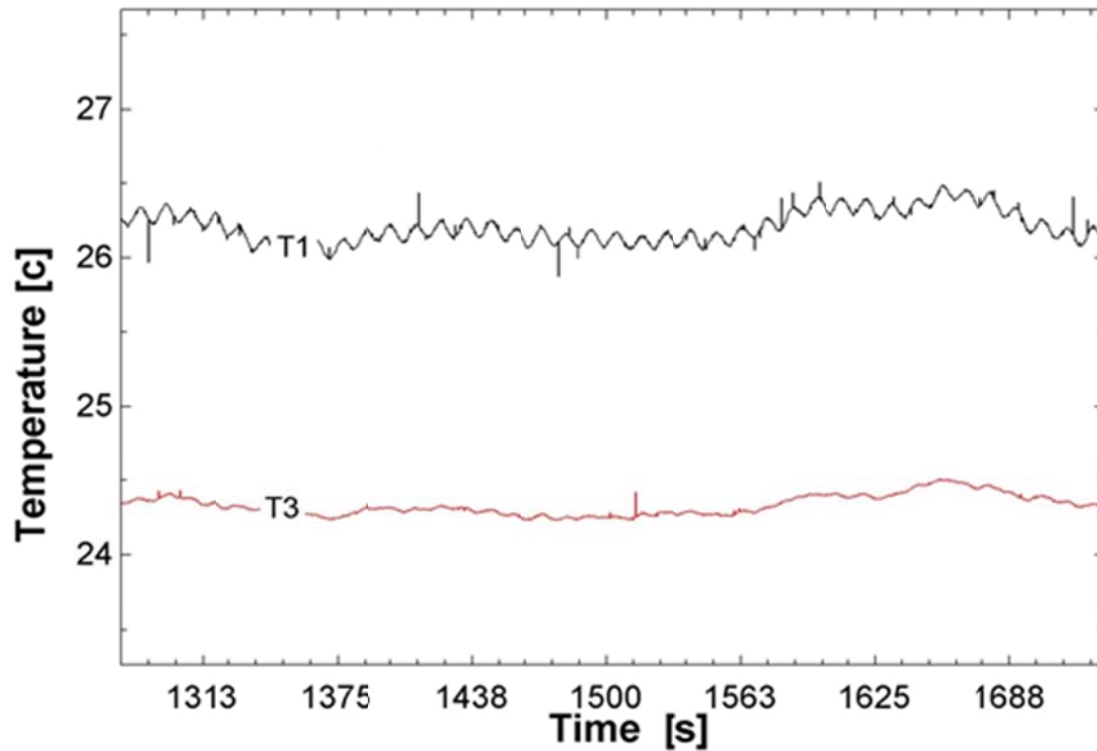


Figure 6-7: A zoomed in view of the attenuation that occurs through the external manifolds.

The fluctuations of the temperature at sensor T3 (located on the external manifold) can be observed through the internal manifold; however, the fluctuations are nearly on the same order as the noise of the measurement due to the attenuation of the thermal wave.

In addition, from section 4.2.3, the ratio of resistance from the inside of device to the outside to the resistance from the center of the device to the edge is above 100. Therefore, at steady state, putting sensors on stainless steel support structure should yield temperature measurements very near the fluid temperature. As a result, temperature sensor T3 was moved such that it was placed on the stainless steel support structure

directly adjacent to the external manifold on the opposite side of the device as temperature sensor T1. The final location of temperature sensor T3 is shown in Figure 6-5

Next, while conducting longer tests it was observed that although, the syringe pump induced oscillating flow, it also induced a net mass flow through the device from T3 to T1. This resulted in the temperatures at T3 being significantly lower than the temperature at T1. The mass flow rate problem was determined to be a measuring frequency error. The LabVIEW program was written so that it could only send a signal to the pump to change the direction at the sampling frequency. Since the specified blow times were not exact multiples of the sampling frequency, a net mass flow rate in one direction was induced. This effect is shown in Figure 6-8.

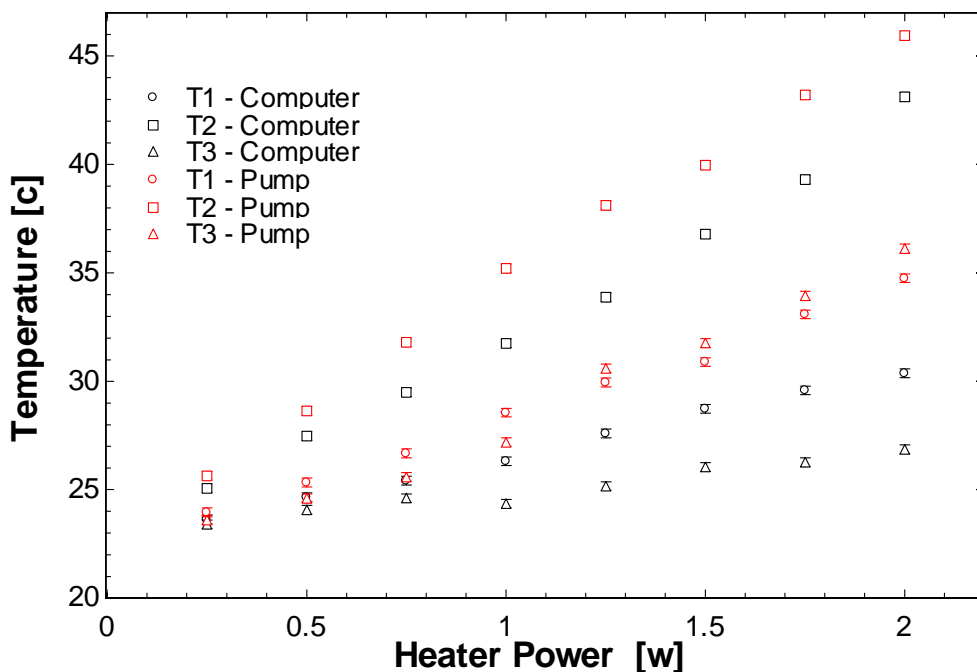


Figure 6-8: Temperature as a function of Heater power when the pump was controlling the flow direction and when the computer was controlling the flow direction.

This problem was fixed by programming the pump to use its internal timer to change the flow direction instead of relying on an external signal. In Figure 6-8 it can be seen that when the pump is controlling the mass flow rate, the temperature is higher than when the computer is controlling the mass flow rate for a given heater power. The explanation for this observation is that, when the computer is controlling the mass flow rate, new room temperature fluid is constantly being introduced into the system.

In addition, the temperatures at both ends of the device are further apart from one another when the computer is controlling the mass flow rate because room temperature water is being introduced from one side of the bed. Therefore, the side that the water is being introduced from will be cooler than the side that the water is leaving from.

Next, temperature sensors, T1 and T2, were both placed on the reinforcing plate on opposite sides of the device. The temperature of the flow was measured to verify that the transient temperatures were 180 degrees out of phase from one another. This is shown in Figure 6-9 with for a flow rate 33.4mL/min, a 5.7 second blow time and while dissipating 1 watt of power.

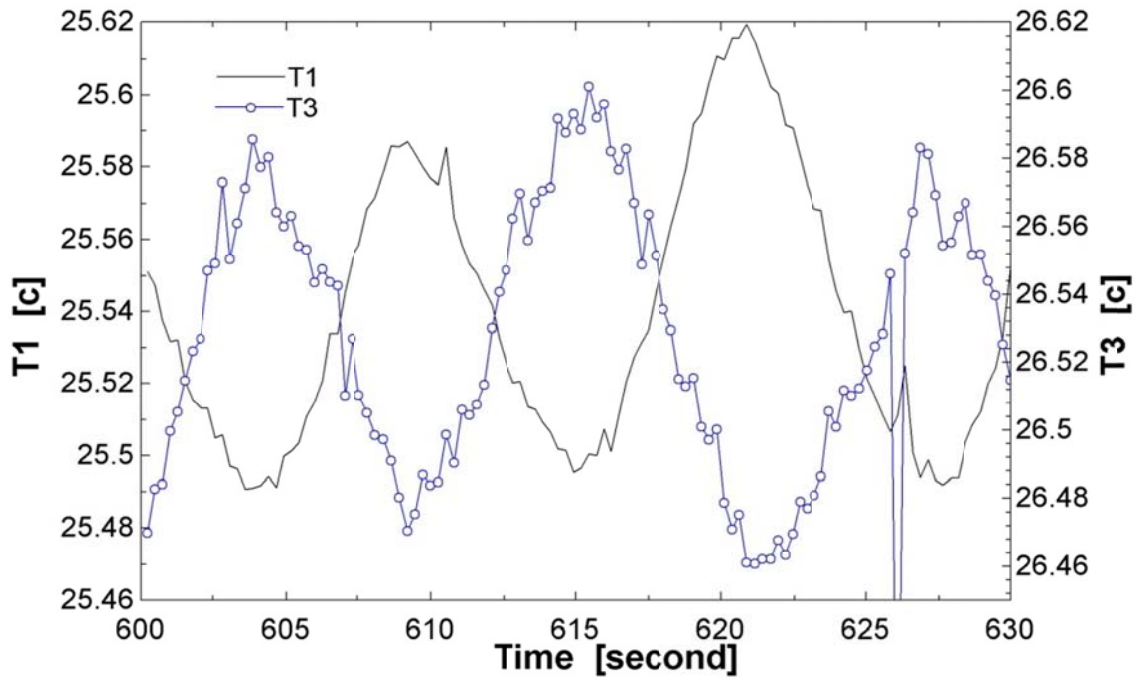


Figure 6-9: Verification that the temperature at the two ends of the device is out of phase.

As expected, the temperature at both ends of the device is out of phase and this shows that the two regenerators are working as expected. The average temperatures at the two locations are not identical, but this could be a result of the two heat exchangers having slightly different effectiveness values.

By setting the mass flow rate to zero, turning on the heater and measuring the temperature along the device the axial thermal resistance of the device can be determined. The axial resistance is calculated according to:

$$R = \frac{T_{center} - T_{edge}}{\dot{q}_{heater}} \quad (6.1)$$

A summary of the thermal resistances for different heater powers are presented in Table 6-1;  $R_{12}$  is the resistance between temperature sensor T1 and T2. Similarly,  $R_{23}$  is the thermal resistance between temperature sensor T2 and T3.

**Table 6-1: A summary of the axial conduction resistances**

Average Heater Power [w] +/- .001	Thermal Resistance $R_{12}$ [K/W]	Thermal Resistance $R_{23}$ [K/W]
0.257	19.84±1.10	19.61±1.10
0.503	18.89±0.56	19.07±0.56
0.750	18.87±0.38	19.19±0.38
0.999	19.12±0.28	19.38±0.28
1.249	18.33±0.23	18.91±0.22

The average axial conduction resistance is 19.2[K/W]. This value is less than the estimated axial conduction resistance found in 4.2.3 of 38 [K/W]. The difference is likely because the collected data were at ambient conditions and therefore, the heat transfer rate due to axial conduction is likely less than what was being dissipated by the heater. Also, the estimated value did not account for the axial conduction of the spacing layers. The axial conduction due to the spacing layers is about 132 K/W. As a result, the calculated thermal resistance is likely under estimated.

### 6.2.1 Calculating effectiveness:

Effectiveness for any heat exchanger,  $\epsilon$ , can be defined as:

$$\epsilon = \frac{Q}{Q_{max}} \quad (6.2)$$

Where  $Q$  is the energy transferred from the fluid to the regenerative material during the hot to cold blow or the cold to hot blow and  $Q_{\max}$  is the maximum possible heat transfer that could occur between the two fluid streams.

If the regenerator effectiveness is unity and it is assumed that the outside of the heat exchanger is adiabatic, once a temperature difference was induced at the center of the device, the temperature difference could be sustained indefinitely. This behavior would result because thermal energy would be completely transferred back and forth between the fluid and regenerator material and, therefore, no thermal energy would be rejected to the environment.

$Q$  can be obtained by conducting an energy balance around the fluid during one of the blow processes:

$$Q = \dot{V} \rho c_f (T_2 - T_1) t_{HTCB} = -\dot{V} \rho c_f (T_1 - T_2) t_{CTHB} \quad (6.3)$$

where  $\dot{V}$  is the volumetric flow rate,  $\rho$  is the fluid density,  $c_f$  is the specific heat of the working fluid,  $T_1$  is the cold side temperature and  $T_2$  is the warm side temperature.  $t_{HTCB}$  and  $t_{CTHB}$  are the hot to cold and cold to hot blow times respectively. However, since:

$$t_b = t_{HTCB} = t_{CTHB} \quad (6.4)$$

equation (6.3) becomes:

$$Q = \dot{V} \rho c_f (T_2 - T_1) t_b \quad (6.5)$$

The maximum thermal energy transfer can be expressed as the sum of the thermal energy transferred between the films and the fluid,  $Q$ , and the thermal energy that could have been transferred but was instead rejected to the surroundings,  $Q_{rejected}$ :

$$Q_{max} = Q + Q_{rejected} \quad (6.6)$$

At quasi steady state, the integral of the thermal energy of the device over an entire cycle is constant for any blow process:

$$C1 = \int_t^{t+2t_b} m_{device} * c_{device} * T_{ave} dt \quad (6.7)$$

where  $C1$  is a constant,  $m_{device}$  is the total mass of the thermal prototype,  $c_{device}$  is the mass weighted average specific capacity and  $T_{ave}$  is the mass weighted average temperature of the device.

Therefore, since during quasi steady state operation with the heater is consistently on, the thermal energy produced by the heater is not being stored by the capacitance of the device. As a result, all of the thermal energy generated by the heater must be rejected to the environment. In other words, the energy that is being generated by the heater is energy that could have been retained by the device but was instead rejected to the environment,  $Q_{rejected}$ . The thermal energy rejected to the environment on a per bed, per blow basis is:

$$Q_{rejected} = \frac{\dot{Q}_{htr} t_b}{2} \quad (6.8)$$

As a result, the effectiveness becomes:

$$\varepsilon = \frac{\dot{V} \rho c_f (T_2 - T_1) t_b}{\dot{V} \rho c_f (T_2 - T_1) t_b + \frac{\dot{Q}_{htr} t_b}{2}} \quad (6.9)$$

To determine the effectiveness, the system was brought to steady state conditions under varying mass flow rates. The steady state temperatures were averaged over several cycles to produce the temperature data presented in Table 6-2.

**Table 6-2: Temperature data various mass flow rates with a heater power of 1 watt and a blow time of 10 seconds**

$\dot{V}$ [mL/min]	T1 [c]	T2 [c]	T3 [c]
1.6	28.76	45.93	30.33
3.3	30.65	45.86	30.56
6.6	29.88	42.1	30.19
11.4	28.41	36.72	28.65
14.7	27.62	33.88	27.62
18	28.77	36.72	29.06
22.4	27.49	32.79	27.7
25.7	26.96	31.54	27.23
29	26.83	29.47	26.95
33.4	26.1	28.12	26.38

Equation (6.9) was then applied to each row in Table 6-2 to produce Figure 6-10.

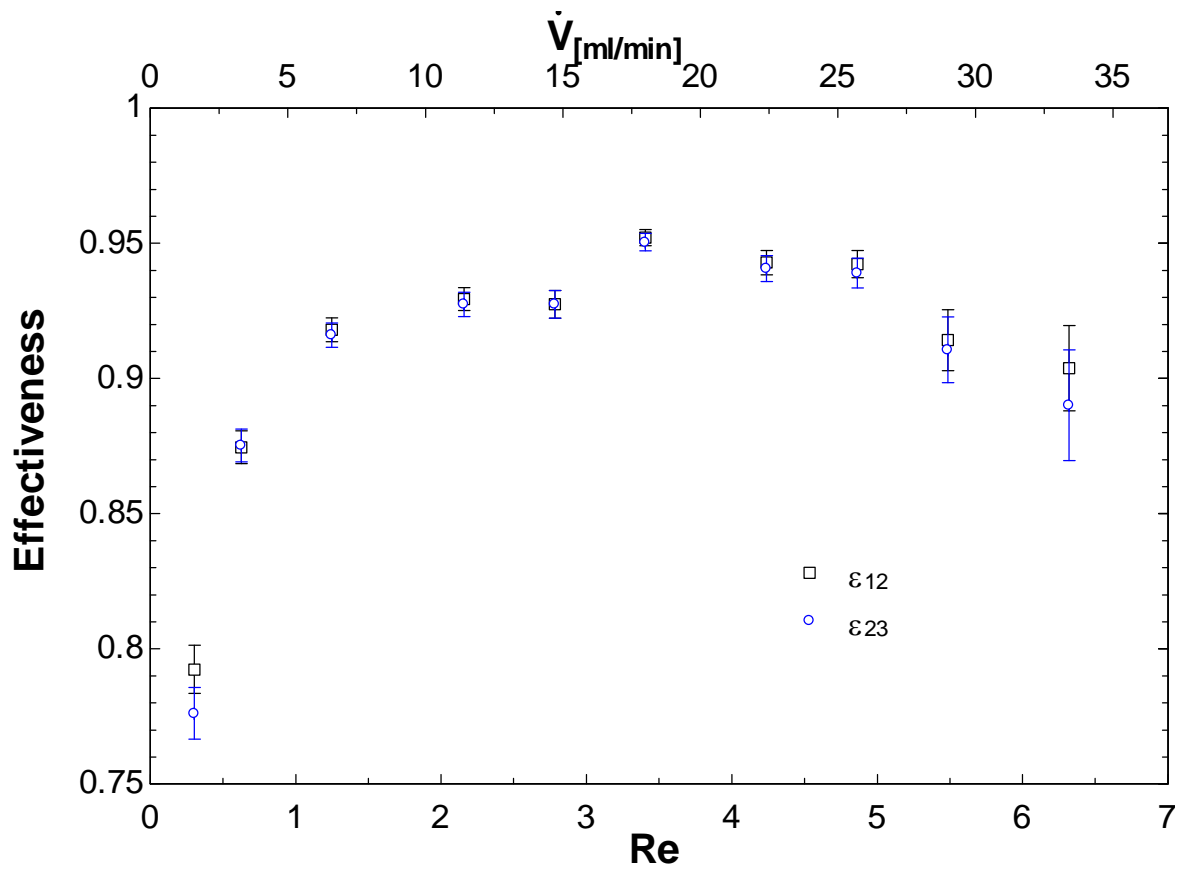


Figure 6-10: Experimental heat exchanger effectiveness as a function of Reynolds number

$\epsilon_{12}$  is the effectiveness calculated using temperature sensors T1 and T2. Similarly,  $\epsilon_{23}$  is the effectiveness of the heat exchanger calculated using temperature sensors T2 and T3. To examine repeatability of these measurements, data were collected four separate times at a flow rate of 22.4 mL/min with a blow time of 10 seconds while the heater was dissipating 1 watt of power. The results are shown in Table 6-3.

**Table 6-3: The measured temperatures and calculated effectiveness for several trials while operating at a flow rate of 22.4 mL/min, a 10 second blow time and 1 watt of power**

Trial	T1 [c]	T2 [c]	T3 [c]	$\epsilon_{12}$	$\epsilon_{23}$
1	27.49	32.79	27.70	0.943	0.941
2	26.63	30.61	26.84	0.925	0.921
3	26.88	31.03	27.19	0.928	0.923
4	27.04	31.91	27.01	0.938	0.938

The standard deviation was calculated from the eight effectiveness values in Table 6-3 and was found to be only 0.008. Therefore, these tests have good repeatability.

### 6.2.2 Axial Conduction and NTU Dominated Regions

Axial conduction of the device can be quantified by calculating an axial conduction parameter,  $\lambda$ . (Nellis & Klein, 2009). The axial conduction parameter is defined as:

$$\lambda = \frac{1}{R_{ac}\dot{C}_{min}} \quad (6.10)$$

where  $R_{ac}$  is the resistance to axial conduction through the heat exchanger and  $\dot{C}_{min}$  is the minimum capacitance rate.  $R_{ac}$  was experimentally determined to be about 19.2 [K/W] in section 6.2. Conceptually,  $\lambda$  can be thought as:

$$\lambda \approx \frac{\text{Heat transfer rate due to axial conduction}}{\text{Heat transfer rate between the two fluid streams}} \quad (6.11)$$

By plotting dimensionless axial conduction parameter against Reynolds number in Figure 6-11 the importance of axial conduction can be observed.

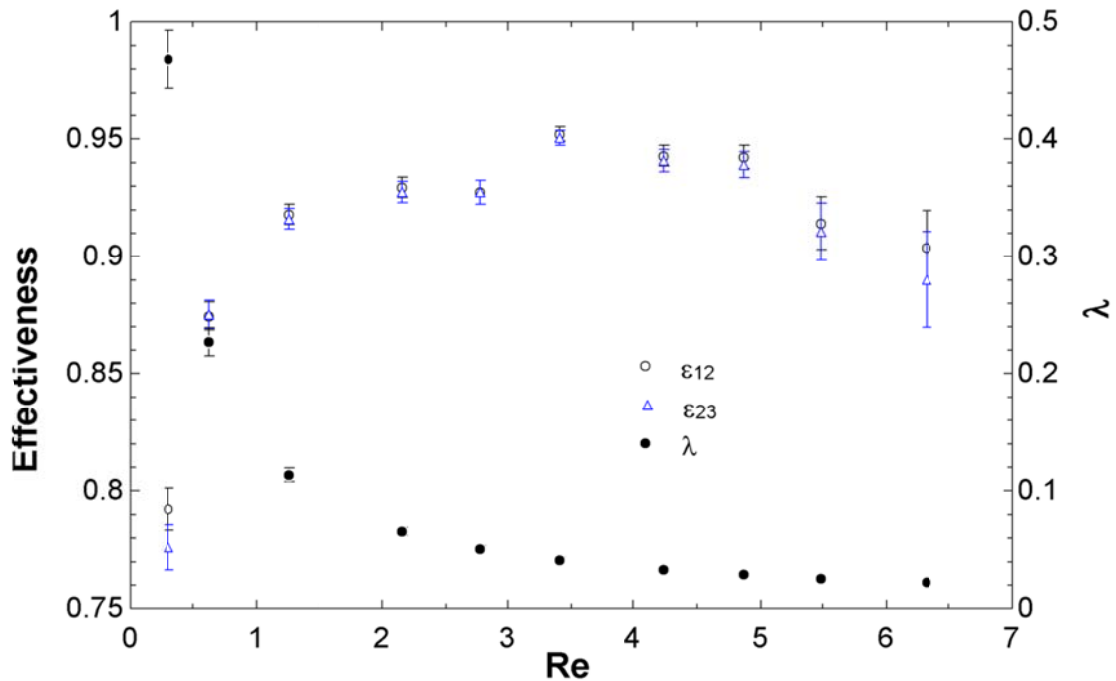


Figure 6-11: Axial conduction parameter as a function of Reynolds number

As the Reynolds number decreases, the relative importance of axial conduction increases. Therefore, the decrease in effectiveness at low Reynolds numbers is caused by an increase in the importance of axial conduction. In addition, as the Reynolds number increases the number of transfer units, NTU, decreases, which can be observed by calculating the NTU:

$$NTU = \frac{\bar{h} A_s}{\dot{m} c_f} \quad (6.12)$$

where  $\bar{h}$  is the average heat transfer coefficient,  $A_s$  is the regenerator surface area,  $\dot{m}$  is the fluid mass flow rate and  $c_f$  is the specific heat of the fluid. From section 2.5, the Nusselt number for a rectangular duct is:

$$Nu = 7.541(1 - 2.610AR + 4.970AR^2 - 5.119AR^2 + 2.702AR^4 - 0.548AR^5) \quad (6.13)$$

where the Nusselt number is defined as:

$$Nu_x \equiv \frac{h x}{k} \quad (6.14)$$

The parameter  $h$  is the local heat transfer coefficient,  $x$  is the location of the Nusselt number from the leading edge and  $k$  is the thermal conductivity of the fluid. As a result the average convection coefficient is:

$$\bar{h} = \frac{1}{L_e} \int_0^{L_e} h dx \quad (6.15)$$

The calculated number of transfer units as a function of Reynolds number is plotted in Figure 6-12.

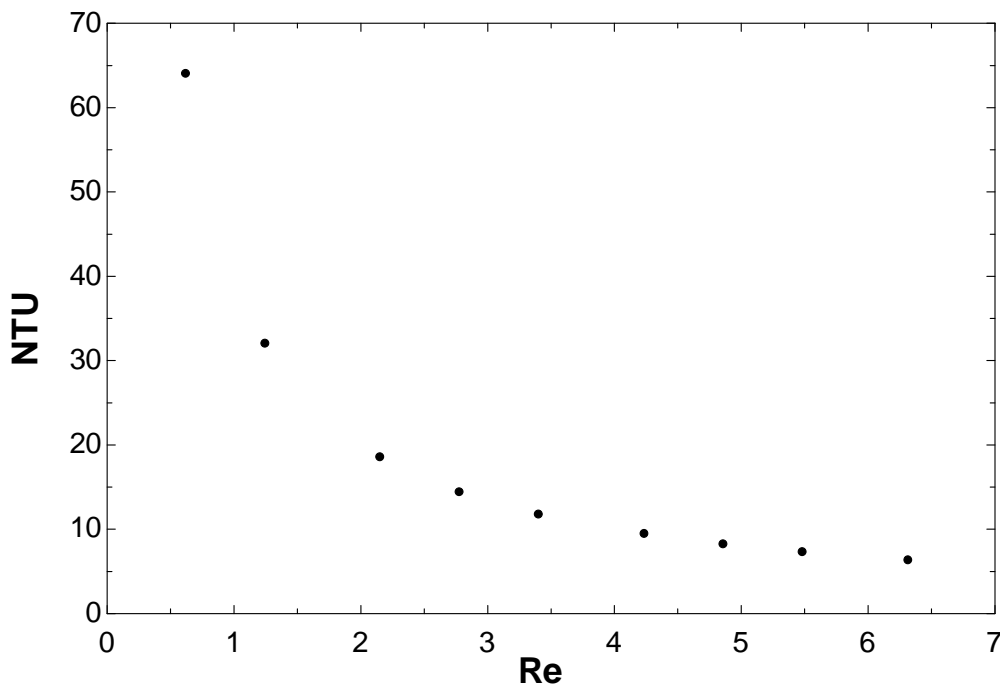


Figure 6-12: Calculated number of transfer units (NTU) as a function of Reynolds number

As the number of transfer units decreases the effectiveness decreases. For this reason, as the mass flow rate increases (which increases Reynolds number), the effectiveness decreases and this is what is observed in Figure 6-10. As a result, the maximum effectiveness is obtained at balance point between axial conduction and the number of transfer units.

### 6.2.3 Support Structure Capacitance

In addition to providing an extra thermal conduction path that degrades performance, the support structure adds additional capacitance to the regenerator that tends to improve the regenerator effectiveness. The inside surface area of the stainless steel is approximately  $28\text{cm}^2$  and the thermal diffusion depth in 10 seconds is:

$$L_d = \sqrt{\alpha t_b} \quad (6.16)$$

where the thermal diffusivity,  $\alpha$ , for stainless steel is about  $3.906\text{e-}6 \text{ m}^2/\text{s}$  and the time of one blow,  $t_b$  is 10 seconds. Equation (6.16) yields a thermal diffusion depth,  $L_d$  of 6.25 mm. However, the effective depth cannot be larger than the thickness of the port plate and reinforcing plates. These two parts are both 1.22mm thick. The affected volume,  $V_s$ , is therefore  $3.42\text{e-}6\text{m}^3$ . The capacitance of the affected support structure can then be calculated:

$$C_s = V_s \rho_{ss} c_{ss} = 13.03 \frac{J}{K} \quad (6.17)$$

where  $C_s$  is the effective capacitance of the support structure,  $V_s$  is the volume of affected region of the support structure,  $\rho_{ss}$  is the density of stainless steel taken to be  $7996 \text{ kg/m}^3$

and  $c_{ss}$  is the specific heat capacity of stainless steel taken to be 477 J/kg-K. Therefore the effective capacitance of the support structure is 13.03 J/k. This value provides a lower bound on the estimated capacitance of the support structure and can be compared to the total capacitance of the regenerator films,  $C_r$ .

$$C_r = th_e w_e L_e \rho_r c_r N_e = 1.79 \frac{J}{K} \quad (6.18)$$

where the thickness of one film,  $th_e$ , is 0.127mm, the width of one film,  $w_e$ , is 2.0 cm, the length of one film,  $L_e$ , is 3.0 cm, the density of the regenerator material,  $\rho_r$ , is 1775 kg/m<sup>3</sup>, the specific heat of the regenerator material,  $c_r$ , is 1325 J/kg-K and the number of films,  $N_e$  is 10. Because the mass of the regenerative material is small compared to the support structure, the capacitance of the support structure is very important. Note however that the support structure capacitance is not well-coupled to the fluid in the way that the regenerative material is.

By assuming that the entire device adds to the capacitance of the device and upper bound can be determined. Table 6-4 provides a summary of the capacitance for the major components of the prototype.

Table 6-4: The thermal capacitance for the major parts of the prototype

part	Material	Density [kg/m <sup>3</sup> ]	Specific Heat [J/kg-K]	Volume [cm <sup>3</sup> ]	Capacitance [J/k]
External Manifold	Copper	8957	389	4.42	15.5
Port Plate	Stainless Steel	7996	477	7.54	28.6
Reinforcing plate	Stainless Steel	7996	477	7.70	29.3
Spacing Layers	Stainless Steel	7996	477	3.28	12.5

Therefore the upper bound on the capacitance is approximately 85.9 J/k. The upper and lower capacitance bounds along with the experimentally determined axial conduction resistance can be used to guide the inputs of the model to account for the additional conductance and thermal capacitance.

### 6.3 A Comparison Between Experimental Results and Modeled Predictions

Figure 6-13 results from the model if the capacitance and thermal conductivity of the regenerative material are used.

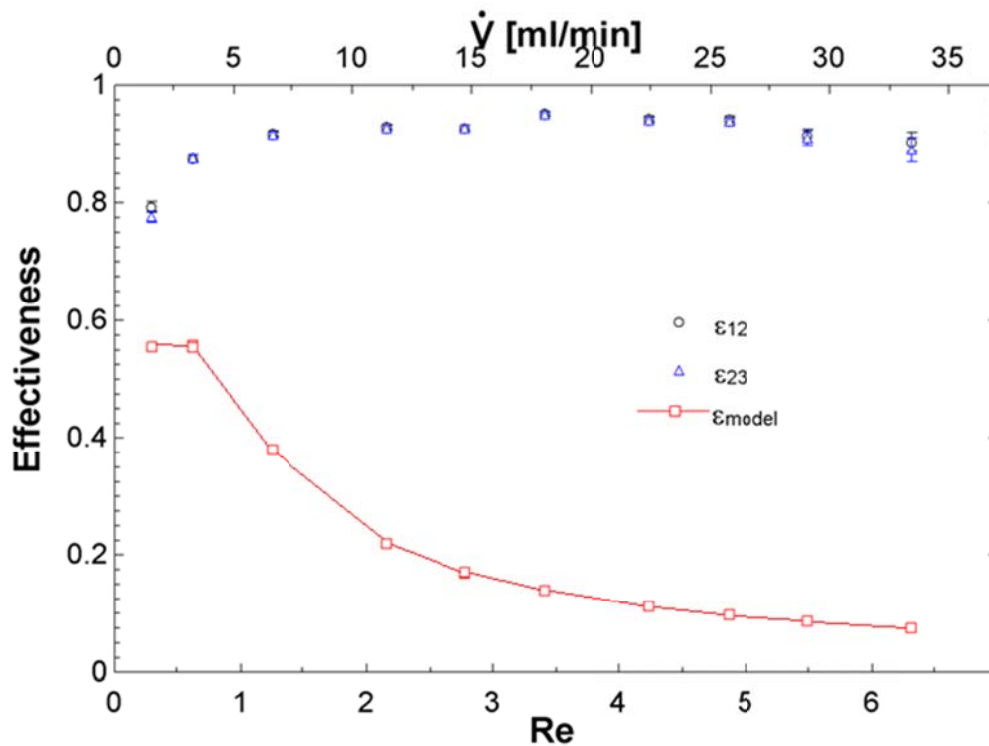


Figure 6-13: Modeled effectiveness and experimentally determined effectiveness as a function of Reynolds number without compensating for the support structure.

$\epsilon_{12}$  is the effectiveness of the passive regenerative heat exchanger between temperature sensors T1 and T2 while  $\epsilon_{12}$  is the effectiveness of the heat exchanger between temperature

sensors T2 and T3. From Figure 6-13 it is clear that, when the support structure is neglected, the trajectory and values of the modeled and experimental results disagree from one another. If the thermal conductance of the support structure is ignored, the model predicts a thermal resistance across one stack of films to be about 1800 K/W. The same conduction resistance was experimentally determined to be about 19.2 K/W. As a result, the decrease in effectiveness caused by axial conduction at low Reynolds numbers is not observed in the modeled results. The decrease in the number of transfer units as the Reynolds number increases dominates the model.

The difference in axial conduction between the model and the experimental device helps to explain the differences in shape between the two but the effectiveness of the experimental device is much higher than the predicted effectiveness. The capacitance of the support structure that is available for regeneration may be sufficient to explain this difference.

### 6.3.1 *Compensating for the Support Structure in the Model*

The axial conduction of the support structure can be approximately accounted for by setting the thermal resistance of the model equal to the experimentally determined thermal resistance of the device. This is accomplished by setting the thermal conductivity to a non-physical value in order to achieve the desired axial thermal resistance. First, the total volume of the regenerator films is:

$$V_{film} = N_{cells} t h_e w_e l_e = 7.62e - 7 m^3 \quad (6.19)$$

where the thickness of one film,  $th_e$ , is 0.127mm, the width of one film,  $w_e$ , is 2.0 cm, the length of one film,  $L_e$ , is 3.0 cm and the number of films,  $N_{ece}$  is 10. In addition, the total cross sectional area of the films and fluid channels,  $A_{xc}$  is:

$$A_{xc} = w_e [N_{ece}(th_e + th_f) + th_f] = 3.7693e - 5 m^2 \quad (6.20)$$

The fluid channel thickness,  $th_f$ , is to 0.0559mm. If the axial conduction resistance R is the 19.2K/W determined from 6.2.2, the effective conductivity must be:

$$k_{eff} = \frac{l_e}{R A_{xc}} = 41.52 \frac{w}{m - k} \quad (6.21)$$

The effective thermal conductivity model was modified from the original model to more closely match the physical system. The effective thermal conductivity  $k_{eff}$  was defined as:

$$k_{eff} = \frac{k_f th_f (N_{ece} + 1) + k_e N_{ece} th_e}{th_f (N_{ece} + 1) + N_{ece} th_e} \quad (6.22)$$

The thermal conductivity of the fluid  $k_f$  was set to the thermal conductivity of water, 0.6132 W/m-K. Therefore the conductivity of the regenerator material can be determined from equation (6.22) and was found to be 62.27W/m<sup>2</sup>-K. Similarly, by increasing the thermal capacitance of the films, the support structure of the capacitance can be accounted for.

The mass of the regenerator films,  $m_r$ , is:

$$m_r = V_{fillm} \rho_r = 0.00135 kg \quad (6.23)$$

From section 6.2.3 the lower capacitance bound is roughly 13.0 J/K and therefore the minimum specific capacitance that should be entered into the model,  $c_{min}$ , is

$$c_{min} = \frac{C_{min}}{2 m_r} = 4,806 \frac{J}{kg \cdot K} \quad (6.24)$$

Similarly, from section 6.2.3, the upper capacitance bound is about 85.9 J/k and therefore the maximum specific heat capacitance that should be entered into the model,  $c_{max}$ , is:

$$c_{max} = \frac{C_{max}}{2 m_r} = 64,360 \frac{J}{kg \cdot K} \quad (6.25)$$

Next the model was run with the same parameters as the physical experiment except regenerator material properties were modified to account for the support structure. The regenerative film's thermal conductivity was set to 62.27 W/m<sup>2</sup>-K and the regenerator specific heat capacity was set to 15,000 J/kg-K. The result is shown in Figure 6-14.

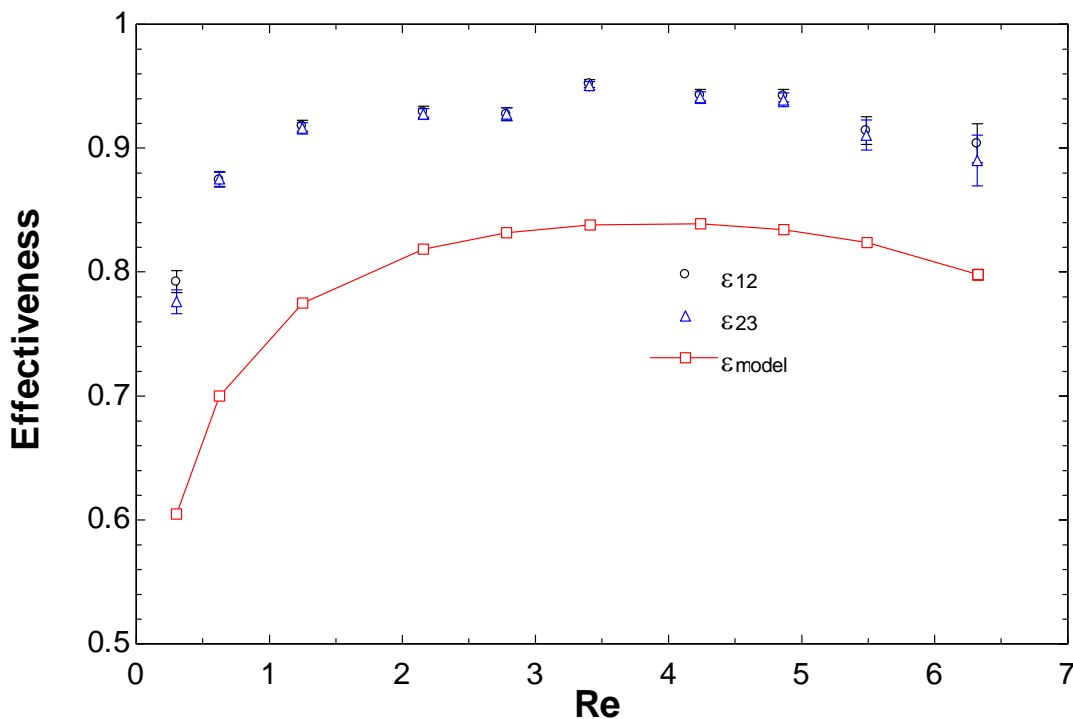


Figure 6-14: Modeled effectiveness and experimentally determined effectiveness as a function of Reynolds number after compensating for the support structure.

When the support structure of the heat exchanger is taken into account, the shape modeled data matches the experimental data well except that the modeled and experimental effectiveness are offset by roughly 0.18.

### 6.3.2 *Fitting the Model to Experimental Data*

The MATLAB optimization routine “fminsearch” was used to minimize an objective function while the specific heat and thermal conductivity of the regenerative material were allowed to vary. The objective function, OBJ, was defined as:

$$OBJ = (\varepsilon_{experimental} - \varepsilon_{model})^2$$

The Matlab routine predicted that a regenerative material that has a thermal conductivity, 13.39 W/m-K and specific heat of 24,454 J/kg-K best fit the data. The specific heat predicted by the Matlab routine is within the estimated minimum and maximum values but the thermal conductivity is less than the predicted value. The modeled effectiveness for these parameters is shown in Figure 6-15.

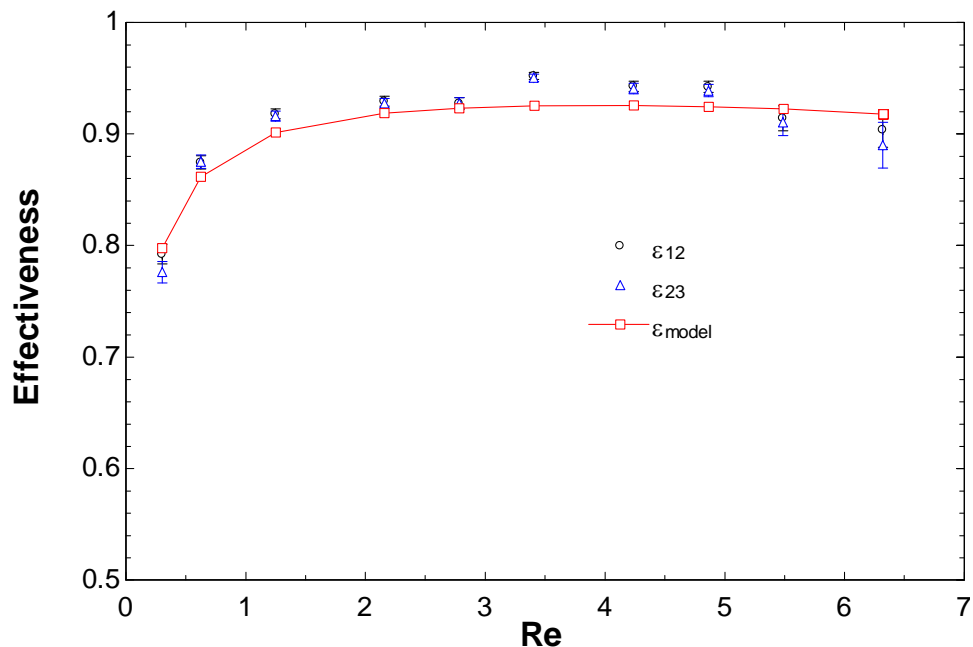


Figure 6-15: Optimized modeled effectiveness and the experimental effectiveness as a function of Reynolds number.

When the Matlab optimization routine is used, it predicts that the effectiveness will not decrease as quickly at large Reynolds numbers. This is likely because data were not obtained at large volumetric flow rates, due to limitations of the syringe pump. At higher Reynolds numbers the effectiveness would likely decrease and this would force the optimization routine to decrease the effectiveness at large Reynolds numbers.

#### 6.4 Model Sensitivity Analysis

Next, the sensitivity of the film's specific heat capacity was examined. In Figure 6-16, the capacitance of the regenerator material was varied and the effectiveness was plotted as a function of the Reynolds number.

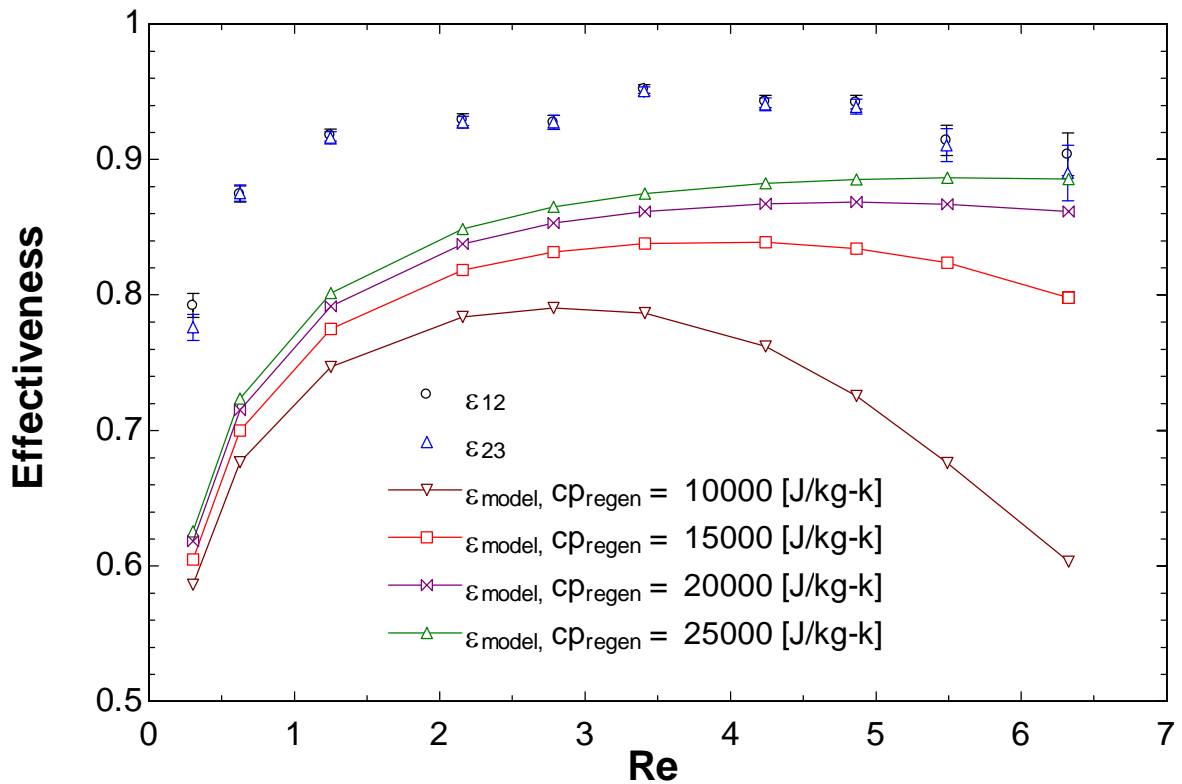


Figure 6-16: An examination of the regenerator effectiveness for several regenerator capacitance values while the thermal conductivity is set to a constant  $62.27 \text{ W/m}^2\text{-K}$

As the capacity of the device increases, the effectiveness also increases because the regenerative material is able to store more energy during each blow process. The effectiveness does not increase as much at low Reynolds numbers because system is dominated by axial conduction instead of the heat transfer rate between the two fluid streams. Next, the effect of the axial conduction on the effectiveness was examined by varying the thermal conductivity of the regenerative material in the model. The results are presented in Figure 6-17.

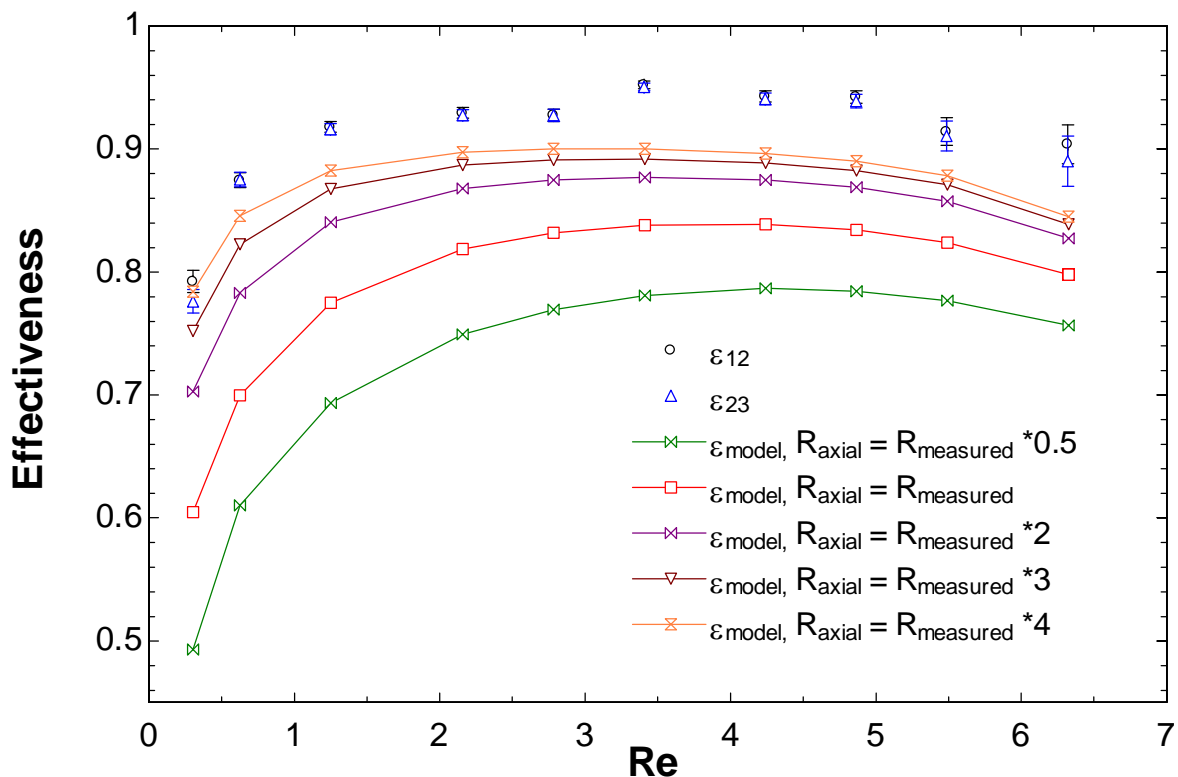


Figure 6-17: An examination of the regenerator effectiveness for several axial conduction resistances while the specific capacity of the regenerator material is set to a constant 15000 J/kg-K.

As the axial conduction decreases, the axial conduction dominated region moves to lower Reynolds numbers. In addition, as the axial conduction resistance decreases, the axial conduction parameter,  $\lambda$ , will also decrease and therefore the effectiveness of the regenerator will increase.

Furthermore, as it was previously mentioned in section 6.2, the experimentally determined axial conduction resistance is likely being underestimated. If the axial conduction resistance could be measured inside a vacuum, the experimentally determined effectiveness would

likely be closer to the modeled values because the axial conduction resistance would be greater.

### 6.5 Conclusions

The electrocaloric effect can be utilized to produce a solid-state refrigeration cycle that has the potential to be more efficient than current solid state cooling methods such as the Peltier Thermoelectric Effect. In addition, the electrocaloric effect does not require the large magnetic fields required when utilizing the Magnetocaloric effect and unlike the vapor compression cycle, it does not require a compressor. From a brief literature search, only three electrocaloric refrigeration systems have been constructed and therefore an accurate model of the refrigeration cycle needs to be developed. This project examined the design and manufacturing techniques of an electrocaloric refrigeration to compare experimental data with modeled predictions.

An iterative MATLAB model was developed from first principles to model an electrocaloric refrigeration cycle that consists of alternating fluid channels and electrocaloric films. The energy balances that describe the system are two coupled, second order with respect to space, first order with respect to time, partial differential equations.

This Matlab model was then used to maximize the cooling power of a two film electrocaloric refrigeration cycle. The design consisted of one electrocaloric film on either side of a load. A working fluid, in this case water, then oscillates through the device while operating the electrocaloric films 180 degrees out of phase. This allows continuous cooling of the load.

The model predicts that the smallest fluid channel that can be reliably manufactured should be used. In addition, the blow time of the system should be set to the smallest time that allows the electrocaloric films to thermally communicate with the flow. The optimal blow time was determined to be 1.63 seconds. Finally, the ideal mass flow rate was determined by varying the mass flow rate in the model while keeping the other parameters constant. The optimum mass flow rate was found to be 0.11 g/s, although ideally, the mass flow rate would decrease slightly as the load temperature drops.

In January 2013 it was determined that electrocaloric films would not be available to use for this project. By placing a heater where the load was to be placed and using passive regenerative material, the physical device could be compared to the model. The model comparison could be accomplished by comparing the new regenerative heat exchanger design to the model when the temperatures on the two ends of the bed were swapped and if the electric field was turned off.

The regenerative heat exchanger consisted of two stacks of 10 films each. The device was constructed by layering the components of the device on top of one another so that uniform channel thicknesses could be achieved. If another device were to be built, the slits in stainless steel in the spacing layers should be cut with a wire EDM prior to assembly instead of using a Dremel or slitting saw after the layers have been assembled.

In addition, about 1N of tension was applied to each film to try to reduce the deflection of each film. The support structure was constructed out of stainless steel to prevent axial conduction.

The fluid channels were spaced using 3M 467 MP transfer tape that has a thickness of 0.0559mm. In addition, precautions should be taken to prevent air from being trapped within the device when charging the system with the working fluid. Air entrapment can be prevented by adding a surfactant to the working fluid and evacuating the system prior to filling the system. Two sets of internal manifolds on each side of the device were put into place to achieve uniform fluid flow across the width of the device. The internal manifolds act as restrictions in the fluid channel to induce a pressure drop larger than the pressure drop through the regenerators and therefore distribute the flow.

The testing indicated that the constructed heat exchanger has an effectiveness of roughly 0.9. For a constant blow time, the effectiveness is dependent on the mass flow rate. At low flow rates the device is dominated by an increase in axial conduction while at higher flow rates the effectiveness devices due to a decrease in the NTU.

If the material properties of the regenerative material are entered into the model without accounting for the support structure, the model does not accurately predict the effectiveness. However, once the experimentally determined thermal conductivity and estimated capacitance of the physical device were accounted for in the model, the shape of modeled results matched the experimental results.

The additional capacitance and thermal conductance of the support structure can be accounted for by increasing the specific heat capacity and the thermal conductivity of the regenerator material to nonphysical values. This is done so that the thermal resistance and total capacitance of the physical device is the same as the modeled device. Once the thermal capacitance and thermal conductance were accounted for the modeled results, the modeled and experimental effectiveness differed by approximately 0.18.

#### *6.6 Next Steps and Future Work*

The model should be modified so that it better accounts for the axial conduction and thermal capacitance support structure of the device. When the electrocaloric effect is enabled, increasing the capacitance of the electrocaloric material may also change the predicted cooling power and COP. These effects should be investigated further.

All of the data that was collected was taken at atmospheric conditions because the bed could not be sealed reliably. Therefore, the next step is to fully seal the device so that data can be taken inside the vacuum chamber. The experimentally determined effectiveness and the axial conduction resistance will likely both increase when the device is tested inside a vacuum.

The edges of the devices were difficult to reliably seal using the Stycast 1266 and 5 minute Devcon epoxies and, therefore, other methods of sealing should be investigated. First, other epoxies should be investigated to seal the edges of the device. Excessive heat cannot be used due to the risk of damaging components inside the bed and, as a result, a mechanical method of sealing the bed would be ideal.

O-rings and gaskets are not ideal sealing methods for this application because they tend to deform as the clamping force changes. This deformation would likely change the channel thicknesses within the bed. However, there may be an undiscovered clever geometry that could take advantage of the good sealing and simplicity that O-rings and gaskets provide.

Once the current device has been tested in the vacuum, a two film demonstration device should be built using real electrocaloric films. Strategic Polymer Sciences was not able to provide films for this project but may be able to do so in the future. Alternatively, other manufacturers of electrocaloric material may exist that could be able to provide the material required to build the electrocaloric refrigeration demonstration device. The two film electrocaloric refrigeration cycle should be built using the same technique that was developed to build the regenerator device and it should be built according to the specifications presented in Table 3-2.

In addition, it may be advantageous create a thermal break in the port plate and reinforcing plates to reduce axial conduction. This might be accomplished by machining a small slot the majority of the width of the parts and then filling the slot using a material with a low thermal conductivity epoxy. This would provide a thermal break in the stainless steel while maintaining the strength and durability of the material. Once the electrocaloric refrigeration cycle is built, it can be used to fully validate the model.

## 6.7 References

Nellis, G., & Klein, S. (2009). *Heat Transfer*. New York: Cambridge University Press.

## APPENDIX

This appendix consists of selected EES code and engineering drawings of the thermal and manifold prototypes.

### Selected EES Code

Thermal Resistance Analysis:

{Nathan Haggerty

This code conducts a 1/4 symmetry thermal resistance model}

"! Determining the time to cool 1k assuming no losses, (radiation or conductive) and all rejected heat is removed from the bed."

q_dot=.5[w]	"Estimated cooling capacity of the ECE films"
T_amb=298[k]	"Ambient temperature outside of the vaccume and inital starting temperature of the bed"
p_amb=1[atm]*convert(atm,pa)	"Ambient pressure"
vol_bed_tot=28407[mm3]*convert(mm3,m3)	"Estimated total volume of metal in the bed"
rho=rho_('Stainless_AISI304', t_amb)	"Density"
m_bed_tot=rho*vol_bed_tot	"Mass of metal in the bed"
cp=c_('Stainless_AISI304', t_amb)	"Specific heat of stainless steel"
capacitance_tot=cp*m_bed_tot	"Total capacitance"
cooling_rate=capacitance_tot/q_dot	"Cooling rate"

"! 1/4 symetry model of the ECE bed"

"used to determine the heat leak between the ends of the bed and the center"	
w_end=2 [in]*convert(in,m)	"Width of one end cap"
l_end=5.5[in]*convert(in,m)	"Length of one end cap"
th_end=.048[in]*convert(in,m)	"Diameter of one end cap"
"DELTA_T=3[k]"	"Difference in water temperature between warm end and cold end"
{T_h=T_amb+DELTA_T/2	
T_c=T_amb-DELTA_T/2}	
T_h=t_amb	"The end of the bed is the same as the ambient temperature"
Axc=w_end*th_end	"Cross sectional area"
k=k_('Stainless_AISI304', T_amb)	"K=k_(Carbon_steel,T_amb)"
R_cond=(l_end/2)/(k*Axc)	"Conduction resistance along the bed walls"

"! Determining if sensors/heaters on the outside will work instead of putting them on the inside"

m_dot = .11[g/sec]*convert(g/s,kg/sec)	"Mass flow rate determined by the model"
HalfCycleTime=1.6[sec]	"1/2 cycle time of refrigeration system"
L_film=3[cm]*convert(cm,m)	"Length of the film space"
W_film=2[cm]*convert(cm,m)	"Width of the film space"
shim_th= .0022[in]*convert(in,m)	"Shim thickness"
film_th=.196[mm]*convert(mm,m)	"Film Thickness"
H_cold=2*shim_th+film_th	
call DuctFlow('water',T_amb,P_amb,m_dot,H_cold,W_film,L_film,0:h_T, h_H ,DELTA_T, Nusselt_T, f, Re)	

$R_{conv\_cold}=1/(h\_T*L\_film*W\_film)$  "Resistance to convection of the cold space"  
 $R_{cond\_cold}=th\_end/(k*L\_film*W\_film)$  "Resistance to convection of the cold space"  
 $R_{rad}=1/(w\_end*I\_end*.5*sigma*epsilon*(T\_s^2+T\_amb^2)*(T\_s+t\_amb))$  "Resistance to radiation"  
  
 $q_{cs}=(T\_s-T\_c)/(R_{conv\_cold}+R_{cond\_cold})$  "Heat transfer from the cold space to the surface"  
 $q_{hs}=(T\_h-T\_s)/R_{cond}$  "Heat transfer from the hot space to the surface"  
 $q_{rs}=(t\_amb-T\_s)/R_{rad}$  "Heat transfer due to radiation"  
 $2*q_{hs}+q_{rs}=q_{cs}$  "Energy balance around the surface node"  
 $q_{leak}=2*q_{cs}$  "Heat leak from the warm side of the bed to the cold space"  
 $q_{leak}=q_{dot}$  "Heat leak"  
 $alpha=k/(rho*cp)$  "Thermal diffusivity"  
 $tau\_diff=th\_end^2/alpha$   
  
 $sigma=5.6703e-8$  "Stefan Boltzmann constant"  
 $epsilon=.8[-]$  "approximant emissivity of steel"

EES duct flow and Darcy pressure drop model:

{Nathan Haggerty

This program conducts two pressure drop models, one that uses the EES duct flow command and another that uses the Darcy pressure drop model}

"! user controlled dimensions"

$fluid\$='water'$   
 $T\_amb=298[k]$  "Ambient Temperatures"  
 $p\_amb=1[atm]*convert(atm,pa)$  "Ambient Pressure"  
 $rho=Density(fluid\$,T=T\_amb,P=P\_amb)$  "Water Density"  
 $cp=Cp(fluid\$,T=T\_amb,P=P\_amb)$  "Water Specific Heat"  
  
 $V\_dot=\{.5833[mL/s]*convert(mL/s,m3/s)\}7[mL/s]*convert(mL/s,m3/s)$   
 $V\_dot\_mls=V\_dot*convert(m3/s,mL/s)$  "Volumetric Flow Rate in mL/s"  
 $V\_dot\_ml\min=V\_dot\_mls*convert(ml/s,ml/min)$  "Volumetric Flow Rate in mL/min"  
 $m\_dot=V\_dot*rho$  "Mass Flow Rate"  
  
 $th\_film=.196[mm]*convert(mm,m)$  "Thickness of an EC film in m"  
 $w\_chan=2[cm]*convert(cm,m)$  "Width of the cooling channel"  
 $L\_chan=3[cm]*convert(cm,m)$  "Length of the cooling channel"  
 $th\_channel\_spacer=.0022[in]*convert(in,m)$  "Thickness of the fluid channel spacer in m"  
 $Dia\_man\_hole=.026[in]*convert(in,m)$  "Diameter of the hole in the external manifold"  
 $Dia\_port\_hole=.026[in]*convert(in,m)$  "Diameter of the holes in the port plate"  
 $Dia\_in\_tubing=.12[in]*convert(in,m)$  "The inner diameter of the tubing that connects to the bed"  
 $th\_chan\_man=.01[in]*convert(in,m)$  "Thickness of the external manifold channel"  
 $W\_chan\_man=.0625[in]*convert(in,m)$  "width of the external manifold channel"  
 $L\_chan\_man=0.6[in]*convert(in,m)$  "Length of the external manifold channel in m"

$th\_in\_man=.0022[in]*convert(in,m)$  "thickness of the internal manifold's channel  
in m"  
 $th\_in\_man\_INCH=th\_in\_man*convert(m,in)$  "Thickness of the internal manifold channel  
in inches"  
 $th\_in\_man\_micrometer=th\_in\_man*convert(m,micrometer)$  "Thickness of the internal manifold  
channel in microns"  
 $th\_port\_plate=.048[in]*convert(in,m)$  "Thickness of the port plate in m"  
  
 $L\_in\_man=.15[in]*convert(in,m)$  "Length of the internal manifold channel"  
 $L\_cold=1.08[in]*convert(in,m)$  "Length of the cold space"  
 $w\_cold=.787[in]*convert(in,m)$  "Width of the cold space"  
 $RelRough=.000045$  "approximate relative roughness"  
  
 $th\_cold=11*th\_channel\_spacer+10*th\_film$  "Thickness of the cold space"  
 $V\_chan=th\_channel\_spacer*L\_chan*w\_chan*convert(m3,mL)$  "Volume of the film channels"  
 $V\_cold=th\_cold*w\_cold*L\_cold*convert(m3,mL)$  "Volume of the cold spacer"  
{v\_chan\_tot=4\*V\_chan}  
  
 $V\_inside=(2*V\_chan+V\_cold)$  "Total fluid volume inside the device"  
{V\_inside=.18[mL]}  
  
"! flow through the tube"  
 $Vol[0]=V\_inside-Vol[2]-Vol[5]-2*vol[13]$  "Volume through the tubing"  
 $A[0]=pi*(Dia\_in\_tubing/2)^2$  "Cross sectional area of the tubing"  
 $Vol[0]=L[0]*A[0]*convert(m3,mL)$  "Determines the length of travel within the  
piping"  
 $a\_w[0]=pi*Dia\_in\_tubing*L[0]$  "Wetted surface area of the tubing"  
  
call PipeFlow(fluid\$,T\_amb,P\_amb,m\_dot,Dia\_in\_tubing,L[0],RelRough:h\_T[0], h\_H[0],DELTA P[0],  
Nusselt\_T[0], f[0], Re[0])  
 $R\_conv[0]=1/(A\_w[0]*h\_H[0])$  "Convection resistance of the tubing"  
  
 $f\_darcy[0]=64/Re[0]$  "Darcy friction factor"  
 $D\_h[0]=Dia\_in\_tubing$  "Hydraulic diameter of the tubing"  
 $V[0]=V\_dot/A[0]$  "Average fluid velocity within the tubing"  
 $DELTA P\_darcy[0]=f\_darcy[0]*(L[0]/D\_h[0])*rho*(V[0]^2/2)$  "Darcy pressure drop"  
  
"! Constriction entering the first manifold"  
 $K\_L[1]=0.5$  "Minor loss coefficient for a restriction"  
 $A[1]=pi*(Dia\_man\_hole/2)^2$  "Cross sectional area coming into the  
restriction"  
 $V[1]=V\_dot/A[1]$  "Average Velocity coming into the restriction"  
  
 $DELTA P[1]=K\_L[1]*0.5*rho*V[1]^2$  "Pressure drop - EES method"  
 $DELTA P\_darcy[1]=DELTA P[1]$  "Pressure drop - Darcy method"  
  
"! Flow through the manifold hole"  
 $L[2]=.5[in]*convert(in,m)$  "Length of flow through the external  
manifold"  
 $A[2]=pi*(Dia\_man\_hole/2)^2$  "Cross sectional area"  
 $A\_w[2]=pi*Dia\_man\_hole*L[2]$  "Area of the channel wall for the manifold  
hole"  
 $Vol[2]=pi*Dia\_man\_hole^2*L[2]*convert(m3,mL)$  "Volume of the manifold hole"

call PipeFlow(fluid\$,T\_amb,P\_amb,m\_dot,Dia\_man\_hole,L[2],RelRough:h\_T[2], h\_H[2] ,DELTA P[2], Nusselt\_T[2], f[2], Re[2])

$R_{conv}[2]=1/(A_w[2]*h_H[2])$  "Convection resistance for the wall of the manifold hole"

$f_{darcy}[2]=64/Re[2]$  "Darcy friction factor"

$D_h[2]=Dia\_man\_hole$  "Hydraulic diameter"

$V[2]=V\_dot/A[2]$  "Volumetric flow rate"

$DELTA P_{darcy}[2]=f_{darcy}[2]*(L[2]/D_h[2])*rho*(V[2]^2/2)$  "Darcy pressure drop"

"! Expansion of the fluid into the manifold channel"

$K_L[3]=1$  "Loss coefficient for expansion"

$A[3]=pi*(Dia\_man\_hole/2)^2$  "Cross sectional area"

$V[3]=V\_dot/A[3]$  "volumetric flow rate"

$DELTA P[3]=K_L[3]*0.5*rho*V[3]^2$  "EES pressure drop"

$DELTA P_{darcy}[3]=DELTA P[3]$  "Darcy pressure drop"

"! Tee, Threaded, Dividing Line Flow"

$K_L[4]=2$  "loss coefficient for splitting a flow in a T"

$A[4]=pi*(Dia\_man\_hole/2)^2$  "Cross sectional area"

$V[4]=V\_dot/A[4]$  "Volumetric flow rate"

$DELTA P[4]=K_L[4]*0.5*rho*V[4]^2$  "EES pressure drop"

$DELTA P_{darcy}[4]=DELTA P[4]$  "Darcy pressure drop"

"!Flow through the first manifold split (only 1/2 the manifold pressure drop is calculated because this is the pressure drop due to the split flow)"

$A_w[5]=L\_chan\_man*W\_chan\_man+2*th\_chan\_man*L\_chan\_man+pi*W\_chan\_man*th\_chan\_man$  "wetted area"

$Vol[5]=L\_chan\_man*W\_chan\_man*th\_chan\_man*convert(m3,mL)$  "Volume of the fluid in the channel"

$A[5]=th\_chan\_man*W\_chan\_man$  "Cross sectional area"

$L[5]=L\_chan\_man/2$  "length of the channel in the internal manifold"

call DuctFlow(fluid\$,T\_amb,P\_amb,m\_dot/2,th\_chan\_man,W\_chan\_man,L[5],RelRough:h\_T[5], h\_H[5] ,DELTA P[5], Nusselt\_T[5], f[5], Re[5])

$R_{conv}[5]=1/(A_w[5]*h_H[5])$  "Convective resistance"

$f_{darcy}[5]=64/Re[5]$  "Darcy friction factor"

$D_h[5]=(4*A[5])/(th\_chan\_man*2+W\_chan\_man*2)$  "Hydraulic diameter"

$V[5]=(V\_dot/2)/A[5]$  "Average velocity"

$DELTA P_{darcy}[5]=f_{darcy}[5]*(L[5]/D_h[5])*rho*(V[5]^2/2)$  "Darcy Pressure drop"

"! Constriction through the port plate"

$K_L[6]=0.5$  "Loss coefficient for a restriction"

$A[6]=pi*(Dia\_port\_hole/2)^2$  "Cross sectional area"

$V[6]=V\_dot/(2*A[6])$  "Velocity"

$DELTA P[6]=K_L[6]*0.5*rho*V[6]^2$  "EES pressure drop"

$DELTA P_{darcy}[6]=DELTA P[6]$  "Darcy pressure drop"

"! Flow through port plate hole"

$A[7]=pi*(Dia\_port\_hole/2)^2$  "Cross sectional area"

```

L[7]=th_port_plate "Channel length"
Vol[7]=A[7]*L[7]*convert(m3,mL) "Average Velocity"
call PipeFlow(fluid$,T_amb,P_amb,m_dot/2,Dia_port_hole,th_port_plate,RelRough:h_T[7], h_H[7]
,DELTA[TAP[7], Nusselt_T[7], f[7], Re[7])

f_darcy[7]=64/Re[7] "Darcy Friction Factor"
D_h[7]=Dia_port_hole "Hydraulic Diameter"
V[7]=V_dot/A[7] "Average Velocity"
DELTA[TAP_darcy[7]=f_darcy[7]*(L[7]/D_h[7])*rho*(V[7]^2/2) "Darcy pressure drop"

"! Expansion out of port plate"
K_L[8]=1 "Loss coefficient for expansion"
A[8]=pi*(Dia_port_hole/2)^2 "Cross sectional Area"
V[8]=V_dot/(2*A[8]) "Average velocity"
DELTA[TAP[8]=K_L[8]*0.5*rho*V[8]^2 "EES pressure drop"
DELTA[TAP_darcy[8]=DELTA[TAP[8] "Darcy pressure drop"

"! Restriction through first internal manifold"
K_L[9]=0.5 "Loss coefficient for a restriction"
A[9]=th_in_man*w_chan "Cross sectional Area"
V[9]=V_dot/(A[9]) "Average Velocity"
DELTA[TAP[9]=K_L[9]*0.5*rho*V[9]^2 "EES pressure drop"
DELTA[TAP_darcy[9]=DELTA[TAP[9] "Darcy Pressure drop"

"! Flow through the first internal manifold"
A[10]=th_in_man*w_chan "Cross sectional area"
L[10]=l_in_man "Length of the channel"
Vol[10]=A[10]*L[10]*convert(m3,mL) "Volume of the channel"

call DuctFlow(fluid$,T_amb,P_amb,m_dot,th_in_man,w_chan,l_in_man,RelRough:h_T[10], h_H[10]
,DELTA[TAP[10], Nusselt_T[10], f[10], Re[10]) "nominal internal manifold thickness
pressure drop"
call DuctFlow(fluid$,T_amb,P_amb,m_dot,th_in_man-
.001[in]*convert(in,m),w_chan,l_in_man,RelRough:h_T[20], h_H[20] ,DELTA[TAP[20], Nusselt_T[20],
f[20], Re[20]) "Lower bound on internal manifold
thickness"
call
DuctFlow(fluid$,T_amb,P_amb,m_dot,th_in_man+.001[in]*convert(in,m),w_chan,l_in_man,RelRough:
h_T[21], h_H[21] ,DELTA[TAP[21], Nusselt_T[21], f[21], Re[21]) "Upper bound on internal manifold
thickness"

f_darcy[10]=64/Re[10] "Darcy friction factor"
D_h[10]=(4*A[10])/(2*th_in_man+2*w_chan) "Hydraulic Diameter"
V[10]=V_dot/A[10] "Average velocity"
DELTA[TAP_darcy[10]=f_darcy[10]*(L[10]/D_h[10])*rho*(V[10]^2/2) "Darcy pressure drop"
{DELTA[TAP[10]=DELTA[TAP[14]*2 } "Restricts the pressure drop across each of
the internal manifolds such that each internal manifold has a pressure drop of twice the bed pressure
drop"
DELTA[TAP_in_man_kpa=DELTA[TAP[10]*convert(pa,kpa) "EES pressure drop for the internal
manifolds in kpa"

"! Expansion out of first manifold"

```

$K_L[11] = (1 - (th\_in\_man * w\_chan)^2 / (th\_cold * w\_chan)^2)$  "Loss coefficient for an expansion"  
 $A[11] = th\_in\_man * w\_chan$  "Cross sectional area"  
 $V[11] = V\_dot / (A[9])$  "Average velocity"  
 $DELTA P[11] = K_L[11] * 0.5 * rho * V[11]^2$  "EES pressure drop"  
 $DELTA P\_darcy[11] = DELTA P[11]$  "Darcy pressure Drop"

**"! Flow through expanded section"**  
 $A[12] = th\_cold * w\_chan$  "Cross sectional area"  
 $L[12] = l\_in\_man$  "Length of the channel"  
 $Vol[12] = A[12] * L[12] * convert(m^3, mL)$  "Volume of the channel"

$call DuctFlow(fluid$, T\_amb, P\_amb, m\_dot, th\_cold, w\_chan, l\_in\_man, RelRough: h\_T[12], h\_H[12], DELTA P[12], Nusselt\_T[12], f[12], Re[12])$

$f\_darcy[12] = 64 / Re[12]$  "Darcy friction factor"  
 $D\_h[12] = (4 * A[12]) / (2 * th\_cold + 2 * w\_chan)$  "Hydraulic diameter"  
 $V[12] = V\_dot / A[12]$  "Average Velocity"  
 $DELTA P\_darcy[12] = f\_darcy[12] * (L[12] / D\_h[12]) * rho * (V[12]^2 / 2)$  "Darcy pressure drop"

**"! Double the first internal manifold to account for the second one"**  
 $DELTA P[13] = DELTA P[9] + DELTA P[10] + DELTA P[11] + DELTA P[12]$  "EES pressure drop of the first internal manifold"  
 $Vol[13] = Vol[10] + Vol[12]$  "Volume of the second internal manifold"  
 $DELTA P\_darcy[13] = DELTA P\_darcy[9] + DELTA P\_darcy[10] + DELTA P\_darcy[11] + DELTA P\_darcy[12]$  "darcy pressure drop of the second internal manifold"

**"! Split flow through the channel this is the flow next to the films"**  
 $A[14] = th\_channel\_spacer * w\_chan$  "Cross sectional area"  
 $L[14] = L\_chan$  "Length of the channel"  
 $call DuctFlow(fluid$, T\_amb, P\_amb, m\_dot / 11, th\_channel\_spacer, w\_chan, L\_chan, RelRough: h\_T[14], h\_H[14], DELTA P[14], Nusselt\_T[14], f[14], Re[14])$

$f\_darcy[14] = 64 / Re[14]$  "Darcy friction factor"  
 $D\_h[14] = (4 * A[14]) / (2 * th\_channel\_spacer + 2 * w\_chan)$  "Hydraulic diameter"  
 $V[14] = (V\_dot / 10) / A[14]$  "Average Velocity"  
 $DELTA P\_darcy[14] = f\_darcy[14] * (L[14] / D\_h[14]) * rho * (V[14]^2 / 2)$  "Darcy Pressure drop"

**"! Flow through 1/2 the cold space"**  
 $A[15] = th\_cold * w\_cold$  "Cross sectional area"  
 $L[15] = L\_cold / 2$

$call DuctFlow(fluid$, T\_amb, P\_amb, m\_dot, th\_cold, w\_cold, L\_cold / 2, RelRough: h\_T[15], h\_H[15], DELTA P[15], Nusselt\_T[15], f[15], Re[15])$

$f\_darcy[15] = 64 / Re[15]$  "Darcy Friction factor"  
 $D\_h[15] = (4 * A[15]) / (2 * th\_channel\_spacer + 2 * w\_chan)$  "Hydraulic Diameter"  
 $V[15] = (V\_dot) / A[15]$  "Average velocity"  
 $DELTA P\_darcy[15] = f\_darcy[15] * (L[15] / D\_h[15]) * rho * (V[15]^2 / 2)$  "Darcy pressure drop"

$DELTA P\_tot = sum(DELTA P[1..15]) * 2$  "Total EES pressure drop in pa"  
 $DELTA P\_tot\_kpa = DELTA P\_tot * convert(pa, kpa)$  "Total EES pressure drop in kpa"  
 $DELTA P\_tot\_atm = DELTA P\_tot * convert(pa, atm)$  "Total EES pressure drop in atm"  
 $DELTA P\_tot\_psi = DELTA P\_tot * convert(pa, psi)$  "Total EES pressure drop in psi"

$\text{DELTA}_{\text{tot\_darcy}} = \text{sum}(\text{DELTA}_{\text{darcy}}[1..15]) * 2$  "Total Darcy pressure drop in pa"  
 $\text{DELTA}_{\text{tot\_kpa\_darcy}} = \text{DELTA}_{\text{tot\_darcy}} * \text{convert}(\text{pa}, \text{kpa})$  "Total Darcy pressure drop in kpa"  
 $\text{DELTA}_{\text{tot\_atm\_darcy}} = \text{DELTA}_{\text{tot\_darcy}} * \text{convert}(\text{pa}, \text{atm})$  "Total Darcy pressure drop in atm"  
 $\text{DELTA}_{\text{tot\_psi\_darcy}} = \text{DELTA}_{\text{tot\_darcy}} * \text{convert}(\text{pa}, \text{psi})$  "Total Darcy pressure drop in psi"

$\text{DELTA}_{\text{mantest}} = \text{sum}(\text{DELTA}[1..13]) + \text{sum}(\text{DELTA}[1..8])$  "Pressure drop prediction (EES) of the manifold only test in pa"  
 $\text{DELTA}_{\text{mantest\_kpa}} = (\text{sum}(\text{DELTA}[1..13]) + \text{sum}(\text{DELTA}[1..8])) * \text{convert}(\text{pa}, \text{kpa})$  "Pressure (EES) drop prediction of the manifold only test in kpa"

$\text{DELTA}_{\text{mantest\_darcy}} = \text{sum}(\text{DELTA}_{\text{darcy}}[1..13]) + \text{sum}(\text{DELTA}_{\text{darcy}}[1..8])$  "Pressure (Darcy) drop prediction of the manifold only test in pa"  
 $\text{DELTA}_{\text{mantest\_darcy\_kpa}} = (\text{sum}(\text{DELTA}_{\text{darcy}}[1..13]) + \text{sum}(\text{DELTA}_{\text{darcy}}[1..8])) * \text{convert}(\text{pa}, \text{kpa})$  "Pressure (Darcy) drop prediction of the manifold only test in kpa"

$\text{error\_toolarge} = (\text{DELTA}[21] - \text{DELTA}[10]) * 4 * \text{convert}(\text{pa}, \text{kpa})$  "The error in the pressure drop (EES) if the internal manifold was 0.001 inch too large"  
 $\text{error\_toosmall} = (\text{DELTA}[20] - \text{DELTA}[10]) * 4 * \text{convert}(\text{pa}, \text{kpa})$  "The error in the pressure drop (EES) if the internal manifold was 0.001 inch too small"

$\text{DELTA}_{\text{tot\_kpa\_darcy\_lowerwin}} = \text{DELTA}_{\text{tot\_kpa\_darcy}} + \text{error\_toolarge}$  "The in the pressure drop (Darcy) if the internal manifold was 0.001 inch too large"  
 $\text{DELTA}_{\text{tot\_kpa\_darcy\_upperwin}} = \text{DELTA}_{\text{tot\_kpa\_darcy}} + \text{error\_toosmall}$  "The in the pressure drop (Darcy) if the internal manifold was 0.001 inch too small"

"! Heat exchanger effectiveness of the external manifold"

$1/R_{\text{tot}} = 1/R_{\text{conv}}[0] + 1/R_{\text{conv}}[2] + 1/R_{\text{conv}}[5]$  "Total resistance"  
 $R_{\text{tot}} = 1/UA$  "Determine UA"  
 $C_{\text{dot}} = m_{\text{dot}} * cp$  "Capacitance rate"  
 $NTU = UA/C_{\text{dot}}$  "Number of NTU"  
 $Eff = 1 - \exp(-NTU)$  "Effectiveness"  
 $\{\text{head} = \text{DELTA}_{\text{tot}} / 9804.139432[m]\}$  "total pressure drop in meters of head"

A study of Non-uniform Fluid Channel Thicknesses

{Nathan Haggerty

This code examines the flow patterns if one or more of the fluid channels is a different thickness as the others}

$T = 300[k]$  "Water temperature"  
 $P = 1[atm] * \text{convert}(\text{atm}, \text{pa})$  "Water pressure"  
 $\rho = \text{Density}(\text{water}, T=T, P=P)$  "Density of water"  
 $\mu = \text{Viscosity}(\text{Water}, T=T, P=P)$  "Viscosity of water"  
 $V_{\text{dot}} = .15[mL/s] * \text{convert}(mL/s, m^3/s)$  "Volumetric flow rate"  
 $m_{\text{dot\_total}} = V_{\text{dot}} * \rho$  "Mass flow rate"  
 $w_{\text{chan}} = 2[cm] * \text{convert}(cm, m)$  "Width of the fluid channel"  
 $l_{\text{chan}} = 3[cm] * \text{convert}(cm, m)$  "Length of one channel"  
 $N = 11$  "Number of channels"

"! percent off"

$\{\text{Percent\_off} = 1.0\}$  "The percent off from the nominal thickness value"



```

{Deflection=(-5.6*10^(-6)) *1[m]}
rho_water=Density(Water,T=Temperature,P=Pressure) "Density of water"
Pressure=1[atm]*convert(atm,pa) "Atmospheric pressure"
Temperature = 300[k] "Atmospheric temperature"
th_chan=.0022[in]*convert(in,m) "Fluid channel thickness"
f_w=9.81[m/s2]*(L*D*th_chan)*rho_water "Force of water on the beam"
V=L*D*h "Volume of the beam"
E=160000 [psi]*convert(psi,pa) "Modulus of Elasticity"
rho=1780 [kg/m3] "Density"
g=9.81[m/s2] "Gravity"

"! Loads"
m_film=V*rho "Mass of film"
f_g=m_film*g "Force due to gravity"
w_a=(f_g+f_w)/L "Distributed load"
a=0 "Distributed load spans the entire beam"
K=(P/(E*I))^(.5) "Loading Factor"
I=(L*h^3)/12 "Second moment of area"
P=.981[n] "Tensile force"
KL=k*L "K multiplied by L"

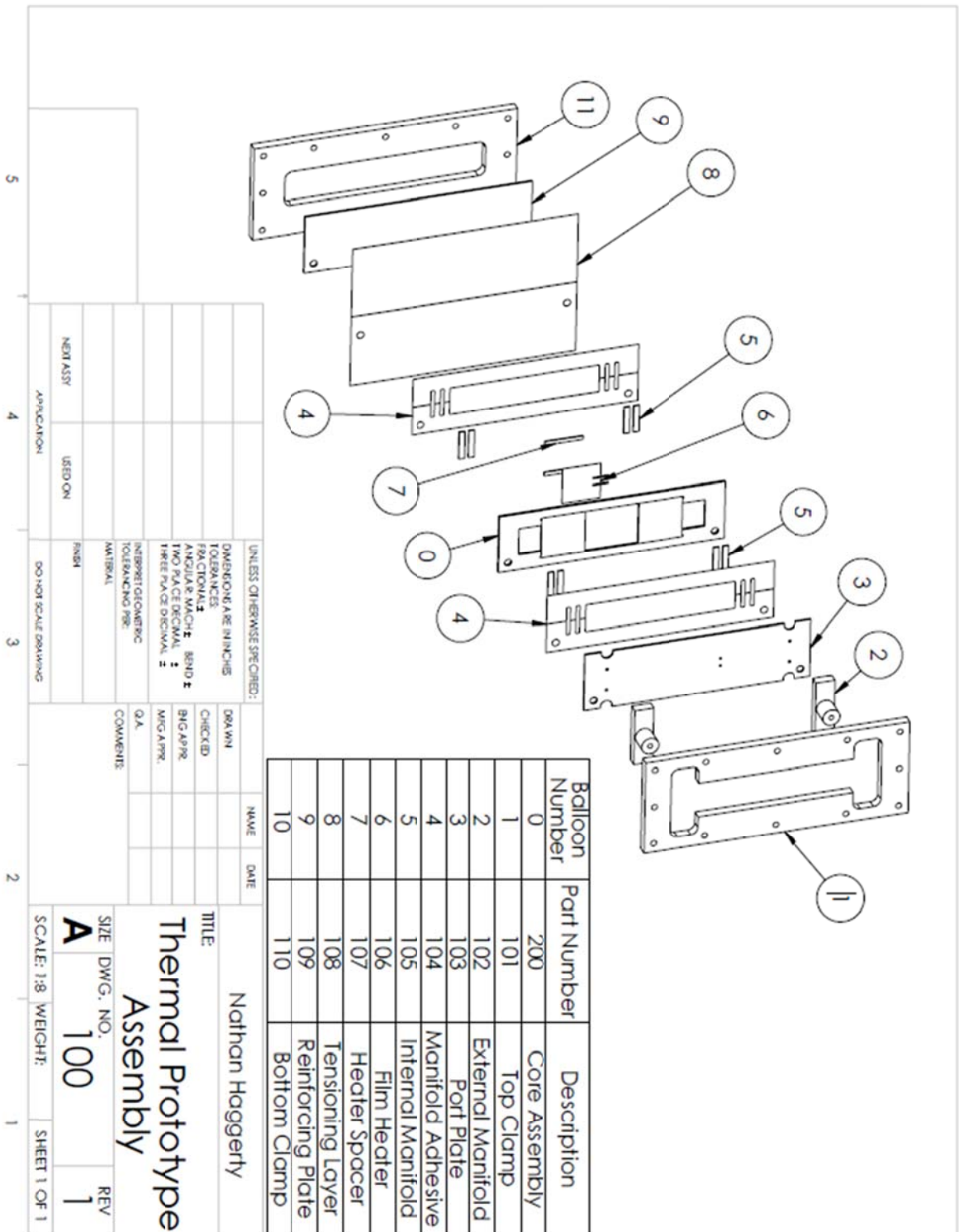
"! Cofactors to determine the reaction at point A"
C[2]=sinh(kl)
C[3]=cosh(kl)-1
C[4]=sinh(kl)-kl
Ca[3]=cosh(k*(l-a))-1
Ca[4]=sinh(k*(l-a))-k*(l-a)
Ca[5]=Ca[3]-(K^2/2)*(L-a)^2
R_a=(w_a/k)*((C[3]*Ca[4]-C[2]*Ca[5])/(C[3]^2-C[2]*C[4])) "Reaction force at point a"
M_a=(-w_a/k^2)*((C[4]*Ca[4]-C[3]*Ca[5])/(C[3]^2-C[2]*C[4])) "Moment at point a"

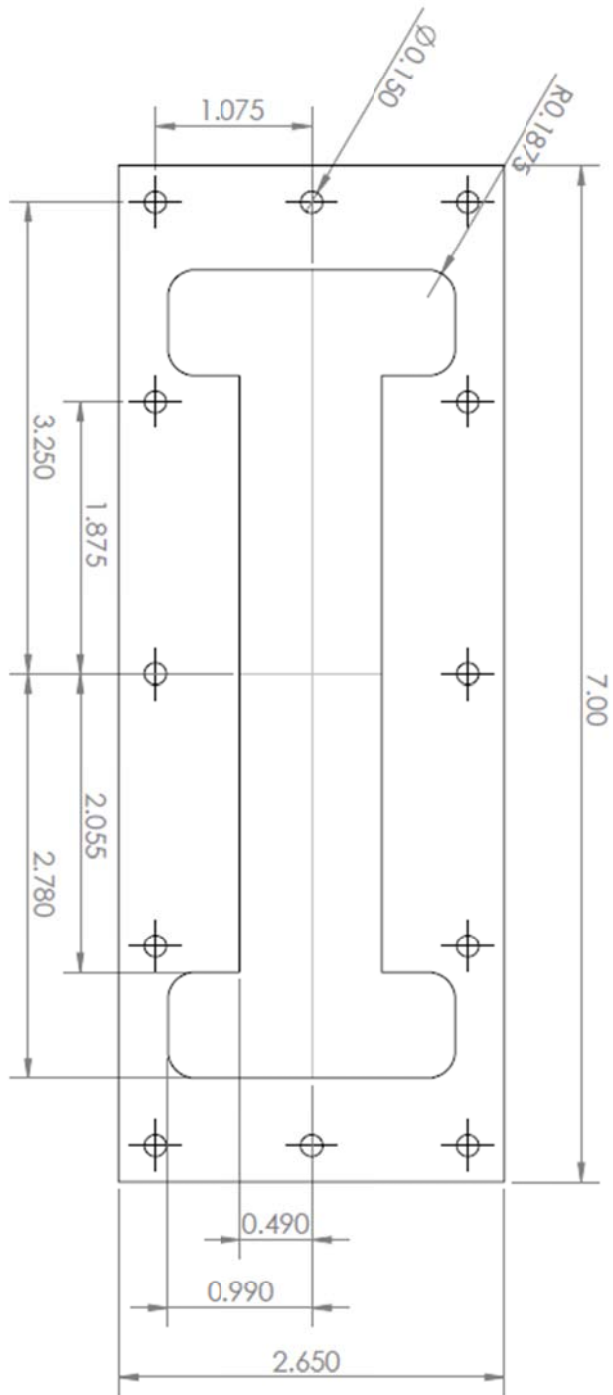
"! Cofactors for determining the deflection"
F[3]=cosh(K*x)-1
F[4]=sinh(k*x)-K*x
Fa[3]=cosh(k*(x-a))-1
Fa[5]=Fa[3]-(k^2/2)*(x-a)^2
LT_y=(-w_a/(P*k^2))*Fa[5]

Deflection=(M_a/P)*F[3]+R_a/(P*k)*F[4]+LT_y "Deflection at the center of the beam"
deflection_in=deflection*convert(m,in) "Deflection in inches"
Axc=h*D "Cross sectional area of the beam"
Force\area=P/Axc
{delta_cant=(-w_a*L^4)/(384*E*I)} "Cantilevered beam"
Percent=(Deflection/((56*10^(-6)) [m]))*100 "Percent deflection"

```

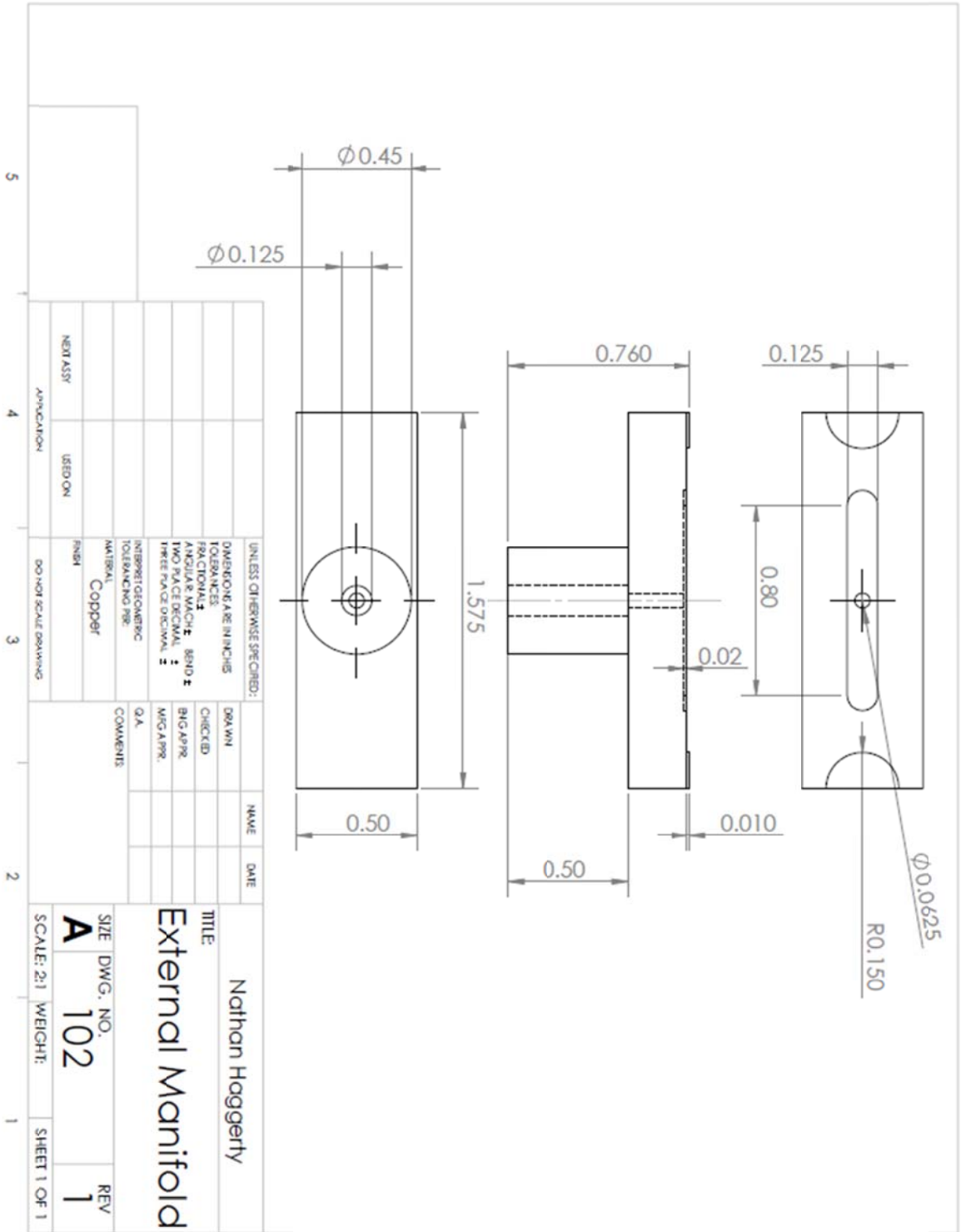
Engineering Drawings



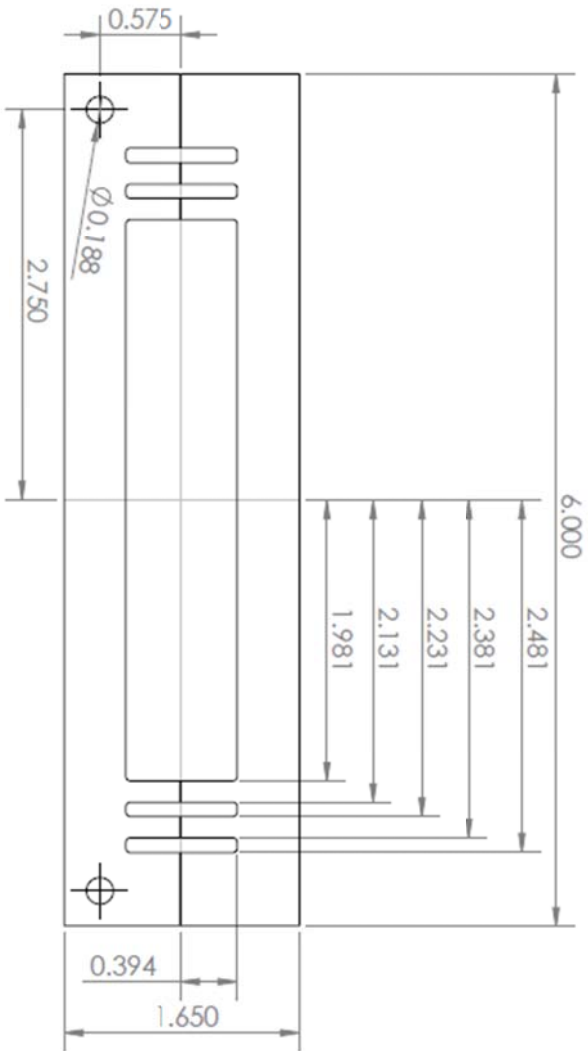


NOTES:  
1. Part to be 0.25 inch thick Aluminum

UNLESS OTHERWISE SPECIFIED:		DRAWN	NAME	DATE	TITLE	
DIMENSIONS ARE IN INCHES		CHECKED			Nathan Hoggerly	
TOLERANCES:		BNG APPR			Top Clamp	
FRACTIONS: 1/16		MFG APPR			SIZE DWG. NO.	REV
ANGULAR: MATCH BEND		Q.A.			A	1
TWO PLACE DECIMAL		COMMENTS			SCALE: 1:2 WEIGHT:	SHEET 1 OF 1
THREE PLACE DECIMAL						
INTERPRET DIMENSIONAL TOLERANCING PER:						
MATERIAL: Aluminum						
FINISH:						
NEXT ASSY:						
USED ON:						
APPLICATION:						
DO NOT SCALE DRAWING						



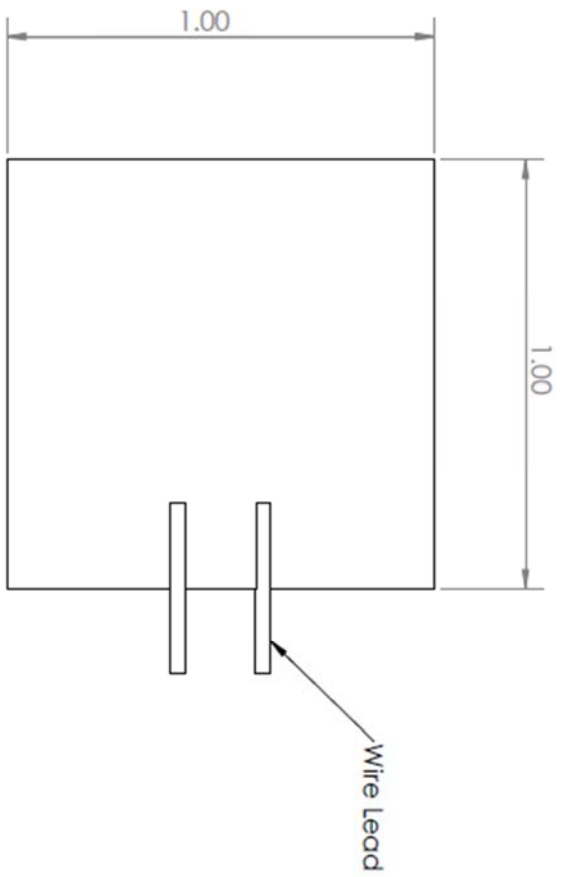




NOTES:  
 1. Part to be made from 0.0022" transfer tape

UNLESS OTHERWISE SPECIFIED:		DRAWN	NAME	DATE
DIMENSIONS ARE IN INCHES		CHECKED		
TOLERANCES:		BIG APPR		
FRACTIONAL: ±		MIG APPR		
DECIMAL: ±		Q.A.		
THREE PLACE DECIMAL: ±		COMMENTS		
INTERPRET GEOMETRIC TOLERANCING PER:				
MATERIAL:				
Finish				
Transfer Tape				
NEW ASSY	USED ON			
APPLICATION				
5	4	3	2	1
DO NOT SCALE DRAWING				
TITLE:		Nathan Haggerty		
Manifold Adhesive				
SIZE	DWG. NO.	REV		
A	104	1		
SCALE: 1:2	WEIGHT:	SHEET 1 OF 1		



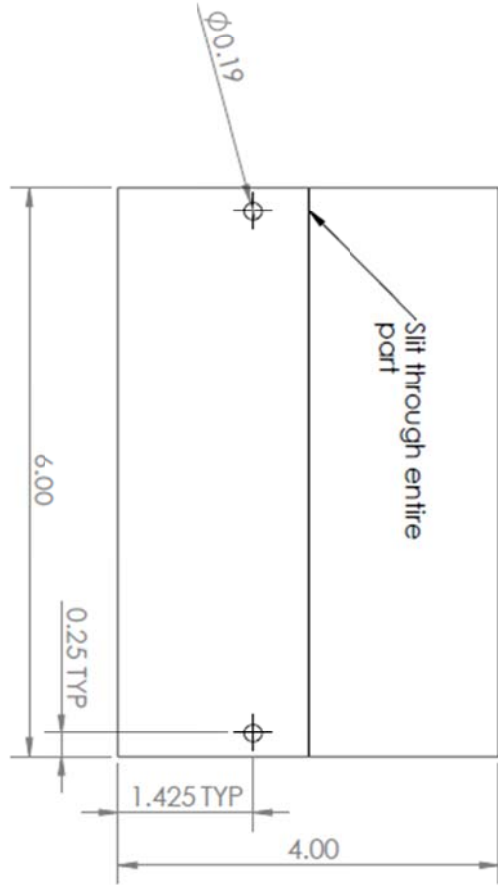


NOTES:  
 1. Part is an Omega KHLV-101/5-P film heater

UNLESS OTHERWISE SPECIFIED:		DRAWN	NAME	DATE	TITLE
TOLERANCES	FRAC TIONALS				Nathan Hogarty Film Heater
ANGULAR	MACH	CHECKED			
TWO FACE DECIMAL	BEND	BIG APPR			
THREE FACE DECIMAL		MCG APPR			
INTERPRETING DIMENSIONING PER:		Q.A.			SIZE DWG. NO.
MATERIAL		COMMENTS			<b>A</b> 106
FINISH					SCALE: 2:1 WEIGHT:
USED ON					1
APPLICATION					SHEET 1 OF 1



NOTES:  
 1. Part to be made from 0.001" brass sheet



UNLESS OTHERWISE SPECIFIED:		DRAWN	NAME	DATE
DIMENSIONS ARE IN INCHES	TOLERANCES	CHECKED		
1 DECIMAL	FRACTIONS	BIG APPR.		
ANGULAR MATCH	BEND	MIC APPR.		
TWO PLACE DECIMAL	THREE PLACE DECIMAL	COMMENTS		
INTERPRET GEOMETRIC TOLERANCING PER MATERIAL		Q.A.		
FINISH				
BRASS				
NEUTRAL	USED ON			
APPLICATION	DO NOT SCALE DRAWING			

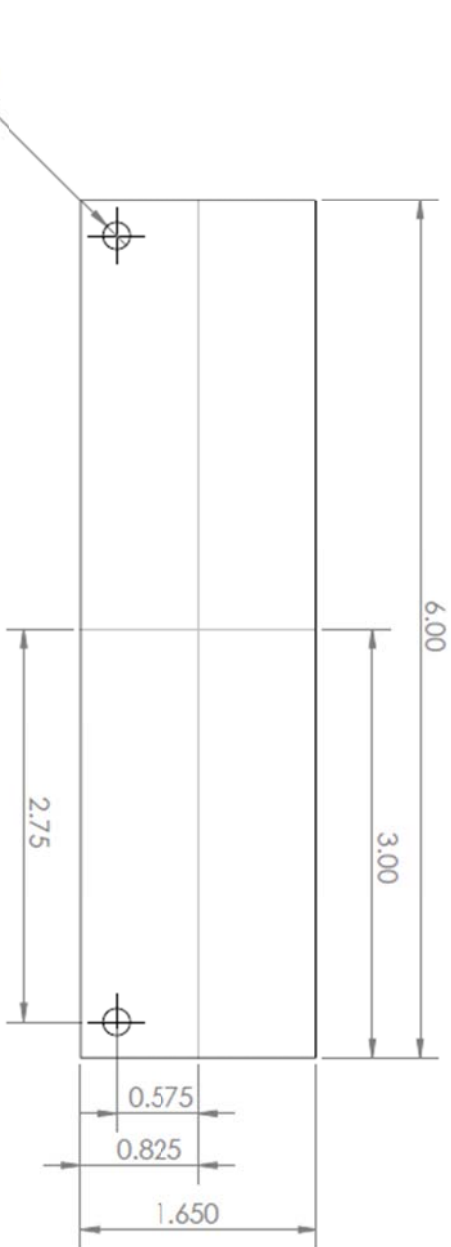
5 4 3 2 1

Nathan Hogarty  
 TITLE: Tensioning Layer

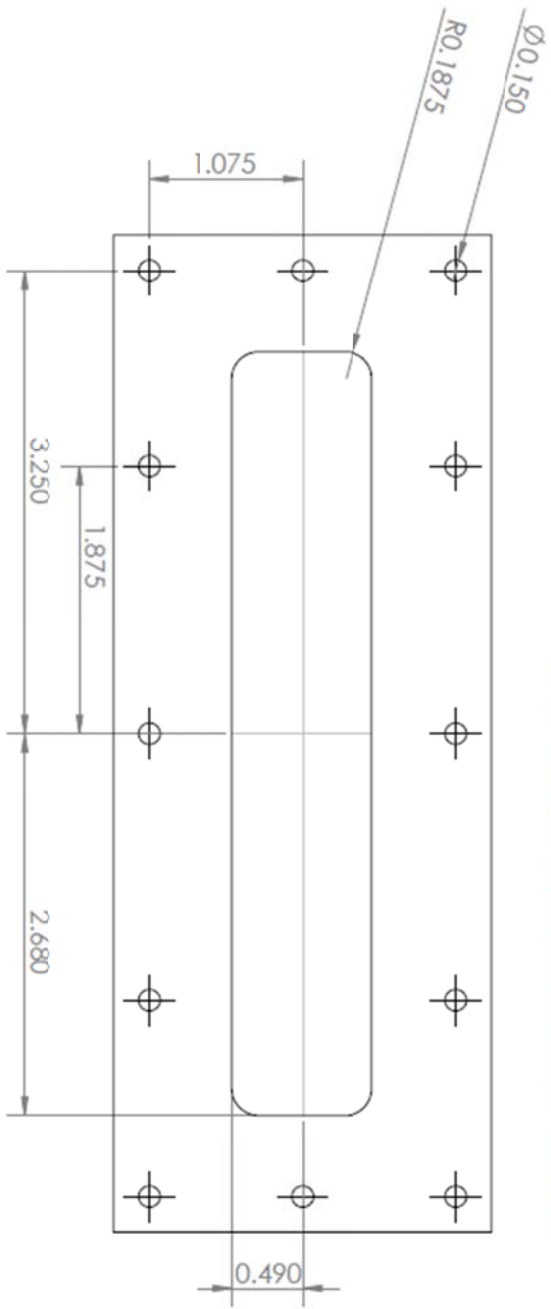
SIZE DWG. NO. 108 REV 1

SCALE: 1:2 WEIGHT: SHEET 1 OF 1

NOTES:  
 1. Part to be made from 0.048" stainless steel plate

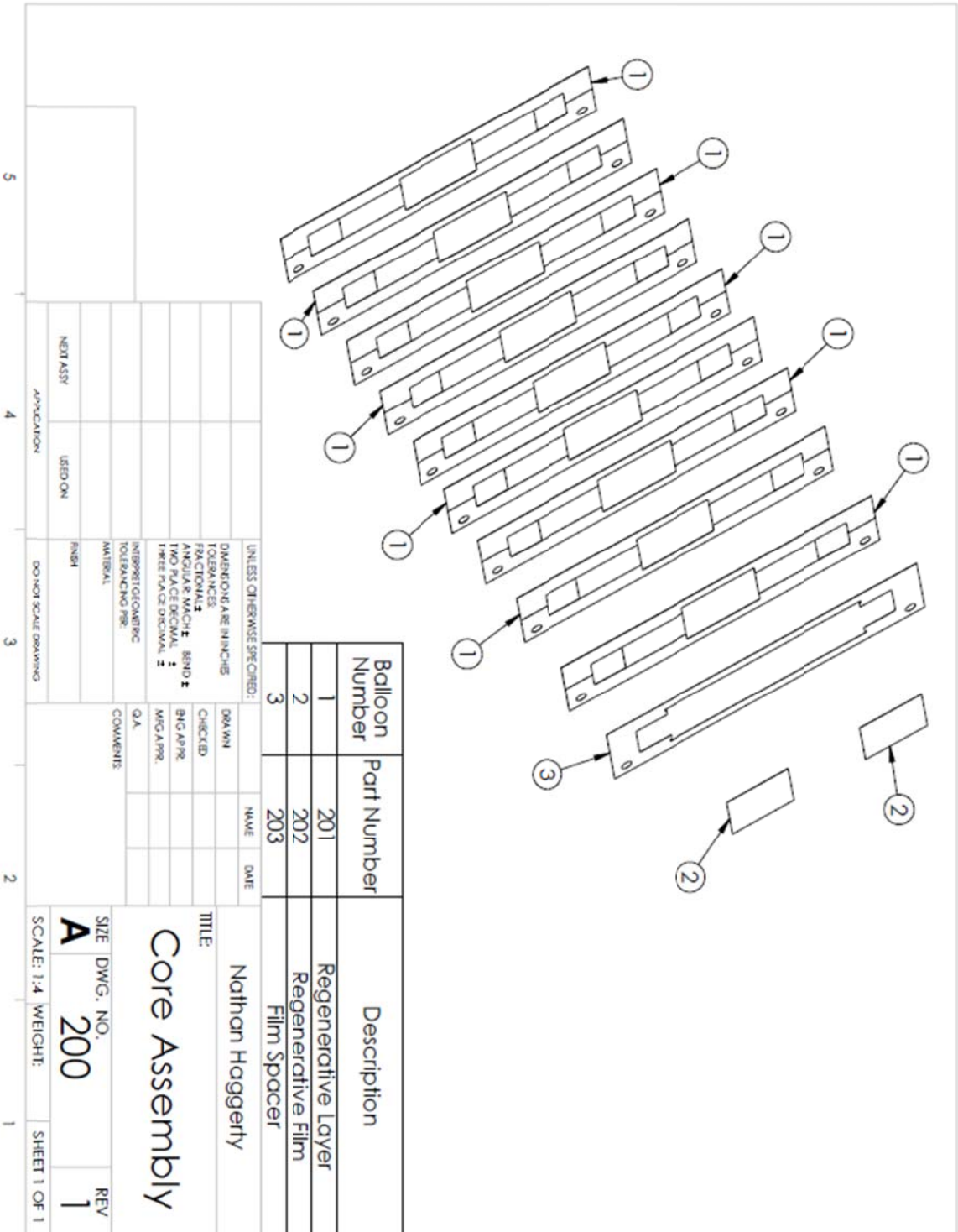


UNLESS OTHERWISE SPECIFIED: DIMENSIONS ARE IN INCHES TOLERANCES FRACTIONAL ANGULAR & HOLE BOND TWO PLACE DECIMAL THREE PLACE DECIMAL		DRAWN	NAME	DATE	TITLE <b>Reinforcing Plate</b> Nathan Hogarty
MATERIAL Stainless Steel		CHECKED			
FINISH		MSG APPR.			SIZE DWG. NO. <b>A 109</b>
INTERPRET OF QUANTIC TOLERANCING PER:		Q.A.			SCALE: 1:1 WEIGHT: SHEET 1 OF 1
APPLICATION		USED ON	DO NOT SCALE DRAWING		REV <b>1</b>
NEXT ASSY					



NOTES:  
1. Part to be made from 0.25 in thick Aluminum

UNLESS OTHERWISE SPECIFIED:		DRAWN	NAME	DATE	TITLE <b>Nathan Haggerty</b>  <b>Bottom Clamp</b>
DIMENSIONS ARE IN INCHES		CHECKED			
TOLERANCES		BIG APPR.			SIZE DWG. NO. <b>A 110</b>
FRACTIONS		MFG APPR.			
ANGULAR MATCH - 80D		Q.A.			SCALE: 1:2 WEIGHT: 1 SHEET 1 OF 1
TWO PLACE DECIMAL		COMMENTS			
THREE PLACE DECIMAL					
INTERPRETING/ENGINEERING TOLERANCING PER:					
MATERIAL					
Aluminum					
FINISH					
NEXT ASSY					
USED ON					
APPLICATION					
DO NOT SCALE DRAWING					



Balloon Number	Part Number	Description
1	201	Regenerative Layer
2	202	Regenerative Film
3	203	Film Spacer

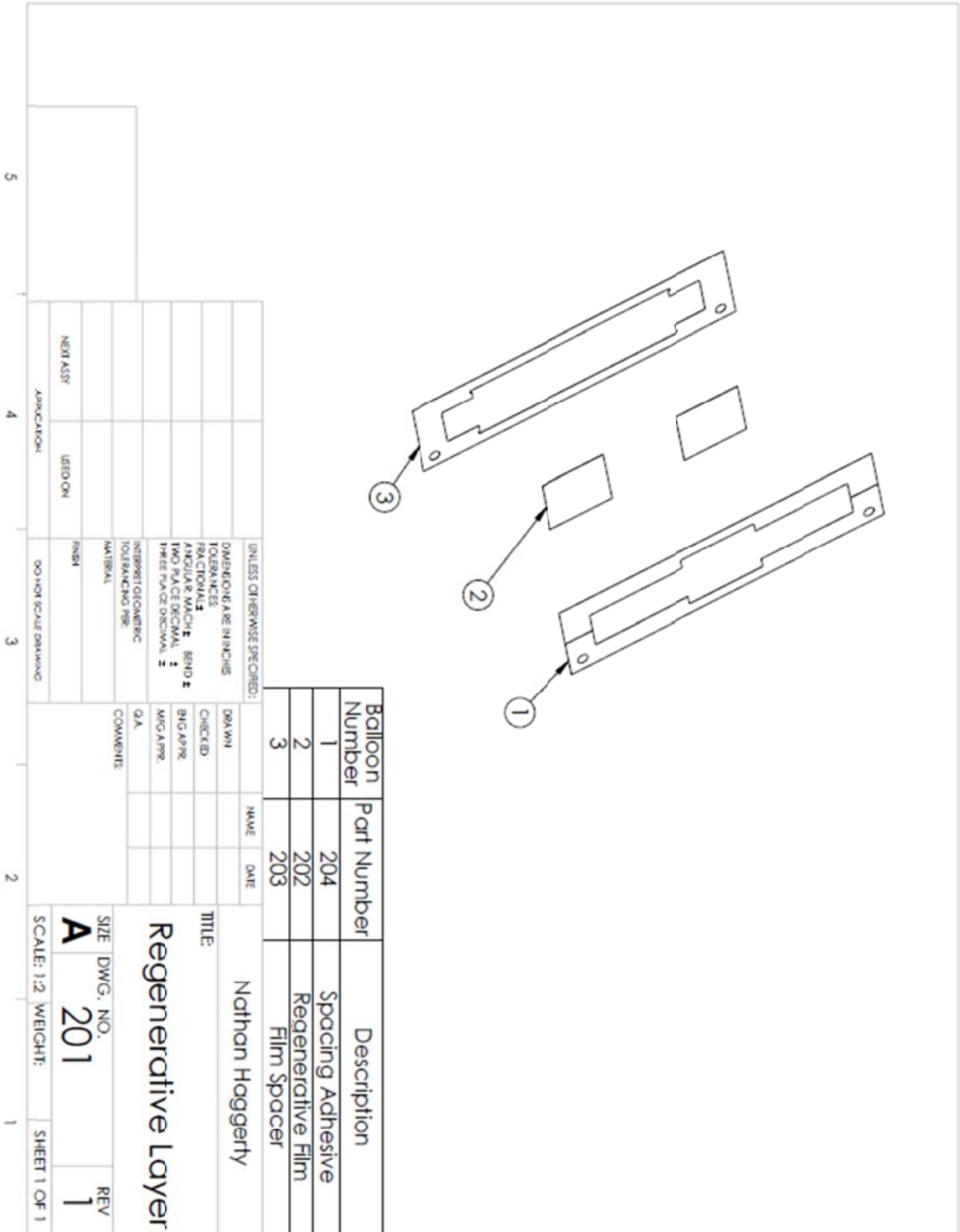
UNLESS OTHERWISE SPECIFIED:		DRAWN	NAME	DATE
TOLERANCES	FRACTIONAL	CHECKED		
ANGULAR MATCH	BOND	BIG APPR		
TWO FACE DECIMAL		MFG APPR		
THREE FACE DECIMAL		Q.A.		
INTERSECTING DIMENSION		COMMENTS		
TOLERANCING PER				
MATERIAL				
FINISH				
USED ON				
APPLICATION				
NEXT ASSY				

5 4 3 2 1

SCALE: 1:4 WEIGHT: SHEET 1 OF 1

TITLE:  
**Core Assembly**  
 Nathan Haggerty

SIZE DWG. NO.  
**A 200**  
 REV  
**1**



Balloon Number	Part Number	Description
1	204	Spacing Adhesive
2	202	Regenerative Film
3	203	Film Spacer

UNLESS OTHERWISE SPECIFIED:  
 DIMENSIONS ARE IN INCHES  
 TOLERANCES:  
 FRACTIONS ±  
 ANGULAR MATCH ± BEND ±  
 TWO PLACE DECIMAL ±  
 THREE PLACE DECIMAL ±  
 INTERPRET GEOMETRIC TOLERANCING PER MATERIAL  
 FINISH  
 DO NOT SCALE DRAWING

DRAWN: \_\_\_\_\_ NAME: \_\_\_\_\_ DATE: \_\_\_\_\_  
 CHECKED: \_\_\_\_\_  
 MFG APPR: \_\_\_\_\_  
 Q.A. \_\_\_\_\_  
 COMMENTS: \_\_\_\_\_

TITLE: **Nathan Hoggerly**  
**Regenerative Layer**

SIZE: \_\_\_\_\_ DWG. NO.: **201** REV: **1**  
 SCALE: 1:2 WEIGHT: \_\_\_\_\_ SHEET 1 OF 1

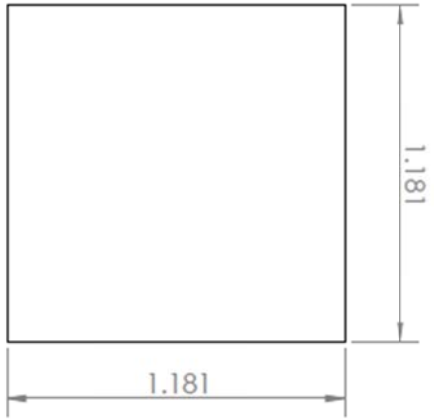
5

4

3

2

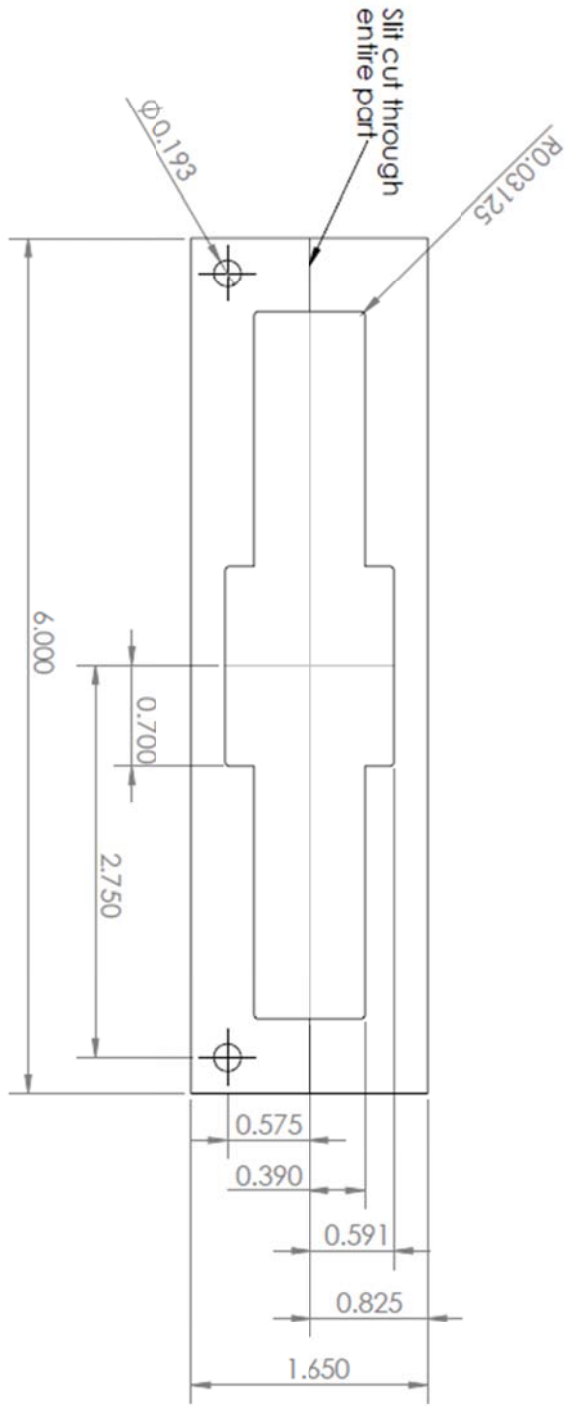
1



NOTES:  
 1. Part to be cut from a sheet of 0.005" Polyvinylidene Floride (PVDF)

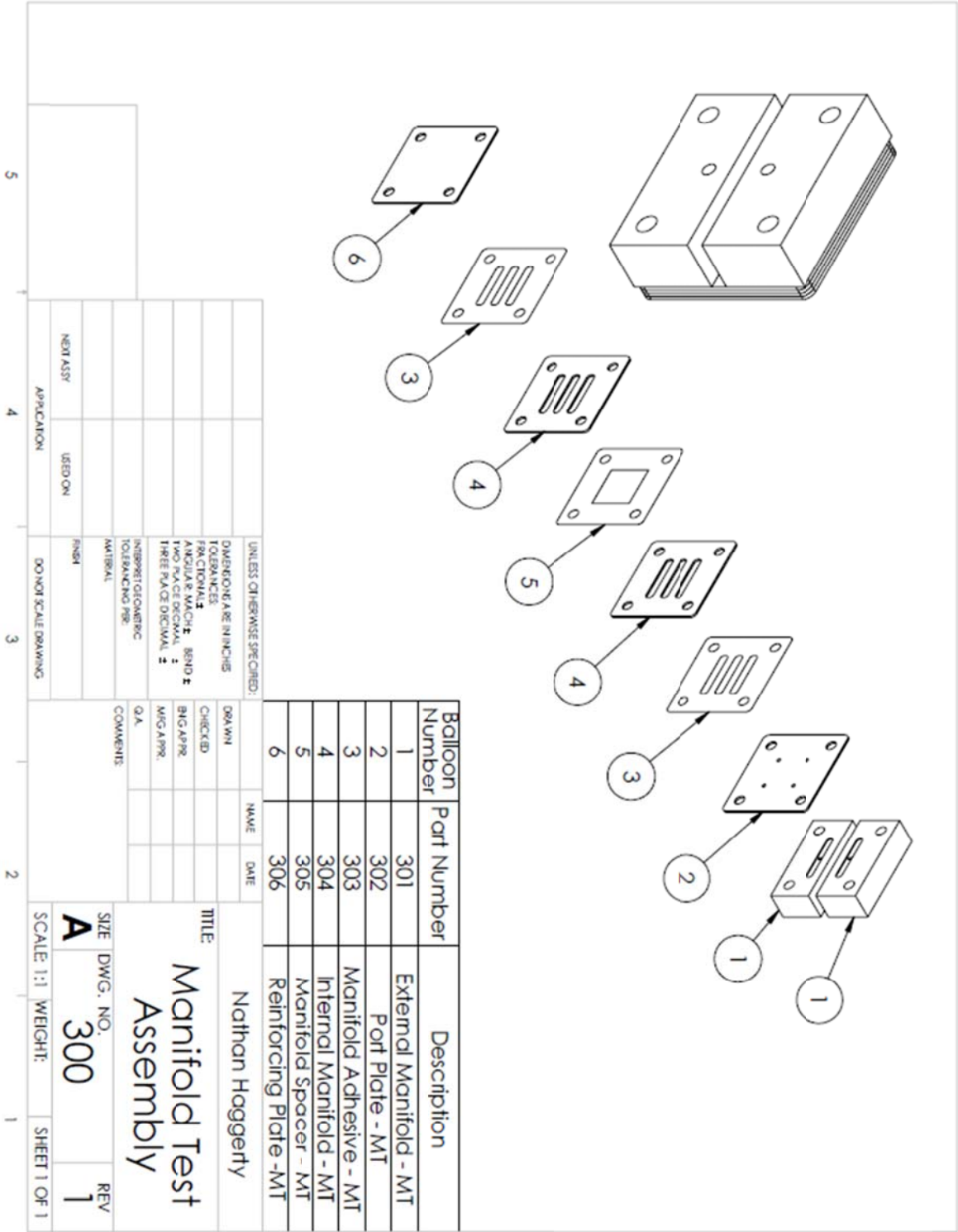
UNLESS OTHERWISE SPECIFIED:		DRAWN	NAME	DATE	TITLE: <b>Nathan Hoggerly</b>  <b>Regenerative Film</b>	SIZE	DWG. NO.	REV
DIMENSIONS ARE IN INCHES TOLERANCES: FRACTIONAL ± ANGULAR MATCH ± .0002 TWO PLACE DECIMAL ± THREE PLACE DECIMAL ±		CHECKED				SCALE: 2:1	WEIGHT:	SHEET 1 OF 1
INTERPRETING/COMERC TOLERANCING PER: MATERIAL: <b>PVDF</b>		COMMENTS						
FINISH								
NEXT ASSY								
APPLICATION								
USED ON								
DO NOT SCALE DRAWING								
5	4	3	2	1				





NOTES:  
 1. Part to be 0.0022" transfer tape

UNLESS OTHERWISE SPECIFIED:		DRAWN		NAME		DATE	
DIMENSIONS ARE IN INCHES		CHECKED		Nathan Haggerty			
TOLERANCES:		BNC APPR					
FRACTIONAL: $\pm$		MFG APPR					
ANGULAR: MACH: BEND: $\pm$		COMMENTS					
TWO PLACE DECIMAL: $\pm$		G.A.					
THREE PLACE DECIMAL: $\pm$		Transfer tape					
INTERPRET TOLERANCE		MATERIAL					
TOLERANCE PER:		FINISH					
NEXT ASSY		USED ON					
APPLICATION		DO NOT SCALE DRAWING					
5		4		3		2	
						SCALE: 1:2 WEIGHT: 1	
						SHEET 1 OF 1	
						REV 1	
						SIZE DWG. NO. 204	
						TITLE Spacing Adhesive	

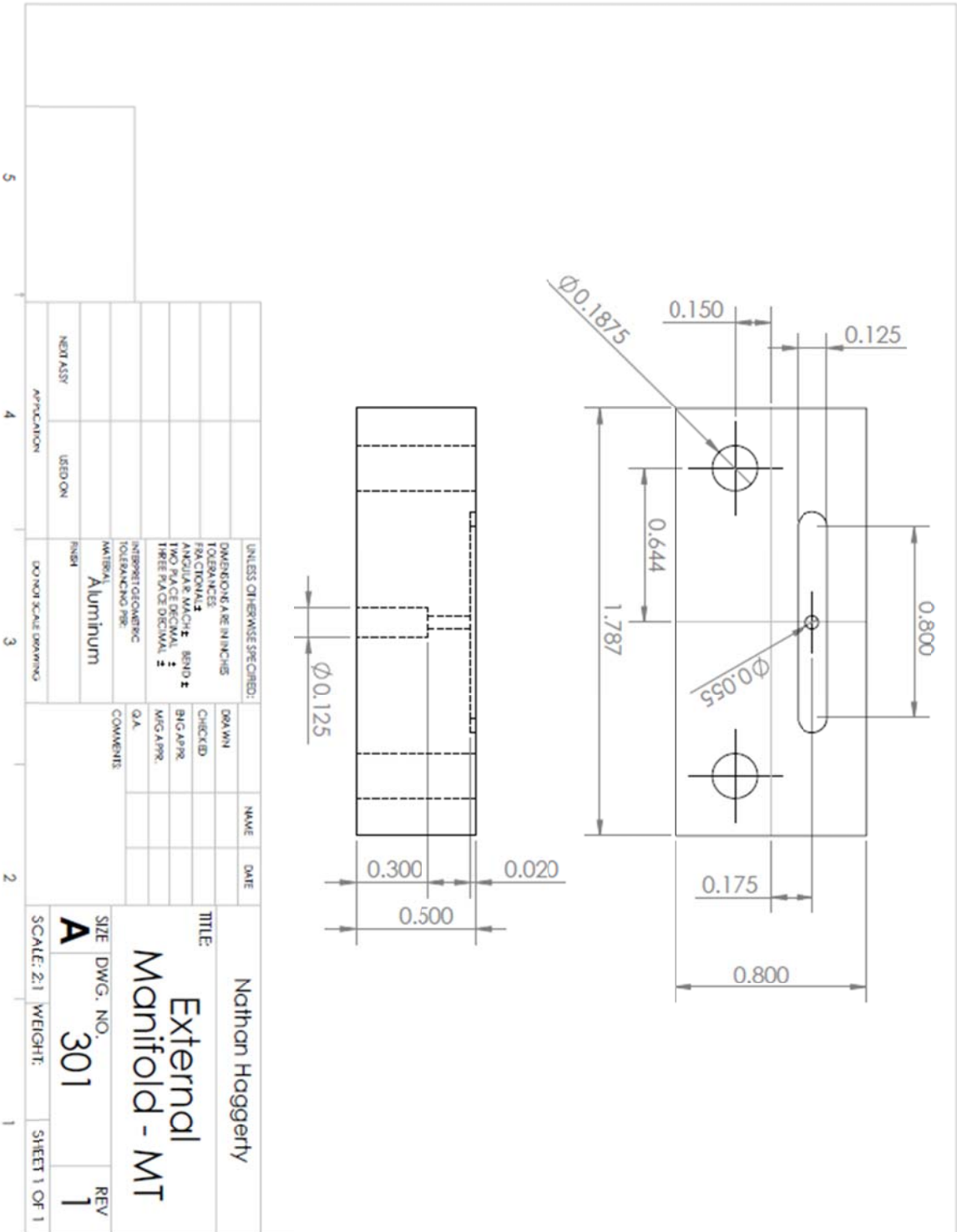


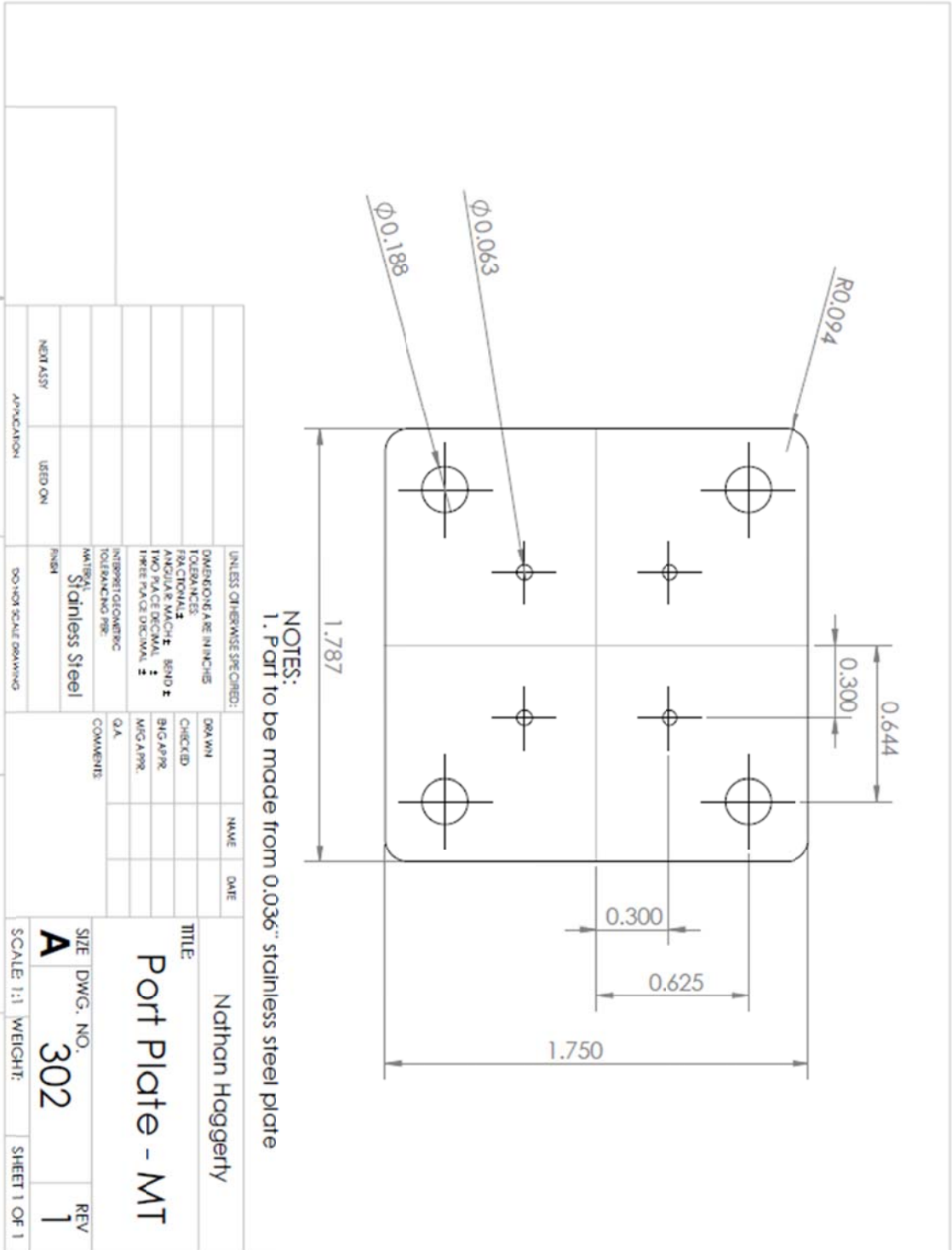
Balloon Number	Part Number	Description
1	301	External Manifold - MT
2	302	Port Plate - MT
3	303	Manifold Adhesive - MT
4	304	Internal Manifold - MT
5	305	Manifold Spacer - MT
6	306	Reinforcing Plate -MT

UNLESS OTHERWISE SPECIFIED:  
 DIMENSION-BARE IN INCHES  
 TOLERANCES:  
 FRACTIONAL: ±  
 ANGULAR MATCH: BEND ±  
 TWO PLACE DECIMAL: ±  
 THREE PLACE DECIMAL: ±  
 INTERPRETING GEOMETRIC TOLERANCING PER MATERIAL  
 FINISH  
 DO NOT SCALE DRAWING  
 USED ON  
 APPLICATION  
 NEXT ASSY

DRAWN: \_\_\_\_\_ NAME: Nathan Hoggerly DATE: \_\_\_\_\_  
 CHECKED: \_\_\_\_\_  
 ENG APPR: \_\_\_\_\_  
 MFG APPR: \_\_\_\_\_  
 Q.A. \_\_\_\_\_  
 COMMENTS: \_\_\_\_\_

TITLE: **Manifold Test Assembly**  
 SIZE: **A** DWG. NO.: **300** REV: **1**  
 SCALE: 1:1 WEIGHT: \_\_\_\_\_ SHEET 1 OF 1





NOTES:  
 1. Part to be made from 0.036" stainless steel plate

UNLESS OTHERWISE SPECIFIED:		DRAWN	NAME	DATE
DIMENSIONS ARE IN INCHES		CHECKED		
TOLERANCES		ENG APPR		
FRACTIONAL		MFG APPR		
ANGULAR MATCH		Q.A.		
TWO PLACE DECIMAL		COMMENTS		
THREE PLACE DECIMAL				
INTERPRET GEOMETRIC TOLERANCING PER:				
MATERIAL: Stainless Steel				
FINISH: RNSM				
NEXT ASSY	USED ON			
APPLICATION	DO NOT SCALE DRAWING			
5	4	3	2	1

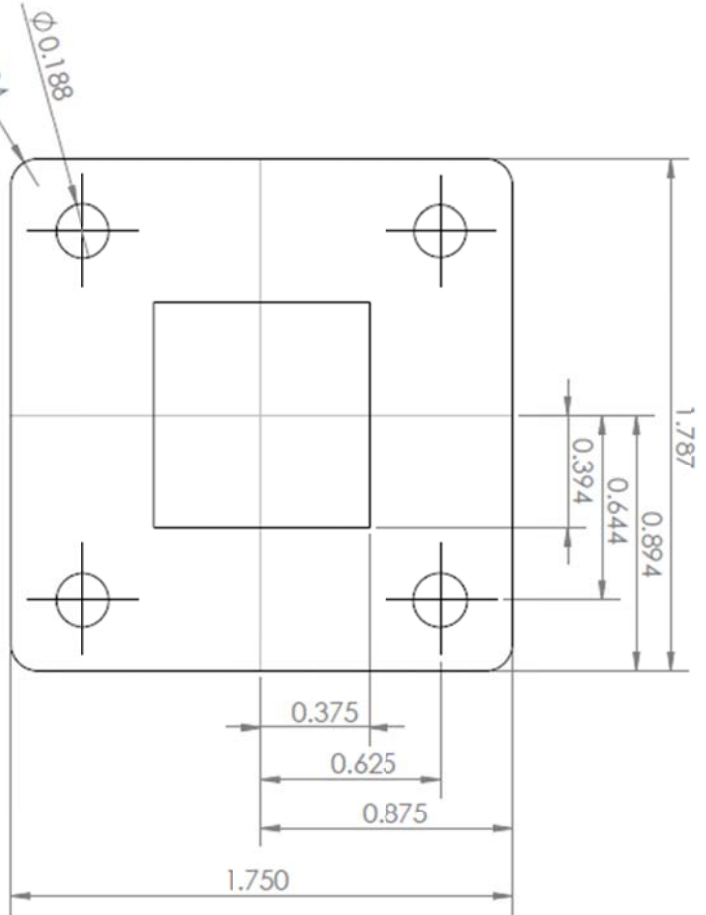
Nathan Hoggerly  
 TITLE  
 Port Plate - MT

SIZE: A  
 DWG. NO.: 302  
 SCALE: 1:1  
 WEIGHT:  
 SHEET 1 OF 1

REV 1

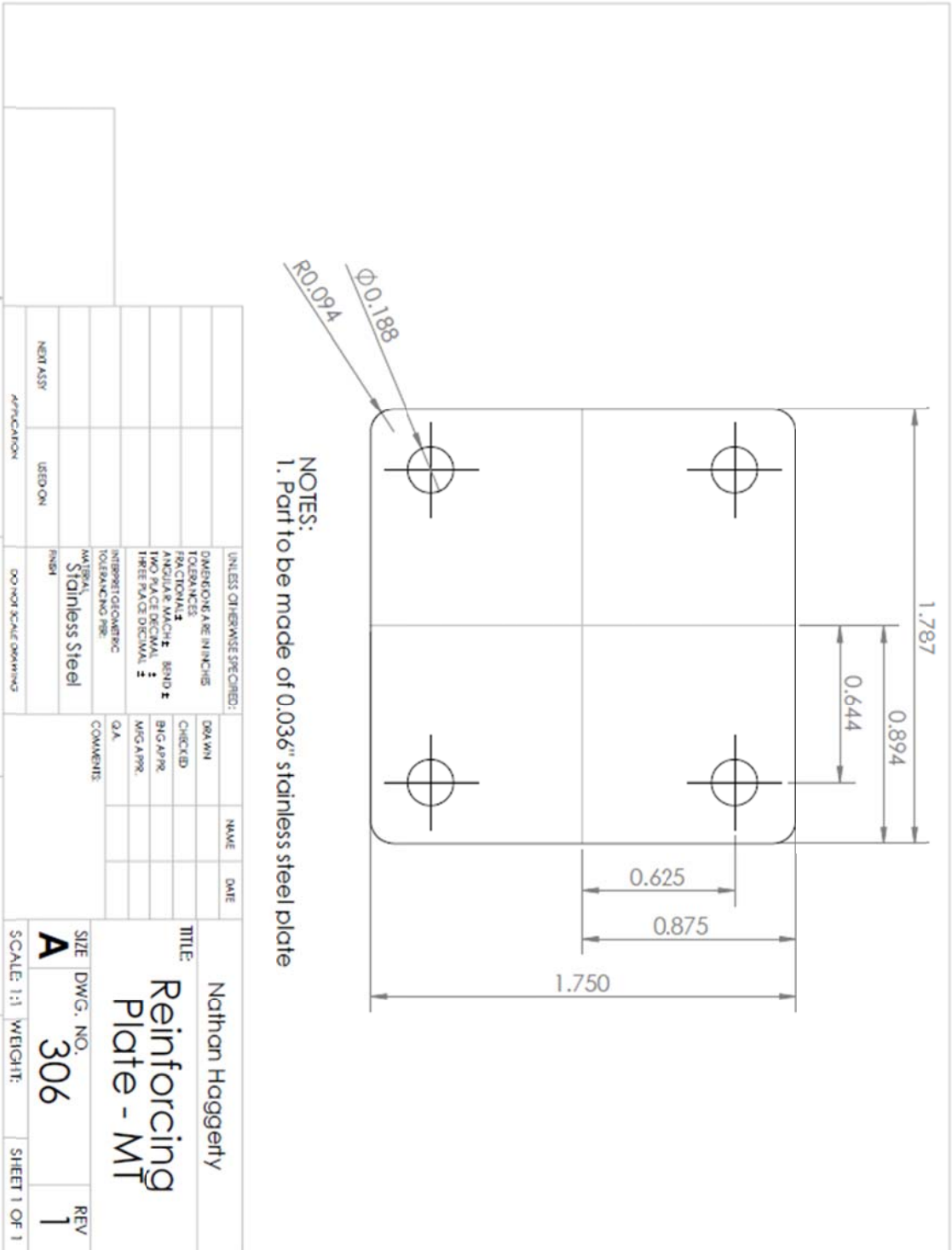






NOTES:  
1. Part to be made from 0.0022" transfer tape

UNLESS OTHERWISE SPECIFIED:		DRAWN	NAME	DATE	TITLE
DIMENSIONS ARE IN INCHES	TOLERANCES	CHECKED			Nathan Haggerty
FRACTIONAL	ANGULAR & MATCH	BIG APPR			Manifold
TWO PLACE DECIMAL	THREE PLACE DECIMAL	MISC APPR			Spacer - MT
INTERPRET GEOMETRIC TOLERANCING PER MATERIAL	FINISH	COMMENTS			
	Transfer Tape				
NEUTRAL	USED ON				SIZE DWG. NO.
APPLICATION	DO NOT SCALE DRAWING				A 305
					SCALE 1:1 WEIGHT:
					1
					SHEET 1 OF 1
					REV
					1



NOTES:  
 1. Part to be made of 0.036" stainless steel plate